APPLICATION OF ERS-1 AND TOPEX/POSEIDON ALTIMETRY USING PRECISE ORBITS

CHRISTOPHER WAI LAM

Doctor of Philosophy

THE UNIVERSITY OF ASTON IN BIRMINGHAM

May 1994

THE UNIVERSITY OF ASTON IN BIRMINGHAM

APPLICATION OF ERS-1 AND TOPEX/POSEIDON ALTIMETRY USING PRECISE ORBITS

CHRISTOPHER WAI LAM
Doctor of Philosophy

May 1994

Thesis Summary

The work described in this thesis concerns the application of radar altimetry, collected from the ERS-1 and TOPEX/POSEIDON missions, to precise satellite orbits computed at Aston University. The data is analysed in a long arc fashion to determine range biases, time tag biases, sea surface topographies and to assess the radial accuracy of the generated orbits through crossover analysis.

A sea surface variability study is carried out for the North Sea using repeat altimeter profiles from ERS-1 and TOPEX/POSEIDON in order to verify two local U.K. models for ocean tide and storm surge effects.

An on-site technique over the English Channel is performed to compute the ERS-1, TOPEX and POSEIDON altimeter range biases by using a combination of altimetry, precise orbits determined by short arc methods, tide gauge data, GPS measurements, geoid, ocean tide and storm surge models.

The remaining part of the thesis presents some techniques for the short arc correction of long arc orbits. Validation of this model is achieved by way of a comparison with actual SEASAT short arcs. Simulations are performed for the ERS-1 microwave tracking system, PRARE, using the range data to determine time dependent orbit corrections. Finally, a brief chapter is devoted to the recovery of errors in station coordinates by the use of multiple short arcs.

Keywords and Phrases

- Satellite altimetry
- Precise orbit determination
- PRARE simulations
- Altimeter bias
- Short arcs

Acknowledgements

I would like to thank sincerely the following people and establishments for their assistance during my period of study : -

- Dr. Philip Moore, for providing me this opportunity to do research and also for his kind and patient supervision over the last three years,

- Dr. Philip Woodworth, for arranging computer facilities at the Proudman Oceanographic Laboratory (POL) at Bidston for my work; also for his advice and suggestions for the work carried out in chapters 5 and 6,

- the staff at POL including Roger Flather, Chris Hughes, Roger Proctor, Sheila Shaw and Jane Smith for their help and advice and the provision of ocean tide, storm surge and tide gauge data,

- Graham Appleby and Dr. Andrew Sinclair at the Royal Greenwich Observatory for supplying laser range data, start vectors, etc. for orbit determination at Aston,

- my colleagues Stuart Carnochan, Dr. Simon Ehlers, Dr. Rory Gray, Gordon Jolly and Ruaraidh Mackenzie for their kind assistance, time and advice over many months,

and finally, I would like to thank NERC, POL and Aston University for their financial assistance during this research.

LIST OF CONTENTS

CHAPTER 4 LONG ARC ANALYSIS OF ERS-1 AND TOPEX/POSEIDON ALTIMETRY

CHAPTER 5 SEA SURFACE VARIABILITY OVER THE NORTH SEA

CHAPTER 6 ON-SITE CALIBRATION OF THE ERS-1, TOPEX AND POSEIDON ALTIMETERS

CHAPTER 7 SHORT ARC ANALYSIS

CHAPTER 8 PRARE SIMULATIONS FOR ERS-1

LIST OF TABLES

LIST OF FIGURES

CHAPTER 1

INTRODUCTION

This thesis concentrates on altimetric data obtained from the ERS-1 and TOPEX/POSEIDON missions. These two satellites alone are collecting an unprecedented amount of quality data and it is of paramount importance that orbits of a high precision are computed. Consequently, the observed sea surface height may be deduced accurately.

The work undertaken in this thesis is primarily concerned with the application of altimetry to precise satellite orbits. The determination of the range biases for ERS-1, TOPEX and POSEIDON altimeters is of key importance and methods for computing these values are detailed. The need for precise orbits is further investigated by the possible use of short arc techniques to improve the satellite radial component.

A brief description of the ERS-1 and TOPEX/POSEIDON missions is given in chapter 2 along with details about the instruments they carry and their orbit characteristics. Much of the work in this thesis is computer based and chapter 3 is devoted to a overview of the software used at Aston University for orbit determination.

Altimetry from both missions is analysed using long arc orbits in chapter 4. The precision of orbits deduced from laser tracking is investigated by examining the pure altimeter and crossover residuals as well as the laser residuals. Certain altimeter errors are solved for such as the range bias and time tag bias. Moreover extensive sea surface topographies are computed and plotted. In addition, a repeat track method is performed to evaluate the difference in the TOPEX and POSEIDON altimeter biases.

Chapter 5 looks at the well-established method of measuring sea surface variability using altimetry over repeating ground tracks. This work concentrates on the North Sea region where variability due to ocean circulation phenomena is known to be small. Hence this provides an opportunity to assess the accuracy of a local U.K. ocean tide (15 tidal constituents) and storm surge models provided by the Proudman Oceanographic Laboratory (POL) at Bidston, U.K.

The subject of the altimeter bias is re-investigated in chapter 6, this time using an 'on-site' or 'short arc' approach. The technique selects the English Channel as a calibration site and computes precise satellite altitudes using laser tracking from the nearby Herstmonceux laser ranger. The sea surface height is deduced from a combination of tide gauge data, GPS measurements and local models for the geoid, ocean tide and storm surge phenomena. Equating the orbital height to the altimetry and sea heights yields the observed altimeter bias.

The remainder of the thesis concentrates on short arc methods, both theoretical and practical. Chapter 7 introduces an analytical model to predict the correlations and rms errors which arise from a short arc correction procedure when solving for constant orbit corrections using laser tracking from one or more ground stations. Results from this model are compared to actual SEASAT orbits in order to validate this model.

This model is extended in chapter 8 to solve for periodic and quadratic short arc corrections in time with the aim of deducing a more precise orbit. This provides some insight as to which station configurations are most likely to reduce the correlations in the solution for the orbital parameters. Simulations are then carried out for the microwave tracking system PRARE for short arcs over the Atlantic Ocean using proposed ground sites.

Finally, chapter 9 looks briefly at the use of short arcs to correct for station coordinate errors.

It is emphasised that all orbital heights for both ERS-1 and TOPEX/POSEIDON were computed at Aston University except for the repeat track method in section 4.10 in chapter 4 and the work undertaken in Chapter 5. In both of these cases, the orbital heights were taken from the altimeter data records. The altimeter datasets used were those available at the time during a particular piece of work. For the long arc analyses in chapter 4, the ESA (European Space Agency) offline precise ocean product OPR 02 (Ocean Product 02) data for ERS-1 and the preliminary IGDRs (Intermediate Geophysical Data Records) for TOPEX/POSEIDON were utilised. In chapter 5 for the sea surface variability study over the North Sea, the preliminary NOAA data for ERS-1 and the preliminary IGDRs for TOPEX/POSEIDON were used. The on-site calibration exercise detailed in chapter 6 took advantage of the OPR 02 ERS-1 data and the full GDR TOPEX/POSEIDON data.

This research project began in October 1990 with the objective of improving long arc orbits with PRARE (Precise Range and Range-rate Equipment) data from the forthcoming ERS-1 system, to be launched in July 1991. Chapters 7 and 8 represent the preliminary analysis. The failure of PRARE shifted the project on to the analysis of satellite altimetry; the work for chapter 5 was then performed followed by chapter 6 and 9. Chapter 4 demonstrates 'state of the art' results at the time of execution in mid 1993. The author acknowledges the technological advances in the field since the work was performed. This also explains the employment of a number of gravity fields and non-gravitational (air drag) models in the course of this study.

CHAPTER 2

MISSION OVERVIEW FOR ERS-1 AND TOPEX/POSEIDON

§ 2.1 Introduction

The altimeter principle was first demonstrated on Skylab in 1973 and had a range resolution of 1 metre. In 1975, GEOS-3 flew an altimeter with an accuracy of 50 cm for over three years. Launched in 1978, SEASAT was operational for 3 months and carried an altimeter capable of 10 cm precision. It is interesting to note that SEASAT orbits at the time had a computed radial rms error of 1.5 to 2 metres, a figure obtained from an analysis of crossover residuals [Schrama, 1989]. In 1985, GEOSAT was launched and Doppler (range-rate) tracked, which somewhat limited precise orbit determination for this mission. Consequently the radial orbit accuracy of the original orbits was comparable to SEASAT but recently the accuracy has been substantially improved [Shum et al., 1990].

This chapter will present some information regarding the mission objectives of the ERS-1 and TOPEX/POSEIDON satellites. A description of the instruments which they each carry and their orbit characteristics will be outlined.

§ 2.2 ERS-1 satellite

The European Remote Sensing satellite, ERS-1, was put into orbit on 17th July 1991 by an Ariane 40 rocket launched from Kourou, French Guiana. The satellite, a product of the European Space Agency (ESA), carries a whole host of instrumentation for monitoring the Earth's environment. Figure 2.1 gives a view of ERS-1 and its payload.

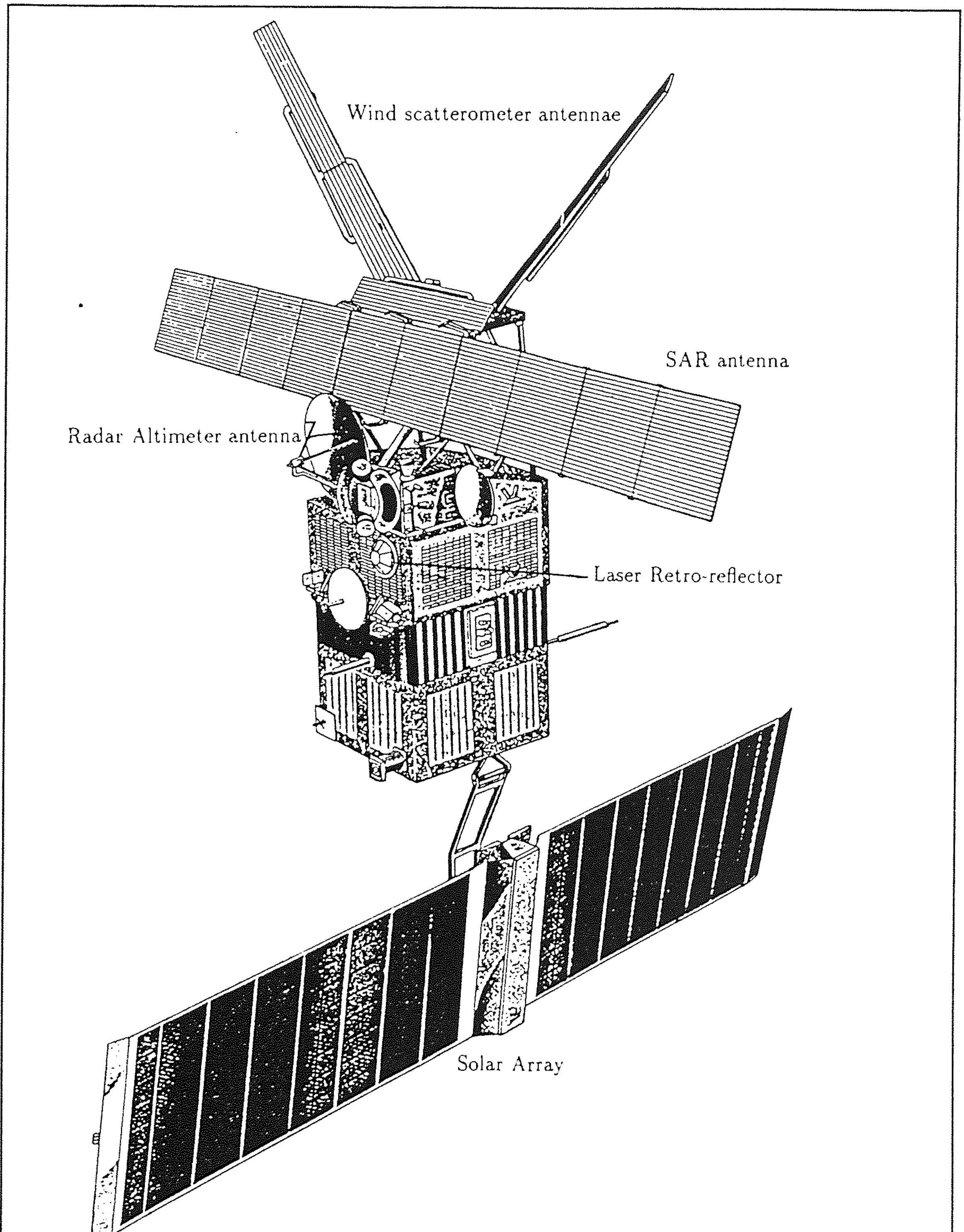

Figure 2.1

§ 2.2.1 ERS-1 instrumentation

On-board the ERS-1 payload are the following instruments :

- A nadir pointing, single frequency (13.8 GHz) **radar altimeter** capable of measuring the vertical distance from the satellite to the sea surface below to an accuracy of 5 to 10 cm after correction for instrumental and geophysical effects. These direct height measurements provide oceanographers with a valuable dataset for the continual monitoring of the Earth's oceans. The altimeter operates in either an ocean or ice mode. In addition, ocean wave heights and wind speeds are observable.

- **Along Track Scanning Radiometer**, or ATSR, which consists of two parts. Firstly, the **infrared radiometer** measures sea surface temperature, vital for global climate research. Secondly, the **microwave sounder** determines the amount of water content in the atmosphere in order to correct altimeter signals for the wet tropospheric delay.

- **Active Microwave Instrument**, or AMI, again has two components. The first is the **synthetic aperture radar**, or SAR, capable of producing high resolution imagery of the ground or sea below in strips of 100 km in width. The second part is the **wind scatterometer** and its purpose is to obtain wind speed and direction at the sea surface which may be compared to the wind data observed by the radar altimeter.

- A microwave tracking system **PRARE** (Precise Range and Range-rate Equipment). The purpose of this device was to have provided much needed range (and to a lesser extent range-rate) data for precise orbit determination over the southern oceans to complement existing laser tracking. Unfortunately, PRARE suffered fatal radiation damage soon after launch and no useful data were ever produced (see chapter 8 for a fuller description).

- **Laser Retro-Reflectors**, LRR, which is a passive device consisting of an array of corner cubes, used as a target for ground-based laser ranging stations.

§ 2.2.2 ERS-1 orbit characteristics

ERS-1 travels in a near circular, near frozen (see section 2.5) retrograde orbit inclined at 98.5° at a nominal altitude of 785 km. This orbit is also Sun-synchronous so that the precession of the orbital plane, caused by the oblateness of the Earth, exactly matches the annual revolution of the Earth around the Sun. The spacecraft must also initially overfly the proposed altimeter calibration site at the Venice Tower in the Adriatic Sea.

In altimetry, the temporal resolution of the orbit must always be compromised with the spatial resolution. For denser spatial coverage the orbit takes a longer time before it repeats. Therefore a number of mission phases were planned for ERS-1. Chronologically, these are the

- **commissioning phase** ; this began in early August 1991 and lasted until 12th December 1991. During this 3 day repeat cycle, ERS-1 completes 43 revolutions with the ground track spaced ~930 km apart at the equator. The phase was dedicated to the calibration and validation of instruments on-board ERS-1, in particular, the radar altimeter calibration over Venice Tower.

- **first ice phase** ; again this was a 3 day repeat cycle lasting from the 28th December 1991 to 30th March 1992 for the purpose of experiments over the Arctic, Antarctic and other related ice areas. The orbit was similar to the commissioning phase except that the ground track was displaced some 2^{o} to the west, a fact taken advantage of in the altimeter calibration exercise over the English Channel performed at Aston University (see chapter 6).

- **multi-disciplinary phase** ; ERS-1 entered a 35 day repeat cycle from the 14th April 1992 to 15th December 1993. Denser spatial coverage of the Earth was now possible allowing altimeter and SAR data to be more comprehensive. ERS-1 completes 501 revolutions in one cycle with the ground track spaced ~ 80 km apart at the equator.

- **second ice phase** ; similar to the first ice phase for the period January to March 1994.

- **geodetic phase** ; from April 1994 until the end of the mission, ERS-1 is planned to fly a repeat cycle of 168 days in which ERS-1 orbits the Earth 2411 times yielding a ground track spaced ~16 km apart at the equator. The objective is to acquire a high density altimetric dataset in an effort to improve the marine geoid.

The mission is proposed to last for at least 3 years. A follow-up project, appropriately named ERS-2, will fly 1994/5. The payload and orbit characteristics are expected to be similar to ERS-1 but with the emphasis on a 35 day repeat cycle.

§ 2.3 TOPEX/POSEIDON satellite

This mission is a joint venture between the U.S. and French space agencies, NASA and CNES. The spacecraft was launched on 10th August 1992 on a Ariane 42P rocket vehicle from Kourou, French Guiana. Figure 2.2 provides the view of the satellite.

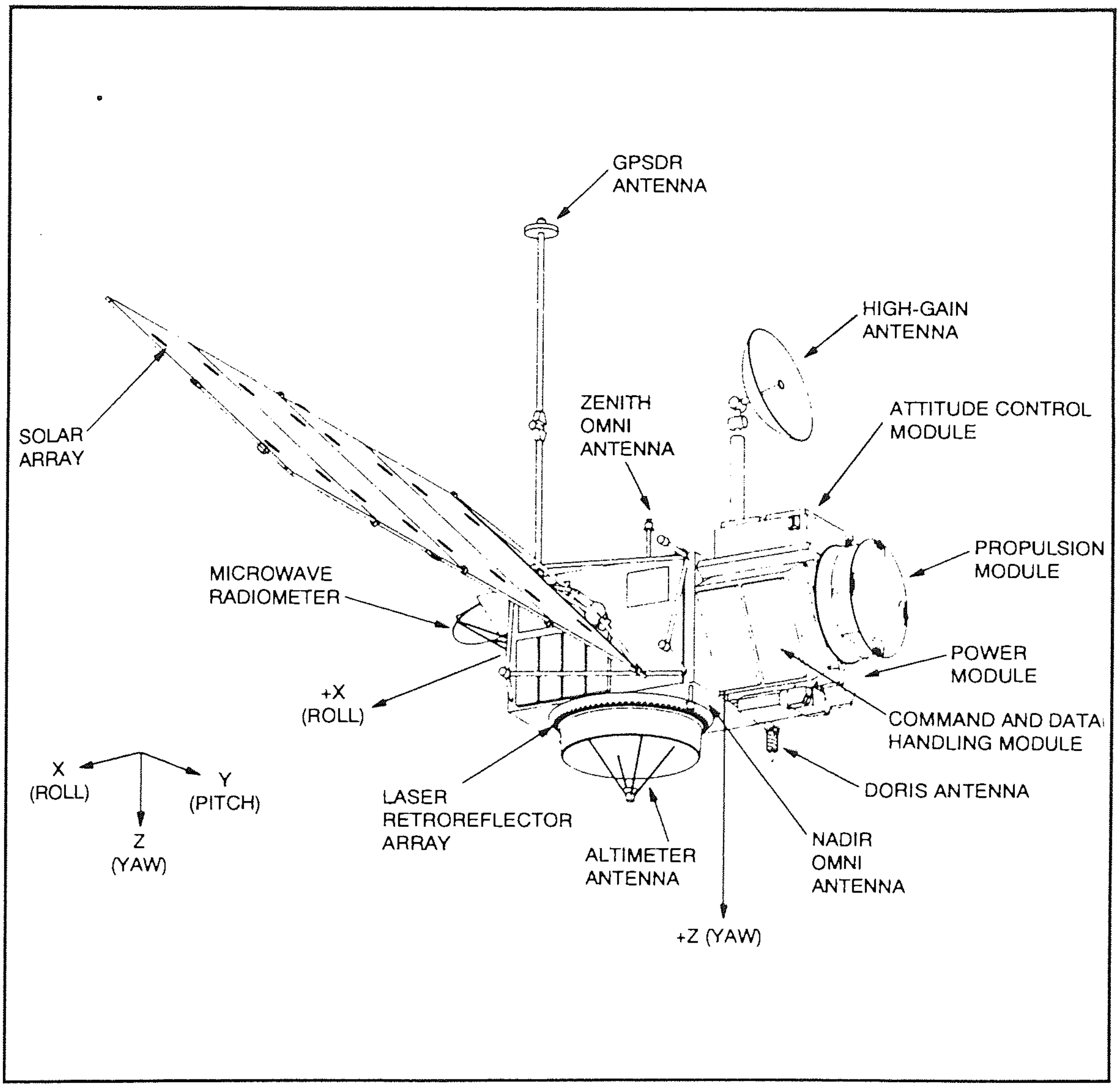

Figure 2.2

§ 2.3.1 TOPEX/POSEIDON instrumentation

Unlike ERS-1, TOPEX/POSEIDON is a purely altimetric satellite dedicated to the monitoring of ocean surfaces. The satellite carries two altimeters which share the same antenna dish though only one can be switched on at any time. In addition, the satellite carries a passive LRR for laser tracking, the French DORIS range-rate tracking system and a receiver for the NASA GPS (Global Positioning System).

TOPEX (an acronym for ocean **Topo**graphy **Ex**periment) is the name of the American radar altimeter and is treated as the primary device. It is built using well-tested technology and operates on two frequencies (5.3 and 13.6 GHz) which permits correction for ionospheric delay. A separate radiometer corrects for wet tropospheric delay and removes the effects of wind speed and cloud cover. The accuracy of the corrected altimetric height is estimated at ~5 cm.

The French altimeter POSEIDON is of an experimental solid-state design which is 75% lighter, smaller and more energy efficient than its American counterpart. Moreover the telemetry data rate is reduced by a factor of 7 because of more extensive on-board processing. It operates on a single frequency (13.6 GHz) with the ionospheric delay computed from the simultaneous dual frequency measurements of the DORIS tracking system. This altimeter will undoubtedly influence the design of such devices for future missions.

The DORIS tracking system computes the spacecraft's range-rate by measuring the Doppler shifts of two microwave frequencies transmitted by a global network of around 50 ground beacons to the receiver on-board the satellite. This technology has been well validated on the French SPOT-2 mission and the anticipated radial accuracy is 5 to 10 cm.

Finally, TOPEX/POSEIDON carries an experimental GPS receiver which provides continuous tracking of the spacecraft using an established network of GPS satellites. The recent processing of 90 days worth of GPS tracking data for TOPEX/POSEIDON by NASA has led to claims that these orbits are accurate to 3 cm rms or better [JPL, 1993 a]. Almost certainly, this system will revolutionize orbit determination in the years to come.

§ 2.3.1 TOPEX/POSEIDON orbit characteristics

The spacecraft flies a near circular, prograde orbit at a nominal altitude of 1350 km in a plane inclined at 66°. The Earth's surface covered is therefore less than for ERS-1 but TOPEX/POSEIDON will repeat the ground track (to within 1 km) every 9.9 days which provides a good balance between the temporal and spatial resolution of the sampled data. In those 9.9 days, the satellite completes 127 revolutions with a ground track spacing of ~315 km at the equator. The higher altitude means that the difficult problem of drag modelling is minimised and the higher order and degree terms for the gravity field also become less important due to the attenuation of the gravitational effect with height. The result is that orbits for TOPEX/POSEIDON determined from conventional laser tracking will be superior to those for ERS-1 (see chapter 4). The satellite must also overfly altimeter calibration sites at Lampedusa in the Mediterranean Sea and Platform Harvest off the west coast of the United States.

The mission is expected to last for at least 3 years with the possibility of a follow-up mission in the future.

§ 2.4 Principles of the radar altimeter

Some general principles relating to the function of the radar altimeter are presented now and apply equally to the ERS-1, TOPEX and POSEIDON altimeters. A more detailed account can be found in 'Satellite Oceanography' [Robinson, 1985].

The radar altimeter is a nadir-pointing, microwave sensor designed to measure the time return echoes from ocean, ice and even some land surfaces. It operates by timing the two way delay for a short duration radio frequency pulse which is transmitted vertically downwards from the antenna on the satellite to the Earth below. The radar beam 'spreads out' as it approaches the Earth and is reflected off the surface below (called the altimeter footprint). At first, the pulse meets the surface at a single point and is reflected; the beam then continues to strike the surface as a circle and later as a series of concentric rings or annuli (see Figure 2.3). The strength of the returned signal depends on the reflecting area and grows rapidly until pulse returned is from an annulus whereupon the power remains constant. When the annulus reaches the edge of the radar beam, the power diminishes and trails off.

A smooth curve is fitted to the returned signals to give a typical profile as shown in Figure 2.4. The shape and timing of the returned pulse yields information about the range distance, wind speed and ocean wave heights since irregularities on the reflecting surface stretch and distort and returning signal. The time taken from the transmission of the pulse to reception of the midpoint of the leading edge, multiplied by the speed of light yields twice the (raw) altitude.

This raw measurement is corrected for the sea surface roughness using information from the returned signal. Corrections for the signal delay due to the troposphere and ionosphere need to be determined separately. The three key corrections are due to the dry troposphere (~240 cm) which depends on the mass of air, the wet troposphere (~10 to ~30 cm which depends on the water content in the air and the ionosphere (~5 to ~20 cm) which depends on the total electron content.

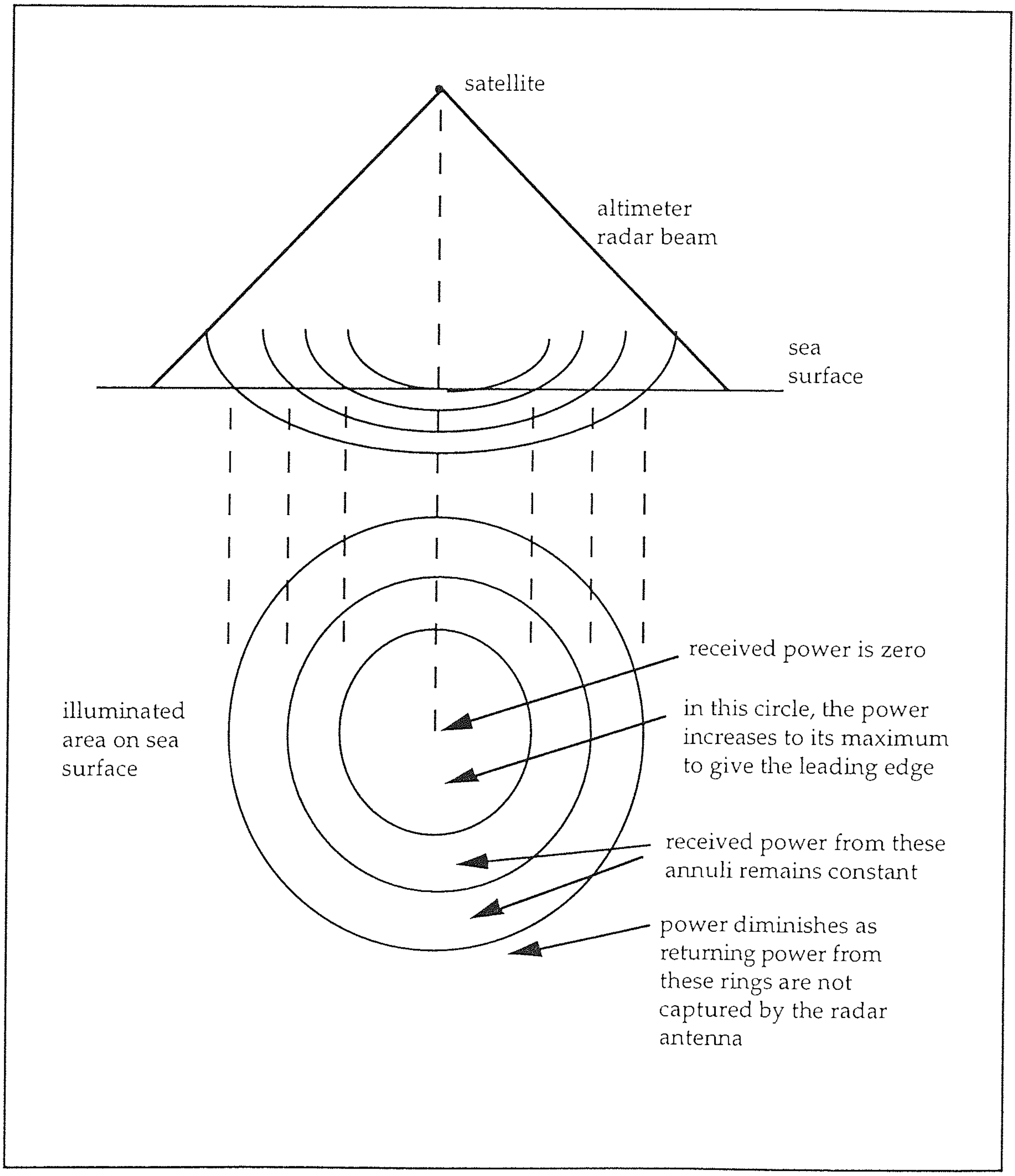

Figure 2.3

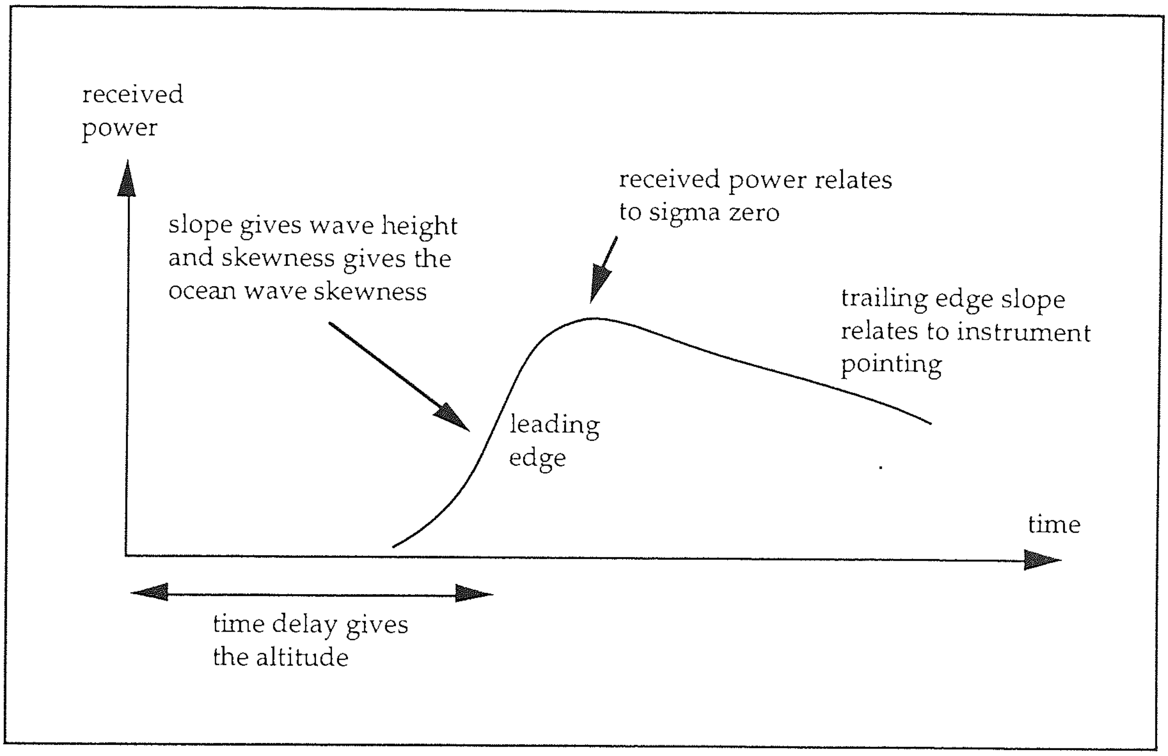

Figure 2.4

The dry troposphere correction is computed from a global model for atmospheric pressure. Although this error is in excess of 2 metres, it is usually the most reliable of the three corrections.

The error due to the wet troposphere is computed for ERS-1 from its on-board microwave sounder and for TOPEX/POSEIDON from an on-board radiometer. Global wet models are also determined as a check and are useful for when the on-board equipment fails to operate.

The TOPEX altimeter can resolve the ionospheric delay from its dual frequency operation; POSEIDON uses the on-board DORIS system and ERS-1 uses a global model for the total electron content in the ionosphere.

The ERS-1 altimeter operates in two modes, ocean and ice. The returned signal from an ice surface tends to be more specular and is comprised of many leading edges. Therefore the centre of gravity of the returned pulse is computed for since it is unique and it is this point which is used to determine the satellite altitude. In the ice mode, the altimeter can still operate perfectly well over oceans.

Although the raw measurement in ocean mode may be precise to about 2 to 5 cm, after allowing for the delay corrections the absolute accuracy is more likely to be 5 to 10 cm.

§ 2.5 General characteristics of a repeating orbit

It is useful to discuss briefly how the choice of orbital parameters defines the temporal and spatial sampling characteristics of a repeating orbit [Vincent, 1990]. Figure 2.5 shows the orbital ellipse in which the semi-major axis, a, and eccentricity, e, determine the size and shape of the ellipse with true anomaly, θ, being the angle subtended at the Earth's centre by the satellite and perigee (nearest point of the orbit to the Earth).

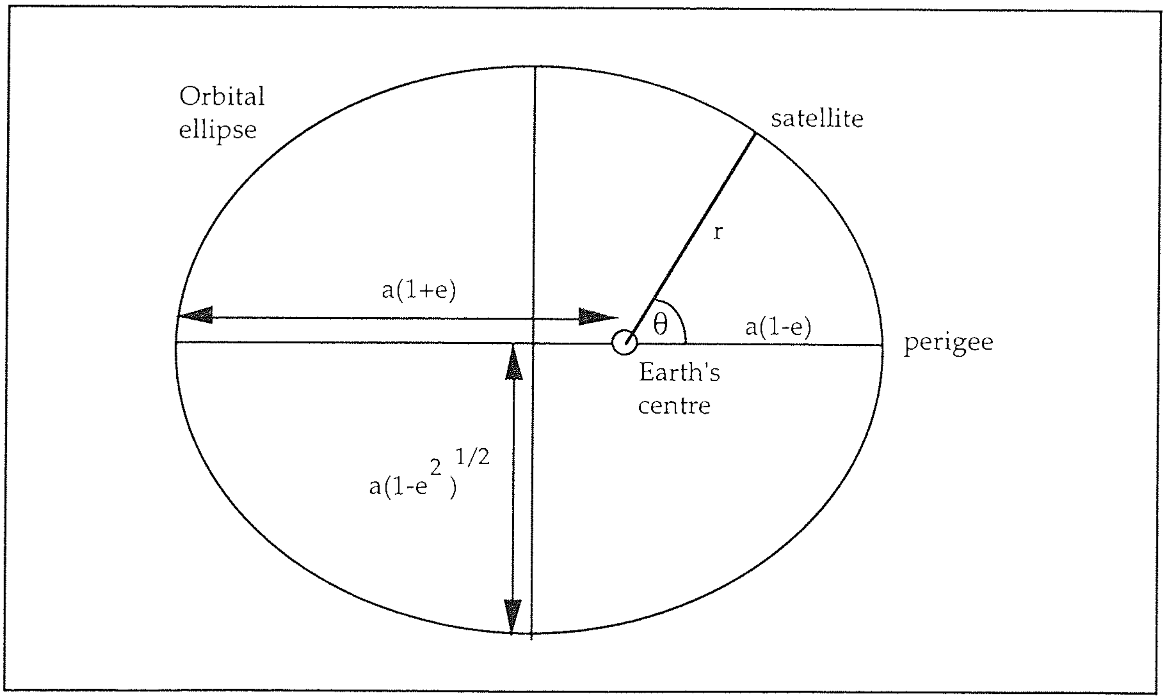

Figure 2.5

Figure 2.6 illustrates the parameters needed to fix the orbital ellipse in space. The focus of the ellipse (i.e. the Earth) is at the centre of the celestial sphere. Angle Ω is known as the right ascension of the ascending node, N, and is measured from the ascending node of the ecliptic (or the vernal equinox) referenced by a star within Aries, γ. The inclination i gives the angle between the orbital and the equatorial planes; angle ω (called the argument of perigee) defines the point of perigee and is measured from the ascending node N.

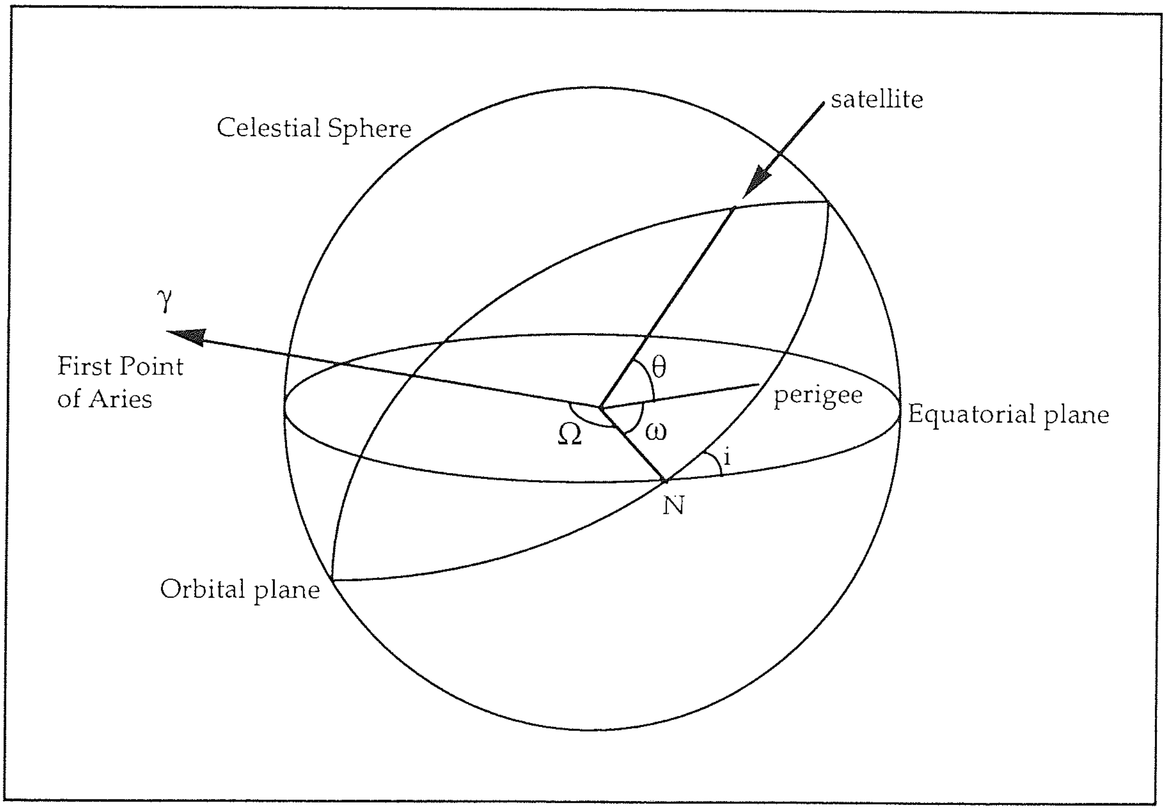

Figure 2.6

The altitude, h, of the satellite directly fixes the orbital period, T, through the relationship

$$T = 2\pi \sqrt{\frac{(R_E + h)^3}{\mu}} \qquad (2.1)$$

wherein μ is the product of the universal gravitational constant G and the mass of the Earth; R_E is the mean radius of the Earth. The regression of the orbital plane [King-Hele, 1964] is approximated by

$$\dot{\Omega} \approx -9.964 \left(\frac{R_E}{R_E + h}\right)^{\frac{7}{2}} \frac{\cos i}{(1 - e^2)^2} \quad \text{degrees per day} \tag{2.2}$$

which depends on the choice of the inclination angle i as well as the altitude h. For the exactly Sun-synchronous ERS-1 orbit, h and i are chosen such that $\dot{\Omega} \approx 0.986^\circ$/day. Hence the orbital plane will always be in the same position relative to the Sun and this provides ERS-1 with constant illumination which benefits the operation of the ATSR and the solar array. The eccentricity e will be small for a near circular orbit and so it is principally the selection of h and i which determines the sampling properties of the orbit.

However, is also desirable to avoid orbits which are nearly synchronous with the Sun in order that the ocean surface is not sampled in phase with any of the major tidal constituents which will alias them into long periods typical of ocean circulation [JPL, 1981]. The result is that the tidal effect will be very difficult to separate from the circulation. This was a key consideration when designing the orbit for TOPEX/POSEIDON and finally h and i were chosen such that $\dot{\Omega} \approx -2.07$ degrees per day. However, ERS-1 needs to fly in a Sun-synchronous orbit in order to meet the power requirements of its various instruments such as the SAR and ATSR.

An exact repeat cycle of approximately Q days is obtained by allowing the satellite to perform an exact number of complete revolutions in exactly Q Earth revolutions relative to the satellite's orbital plane which depends on $\dot{\Omega}$ [Robinson, 1985]. In practice, periodic manouevres keep the satellite to within 1 km of its ideal ground path. Very subtle changes to the altitude and inclination of ERS-1 allow this spacecraft to move from a 3 day to a 35 day repeat orbit [ESA, 1992]; see Table 2.1.

Table 2.1: ERS-1 altitude and inclination for 3 and 35 day repeat cycles

Revolutions	**Repeat**	**Altitude (km)***	**Inclination**
43	3 days	775.138	98.5162°
501	35 days	781.495	98.5429°

* relative to a mean Earth radius of 6378 km.

To help keep proper control of the satellite over the selected ground track, a near frozen orbit is preferred in which the mean values of the eccentricity e and argument of perigee ω are constant for given values of h and i. In reality, e and ω will oscillate about their mean values with a long period. ERS-1 is in such an orbit but not TOPEX/POSEIDON. Instead, the inclination for TOPEX/POSEIDON of 66° is very close to the critical inclination of 63.5° at which $\dot{\omega} \approx 0$ and so the drift of perigee for this satellite will be small.

After the selection of a, i, e and ω, it is a simple matter to select Ω such that verification sites are overflown. The mean anomaly M is arbitrary. Figures 2.7 and 2.8 show the global ground tracks for ERS-1 and TOPEX/POSEIDON respectively.

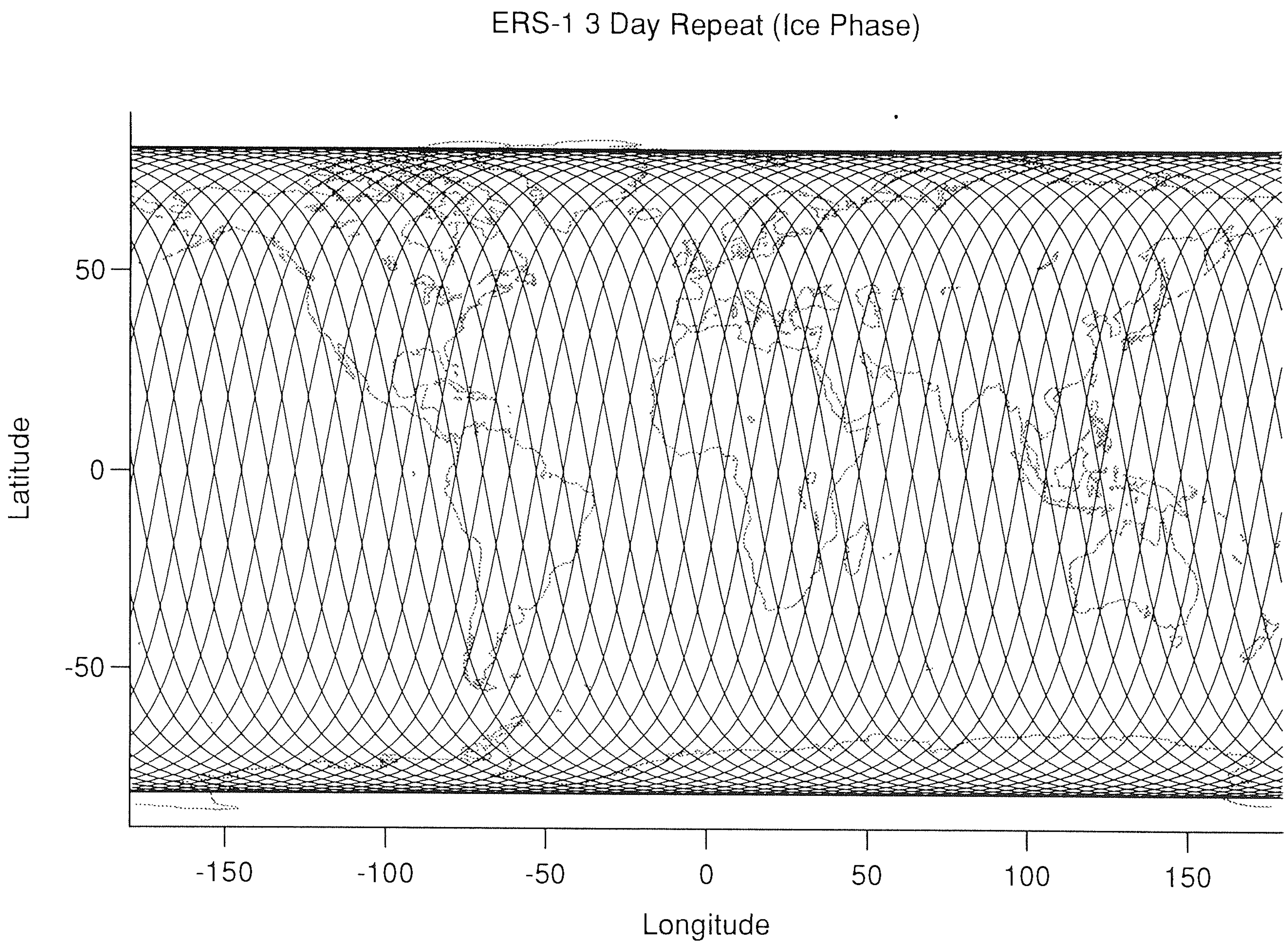
ERS-1 3 Day Repeat (Ice Phase)
Latitude
50
0
-50
Longitude
-150
-100
-50
0
50
100
150

Figure 2.7

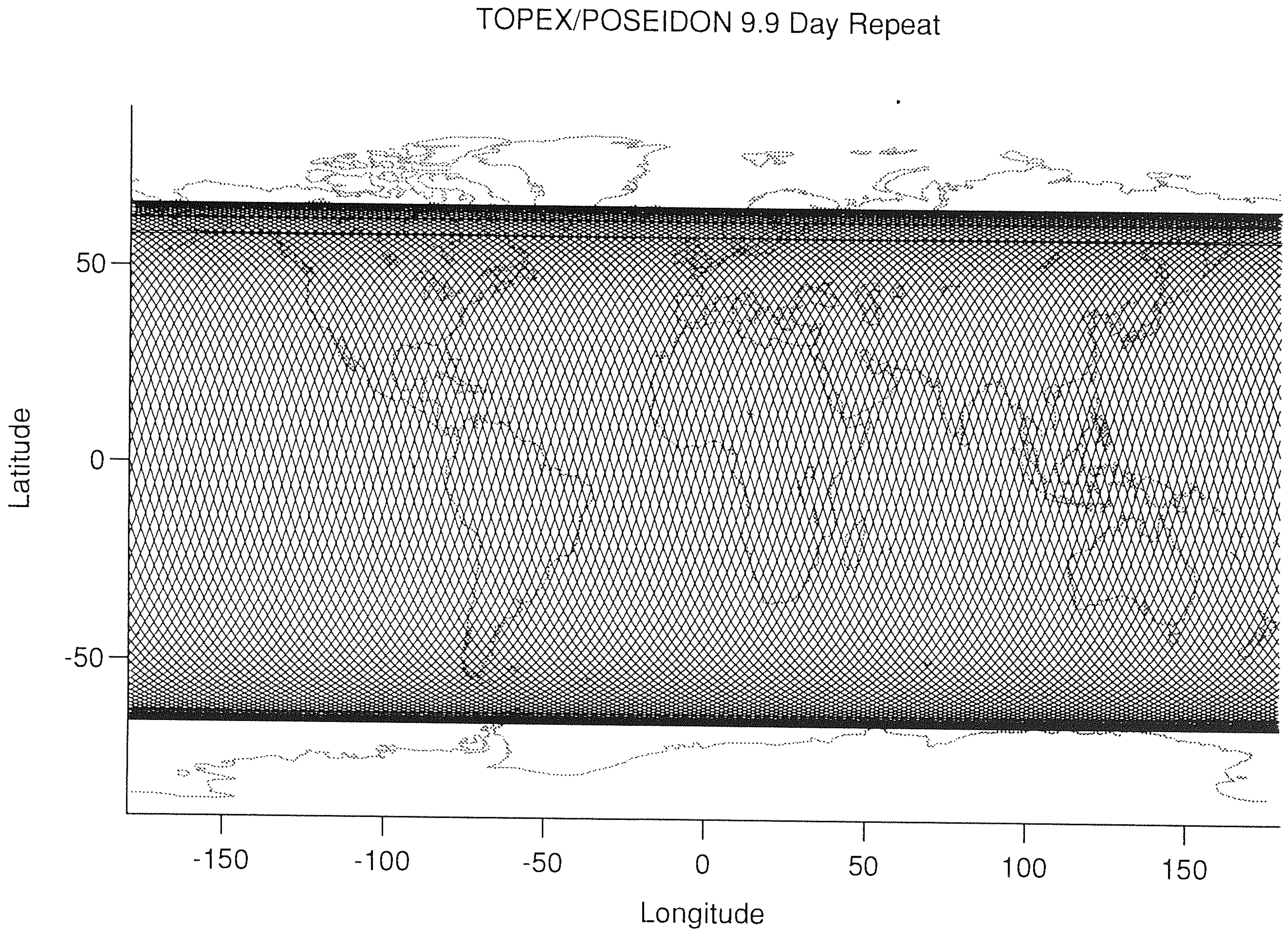
TOPEX/POSEIDON 9.9 Day Repeat
Latitude
50
0
-50
Longitude
-150
-100
-50
0
50
100
150

Figure 2.8

The higher altitude of TOPEX/POSEIDON has some important advantages. Firstly, the spacecraft will experience far less drag forces than its lower companion ERS-1. Drag forces are difficult to model well, due to uncertainties in atmospheric density at those altitudes, and so the fact that they play a lesser role means computed orbits will be more precise. The satellite also decays slower and hence fewer manouevres are required. Moreover, the attentuation of gravity with height means that the higher order and degree terms for the gravitational field become less significant. However other forces such as direct solar radiation pressure will become more prevalent. Secondly, the amount of time during which a ground laser station can track is greatly increased. The satellite moves slower across the sky and can therefore be seen more frequently and for longer arcs which generates more laser tracking data which can only benefit the orbit computation process. Hence a higher orbit helps to reduce the satellite radial orbit error.

Disadvantages of a higher orbit include the fact that the area of the sea surface that reflects the altimeter pulse (known as the 'footprint') is increased which lowers spatial resolution. Moreover, a higher altimeter needs more power or a more directional antenna or a more sensitive receiver (or a combination of all three). These requirements will increase the cost and complexity of the altimeter.

§ 2.6 Conclusions

The instrumentation and orbit characteristics of both ERS-1 and TOPEX/POSEIDON satellites have been discussed. Both carry radar altimeters for surveying the ocean surface. Since TOPEX/POSEIDON orbits and altimetric data are more accurate than for ERS-1, this is certainly the mission of most interest to the oceanographer. Nevertheless many researchers will combine the data from both missions to produce a consistent and valuable dataset for study of ocean phenomena.

CHAPTER 3

ORBIT DETERMINATION USING THE SATAN SOFTWARE

§ 3.1 Introduction

The suite of computer programs used throughout this thesis for the determination of SEASAT, ERS-1 and TOPEX/POSEIDON orbits is the SATAN (**Sat**ellite **An**alysis) software originally developed at the Royal Greenwich Observatory for use with laser ranging data [Sinclair and Appleby, 1986]. Over the years, the software has been extensively modified at Aston University to incorporate altimetry and crossovers [Rothwell, 1989] and Doppler range-rate data [Ehlers, 1993] as tracking data in the orbit determination procedure.

§ 3.2 The orbit determination process

This process involves two stages. Firstly, the equations of motion for the satellite are numerically integrated from an initial start vector $\underline{P}$ which includes the initial satellite position $\underline{x}_0$ and velocity $\dot{\underline{x}}_0$ along with parameters relating to the force modelling of, for example, atmospheric drag and solar radiation pressure.

Secondly, the generated orbit is fitted to suitably weighted observation data (e.g. laser, altimetry, crossovers or Doppler) in a least squares differential correction procedure such that small corrections $\Delta\underline{P}$ to the start vector are solved for. The start vector is then updated and the entire process repeated until the fit of the generated orbit to the observation data cannot be further improved. This measure of fit gives an indication of how precise the computed ephemeris is.

§ 3.3 Numerical integration

The equations of motion for an orbiting satellite, to be detailed in section 3.4, take into account the accelerating forces acting on the spacecraft, namely, the gravitational attraction of the Earth and other large bodies in the solar system, the tidal effects of the Sun and Moon on the Earth's gravitational potential, retardation forces due to the Earth's atmosphere and direct and indirect solar radiation pressure. For brevity, the equations may be written as

$$\ddot{\underline{x}} = \underline{F}(\underline{P}, t) \tag{3.1}$$

wherein $\ddot{\underline{x}}$ is the cartesian vector $(\ddot{x}, \ddot{y}, \ddot{z})^T$ and $\underline{F}$ is the total force function acting on the satellite (per unit mass) defined by the initial conditions $\underline{P}$ and t is time. The equations 3.1 are numerically integrated within the SATAN software using an 8th order Gauss-Jackson method [Merson, 1975]. The integration step length is usually taken as 30 seconds and the software can reliably integrate ahead for long arc analyses of about 6 days for SEASAT and ERS-1 and 10 days for TOPEX/POSEIDON.

The SATAN software performs the integration in an inertial reference frame, J2000, based on the position of the equatorial plane and vernal equinox on January 1.5 in the year 2000 [Sinclair, 1987]. However the acceleration due to the Earth's gravity field is most conveniently computed in Earth-fixed coordinates. Conversion of the J2000 coordinates into an Earth-fixed frame requires the calculation of the rotation matrices

P, N for the effect of precession and nutation (secular and periodic motion of the Earth's rotational pole respectively) and S for effect of polar motion and rotation to sidereal time such that

$$\underline{x}_{\text{Earth}} = S\,.\,N\,.\,P\,\underline{x}_{J2000}\,. \tag{3.2}$$

The satellite position and velocity are calculated by numerical integration at the time of each observation, as are the partial derivatives $\partial\underline{x}/\partial p_j$ for each orbital parameter p_j in $\underline{P}$. These values are computed in the J2000 reference frame and are required for the data reduction process. Furthermore, the position and velocity of the spacecraft may be recorded at each integration step either in J2000 or Earth-fixed coordinates.

§ 3.4 Force modelling

The total force acting on the satellite with respect to the Earth's fixed reference frame results in the following acceleration, namely

$$\ddot{\underline{x}} = \underline{F}(\underline{P}, t) = \text{grad } V + \text{grad } \Delta U_2 + \ddot{\underline{x}}_{TB} + \ddot{\underline{x}}^{\text{skin forces}} + \ddot{\underline{x}}^{\text{along-track}}_{1/\text{rev}} + \ddot{\underline{x}}^{\text{across-track}}_{1/\text{rev}} + \ddot{\underline{x}}_{ISRP} \tag{3.3}$$

wherein grad V, grad ΔU_2, $\ddot{\underline{x}}_{TB}$, $\ddot{\underline{x}}^{\text{skin forces}}$ and $\ddot{\underline{x}}_{ISRP}$ are the individual accelerations due respectively to the Earth's gravitational potential, solar and lunar tidal effects, third body attraction, non-gravitational skin forces (atmospheric retardation and direct solar radiation pressure) and indirect radiation pressure. Terms are also included to absorb any residual once per revolution (1/rev) error in the along-track and across-track directions. The 'grad' operator gives the gradient of the potential, either V or ΔU_2, to derive the resulting acceleration. Each of these components are now discussed.

§ 3.4.1 Earth's gravitational potential

The Earth's gravitational field may be expressed as a scalar quantity called a potential. In spherical polar coordinates (r, ϕ, λ) the geopotential V can be written

$$V = \frac{\mu}{r} \sum_{l=0}^{\infty} \sum_{m=0}^{l} \left(\frac{R_E}{r}\right)^l \left(C_{lm} \cos m\lambda + S_{lm} \sin m\lambda\right) P_{lm} (\sin \phi) \tag{3.4}$$

in which μ is the product of the universal gravitational constant, G, and the mass of the Earth, M_E; R_E is the radius of the Earth; r is the radial distance to the external point (or satellite) and ϕ, λ are the geocentric latitude and longitude respectively; $P_{lm}(\sin \phi)$ are the associated Legendre polynomials of degree l and order m; C_{lm} and S_{lm} are the harmonic coefficients which define the gravity field. Equation 3.4 is the solution of the Laplace's equation in spherical polar coordinates, accomplished by the separation of variables [Kaula, 1966]. The acceleration of the satellite due to the geopotential V is then simply grad V.

An important feature of equation 3.4 is the attenuation (or weakening) of V with the radial satellite distance r due to the term $(R_E / r)^l$. The larger r is, the faster this term becomes smaller which means the accuracy of the higher degree and order cofficients are less important. Hence TOPEX/POSEIDON with its higher orbit does not suffer the consequences of gravitational mismodelling to the same extent as its lower companion ERS-1.

For practical purposes, the infinite series V is truncated and recent developments have led to the JGM-2 gravity field model [Lerch et al., 1993] which is computed to degree and order 70.

§ 3.4.2 Third body attraction

Other large bodies within the solar system also exert a significant gravitational force upon Earth orbiting satellites. The third body attractions modelled for within SATAN are the Sun, Moon, Venus, Mars, Jupiter and Saturn. These bodies are treated as point masses and their positions are determined at each integration step from planetary data. Thus it is possible to deduce the acceleration of the satellite relative to the Earth due to each of these bodies.

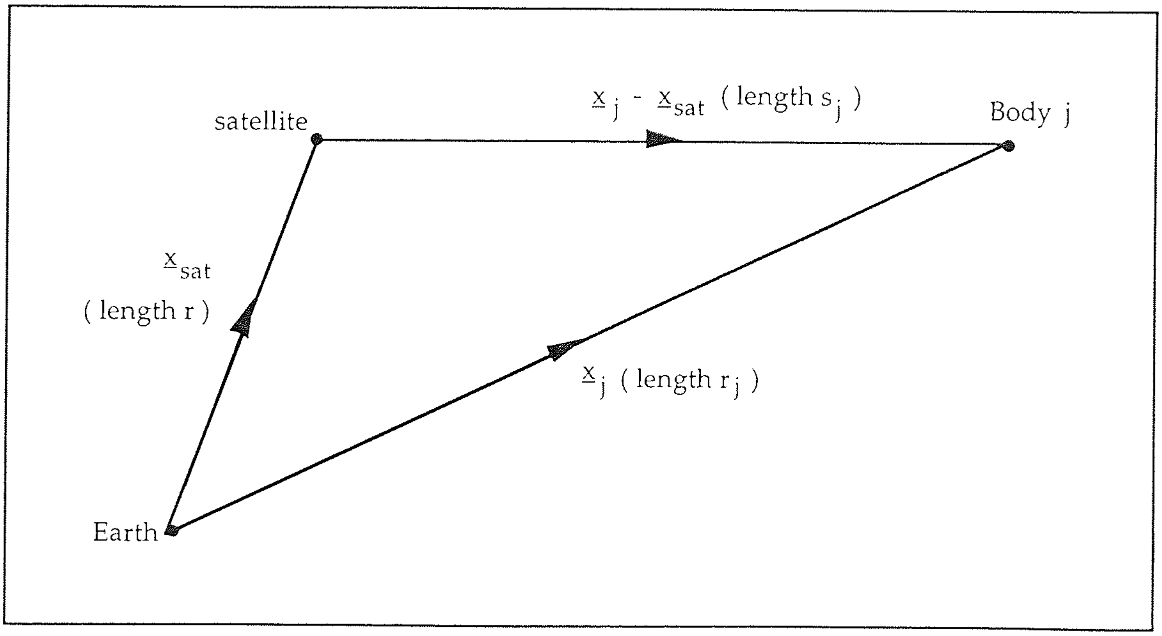

Figure 3.1

On referring to Figure 3.1, let $\underline{x}_{sat}$ and $\underline{x}_j$ be the position vectors of the satellite and body j respectively, relative to the Earth's centre. The acceleration of the satellite due to the Earth and body j is

$$\ddot{\underline{x}}_{sat} = \frac{-GM_E}{r^3}\underline{x}_{sat} + \frac{GM_j}{s_j^3}(\underline{x}_j - \underline{x}_{sat}) \tag{3.5}$$

and the acceleration of the Earth due to body j is $\ddot{\underline{x}}_E = \frac{GM_j}{r_j^3}\underline{x}_j$ wherein M_j is the mass of body j and $s_j = |\underline{x}_j - \underline{x}_{sat}|$. The acceleration of the spacecraft relative to the Earth is th]ore

$$\ddot{\underline{x}}_{sat} - \ddot{\underline{x}}_E = \frac{-GM_E}{r^3}\underline{x}_{sat} + GM_j\left\{\frac{\underline{x}_j - \underline{x}_{sat}}{s_j^3} - \frac{\underline{x}_j}{r_j^3}\right\} \tag{3.6}$$

in which the central term of the Earth's gravity is accounted for within equation 3.4 in section 3.4.1. The total acceleration of the satellite due to all the third bodies concerned is thus

$$\ddot{\underline{x}}_{TB} = G\sum_j M_j\left\{\frac{\underline{x}_j - \underline{x}_{sat}}{s_j^3} - \frac{\underline{x}_j}{r_j^3}\right\}. \tag{3.7}$$

§ 3.4.3 Tidal effects on the Earth's gravity field by the Sun and Moon

The Earth is not a rigid body and is therefore deformed by the presence of other bodies in the solar system, in particular, the Sun and Moon. The motion of the solid earth coupled with the tidal effects on the oceans causes the Earth's gravity potential to change with time. With reference to Figure 3.2, the tide generating potential due to the presence of body j is given by

$$U(R) = GM_j \left\{ \frac{1}{|R - r_j|} - \frac{\underline{r} \cdot \underline{r}_j}{r_j^3} \right\} \qquad (3.8)$$

in which R is the mean radius of a spherical elastic Earth and all other components are as detailed in sections 3.4.1 and 3.4.2 [Lambeck, 1980]. By expanding U in terms of Legendre polynomials, equation 3.8 becomes

$$U(R) = \frac{GM_j}{r_j} \sum_{l=2}^{\infty} \left(\frac{R}{r_j} \right)^l P_{l0}(\cos S) \qquad (3.9)$$

wherein S is the angle subtended at the geocentre by the point on the Earth's surface and the perturbing body, here taken to be a point mass.

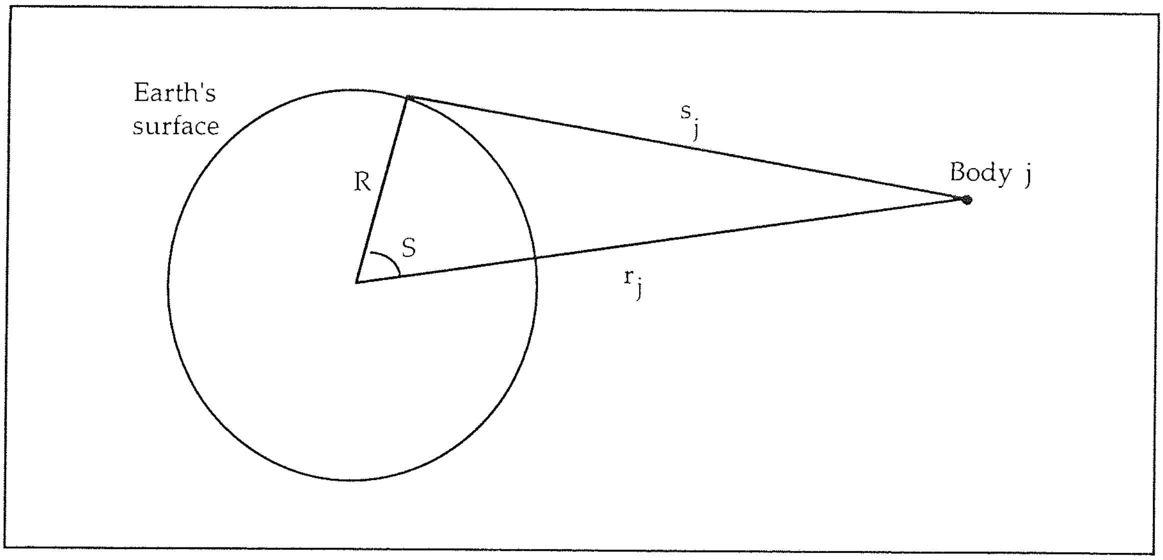

Figure 3.2

The Earth will deform under this potential and the additional potential resulting from this new distribution of mass is

$$\Delta U(R) = \sum_{l=2}^{\infty} k_l \, U_l(R)$$

$$= \frac{GM_j}{r_j} \sum_{l=2}^{\infty} k_l \left(\frac{R}{r_j}\right)^l P_{l0}(\cos S) \qquad (3.10)$$

on assuming instantaneous response for the Earth due the the perturbing body. The values k_l are the potential Love numbers. Beyond the Earth, Dirichlet's theorem [Lambeck et al., 1974] is used and the potential due to the deformation at distance r from the geocentre is

$$\Delta U(r) = \frac{GM_j}{r_j} \sum_{l=2}^{\infty} k_l \left(\frac{R}{r_j}\right)^l \left(\frac{R}{r}\right)^{l+1} P_{l0}(\cos S) \qquad (3.11)$$

The dominant second order term of equation 3.11 summed over all the perturbing bodies is thus

$$\Delta U_2 = \sum_j \frac{GM_j}{r_j^3} \frac{R^5}{r^3} k_2 \left(\frac{3}{2}\cos^2 S - \frac{1}{2}\right) \qquad (3.12)$$

where the index j refers to the bodies Sun and Moon. Higher order terms are deemed negligible and ΔU_2 is frequency independent. Equation 3.12 is therefore used to model changes in the Earth's potential due to the Sun and Moon. The Love numbers are in fact frequency dependent due to resonant effects from the Earth's liquid core and this is accounted for as variations in the gravity coefficients C_{lm} and S_{lm}.

§ 3.4.4 Atmospheric retardation and direct solar radiation pressure

Satellites in a low Earth orbit travel through the upper atmosphere and experience a retardation force. This effect diminishes exponentially with the orbital height. In the past, this force has been modelled as an along-track deceleration depending on the area-to-mass ratio of the satellite and atmospheric density [King-Hele, 1964]. The motion of the satellite is further disturbed by the impact of photons from the Sun, this force is known as direct solar radiation pressure (SRP).

Recent developments at Aston University have led to the employment of a satellite skin force and torque modelling technique [Ehlers, 1993]. Since ERS-1 is particularly susceptible to large orbit errors on account of its nominal altitude of 780 km, most of the work was concentrated on this spacecraft. Briefly, the method uses a detailed geometric model for ERS-1 and computes the visible faces from a number of different angles (for TOPEX/POSEIDON a cruder box/wing model was sufficient because of its higher orbit). The force modelling software then interpolates these 'tables' to calculate the precise visible surfaces for any given angle of view. The force modelling works on the principle of momentum exchange between the impacting air molecules or photons upon the surfaces of the satellite. Hence in this manner, drag, lift and direct SRP forces are accounted for; let the resulting acceleration be denoted by $\ddot{\underline{x}}^{\text{skin forces}}$.

The retardation coefficients, C_D, may be determined in a number of ways over a given period, for example, as a step function with C_D taking a different value for each 24 hour interval. It may also expressed as a continuous saw-tooth function, the intention being to model C_D more realistically and this was implemented into the SATAN software [Ehlers, 1993]. This extra parameterisation will lead to higher correlations in the data reduction process and hence some care is required to ensure the orbit produced is realistic.

A further improvement is to include a 1/rev variation in the along-track direction, namely

$$\ddot{\underline{x}}^{\text{along-track}}_{1/\text{rev}} = \left\{ C_1\cos(\omega+M) + S_1\sin(\omega+M) \right\} \underline{v}_r \tag{3.13}$$

which absorbs any further deficiency in the drag mismodelling [Ries et al., 1992]. Here ω is the argument of perigee, M the mean anomaly and $\underline{v}_r$ is the velocity vector of the spacecraft relative to the ambient atmosphere; C_1 and S_1 are the acceleration coefficients to be determined for the long arc orbit. A similar function, $\ddot{\underline{x}}^{\text{across-track}}_{1/\text{rev}}$, may be included to compensate for any across-track error. For ERS-1 at a nominal height of 780 km, these 1/rev terms absorb mostly drag errors; in the case of TOPEX/POSEIDON, these terms mainly correct for shortcomings in the solar radiation pressure model. Not all the orbits computed for this thesis employed these 1/rev corrections since, in some cases, they were too highly correlated with other orbital parameters and were therefore omitted.

§ 3.4.5 Indirect radiation pressure

Indirect forces act on the satellite from Earth-reflected (albedo) radiation and infra-red (IR) radiation emitted from the Earth. These are modelled using

$$d\ddot{\underline{x}}_{ISRP} = -\left\{ C_R\,\gamma\,P\cos\theta + \frac{P_{IR}}{c} \right\} \left(\frac{A}{m}\right) \frac{\cos\alpha\; dA}{\pi d^2}\, \hat{\underline{e}}_d \tag{3.14}$$

where γ is the albedo (proportion of direct radiation which is reflected from the Earth) of the surface element dA; θ is the angle between the surface normal and the Sun; P_{IR} the emitted IR flux of the surface element; α the angle between the surface element's normal and the satellite; c the speed of light; d the distance of the satellite from the surface element and $\hat{\underline{e}}_d$ is the unit vector from the satellite to the surface element. If $\theta > \pi/2$ then $\gamma = 0$. The total Earth reflected and IR radiation should be calculated by integrating equation 3.14 over the surface of the Earth visible to the satellite. This integration is approximated by summing over 13 surface elements [Wakker et al., 1983] to yield

$$\ddot{\underline{x}}_{ISRP} = \sum_{i=1}^{13} d\ddot{\underline{x}}^{i}_{ISRP} \qquad (3.15)$$

§ 3.5 Data reduction process

The computed orbit is now compared to observation data which are usually normal points, a single normal point being derived from many actual data points in order to reduce the quantity of data. The observed differences are minimised using a least squares differential correction procedure to estimate small corrections to the start vector $\underline{P}$ which will include the initial position and velocity and other parameters relating to drag and solar radiation pressure as well as gravity field coefficients.

For each observed measurement d_i^{ob} at time t_i with an 'a priori' standard error σ_i, the SATAN software computes a corresponding measurement d_i^{+} which is dependent on the start vector $\underline{P}^{+}$, wherein the + symbol denotes the best estimate so far. The start vector sought is the vector $\underline{P}^*$ which will give rise to computations of d_i^* which will best fit d_i^{ob} in a least squares sense. Hence the correction vector $\Delta\underline{P}$ is to be determined where

$$\underline{P}^* = \underline{P}^+ + \Delta\underline{P} . \qquad (3.16)$$

The least squares differential correction process involves the minimisation of the function

$$I = \sum_{i=1}^{N} w_i \left(d_i^{ob} - d_i^* \right)^2 \qquad (3.17)$$

where N is the number of acceptable observations and w_i is the weight deduced as $1/\sigma_i^2$. It is necessary for the laser data to be more significantly weighted compared to altimetry and crossovers since it is the most precise (the range measurement is 1 to 2 cm rms, not including possible errors in station coordinates). Function I needs to be minimised with respect to all the orbital parameters of $\underline{P}$ for which corrections are sought, say m' where $1 \leq m' \leq m$, m being the total number of components within $\underline{P}$. This gives rise to m' partial derivatives of the form

$$\frac{\partial I}{\partial p_j} = -2 \sum_{i=1}^{N} w_i \left(d_i^{ob} - d_i^* \right) \frac{\partial d_i^*}{\partial p_j} = 0 \qquad (3.18)$$

for j=1..m'. The value d_i^* can be expanded using Taylor's theorem such that

$$d_i^* = d_i^+ + \sum_{k=1}^{m'} \frac{\partial d_i^+}{\partial p_k} \Delta p_k + O(\Delta P^2) \qquad (3.19)$$

wherein Δp_k are small corrections to parameters p_k. On assuming the residual $(d_i^{ob} - d_i^+)$ to be accurate to order $O(\Delta P)$, substitution of equation 3.19 into 3.18 gives

$$\sum_{i=1}^{N} w_i \left\{ \left(d_i^{ob} - d_i^+ \right) - \sum_{k=1}^{m'} \frac{\partial d_i^+}{\partial p_k} \Delta p_k \right\} \frac{\partial d_i^+}{\partial p_j} = 0 \tag{3.20}$$

which is precise to order $O(\Delta P)$. Since there are m' such equations for j=1..m', rearrangement yields the matrix equation

$$D\Delta\underline{P} = \underline{b} \tag{3.21}$$

which are called the 'normal equations'. The elements of the symmetric positive definite matrix D of dimension m' x m' are

$$D_{jk} = \sum_{i=1}^{N} w_i \frac{\partial d_i^+}{\partial p_j} \frac{\partial d_i^+}{\partial p_k}, \tag{3.22}$$

the elements of the column vector $\underline{b}$ of length m' are

$$b_j = \sum_{i=1}^{N} w_i \left(d_i^{ob} - d_i^+ \right) \frac{\partial d_i^+}{\partial p_j} \tag{3.23}$$

and the vector $\Delta\underline{P}$ consists of the required m' corrections. Inversion of matrix D yields the result $\Delta\underline{P} = D^{-1}\,\underline{b}$.

The corrected start vector, $\underline{P}^+ + \Delta\underline{P}$, is now taken to be the new start vector and the process of numerical integration followed by data reduction repeated until the fit of the observed and computed orbits cannot be further improved whereupon $\Delta\underline{P} \approx \underline{0}$. For the SATAN software, an approximate start vector to within 1 km of the true satellite position is required.

To compute D and $\underline{b}$, the values d_i^+ and $\partial d_i^+/\partial p_j$ need to be evaluated for each observation at time t_i. These are calculated using $\underline{x}, \dot{\underline{x}}$ and the partial derivatives $\partial \underline{x}/\partial p_j$ generated by the numerical integration process. For example, a laser range measurement is given by the equation

$$d_i^{R+} = \sqrt{(x_i - x_s)^2 + (y_i - y_s)^2 + (z_i - z_s)^2} \tag{3.24}$$

in which (x_i, y_i, z_i) is the satellite position at time t_i and (x_s, y_s, z_s) is the station position, both in J2000. Partially differentiating equation 3.24 with respect to parameter p_j gives

$$\frac{\partial d_i^{R+}}{\partial p_j} = \frac{1}{d_i^{R+}} \left\{ (x_i - x_s) \frac{\partial x_i}{\partial p_j} + (y_i - y_s) \frac{\partial y_i}{\partial p_j} + (z_i - z_s) \frac{\partial z_i}{\partial p_j} \right\} \tag{3.25}$$

as required. For altimeter data, the partials needed are sufficiently well approximated by

$$\frac{\partial d_i^{h+}}{\partial p_j} \approx \frac{\partial r_i}{\partial p_j} = \frac{1}{r_i} \left\{ x_i \frac{\partial x_i}{\partial p_j} + y_i \frac{\partial y_i}{\partial p_j} + z_i \frac{\partial z_i}{\partial p_j} \right\} \tag{3.26}$$

with the radial distance to the spacecraft, r_i, defined by $r_i^2 = x_i^2 + y_i^2 + z_i^2$.

§ 3.6 Conclusions

The mathematical principles involved in numerically integrating an Earth orbiting satellite and refining it in a least squares differential manner to observation data such as laser ranging have been discussed. These are the techniques employed in the SATAN software which are used at Aston University to produce precise orbits for SEASAT, ERS-1 and TOPEX/POSEIDON.

CHAPTER 4

LONG ARC ANALYSIS OF ERS-1 AND TOPEX/POSEIDON ALTIMETRY

§ 4.1 Introduction

In this study, ERS-1 and TOPEX/POSEIDON altimetry are analysed in a long arc solution to determine the biases for the ERS-1, TOPEX and POSEIDON altimeters as well as the time tag biases associated with them. A crossover analysis will also give an indication of the accuracy of the numerical orbits. In addition, the sea surface topography is computed to degree and order 30. For ERS-1 one complete 35 day cycle during September 1992 is used and for TOPEX/POSEIDON cycles 2 to 10 and 20 to 22 are employed.

§ 4.2 Satellite altimetry

Radar altimeters such as those on board ERS-1 and TOPEX/POSEIDON provide accurate measurements from the satellite to the sea surface below. Short radar pulses are transmitted towards the Earth's surface and the time taken for the signal to return to the spacecraft multiplied by the speed of light yields twice the altimetric range. Consequently the raw measurement h_i^{raw} at time t_i is derived. However the radar signal is slowed down as it passes through the troposphere and ionosphere, the combined effect of which will lead to a height error in excess of 2 metres. Moreover the roughness of the sea surface due to strong winds or swell results in a sea-state bias which is the sum effect of the tracker bias (due to difficulties for the logic algorithm to cope with rough sea surface) and the electromagnetic bias (due to return pulse being stronger for troughs than for crests). This error is usually estimated as a function of the significant wave height (SWH) which is deducible from the returned radar pulse. Section 2.4 in chapter 2 gives a more detailed summary of the altimeter function.

Other errors associated with the raw altimeter height are essentially instrumental in nature and include the altimeter bias (caused by a delay within the electronics of the altimeter) , the height error resulting from a time tag bias and the centre-of-mass correction (the vertical distance between the altimeter electronic centre and the satellite centre-of-mass). Establishing the altimeter bias is crucial for oceanographic work with altimetry and rigorous calibration/validation campaigns are usually carried out during the first few months of the missions to determine its value. In this chapter, the bias will be estimated from an analysis of the altimeter residuals. In chapter 6, the bias is derived by a precise 'on-site' technique.

Concisely the corrected observed altimeter reading, h_i^{alt}, of the instantaneous sea surface at time t_i may be expressed

$$\begin{aligned} h_i^{alt} = \quad & h_i^{raw} + \\ & h_i^{dry} + h_i^{wet} + h_i^{iono} + h_i^{ssb} + \qquad \text{(geophysical corrections)} \\ & h^{com} + h_i^{ttb} - h^{bias} \qquad \text{(instrumental corrections)} \end{aligned} \tag{4.1}$$

where

h_i^{raw} : raw altimeter range above instantaneous sea surface

h_i^{dry} : dry tropospheric correction

h_i^{wet} : wet tropospheric correction

h_i^{iono} : ionospheric correction

h_i^{ssb} : sea-state bias

h^{bias} : altimeter bias (not applied)

h_i^{ttb} : height error due to time tag bias (not applied)

h^{com} : centre-of-mass correction

(see Figure 4.1). The corrections h^{bias} and h_i^{ttb} are included in equation 4.1 for completeness but as their values are initially unknown they are assumed zero.

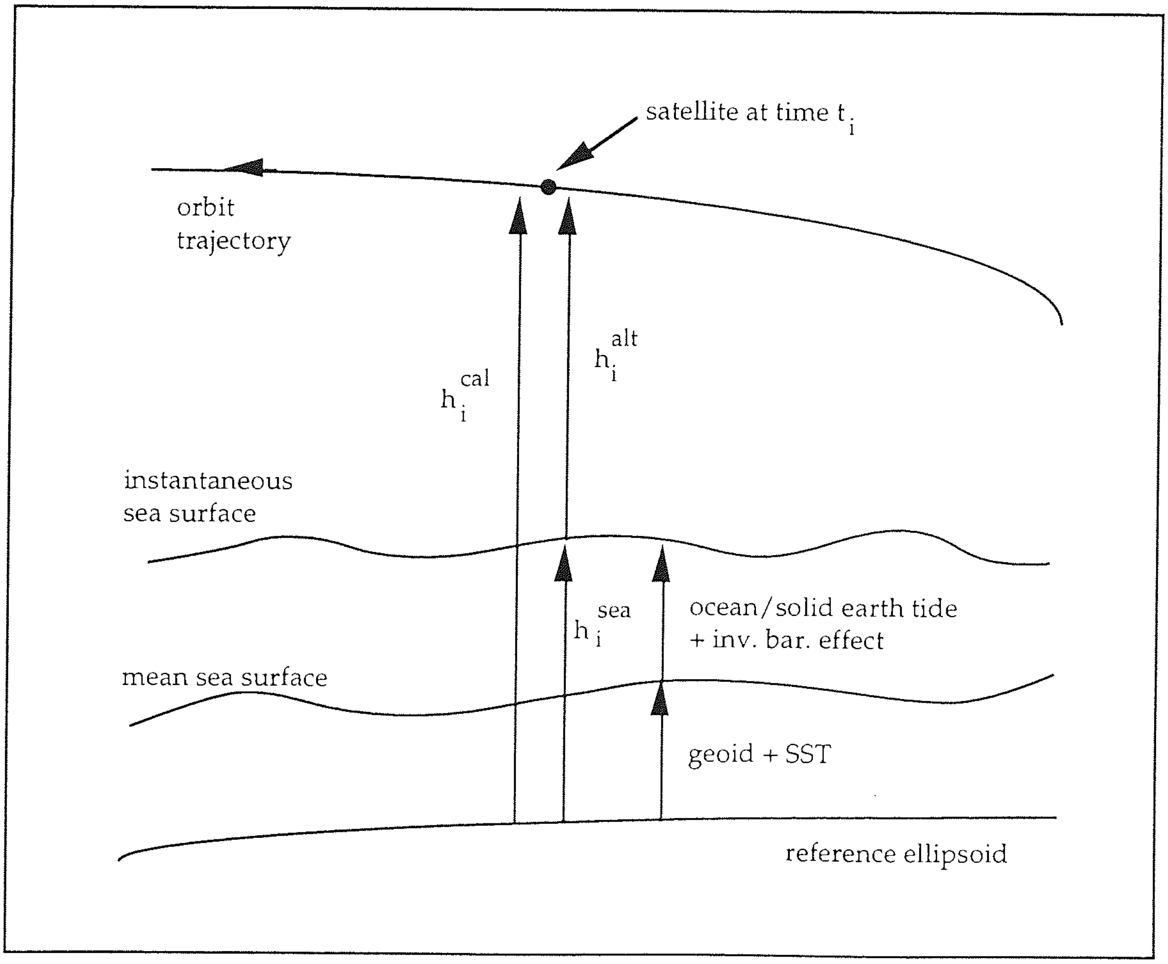

Figure 4.1

The altimeter bias, by definition, is subtracted from the uncorrected reading, h_i^{raw}, and therefore a negative bias implies the altimeter is measuring too short. Conversely the height error, h_i^{ttb}, due to a timing bias is added to h_i^{raw} because of the way it is defined in section 4.9.

§ 4.3 Instantaneous sea surface

For an altimetric measurement made at time t_i at geodetic position (ϕ_i , λ_i) it is imperative to determine the elevation of the sea surface at the same time and location with respect to a reference ellipsoid, which is taken to be an oblate spheroid of revolution whose surface approximates the geoid. In turn, the geoid (or more precisely the 'zero' geoid) is the equipotential surface of the Earth's gravitational field and centrifugal rotation and may be considered to be the mean sea surface if there were no ocean circulation phenomena, sea density variation and winds. The 'mean' geoid, as used for these analyses, is computed by adding $-9.9\ (3 \sin^2\phi - 1)$ cm to the zero geoid, with ϕ being the latitude [Engelis and Knudsen, 1989]. This extra term allows for the constant Earth deformation from the direct gravitational effect of the Sun and Moon.

Temporal variations such as ocean/solid earth tides (caused by lunar and solar gravitation) and the inverse barometer effect (due to the depression of the sea surface by the weight of the atmosphere) must also be considered. Remaining temporal effects are caused by the wind and heat driven ocean currents and is termed the sea surface topography (SST).

Combining these individual components together yields the instantaneous sea surface, namely

$$h_i^{sea} = h_i^{g} + h_i^{SST} + h_i^{ot} + h_i^{set} + h_i^{inv} \tag{4.2}$$

where

h_i^{g} : geoid effect

h_i^{SST} : sea surface topography

h_i^{ot} : ocean tide effect

h_i^{set} : solid earth effect

h_i^{inv} : inverse barometer effect.

§ 4.4 Altimeter data records

Altimeter data are made available as Geophysical Data Records (GDR) or as Intermediate GDRs (IGDR) if the data are preliminary. The data are usually supplied on tapes, CD roms or accessible over the computer network. The files will contain most of the the corrections outlined above including the geoid and tides. Altimeter measurements are provided at a rate of about one per second and hence about 50,000 readings can be expected in one day. This presents problems with storing the data and also with the amount of computer time required for analysing this volume of information. For long arc orbits or determination of long wavelength phenomena this number is excessive and it is usual to 'compress' these data points into normal points which have a time resolution of , say , 15 seconds as chosen for this work.

For ERS-1, the ESA product OPR 02 data [CNES, 1992] was used for the work in this particular chapter. This particular 35 day cycle of data was transferred via the network from POL.

The preliminary IGDR CD roms were employed for the TOPEX/POSEIDON results [JPL, 1992 c].

§ 4.5 Error budget

The precision of the raw altimeter reading is about 3 to 5 cm. However the corrections themselves will also in error of a few cm but an overall precision of 10 cm is expected for h_i^{alt}.

Table 4.1: Error budget for altimetry data ; it shows the amplitude and wavelength of the unmodelled error and the residual error after modelling.

Type of error	Source	Amplitude (cm)	Residual (1 σ cm)	Wavelength (km)
Altimeter	Noise	-	5	-
Troposphere (dry)	Mass of air	240	0.7	1000
Troposphere (wet)	Water vapour	10-40	3	50 - 500
Ionosphere	Free electrons	2-20	3	50 - 10,000
Sea-state bias	Wave heights	2% SWH	2	500 - 1000
Geoid	Mass of Earth	100 m	30	2000 - 5000
Solid earth tide	Sun, Moon	20	2	20,000
Ocean tide	Sun, Moon	100	10	500 - 1000
Inv. bar. effect	Atmospheric pressure	50	3	200 - 1000
Orbital error	Gravity	10 km	10	40,000
"	Air drag	300	3	10,000
"	Solar radiation	300	3	10,000

Therefore the satellite ephemeris needs to be computed to the same degree of accuracy if full advantage is to be taken of the altimetry data. As will be demonstrated, the key source of error now is not the orbit trajectory, as used to be the case with the early orbits for SEASAT and GEOSAT, but the ocean geoid. Table 4.1 lists the possible errors and their sources [Schrama, 1989] which typically apply to ERS-1 and TOPEX/POSEIDON.

§ 4.6 Analysis of the altimeter residuals

The process of orbit determination computes the satellite altitude h_i^{cal} (the geodetic height of the satellite centre-of-mass with respect to a reference ellipsoid) for each altimeter normal point and the residual error is given as

$$\Delta h_i^{ob} = h_i^{ob} - h_i^{cal} \tag{4.3}$$

where the observed satellite height is

$$h_i^{ob} = h_i^{alt} + h_i^{sea} \tag{4.4}$$

(see Figure 4.1). It is stressed that altimetry is not used here as radial tracking data to improve the orbit ; instead the converged orbit is held fixed and the residuals computed. The residuals Δh_i^{ob} are predominately due to mismodelling in the orbit, geoid, SST and ocean tides as well as the altimeter bias and time tag bias and may be modelled by some function Δh_i^{cal}. The parameters within Δh_i^{cal}, such as the altimeter bias and time tag bias, are determined by fitting the function to the residuals Δh_i^{ob} in a least squares sense.

§ 4.7 Sea surface topography

The SST may be considered as the difference between the ocean geoid and the mean sea surface caused by ocean circulation phenomena, water density and winds. From equation 4.2, the observed SST is

$$h_i^{SST} = h_i^{cal} - h_i^{alt} - h_i^{g} - h_i^{ot/set/inv} \qquad (4.5)$$

The SST is conveniently modelled by a finite spherical harmonic expansion to degree and order M, i.e.

$$h_i^{SSTC} = \sum_{n=0}^{M} \sum_{m=0}^{n} \left(C_{nm} \cos m\lambda_i + S_{nm} \sin m\lambda_i \right) P_{nm}^{*} (\sin \phi_i) \qquad (4.6)$$

where P_{nm}^{*} are the normalized associated Legendre functions of degree n and order m and C_{nm}, S_{nm} are the coefficients to be determined. To ease computation, it preferable rewrite equation 4.6 as

$$h_i^{SSTC} = \sum_{n=0}^{M} \sum_{m=0}^{n} \sum_{\alpha=1}^{2} A_{nm}^{\alpha} \, Y_{nmi}^{\alpha} \qquad (4.7)$$

where

$$\begin{aligned} A_{nm}^{\alpha} &= C_{nm} \quad ; \quad \alpha = 1 \\ &= S_{nm} \quad ; \quad \alpha = 2 \end{aligned} \qquad (4.8)$$

and

$$\begin{aligned} Y_{nmi}^{\alpha} &= P_{nm}^{*} (\sin \phi_i) \cos m\lambda_i \quad ; \quad \alpha = 1 \\ &= P_{nm}^{*} (\sin \phi_i) \sin m\lambda_i \quad ; \quad \alpha = 2 \end{aligned} \qquad (4.9)$$

By using the following substitution

$$k = n^2 + n + 2m + \alpha \qquad (4.10)$$

equation 4.7 can be written more simply as

$$h_i^{SSTC} = \sum_{k=1}^{M'} x_k \, Y'_{ki} \qquad (4.11)$$

wherein

$$x_k = A_{nm}^{\alpha} \; ; \qquad Y'_{ki} = Y_{nmi}^{\alpha} \; ; \qquad M' = (M+1)(M+2) \qquad (4.12)$$

and M' is the number of coefficients for an expansion to degree and order M. For a SST expansion to degree and order 30, many of the C_{nm}, S_{nm} will be highly correlated and an ill-determined solution will result. The method of least squares collocation [Moritz, 1980] provides a constrained solution for C_{nm}, S_{nm} and involves the minimisation of the function Q as defined by

$$Q = \sum_{i=1}^{N} \left(h_i^{SST} - h_i^{SSTC} \right)^2 + \sum_{k=1}^{M'} \left(x_k^o - x_k \right)^2 w_k \qquad (4.13)$$

where N is the number of acceptable observations ; observed h_i^{SST} are assumed to be unit weighted and $w_k = 1/(\sigma_k^2)$ where σ_k is the 'a priori' standard error of x_k and x_k^o is the 'a priori' estimate of parameter x_k. Hence the difference between x_k and x_k^o is minimised. Putting equation 4.11 into 4.13 and minimising Q with respect to x_j

$$\frac{\partial Q}{\partial x_j} = -2 \sum_{i=1}^{N} \left(h_i^{SST} - \sum_{k=1}^{M'} x_k \, Y'_{ki} \right) Y'_{ji} - 2 \left(x_j^o - x_j \right) w_j = 0$$

(4.14)

and upon rearranging

$$\left(\sum_{k=1}^{M'}\left(\sum_{i=1}^{N} Y'_{ji}\ Y'_{ki}\right)x_k\right) + w_j\,x_j = \left(\sum_{i=1}^{N} h_i^{SST}\ Y'_{ji}\right) + w_j\,x_j^{o} \tag{4.15}$$

for j = 1 . . M'. Equation 4.15 can be expressed in matrix notation as

$$(\,D + W\,)\ \underline{x} \;=\; \underline{b} \;+\; W^{o} \tag{4.16}$$

where D is the positive definite symmetric matrix of size M' x M' ; W is a diagonal matrix of size M' x M' ; W^o and $\underline{b}$ are column vectors of size M' and $\underline{x}$ is the column vector of unknowns x_k. Their elements are

$$D_{jk} = \sum_{i=1}^{N}\left(\frac{\partial h_i^{SSTC}}{\partial x_j}\right)\left(\frac{\partial h_i^{SSTC}}{\partial x_k}\right) = \sum_{i=1}^{N} Y'_{ji}\ Y'_{ki}$$

$$\begin{aligned} W_{jk} &= \frac{1}{\sigma_k^2} \qquad ; \qquad j = k \\ &= 0 \qquad ; \qquad j \neq k \end{aligned}$$

$$b_j = \sum_{i=1}^{N} h_i^{SST}\left(\frac{\partial h_i^{SSTC}}{\partial x_j}\right) = \sum_{i=1}^{N} h_i^{SST}\ Y'_{ji}$$

and

$$W_j^{o} = \frac{x_j^{o}}{\sigma_j^2} \tag{4.17}$$

for $1 \le j, k \le M'$. The unknowns x_k are related to the spherical harmonic coefficients C_{nm}, S_{nm} by equation 4.10 and are determined by inverting (D+W) to yield the solution $\underline{x} = (D+W)^{-1}\ (\underline{b} + W^{o}\,)$. Equation 4.12 shows how there are (M+1)(M+2) coefficients for an SST expansion of degree and order M. Hence for M = 30 as chosen for this study there are 992 unknowns to solve for.

Instead of solving for the SST from scratch, a preliminary SST (PSST) expansion is introduced into equation 4.5 such that it becomes

$$h_i^{SST} = h_i^{cal} - h_i^{alt} - h_i^{g} - h_i^{ot/set/inv} - h_i^{PSST} \tag{4.18}$$

where h_i^{PSST} is the PSST elevation associated with h_i^{alt}. The PSST expansion utilised for this study is of degree and order 15 and was determined using GEOSAT data [Lerch et al., 1992]. The unknowns C_{nm}, S_{nm} will therefore be corrections to the PSST to degree and order 15, beyond which they are the actual values to degree and order 30. The corrections and higher order terms are assumed small and their expected values may be taken as zero. Hence the elements of the column vector W^o are zero. The standard error σ for each C_{nm}, S_{nm} is taken as 2 cm in accordance with the PSST used. This constraint significantly lowers correlations and permits the corrections for the harmonic coefficients to be determined as acceptable values. Incorporating a PSST has the advantage that good altimeter measurements are not rejected on account of omitting the effect of the SST.

§ 4.8 Crossovers

The intersection between ascending and descending satellite ground tracks forms a crossover point as illustrated in Fig. 4.2. The ground track is the geodetic projection of the satellite orbit on the surface of the Earth.

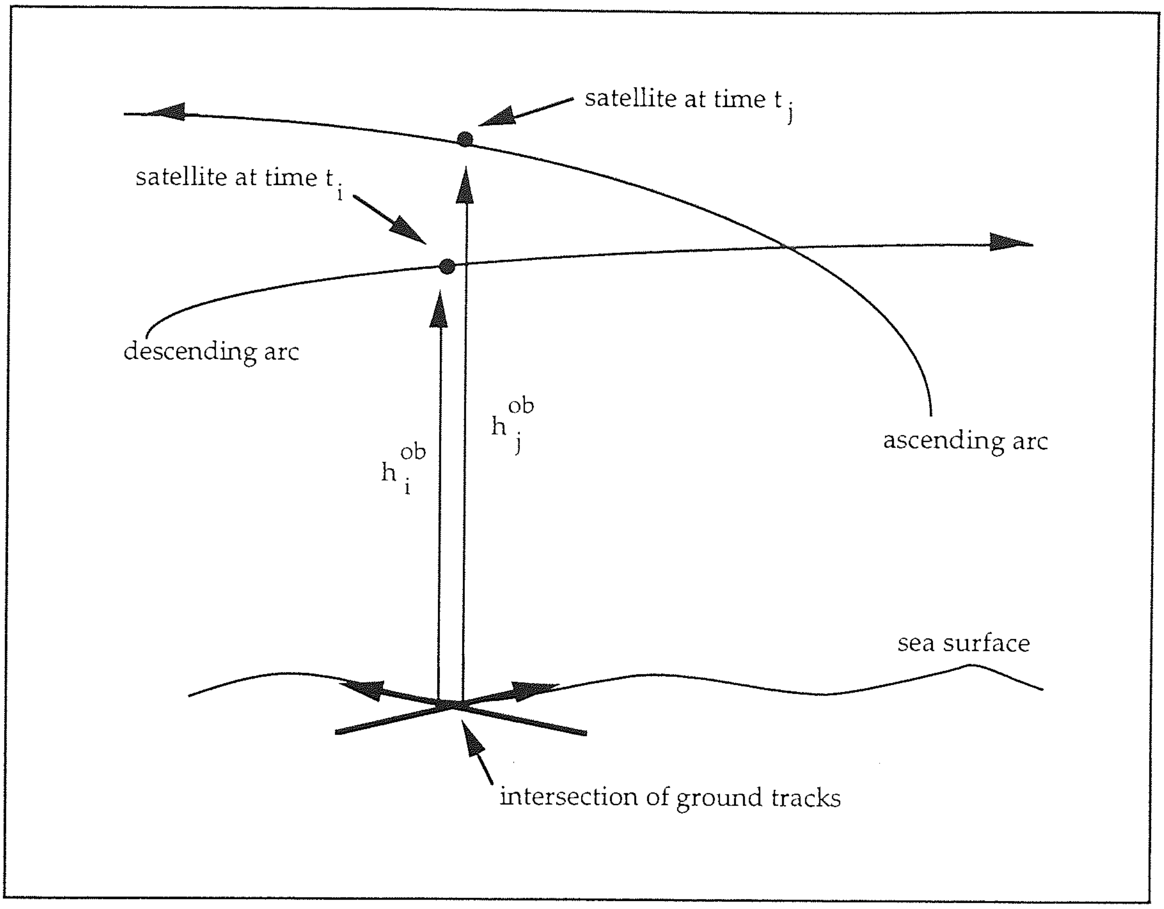

Figure 4.2

Let h_i^{cal} and h_j^{cal} be the calculated geodetic heights of the spacecraft and similarly let h_i^{ob} and h_j^{ob} be the corrected observed height at times t_i, t_j as defined by equation 4.4 . The crossover height residual is then

$$\Delta C_{ij}^{ob} = C_{ij}^{ob} - C_{ij}^{cal} \tag{4.19}$$

wherein

$$C_{ij}^{ob} = h_i^{ob} - h_j^{ob} \quad \text{; observed crossover difference} \tag{4.20}$$

and

$$C_{ij}^{cal} = h_i^{cal} - h_j^{cal} \quad \text{; calculated crossover difference} \tag{4.21}$$

Equation 4.20 shows how time invariant components within h_i^{ob} and h_j^{ob} such as the altimeter bias, centre-of-mass correction, SST and , in particular, the geoid height all cancel out. Similarly within equation 4.21 the centre-of-mass correction to the laser retro-reflector and the constant and geographically correlated components of the radial orbit error also, for the most part, cancel out. Hence the crossover residual ΔC_{ij}^{ob} will be mainly due to residual radial orbit error and provides an independent check on the precision of the satellite trajectory. The crossover points $(\phi_{ij}, \lambda_{ij})$ are calculated from ephemeris files created during the numerical integration and hence these points are not the 'true' crossover points but rather 'pseudo' crossover points, sufficiently accurate to provide a useful analysis. The crossover residuals are not used within this study to refine the orbit determination but are calculated to evaluate the time tag bias.

§ 4.9 Time Tag Bias

The time tag bias τ introduces a height error h_i^{ttb} which is due to the time t_i being tagged to altimeter observation h_i^{alt} rather than the true time T_i (where $t_i = T_i + \tau$). Therefore h_i^{alt} is strictly an observation at time T_i and needs correcting to time t_i. Orbit determination computes the spacecraft height at time t_i and associates this altitude with h_i^{alt}.

Figure 4.3 shows how the timing error translates into a vertical height error. The error τ is assumed to be a small constant, in the order of a few milliseconds, and hence the correct altimeter height required at time t_i may be expressed as a Taylor series

$$h^{alt}(t_i) = h^{alt}(T_i + \tau) = h^{alt}(T_i) + \left(\frac{dh_i}{dt}\right)\tau + O(\tau^2) \qquad (4.22)$$

wherein the height error is

$$h_i^{ttb} = \left(\frac{dh_i}{dt}\right)\tau \qquad = \dot{h}_i\,\tau \tag{4.23}$$

and the dot represents differentiation with respect to time.

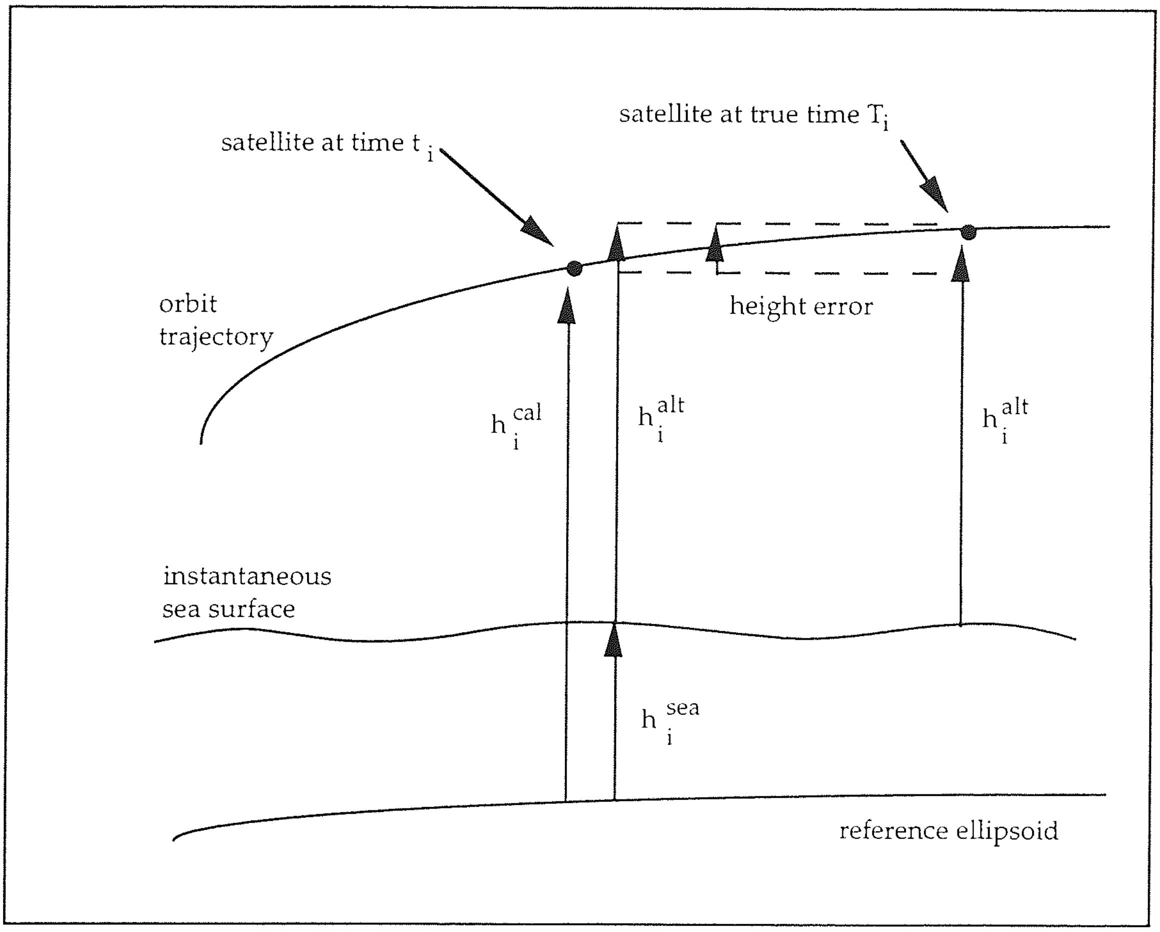

Figure 4.3

Ignoring higher order terms $O(\tau^2)$ is permissible since the second order term $(\ddot{h}_i\tau^2)/2$ is less than 1 cm for, say, $\ddot{h}_i = 1\ m/s^2$ and $\tau = 0.01$ second. The rate of change $\dot{h}_i$ may be computed with sufficient accuracy as $\dot{r}_i$ where r_i is the computed geocentric (or radial) height of the satellite at time t_i, assuming the geoid effect on $\dot{h}_i$ to be negligible. Since

$$\dot{r}_i = \frac{\partial r_i}{\partial x_i}\frac{dx_i}{dt} + \frac{\partial r_i}{\partial y_i}\frac{dy_i}{dt} + \frac{\partial r_i}{\partial z_i}\frac{dz_i}{dt} \tag{4.24}$$

and

$$r_i^2 = x_i^2 + y_i^2 + z_i^2 \tag{4.25}$$

hence

$$\dot{r}_i = \frac{1}{r}\left(x_i\,\dot{x}_i + y_i\,\dot{y}_i + z_i\,\dot{z}_i\right). \tag{4.26}$$

The rate of change $\dot{r}_i$ is invariant under rotation and may be computed in the J2000 or Earth-fixed reference frame. Computation of $\dot{r}_i$ is simple since the satellite position and velocity is generated at each time t_i by numerical integration. Similar studies have been carried out for SEASAT [Marsh and Williamson, 1982; Schutz et al., 1982]. Determination of the time tag error τ may be accomplished by two different methods ; the 'direct' method and the 'crossover' method.

§ 4.9.1 Direct Method for the Time Tag Bias

It is possible to solve for the time tag bias τ directly from pure altimetry by modelling the observed altimeter residuals Δh_i^{ob} as

$$\Delta h_i^{cal} = b + \dot{h}_i\,\tau + C_1 \cos M_i + S_1 \sin M_i + C_2 \cos 2M_i + S_2 \sin 2M_i \tag{4.27}$$

where b may be interpreted as the altimeter bias, M_i the mean anomaly and C_1, S_1, C_2, S_2 the constant coefficients. The once and twice per revolution terms will absorb periodic errors, in particular the dominant 1/rev radial orbit error. A least squares solution for the 6 parameters within Δh_i^{cal} requires the minimisation of the function I where

$$I = \sum_{i=1}^{N} \left(\Delta h_i^{ob} - \Delta h_i^{cal} \right)^2 \tag{4.31}$$

where N is the number of acceptable observations. On minimising I with respect to parameter x_k

$$\frac{\partial I}{\partial x_k} = -2 \sum_{i=1}^{N} \left(\Delta h_i^{ob} - \Delta h_i^{cal} \right) \left(\frac{\partial \Delta h_i^{cal}}{\partial x_k} \right) = 0 \tag{4.32}$$

and is equivalent to solving the system of equations D $\underline{x} = \underline{b}'$ (to order $O(\Delta h)$) where

$$D_{jk} = \sum_{i=1}^{N} \left(\frac{\partial \Delta h_i^{cal}}{\partial x_j} \right) \left(\frac{\partial \Delta h_i^{cal}}{\partial x_k} \right)$$

$$b'_j = \sum_{i=1}^{N} \Delta h_i^{ob} \left(\frac{\partial \Delta h_i^{cal}}{\partial x_j} \right) \tag{4.33}$$

for $1 \leq j,k \leq 6$ and $\underline{x}$ is the column vector of the 6 parameters within equation 4.27. The partial derivatives required for the computation of elements in equation 4.33 are

$$\frac{\partial \Delta h_i^{cal}}{\partial b} = 1 \; ; \qquad \frac{\partial \Delta h_i^{cal}}{\partial \tau} = \dot{h}_i$$

$$\frac{\partial \Delta h_i^{cal}}{\partial C_1} = \cos M_i \; ; \qquad \frac{\partial \Delta h_i^{cal}}{\partial S_1} = \sin M_i$$

$$\frac{\partial \Delta h_i^{cal}}{\partial C_2} = \cos 2M_i \; ; \qquad \frac{\partial \Delta h_i^{cal}}{\partial S_2} = \sin 2M_i \qquad (4.34)$$

Inversion of matrix D yields the solution $\underline{x} = D^{-1}\,\underline{b}'$. Because this method uses pure altimetry, the solution will be affected by the presence of the geoid error.

§ 4.9.2 Crossover Method for the Time Tag Bias

Rather than analysing the pure altimeter residuals Δh_i^{ob} which include a significant geoid error, a study of the crossover residuals may be performed to determine the time tag bias τ. The residuals ΔC_{ij}^{ob} can be modelled by taking the difference between Δh_i^{cal} and Δh_j^{cal} as defined by equation 4.27, namely

$$\begin{aligned} \Delta C_{ij}^{cal} &= \Delta h_i^{cal} - \Delta h_j^{cal} \\ &= \Delta b + (\dot{h}_i - \dot{h}_j)\,\tau \\ &\quad + C'_1(\cos M_i - \cos M_j) + S'_1(\sin M_i - \sin M_j) \\ &\quad + C'_2(\cos 2M_i - \cos 2M_j) + S'_2(\sin 2M_i - \sin 2M_j) \qquad (4.35) \end{aligned}$$

Since the bias may originate partly from non-instrumental sources, it is assumed not to cancel out completely at the crossover point and the difference Δb is included although it is expected to be only a few centimetres. Once again a least squares process is performed to determine the 6 parameters within equation 4.35 and involves the minimisation of the function I where

$$I = \sum_{\alpha=1}^{N_c} \left(\Delta C_\alpha^{ob} - \Delta C_\alpha^{cal} \right)^2 \qquad (4.36)$$

where N_c is the number of acceptable crossover points and α denotes the crossover at times t_i^α and t_j^α. Equation 4.36 is minimised and the parameters within ΔC_α^{cal} solved for as outlined in section 4.9.1 . Since the geoid error is removed, this analysis should provide a more reliable value for τ than the direct method.

§ 4.10 Repeat track analysis for TOPEX/POSEIDON data

For cycle 20 of the TOPEX/POSEIDON mission, the POSEIDON altimeter was operating continually and represents the first complete cycle of POSEIDON data. On the following cycle, 21, TOPEX operated continually. These two cycles therefore provide an opportunity to carry out a repeat track study to determine the difference between the TOPEX and POSEIDON altimeter biases. The repeat track method [Cheney et al., 1983] is described fully in chapter 5 but will outlined briefly here.

Initially the two cycles need to be aligned such that at times t_0^T and t_0^P (at the start of the TOPEX and POSEIDON cycles respectively) the satellite is at exactly the same geodetic latitude during the same pass. The times t_0^T and t_0^P are determined by simple linear interpolation and are taken here to be as early as possible into each cycle. Then for each cycle the observed height residuals Δh_i^{ob} (computed by subtracting the CNES orbit height, supplied on the IGDR, from the corrected observed altimeter measurement) are determined and interpolated at regular one second intervals from start times t_0^T, t_0^P onwards to derive the regular one per second residuals ΔH_k^{int}, k being the new index for the interpolated values which denotes the number of integer seconds since times t_0^T, t_0^P. Also the ground position is interpolated for, namely $(\phi_k, \lambda_k)^T$ and $(\phi_k, \lambda_k)^P$. Hence TOPEX and POSEIDON residuals $(\Delta H_k^{int})^T$, $(\Delta H_k^{int})^P$ are determined at approximately the same geodetic position (ϕ_k, λ_k) along the ground track of the two cycles and may be compared with each other. The observed difference between these residuals is

$$\Delta H_k^{ob} = (\Delta H_k^{int})^T - (\Delta H_k^{int})^P \tag{4.37}$$

and is analogous to the observed crossover residual ΔC_{ij}^{ob} discussed in section 4.8 and hence will be free of geoid error and other time invariant effects such as the centre-of-mass correction. Within ΔH_k^{ob} is the altimeter bias difference as well as residual radial orbit error and other errors due to mismodelling of tides, etc. Hence the observed residual ΔH_k^{ob} may be modelled by

$$\begin{aligned}\Delta H_k^{cal} = {} & b^{diff} + C''_1 \cos M_k + S''_1 \sin M_k \\ & + C''_2 \cos 2M_k + S''_2 \sin 2M_k\end{aligned} \tag{4.38}$$

wherein b^{diff} is the bias offset of the TOPEX altimeter relative to the POSEIDON altimeter. The once and twice per revolution terms are included to absorb the effect of the residual radial orbit error. The least squares procedure and the partial derivatives required to solve for the 5 parameters is similar to that outlined in section 4.9.1 and will not be described here.

The geodetic ground position (ϕ_k , λ_k) of the satellite for time $t_0^T + k$ during the TOPEX cycle will not be exactly the same as for time $t_0^P + k$ during the POSEIDON cycle, but the mean difference should be about 1 km. The distance d_k between $(\phi_k, \lambda_k)^T$ and $(\phi_k, \lambda_k)^P$ along the ground is approximated spherically as

$$d_k = \frac{R_E}{2\pi} \cos^{-1} (\hat{\underline{r}}_k^T \cdot \hat{\underline{r}}_k^P) \tag{4.39}$$

where $\hat{\underline{r}}_k$ is the unit radial vector of the sub-satellite point defined by

$$\hat{\underline{r}}_k = (\cos\phi_k \cos\lambda_k)\, \underline{i} + (\cos\phi_k \sin\lambda_k)\, \underline{j} + \sin\phi_k\, \underline{k} \tag{4.40}$$

and R_E is taken as 6378 km. Hence residuals ΔH_k^{ob} with $d_k > 1.5$ km, for example, may be rejected.

§ 4.11 Numerical Results

Analysis of the altimetry and crossover points is achieved by presenting these data to the converged long arc orbits computed at Aston University as described in chapter 3. The ERS-1 35 day repeat cycle is broken down into 7 contiguous passes, each one 5 or 6 days in duration, so as to ensure the accuracy of the calculated orbits. Pass 1 is only 1.5 days long since a manoeuvre was performed very soon afterwards which disrupted the numerical integration process. The TOPEX/POSEIDON cycles repeat approximately every 9.9 days and an orbit was generated for each cycle of the same duration. All these cycles utilised TOPEX altimetry only except for cycle 20 which is only POSEIDON data. The fit (root mean square or rms) of the observed data to the computed values is tabulated in Table 4.2 for ERS-1 and Table 4.3 for TOPEX/POSEIDON.

§ 4.11.1 Long arc orbits

All the ERS-1 and TOPEX/POSEIDON long arc orbits (except for the TOPEX/POSEIDON repeat track analysis) employed in this chapter were computed with the JGM-2 gravity field of degree and order 70 [Lerch et al., 1993] using the SATAN suite of programs [Sinclair and Appleby, 1986]. The geoid is computed up to degree and order 70 from the JGM-2 gravity field and then from 70 to degree and order 360 using the OSU91A gravity field [Rapp et al., 1991]. The laser range normal point data and approximate start vectors were supplied by the RGO. The rejection level for the laser residuals for both ERS-1 and TOPEX/POSEIDON is chosen at 50 cm, though with hindsight this is somewhat severe for ERS-1 since in some cases one fifth of the data was rejected. A 1/rev along-track correction and a daily saw-tooth drag model were included for both satellites and moreover a 1/rev across-track correction for TOPEX/POSEIDON. From Table 4.2, the ERS-1 orbits are of a good fit, with pass 1 having a rms of 1.7 cm which is due to the brevity of the orbit. Table 4.3 shows the TOPEX/POSEIDON orbits to be of a consistent level of accuracy with a rms of fit between the computed and observed laser ranges of about 10 cm or better.

The crossover rms is the fit before the time tag bias or any other terms are solved for. This measure of fit gives an indication of how precise the radial component (excluding the geographically correlated component) of the computed orbits is since geoid error is not present, as described in section 4.8. Hence for ERS-1 the radial height accuracy is about 25 cm rms and about 13 cm rms for TOPEX/POSEIDON. However the crossover residuals contain other mismodelled phenomena such as ocean tides and these will have contributed to the overall rms. The rejection level for the crossovers residuals is chosen at 50 cm for ERS-1 and 30 cm for TOPEX/POSEIDON.

The pure altimetry rms values presented are the fits after solving for the altimeter bias and sea surface topography (SST) which absorbs some of the long wavelength geoid error. Hence the altimeter rms is due primarily to the geoid mismodelling, radial orbit error and ocean tide errors. Results show that the altimetry fit for ERS-1 is around 33 cm rms and for TOPEX/POSEIDON about 23 cm rms. The rejection level for the pure altimeter residuals is 1 metre.

The superior measures of fit for TOPEX/POSEIDON data is chiefly a consequence of the more accurate orbits which are far better determined than for ERS-1 because of denser laser tracking and fewer difficulties in atmospheric drag and gravity field modelling due to the higher orbital height.

§ 4.11.2 Altimeter bias

Initial bias estimates of -70 cm for ERS-1, -40 cm for TOPEX and zero for POSEIDON were subtracted from the observed altimeter points in order that points were not rejected on account of the bias error. These approximate values were determined from preliminary long arc solutions. Hence corrections are derived relative to these initial values. The solution for a bias in the altimeter residuals means that all time-invariant errors, such as in the Earth semi-major axis, centre-of-mass corrections and indeed the altimeter itself, cannot be separated. Thus it is necessary to state that the bias results computed here are relative to a reference ellipsoid with a semi-major axis of 6378136.3 metres and a reciprocal flattening of 298.257.

The ERS-1 altimeter bias for each of the 7 passes is determined from the unconstrained solution for a 2x2 SST. Table 4.2 shows the bias to be about -70 cm (ERS-1 altimeter is measuring 70 cm too short). On combining the normal equations for the 30x30 SST coefficients, which were determined for each of the 7 passes, and solving for a full 30x30 SST over the 35 day period, the altimeter bias is evaluated at -69.2 cm.

The TOPEX altimeter bias for each cycle is computed from a solution for a 30x30 SST. Table 4.3 shows the bias to be about -40 cm (TOPEX measuring 40 cm too short). The slightly larger values for cycles 2, 3, and 4 initially suggest a drift in the TOPEX bias but this is certainly refuted during the later cycles. On solving the combined normal equations for the 30x30 SST for cycles 2-10, an overall bias value of -41.4 cm is obtained. Similarly the combined cycles of 21 and 22 yield a bias of -39.6 cm. By weighting these two values with the number of observations and taking a simple average, the TOPEX bias is estimated at -41.0 cm

From cycle 20, the POSEIDON altimeter bias is estimated at -17.7 cm, again derived from a solution of the 30x30 SST (POSEIDON measuring some 18 cm too short).

These TOPEX and POSEIDON results were published [Lam and Moore, 1993; Lam et al., 1993] and agree very well with findings from other investigators [JPL, 1993 a, b]. The computed standard errors are not listed for the altimeter biases in Tables 4.2 and 4.3 since these values were very small (less than a cm) and provide very little information.

Table 4.2: ERS-1 results for 35 day cycle (1st Sept to 5th Oct 1992) ; all measurements are in cm with the number of accepted observations in brackets. The altimeter bias is determined from a 2x2 SST for passes 1 to 7. Combining all the passes 1-7, a 30x30 SST is solved for to obtain the overall bias for the entire 35 day cycle. Bias values are relative to an Earth semi-major axis of 6378136.3 metres.

Pass	Epoch (MJD)	Days	Laser RMS	Crossover RMS	Altimetry RMS	Altimeter bias
1	48866.0 - 48867.5	1.5	1.7 (219)	25.6 (59)	33.1 (3558)	-68.4
2	48868.0 - 48873.0	5	10.6 (477)	25.5 (407)	33.1 (8794)	-71.6
3	48873.0 - 48879.0	6	14.8 (481)	23.8 (1127)	30.6 (14567)	-72.0
4	48879.0 - 48884.0	5	16.0 (657)	29.1 (767)	36.8 (13194)	-71.6
5	48884.0 - 48890.0	6	11.2 (658)	19.6 (1093)	29.6 (15083)	-70.4
6	48890.0 - 48896.0	6	17.9 (567)	25.9 (831)	35.1 (14185)	-67.5
7	48896.0 - 48902.0	6	10.9 (485)	22.7 (708)	33.8 (12728)	-68.7
1-7	48866.0 - 48902.0	35	-	24.2 (4992)	30.7 (82109)	-69.2

Table 4.3: Results for TOPEX cycles 2-10 & 21-22 and POSEIDON cycle 20 ; all measurements are in cm with the number of accepted observations in brackets. Bias values are relative to an Earth semi-major axis of 6378136.3 metres and are determined from a 30x30 SST.

Cycle	Epoch (MJD)	Laser RMS	Crossover RMS	Altimetry RMS	Altimeter bias
2	48898.07 - 48907.98	10.0 (4252)	12.6 (7584)	22.0 (30334)	-44.7
3	48907.98 - 48917.89	9.7 (3356)	13.6 (5623)	22.4 (23895)	-43.3
4	48917.89 - 48927.81	9.5 (2400)	13.5 (6569)	22.3 (22901)	-43.1
5	48927.81 - 48937.73	9.4 (2719)	12.1 (5271)	22.2 (27639)	-41.9
6	48937.73 - 48947.64	10.9 (3580)	14.6 (4300)	22.9 (24829)	-40.0
7	48947.64 - 48957.58	10.4 (1317)	14.2 (4422)	27.0 (32475)	-40.4
8	48957.58 - 48967.49	8.8 (1702)	13.6 (5085)	22.3 (28250)	-38.9
9	48967.49 - 48977.40	9.3 (1756)	14.4 (3829)	26.4 (23694)	-40.2
10	48977.40 - 48987.30	9.0 (1780)	11.4 (3593)	22.2 (25486)	-40.3
2-10	**48898.07 - 48987.30**	-	**13.3** **(46276)**	**23.5** **(239503)**	**-41.4**
20	49076.55 - 49086.46	9.0 (5369)	12.3 (6760)	23.1 (32086)	-17.7P
21	49086.46 - 49096.38	7.4 (4035)	11.8 (6962)	22.2 (33874)	-39.5
22	49096.38 - 49106.30	8.7 (4466)	11.6 (6890)	22.1 (33597)	-39.8
21-22	**49086.46 - 49106.30**	-	**11.7** **(13852)**	**21.7** **(67840)**	**-39.6**

§ 4.11.3 Sea surface topography

The sea surface topography or SST is solved for in order to absorb the permanent and temporal features of the SST over a particular period and hence provide a more reliable value for the altimeter bias. The bias component of the solution is not a feature of the SST and may be interpreted as a correction to the initial bias value. However geoid and radial orbit error are also absorbed into the solution and therefore the final solution is not an exact representation of the true SST for that time span. Other errors such as tides will tend to appear random and hence are unlikely to seriously contaminate the solution. As detailed in section 4.7, a preliminary SST (PSST) was included in the altimeter observations and the solution constrained to provide a correction to this PSST. The PSST is of degree and order 15 and is depicted in figure 4.4. The omission of terms beyond degree and order 30 is not serious since the SST is known to possess most of its power in the lower frequencies [Lerch et al., 1992]. Figure 4.5 shows the full 30x30 SST for the ERS-1 35 day repeat during 1st Sept to 5th Oct 1992. Figure 4.6 is the SST for TOPEX cycle 2 only, figure 4.7 TOPEX is for cycles 2 to 10 inclusive, figure 4.8 is for POSEIDON during cycle 20 and figure 4.9 is for TOPEX during cycles 21 and 22 combined. The bias values are not included in these contour plots.

§ 4.11.4 Time tag bias

The normal equations for the solution of the time tag bias by both the direct and crossover methods (as detailed in section 4.9) were computed for each of the seven ERS-1 passes and each of the TOPEX/POSEIDON cycles. The normal equations of the seven ERS-1

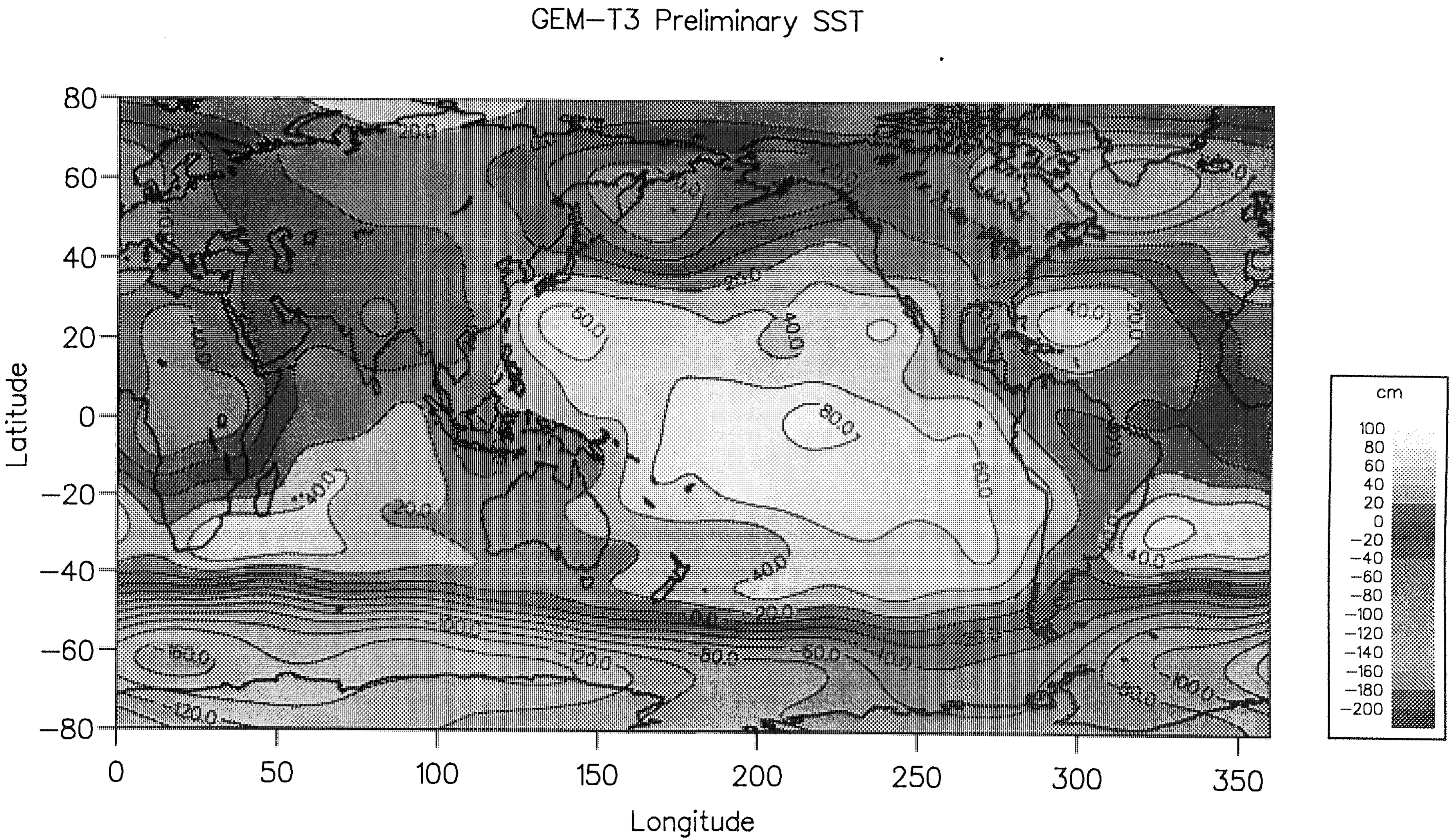
GEM-T3 Preliminary SST

Figure 4.4

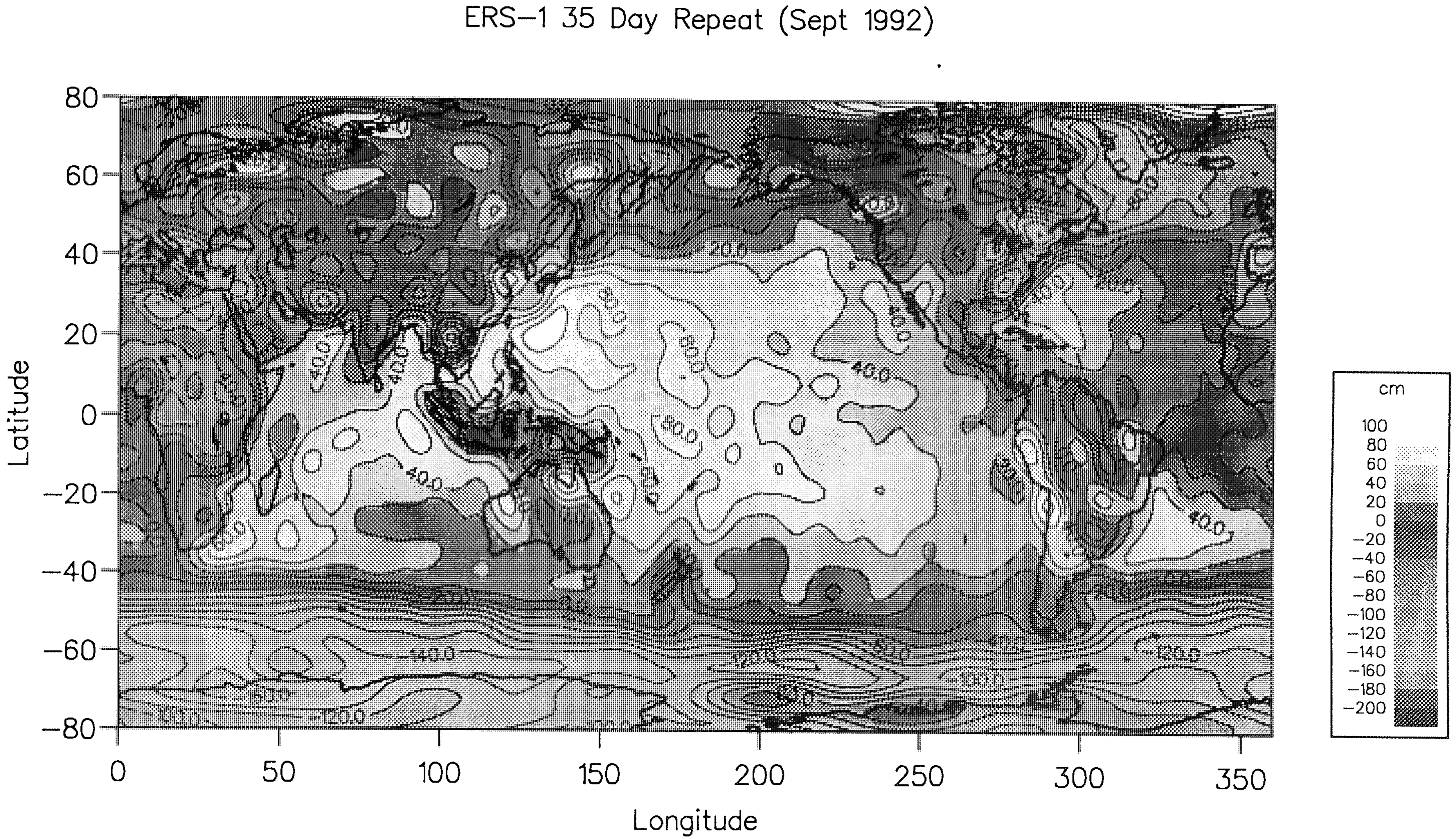
ERS–1 35 Day Repeat (Sept 1992)
Latitude
80
60
40
20
0
–20
–40
–60
–80
Longitude
0
50
100
150
200
250
300
350
cm
100
80
60
40
20
0
–20
–40
–60
–80
–100
–120
–140
–160
–180
–200

Figure 4.5

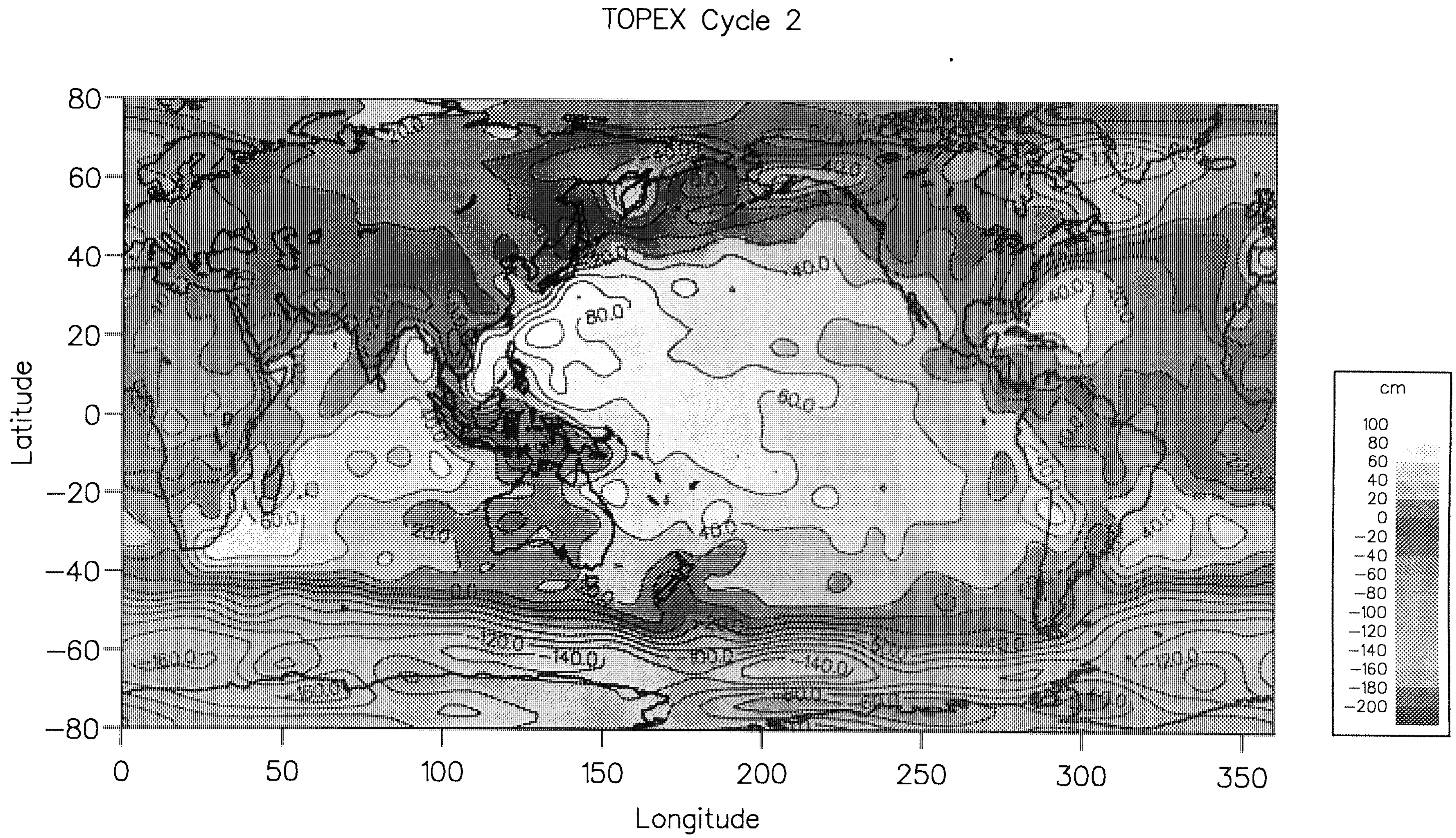
TOPEX Cycle 2
Latitude
80
60
40
20
0
−20
−40
−60
−80
Longitude
0
50
100
150
200
250
300
350
cm
100
80
60
40
20
0
−20
−40
−60
−80
−100
−120
−140
−160
−180
−200
80.0
60.0
40.0
20.0
0.0
-120.0
-140.0
-160.0

Figure 4.6

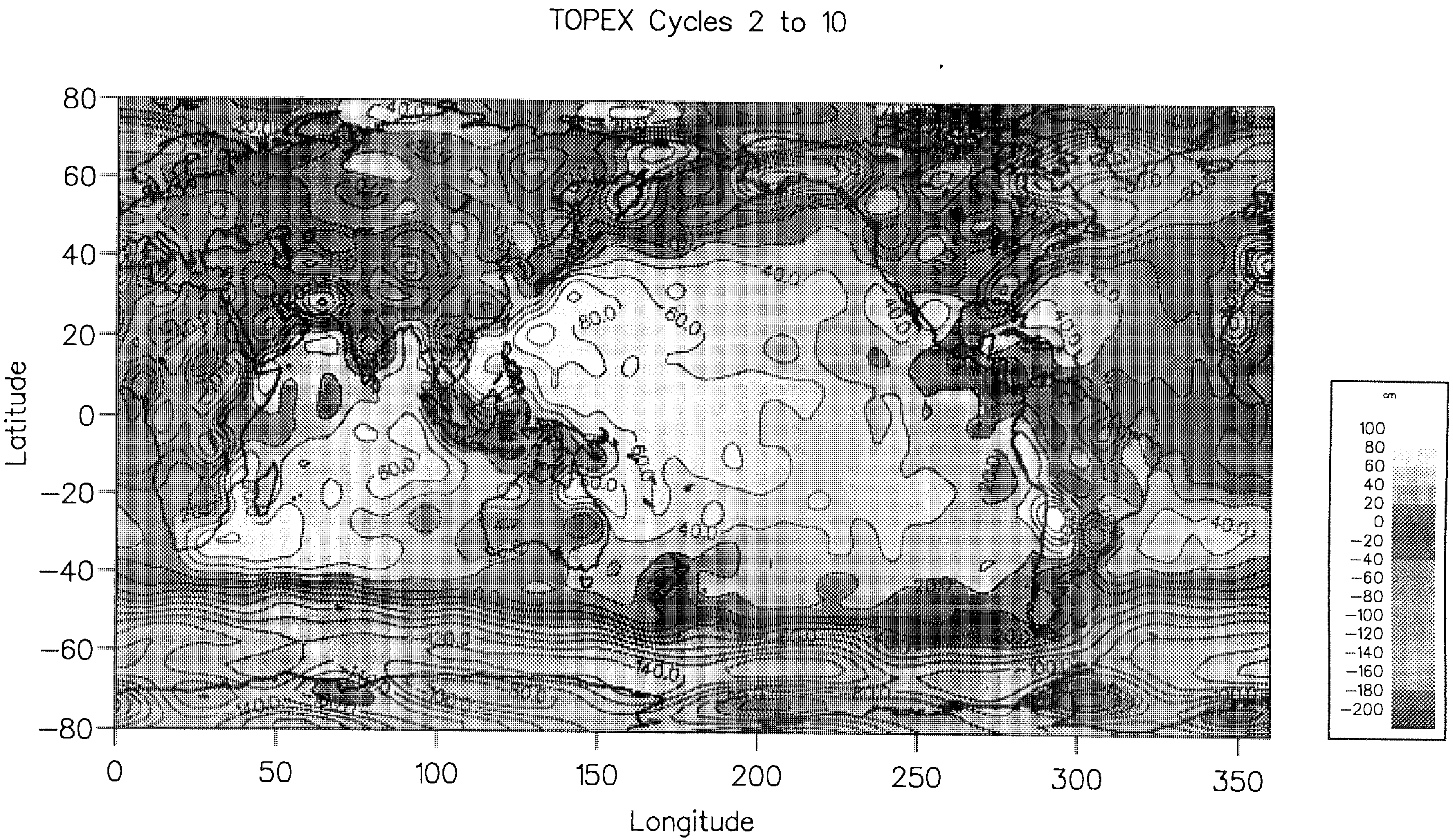
TOPEX Cycles 2 to 10
Latitude
80
60
40
20
0
−20
−40
−60
−80
Longitude
0
50
100
150
200
250
300
350
cm
100
80
60
40
20
0
−20
−40
−60
−80
−100
−120
−140
−160
−180
−200
80.0
60.0
40.0
120.0
140.0

Figure 4.7

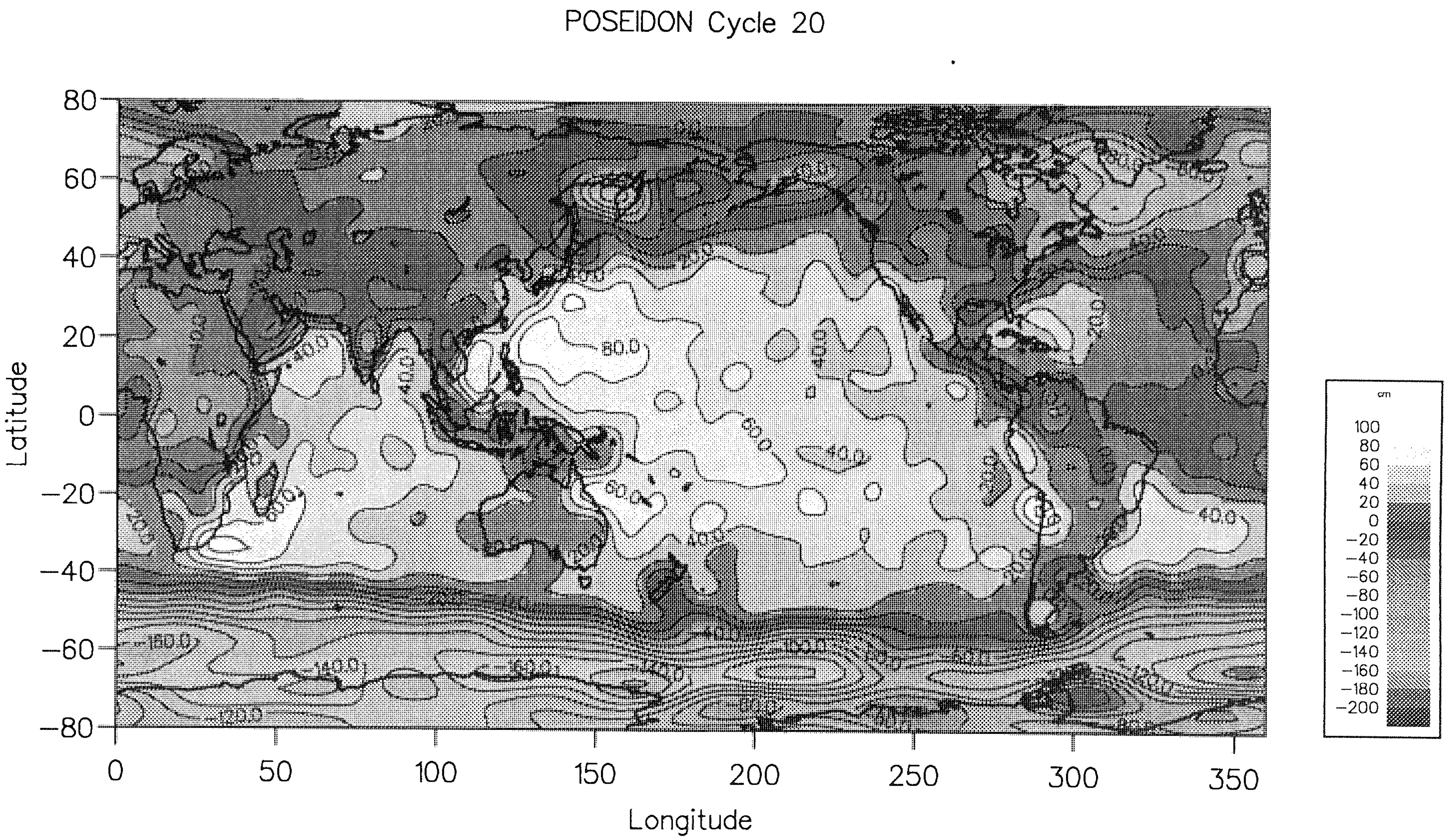
POSEIDON Cycle 20

Figure 4.8

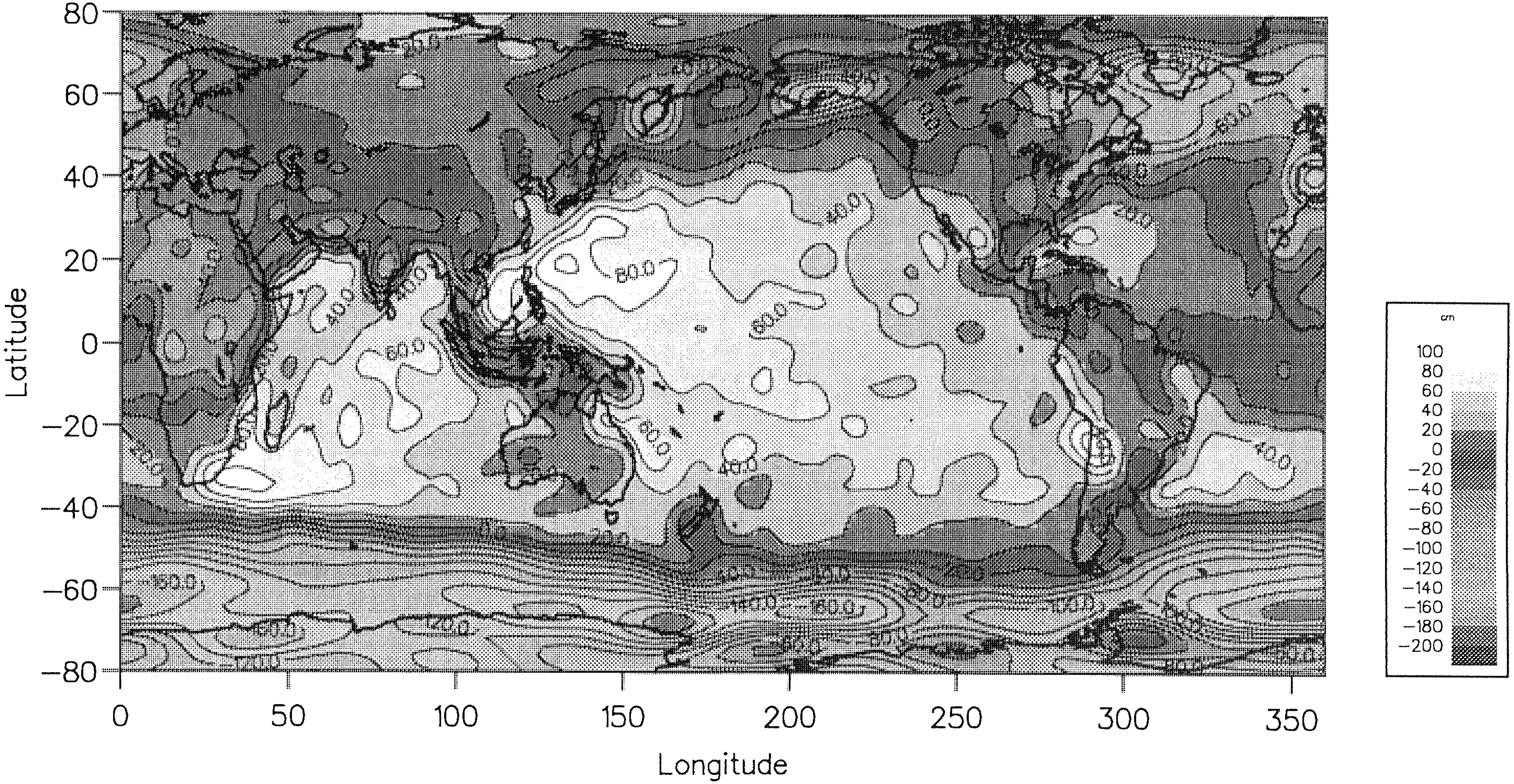
TOPEX Cycles 21 to 22

Figure 4.9

passes were then summed and solved for, as were cycles 2 to 10 for TOPEX. The normal equations for cycles 21 & 22 were summed together and solved for, distinct from 2 to 10, to detect a possible change in the TOPEX time tag bias over time. The results are presented in Table 4.4 .

Table 4.4: Time tag bias results for ERS-1, TOPEX and POSEIDON ; the time tag bias is shown in milliseconds (ms) with all other values in cm.

Direct Method

	Time tag bias τ	Alt. bias	cosM	sinM	cos2M	sin2M
ERS-1 (35 day cycle)	-2.08	-67.7	---	17.8	6.6	-2.1
TOPEX (Cycles 2-10)	4.97	-38.7	-4.9	-0.9	1.2	0.4
TOPEX (Cycles 21-22)	0.45	-38.1	12.6	2.5	---	---
POSEIDON (Cycle 20)	3.89	-17.3	0.7	14.7	---	---

Crossover Method

	Time tag bias τ	Delta bias	cosM	sinM	cos2M	sin2M
ERS-1 (35 day cycle)	-0.60	-0.9	---	-19.1	---	---
TOPEX (Cycles 2-10)	-0.01	0.0	-0.4	0.2	-0.6	0.0
TOPEX (Cycles 21-22)	0.74	-0.1	-0.2	3.6	---	---
POSEIDON (Cycle 20)	3.73	-4.8	0.2	24.5	---	---

From analysing the computed ephemerides, ERS-1 has a maximum rate of change in the radial direction of about 10 m/sec whereas for TOPEX/POSEIDON it is around 30 cm/sec. If the altimeter height error due to the time tag bias τ is not to exceed 10 cm then τ must be within ~10 milliseconds (ms) for ERS-1 and ~30 ms for TOPEX/POSEIDON. Hence the results clearly show that there are no significant timing biases for any of the three altimeters. In some cases the 1/rev and 2/rev terms were not solved for because the solution for τ is sensitive to high correlations with these terms. The altimeter biases derived from the direct method agree very well with those computed in the solution for the SST in section 4.11.2.

§ 4.11.5 Repeat track analysis

The repeat track method using the POSEIDON-only cycle 20 and TOPEX-only cycle 21 estimates the difference between the two altimeters to be -21.4 cm. This value implies that the TOPEX is measuring 21.4 cm shorter than POSEIDON, i.e. the TOPEX bias is more negative by 21.4 cm. This result is in full agreement with the values presented in section 4.11.2 and 4.11.3 where the TOPEX bias is about -40 cm and POSEIDON about -18 cm. Table 4.5 shows the complete solution. The rms of the residuals before fit is 10.7 cm which is slightly better than the crossover rms in table 4.3. The amplitudes of the 1/rev and 2/rev terms are very small which suggests that most the error is from tidal mismodelling and random in nature. In all, 426,546 one per second interpolated residuals were computed and accepted. The mean approximate distance, $\bar{d}_k$, between two 'identical' observations was 775 m with a standard deviation of 247 m which demonstrates that TOPEX/POSEIDON is repeating its orbit to an accuracy of around 1 km as expected. Table 4.5 shows the distribution of the distances d_k in more detail. The CNES orbit on the IGDRs were used for this particular analysis.

Table 4.5: Repeat track analysis of the difference between the TOPEX and POSEIDON altimeter biases using cycles 20 and 21.

Bias difference	cosM	sinM	cos2M	sin2M
-21.4 cm	0.8 cm	0.7 cm	-0.3 cm	-1.6 cm

TOPEX is therefore measuring 21.4 cm shorter than POSEIDON.

Number of possible points = 440,568
Rejected with residual > 30 cm = 13933
Rejected with $d_k > 1.5$ km = 89

Number of accepted points = **426,546**
RMS of residuals = 10.7 cm

Number of points with $d_k < 0.5$ km = 64992
Number of points with $0.5 < d_k < 1.0$ km = 283152
Number of points with $1.0 < d_k < 1.5$ km = 78402
Number of points with $d_k > 1.5$ km = 89

§ 4.12 Conclusions

The main objective of the work presented in this chapter is to estimate the altimeter and time tag biases associated with the ERS-1, TOPEX and POSEIDON altimeters. The final results are displayed in table 4.6.

The altimeter biases computed from the 30x30 SST and the direct method (for the time tag bias) agree to within 3 cm for all three altimeters. The time tag bias values are extremely small and hence the height error due to these can be dismissed with confidence. The repeat track analysis demonstrates that TOPEX is measuring some 21 cm shorter than POSEIDON which agrees extremely well with the findings in Table 4.6.

Table 4.6: Results of the ERS-1, TOPEX and POSEIDON altimeter and time tag biases by long arc solution

	--- Altimeter bias (cm) ---		--- Time tag bias (ms) ---	
	A *	B *	Direct	Crossover
ERS-1 (35 day cycle)	-69.2	-67.7	-2.1	-0.6
TOPEX (cycles 2-10)	-41.4	-38.7	5.0	0.0
TOPEX (cycles 21-22)	-39.6	-38.1	0.5	0.7
TOPEX (cycles 2-10,21-22)	-41.0	-	-	-
POSEIDON (cycle 20)	-17.7	-17.3	3.9	3.7

A = determined from a solution for the 30x30 SST
B = determined from a solution for the time tag bias by the direct method

* relative to an Earth semi-major axis of 6378136.3 metres and 1/f = 298.257.

The numerical orbits were computed using the SATAN software and the JGM-2 gravity field. The crossover residuals indicate a radial accuracy in the region of ~25 cm rms for ERS-1 and ~12 cm rms for TOPEX/POSEIDON. The pure altimeter residuals yield ~33 cm rms for ERS-1 and ~22 cm rms for TOPEX/POSEIDON, although these measurements will include the geoid error. These figures therefore suggest that the TOPEX/POSEIDON orbits are significantly better than for ERS-1.

CHAPTER 5

SEA SURFACE VARIABILITY OVER THE NORTH SEA

§ 5.1 Introduction

The method of using satellite altimetry from repeat (or collinear) ground tracks to provide information about the mesoscale sea surface variability over the deep oceans [Cheney et al., 1983] is a well established technique. Geoid, orbit error, ocean tide and inverse barometer effects are removed to leave the mesoscale signal (up to a wavelength of several 100 km). High variability of the mesoscale signal may therefore be attributed to strong currents and eddies. For a shelf region, such as the North Sea where any height signal due to the variability of the thermohaline circulation will be considerably less than that of tides and surges, this method can be used to assess how well the dominant phenomena, the ocean tide and storm surge, are modelled [Oskam, 1990]. Therefore the purpose of this chapter is to establish how accurately the POL models for the North Sea regions predict these phenomena. The surge model is used later in chapter 6 (altimeter calibration) together with a variant of the ocean tide model used here.

§ 5.2 Tides

Tides are caused by the gravitational attraction of the Sun and Moon acting on the waters of the rotating Earth, and the centrifugal forces resulting from the motions of these three bodies. They contribute significantly to the observed sea surface height and need to be well predicted and removed in order to observe other phenomena such as the storm surge or thermohaline ocean circulation. The overall tidal effect is composed of several distinct tides, namely, ocean tides and earth body tides and also to a lesser extent the loading tide and a tide-like effect caused by the motion of the Earth's pole.

If the Earth was covered by an ocean of uniform depth, the bottom of which was frictionless then such tides would be simple to predict. Naturally, this is not the case; the ocean depths vary and the land masses hinder the movement of the waters as the Sun and Moon exert their influence. The effect of the Moon on ocean tides is about twice that of the Sun.

Table 5.1: Key lunar and solar partial tides

Symbol	Period (solar hrs)	Relative amplitude ($M_2 = 100$)	Description
M_2	12.42	100.0	Main lunar, semi-diurnal constituent
S_2	12.00	46.6	Main solar, semi-diurnal constituent
N_2	12.66	19.1	Lunar constituent due to monthly variation in moon's distance
K_2	11.97	12.7	Soli- lunar, semi-diurnal constituent due to declination changes
K_1	23.93	58.4	Soli-lunar constituent
O_1	25.82	41.5	Main lunar, diurnal constituent
P_1	24.07	19.3	Main solar, diurnal constituent

At tide gauge stations it is usual to predict ocean tides using harmonic analysis of historical data, parameterising the data in terms of the various components of the ocean tides or 'partial' tides. These constituents are determined by observation and only a small number are needed to predict the ocean tide quite accurately, say, to around 1 cm rms, depending on location. The key partial tides are listed in Table 5.1 [Thurman, 1981] and the entire ocean tide phenomena has a nodal period of 18.6 years. The vertical displacement of the ocean tide may well in excess of 2 metres over the North Sea. Solid earth (body) tides occur due to the elasticity of the Earth's surface and the vertical tidal effect may be up to 20 cm for the North Sea [Baker, 1984]. The solid earth is further deformed under the weight of the moving oceans, which is called the loading tide.

§ 5.3 Storm surges

Storm surge is a term used for the meteorological effects of winds and atmospheric pressure on sea level in shallow water areas. In the deep open ocean, the key component is atmospheric pressure; an increase of 1 millibar in air pressure decreases the sea level by approximately 1 cm. This is known as the 'inverse barometer' effect and serves as a good general rule of thumb for sea level changes on timescales longer than 1 or 2 days. However over the North Sea winds cause the major change in the sea level rather than air pressure and strong coastal winds over shallow waters can prove catastrophic for nearby towns. In practice, these two phenomena are coupled together in shallow water wave equations and are usually predicted as a total elevation along with the tidal component. The tidal part is then calculated separately and subtracted to leave the sea level change due to the storm surge [Flather et al., 1991]. These wind and air pressure variations can raise or lower sea level by up to a metre around the U.K. coast over a period ranging from a few hours to 2 or 3 days.

§ 5.4 Repeat track method

A satellite in a precise repeat orbit will travel over the same ground path, to within ±1 km, after a certain predefined time. For ERS-1 in the ice phase this is 3 days; for TOPEX/POSEIDON it is 9.9 days. Therefore, after a while, a number of repeat altimetric passes will be available. The sea surface heights, h, are computed by subtracting the altimeter range measurement (corrected for solid earth/ocean tides, inverse barometer effect and sea-state bias as well as the dry/wet tropospheric and ionospheric effects) from the orbit height as provided in the altimeter datasets or IGDRs. The sea surface heights thus derived will not be at identical sub-satellite points from pass to pass; however this is overcome by aligning all the passes to some geographic origin (say, a certain latitude) and then interpolating the data points as outlined in section 4.10. In detail, for each pass, the time at which the satellite crosses the origin is interpolated for and then subtracted from the times of all the sea surface measurements for that particular pass. The new times will therefore be relative to the same origin for all the passes. Interpolation at regular 1 second intervals for each pass then results in a dataset where the altimetric points coincide at the same ground positions between all passes.

The sea surface height (derived using the orbit heights from the altimeter records themselves) at time t_i (with respect to the geographic origin) may be expressed as

$$h_i = N_i + w_i^0 + w_i^t + \Delta M_i - \Delta r_i \tag{5.1}$$

where ΔM is error due to the mismodelling of M (the solid earth & ocean tide and storm surge effect). The other terms within equation 5.1 are

N : geoid height

w^0 : stationary sea surface topography (SST)

w^t : time dependent SST

Δr : radial orbit error.

The average sea surface height is then obtained by computing the mean sea height at each 1 second interval between all the passes. The resulting profile will be composed essentially of the geoid and w^0 plus the time-average of all the other effects. This mean profile is then subtracted from each pass wherein the resulting profiles h' are expressed by

$$h'_i = w'^t_i + \Delta M'_i - \Delta r'_i \qquad (5.2)$$

which is principally the residual effects of w^t_i, ΔM_i and Δr_i (denoted with the ' symbol since the time-average components are removed). Finally a best-fit straight line is removed from each pass to eliminate the residual radial orbit error $\Delta r'$ which is the major contribution in equation 5.2. The radial orbit error is known to exhibit a predominately 1/rev behaviour with a wavelength of 40,000 km [Wagner, 1985] and so over a few 100 km across the North Sea its effect is well approximated by a straight line. Subtraction of a best-fit line will also remove the lower frequency components of w'^t_i and $\Delta M'_i$. The resulting profile h'' for each pass is then expressed by

$$h''_i = w''^t_i + \Delta M''_i \qquad (5.3)$$

and may be considered the 'mesoscale variation' of the sea surface h for each pass. If $\Delta M''_i$ is assumed small compared to w''^t_i then the standard deviation of h'' computed at each sub-satellite point over all the passes gives an overall indication of the variability. The phenomena which h'' reflects have wavelengths up to the length of the repeat passes chosen and a timescale equivalent to the period spanned by the passes. However for the North Sea it is w''^{t}_{i} which is small compared to $\Delta M''_{i}$ and so the profiles h" will provide information concerning the mismodelling of M.

§ 5.5 Data and models

For ERS-1 the fast delivery data for the month of January 1992 as edited by NOAA are employed as this was the only reliable altimetric dataset available at the time of study. NOAA provided their own wet and dry tropospheric and ionospheric corrections. They also allowed for a centre-of-mass correction of 85.2 cm whilst retaining the ESA correction for the electromagnetic bias of 1.8% of the significant wave height. Corrections for the geoid, ocean tide, solid earth tide are also provided. It is emphasised that the ERS-1 results presented here are calculated from preliminary altimetry.

For TOPEX/POSEIDON the data during September to December 1992 on the IGDR CD roms are employed. The altimetry is corrected for atmospheric delay effects and sea-state bias as discussed in section 4.2. The orbit height and solid earth tide are taken from the IGDRs.

The ocean tide model for the U.K. was supplied by POL. It utilises some 15 constituents and has a resolution of about 12 km x 12 km (see Figure 5.1) . The accuracy for the shelf as a whole is estimated at 10 cm rms, although larger errors could apply in certain areas.

Storm surge elevations for the U.K. seas are computed by models run routinely at the Meteorological Office with the assistance of POL. The data is generated with 12 hour hindcast and 36 hour forecast and sent to POL for archiving. Software is available to access this information which is of the same spatial resolution as the POL ocean tide model and has a temporal resolution of 1 hour.

Details on ocean tide and surge modelling at POL may be found in 'Computer Modelling in the Environmental Sciences' [Flather et al., 1991].

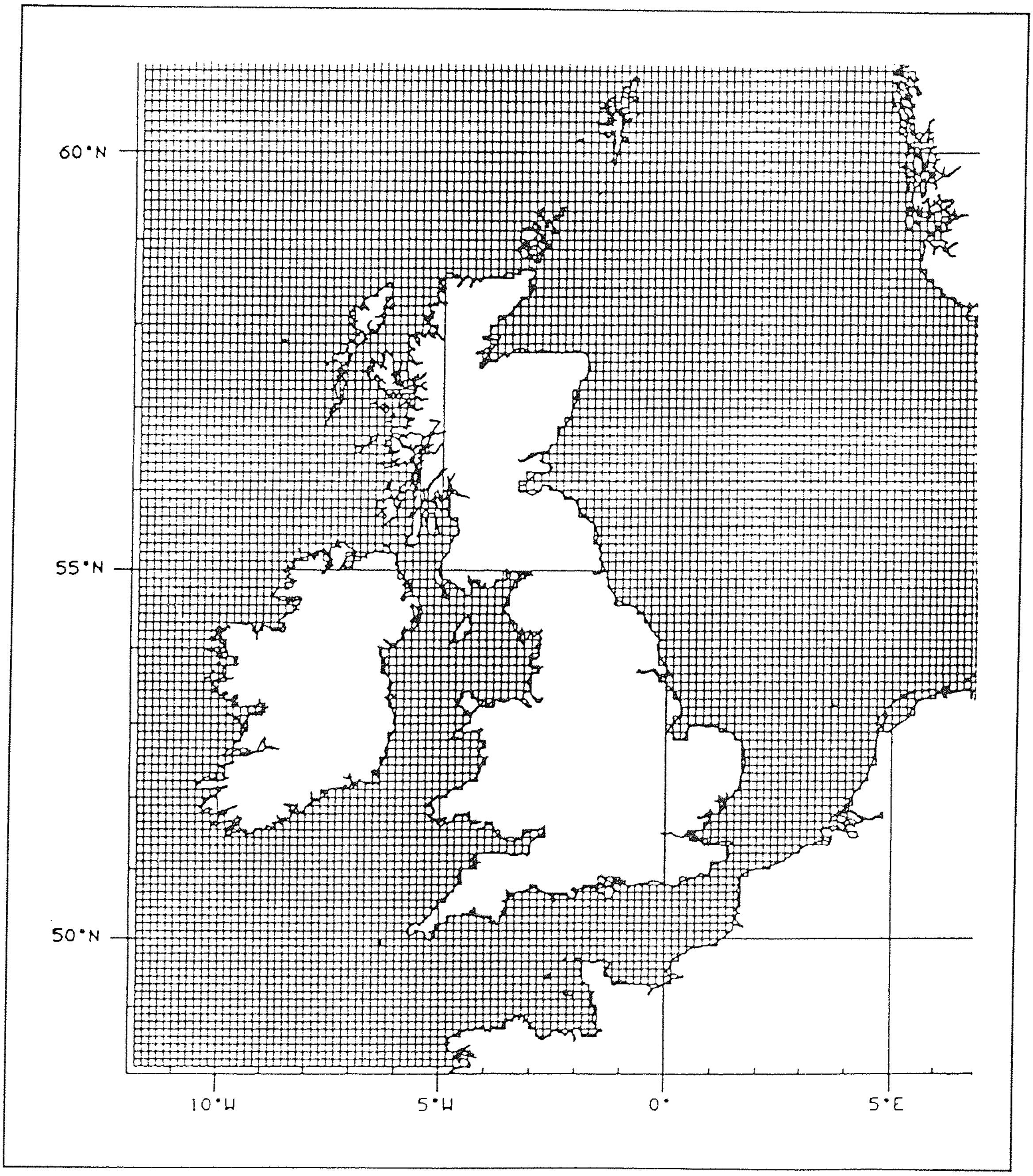

Figure 5.1

§5.6 Results

Three arcs for each satellite ERS-1 and TOPEX/POSEIDON are chosen over the North Sea and are illustrated in Figures 5.2(a) and 5.2(b) respectively. Details of these arcs are presented in Table 5.2.

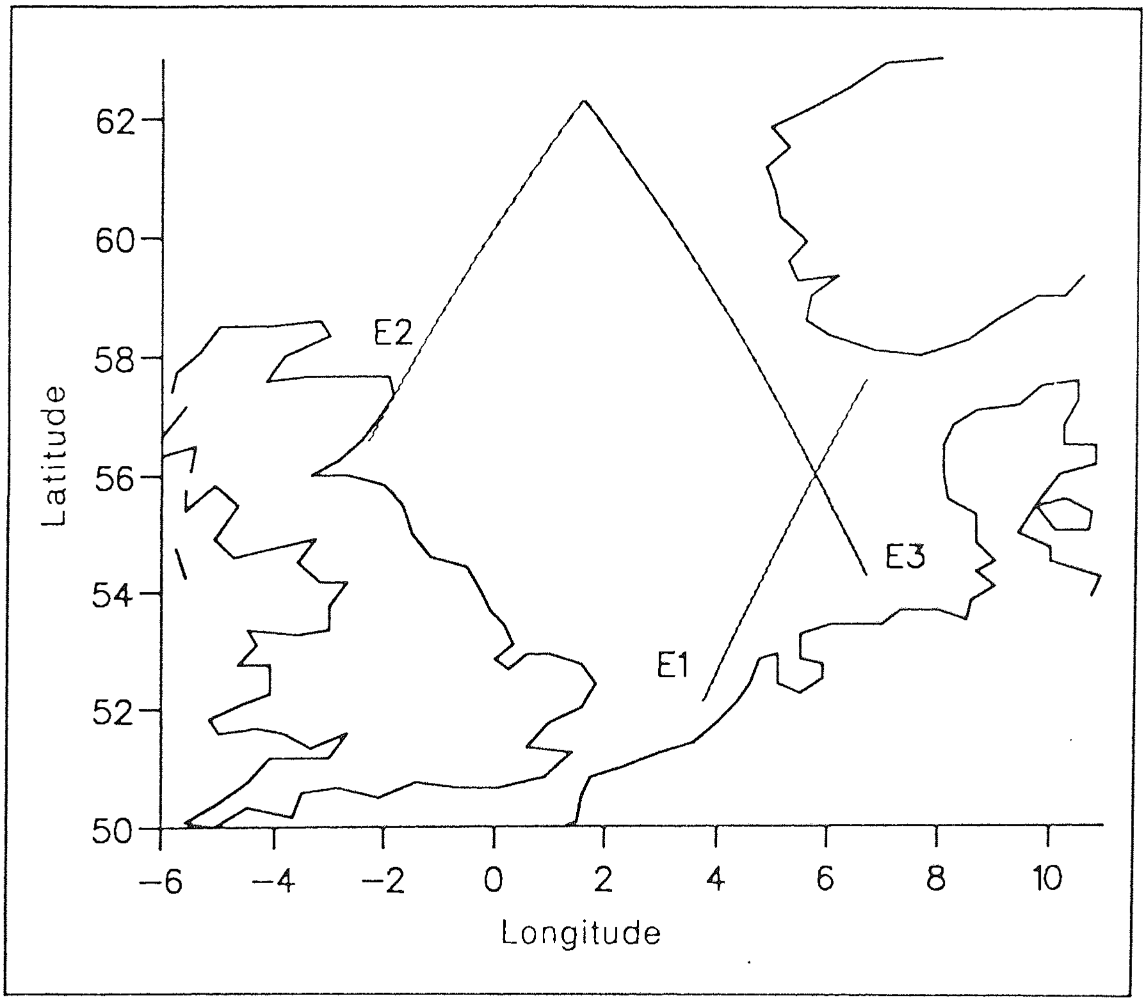

Figure 5.2(a)

Since the TOPEX and POSEIDON altimeters fly the same ground track, it does not matter, for this exercise, which one is switched on over the repeat passes since both instruments are of comparable precision.

The results for ERS-1 are depicted in Figures 5.3 - 5.5 and for TOPEX/POSEIDON in Figures 5.6 - 5.8. The top graph in each figure compares the profile of the average sea surface height against the geoid profile from the Oxford geoid model (see section 6.5.3). It can be seen that the altimeter profile matches the detail of the geoid model very well, the constant offset is due chiefly to the omission of the zero order term which is about a metre in the North Sea [Featherstone, 1992]. Additional differences arise from omission of the mean SST and the inclusion of time averaged constants from other effects.

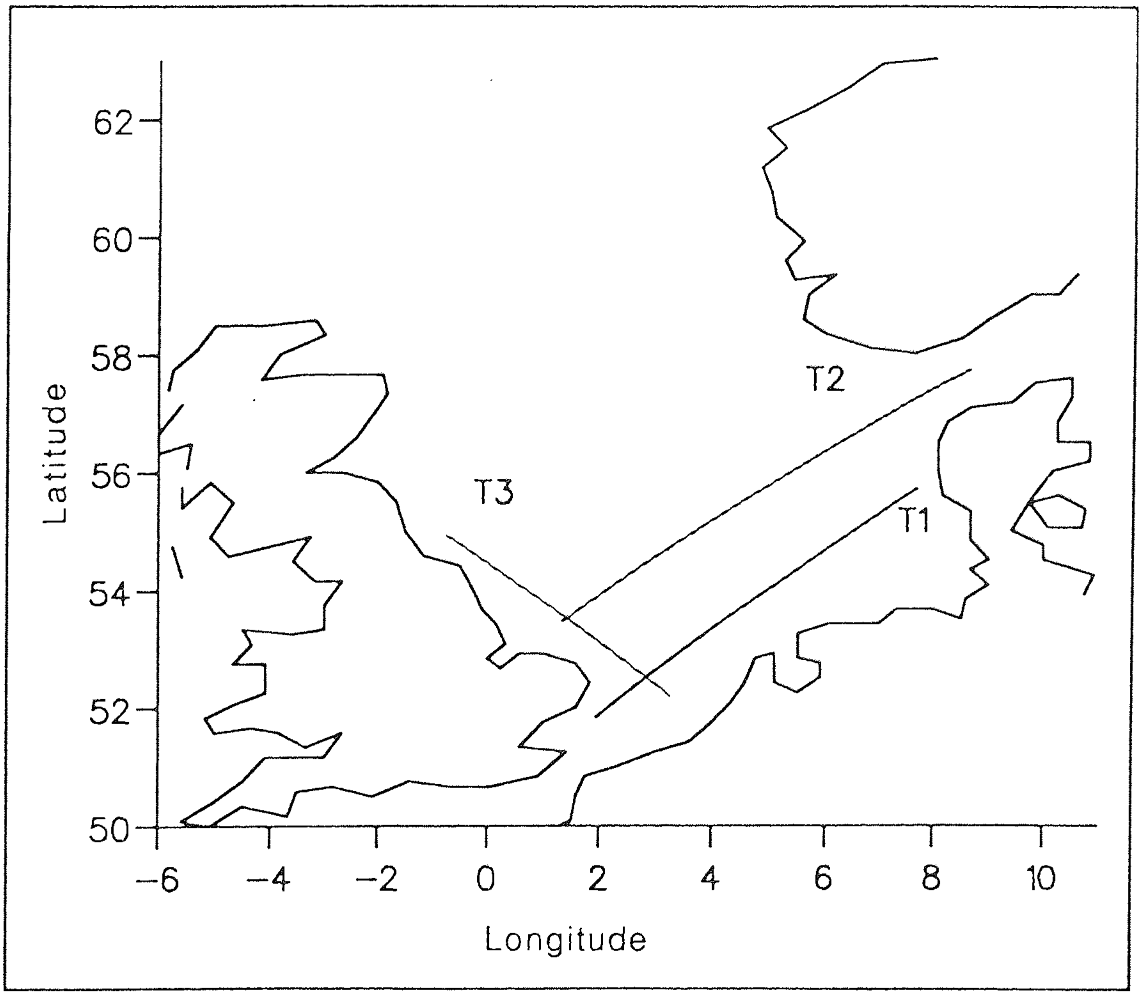

Figure 5.2(b)

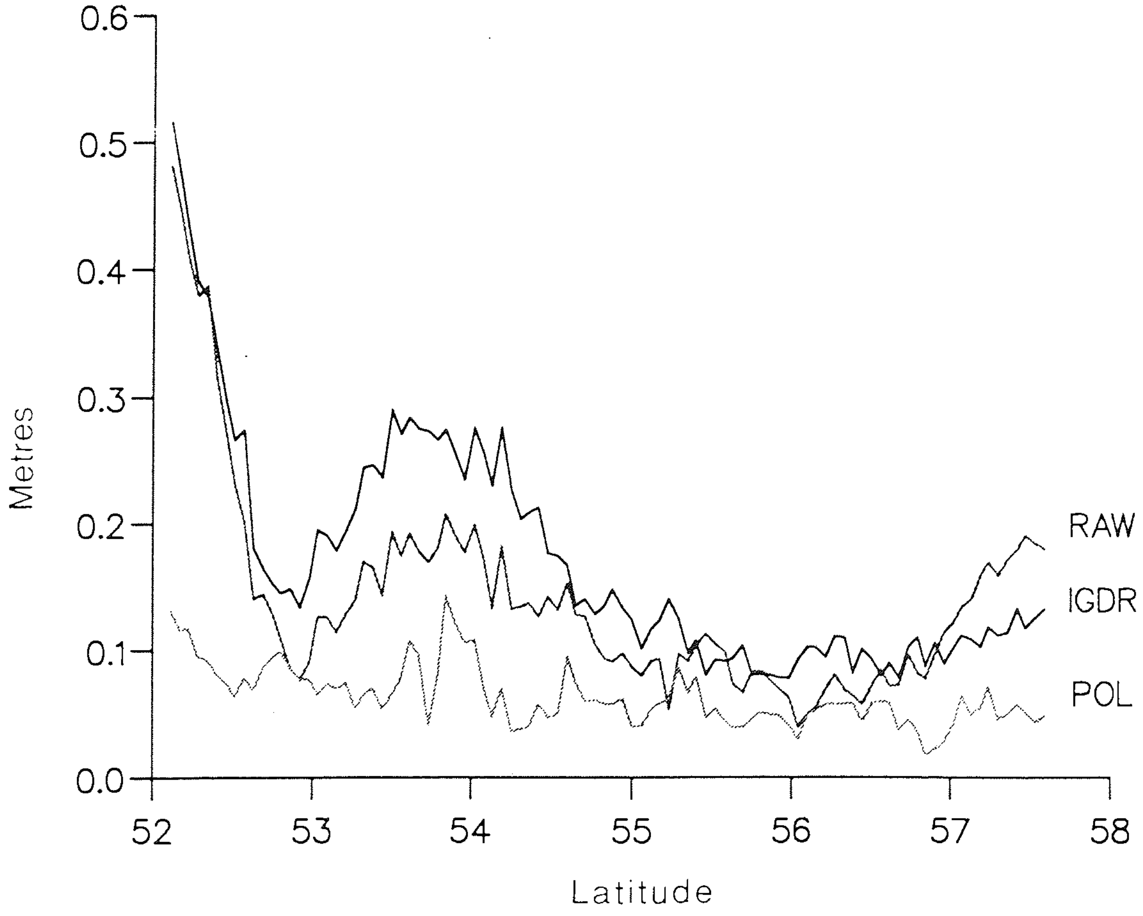

ERS-1 Arc E1
Figure 5.3

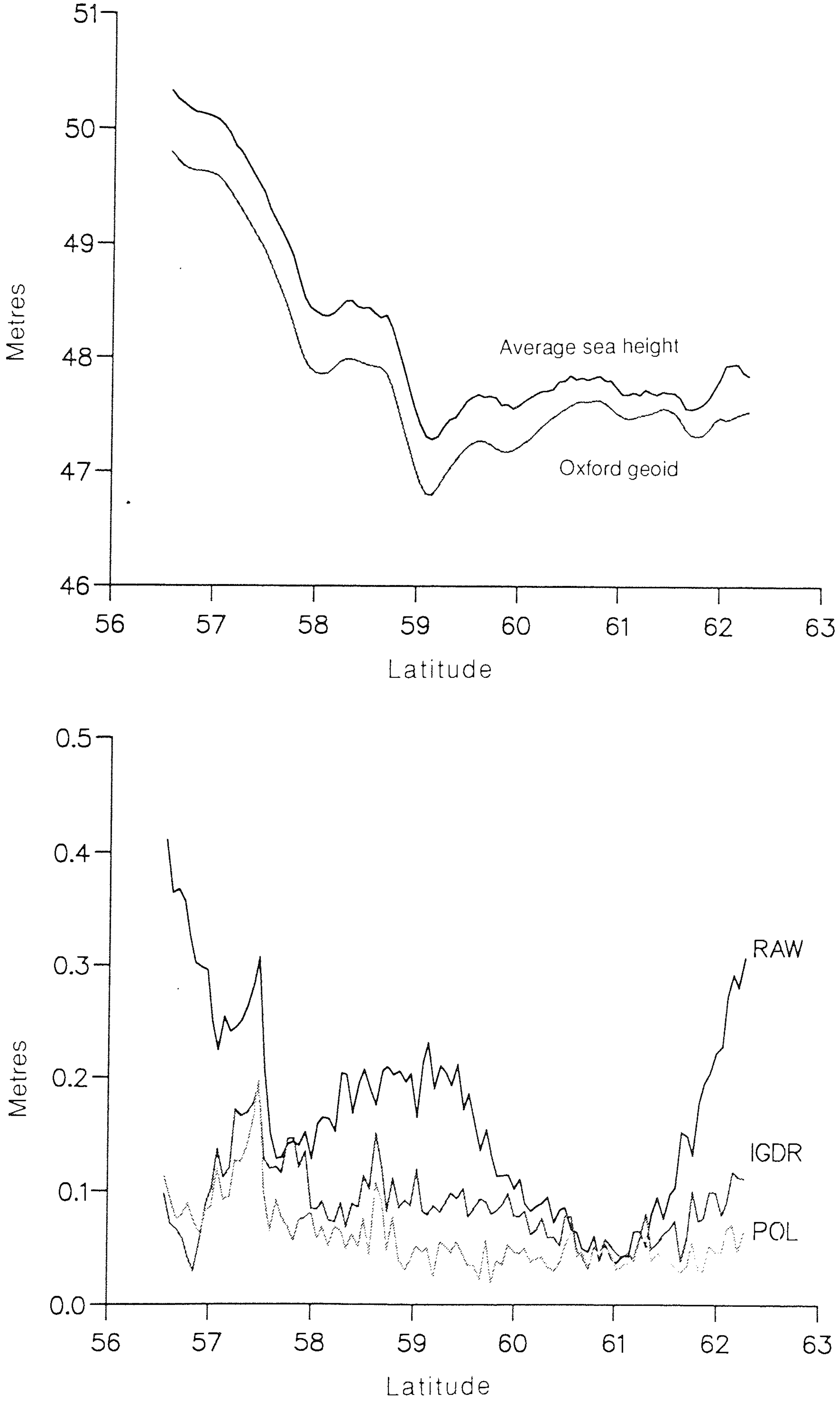

ERS-1 Arc E2
Figure 5.4

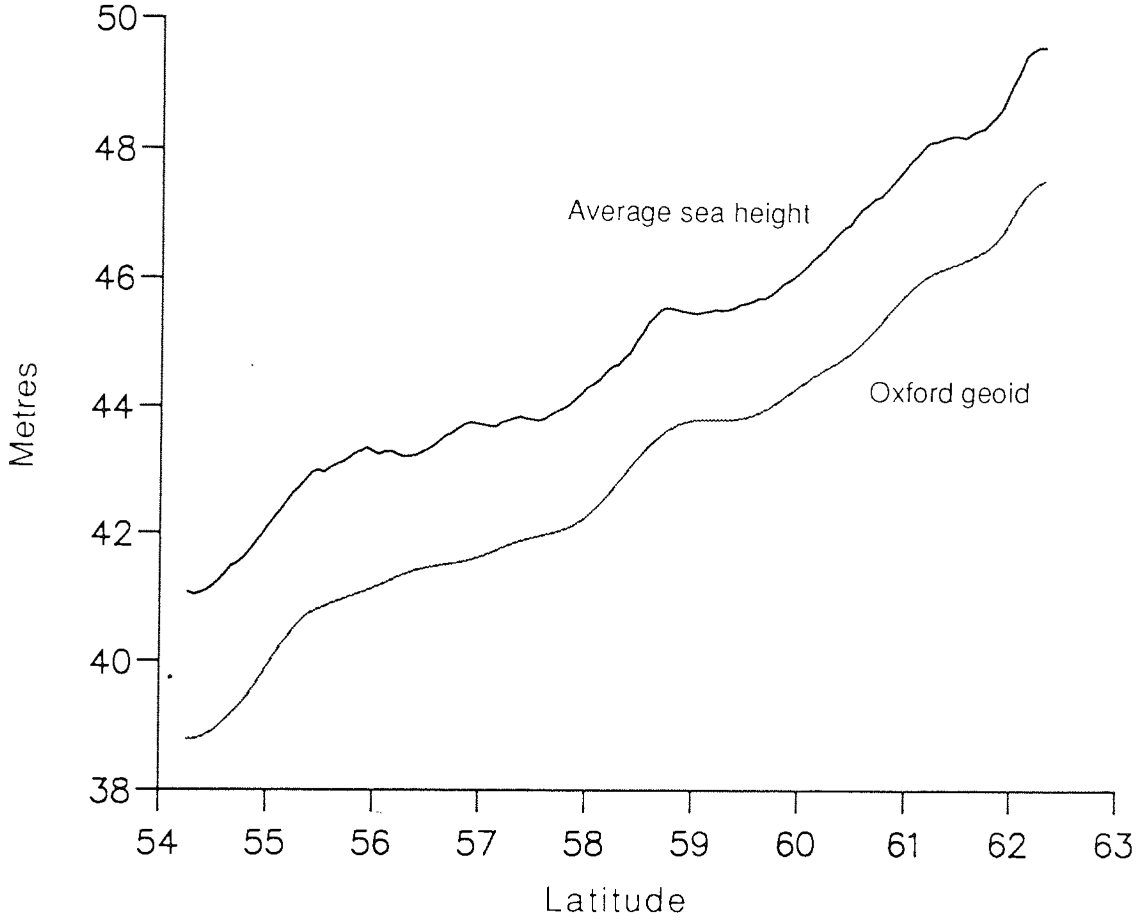

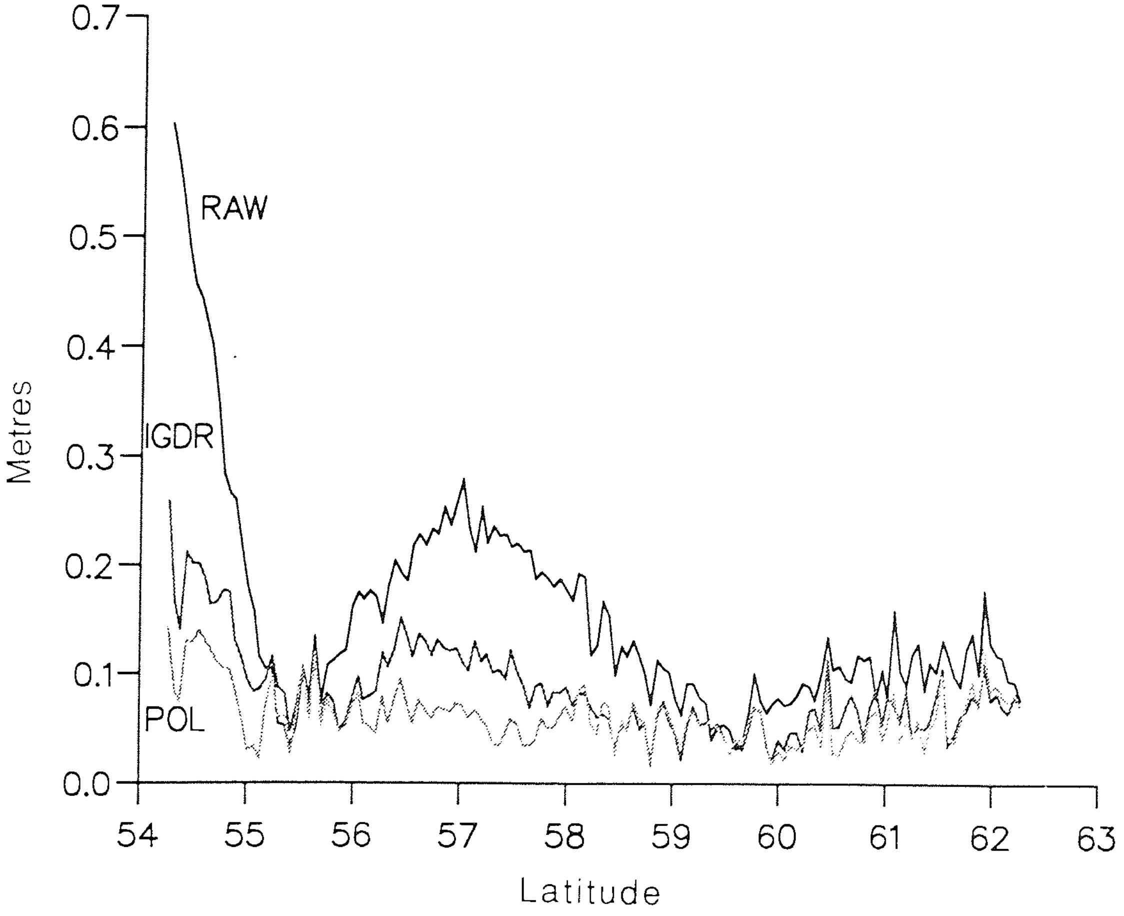

ERS-1 Arc E3
Figure 5.5

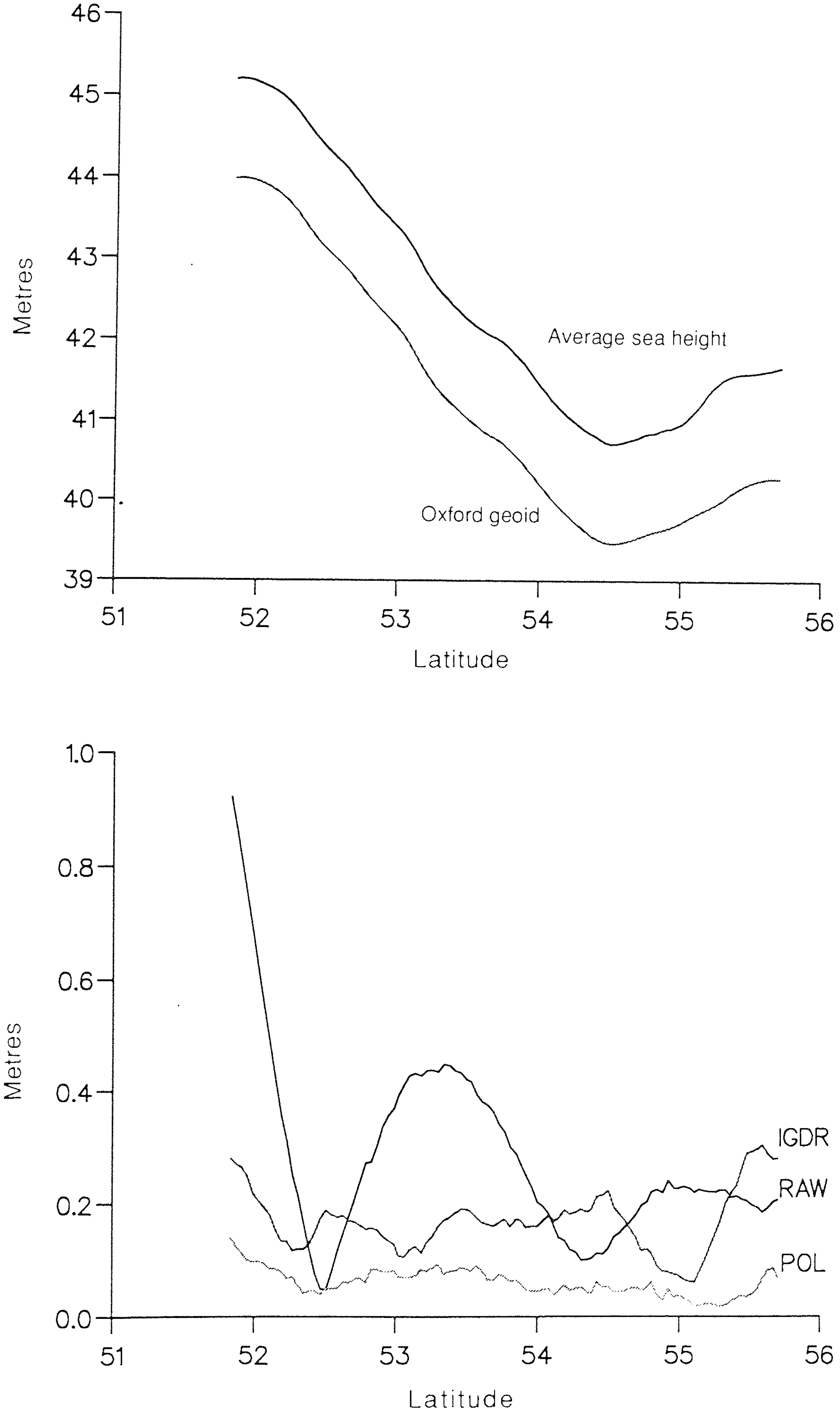

TOPEX/POSEIDON Arc T1
Figure 5.6

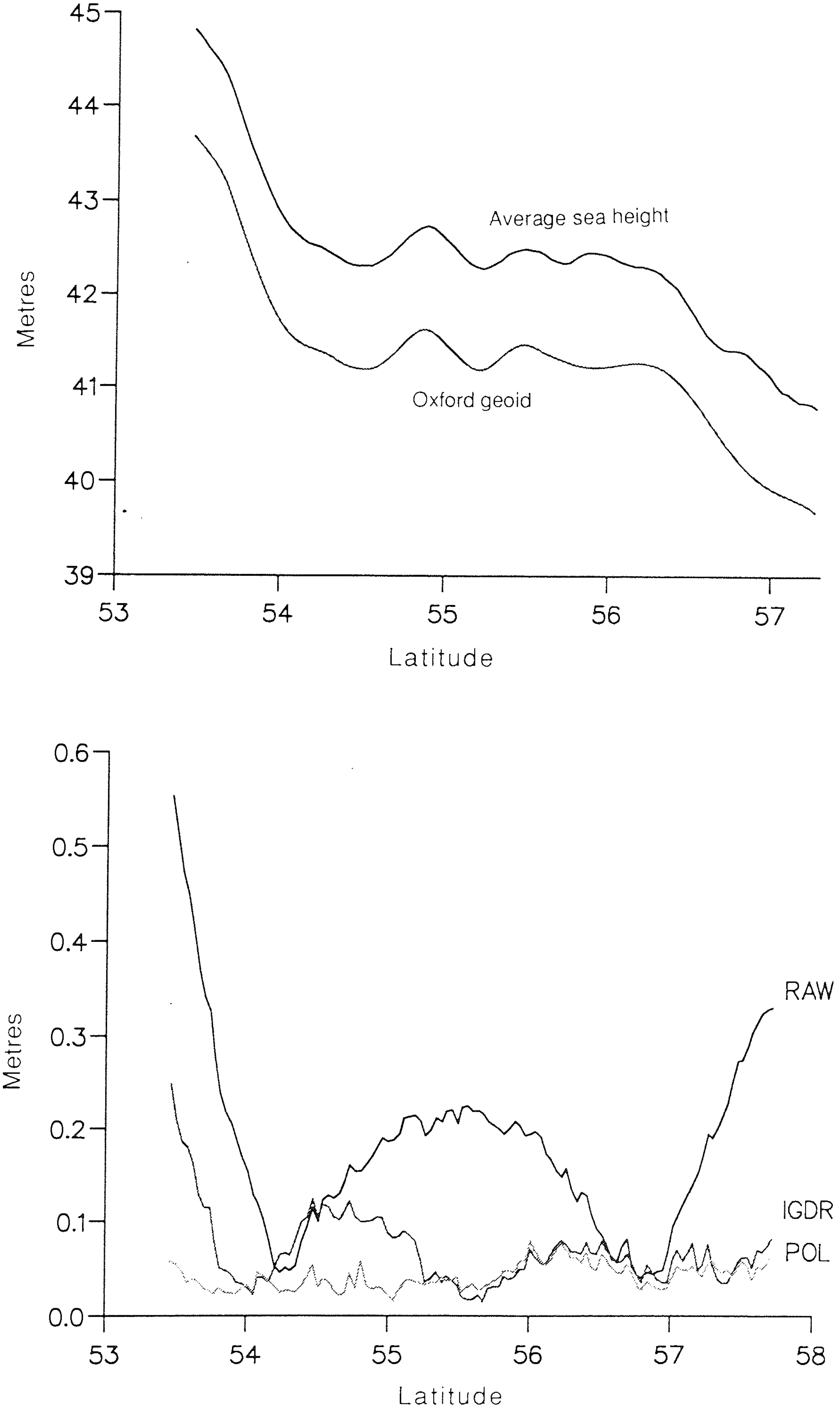

TOPEX/POSEIDON Arc T2
Figure 5.7

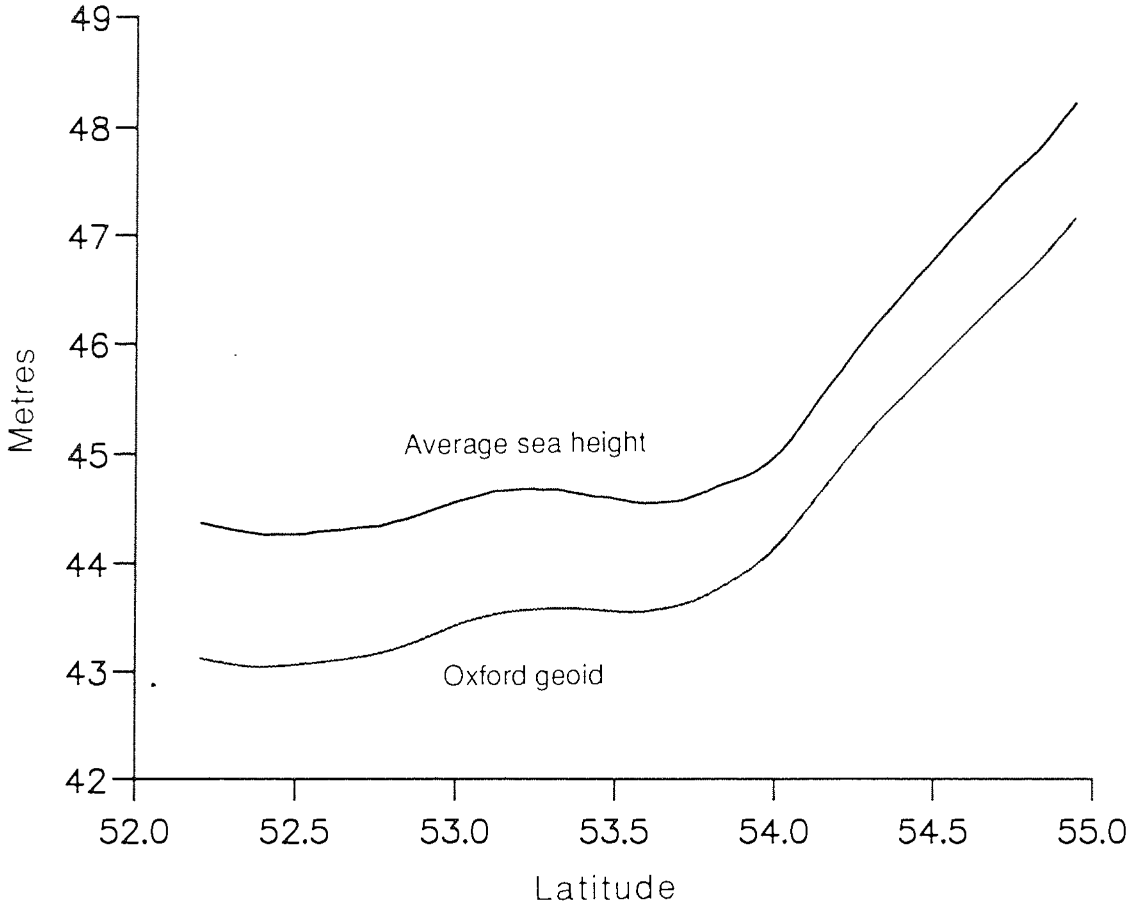

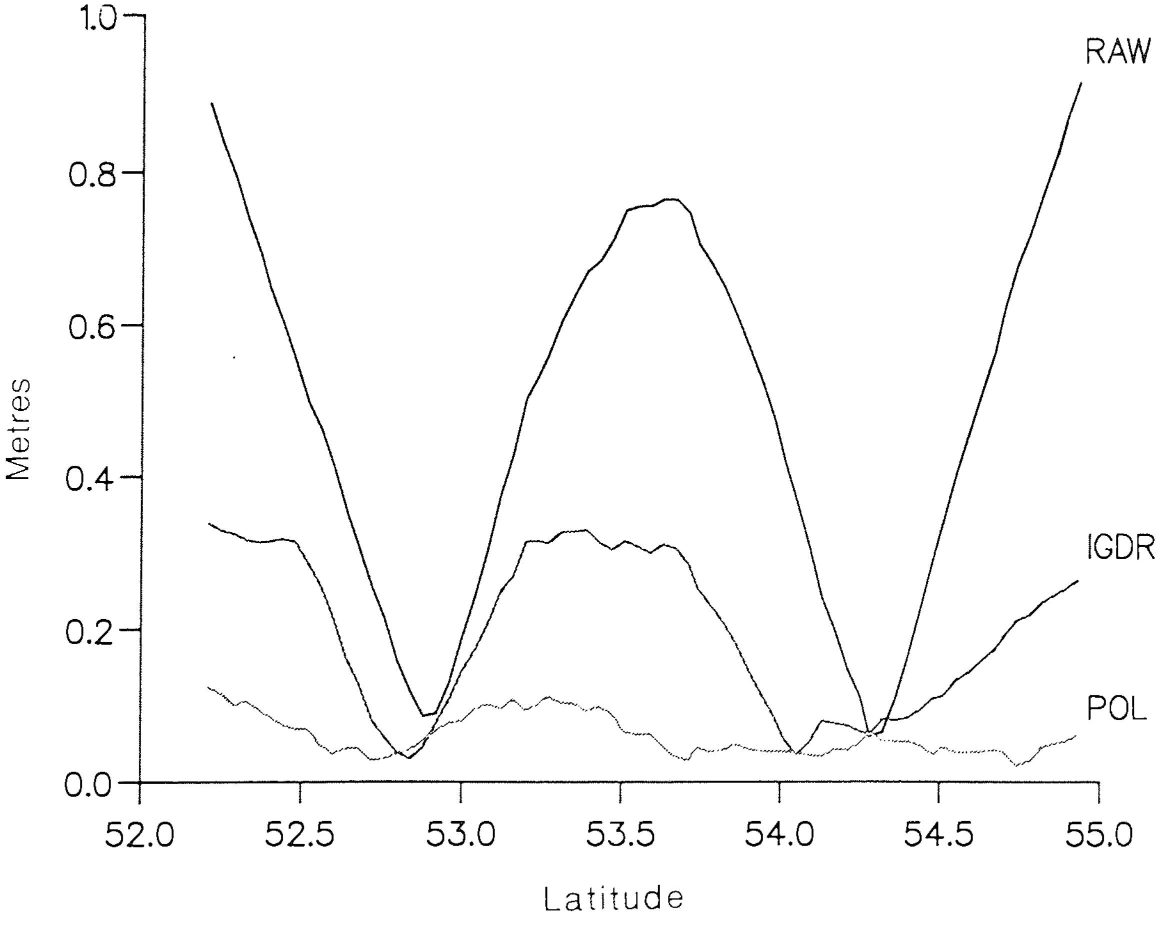

TOPEX/POSEIDON Arc T3
Figure 5.8

Table 5.2: Details of repeat passes over the North Sea.

Pass	Ascending/ Descending	Number of repeat arcs	Period	Altimeter
E1	D	6	Jan 1992	ERS-1
E2	D	9	Jan 1992	ERS-1
E3	A	7	Jan 1992	ERS-1
T1	A	7	Sept-Dec 1992	T/P
T2	A	7	Sept-Dec 1992	T/P
T3	D	7	Sept-Dec 1992	T/P

The bottom graph in each figure compares the standard deviation of h'' (as defined in equation 5.3) over all the repeat passes. These are labelled

i) RAW (no ocean tide or storm surge correction)

ii) IGDR (the IGDR global ocean tide value and POL storm surge corrections used)

iii) POL (the POL ocean tide and storm surge corrections used).

Within the ERS-1 NOAA dataset, the global Schwiderski ocean tide [Schwiderski, 1980] is provided while for TOPEX/POSEIDON IGDR dataset the enhanced Schwiderski tide is supplied. All three are corrected for the earth body tide. The variability shown in these lower graphs may be attributed mainly to the mismodelling of the ocean tide since it is this phenomena that exhibits the largest amplitude; however the variability will of course contain errors from any number of sources.

All the figures show the POL model values to be superior to those of the IGDR which is hardly surprising as the POL model was developed specifically for the U.K. shelf region. It can be seen that the claim of 10 cm rms accuracy is justified in view of the dramatic improvement in Figures 5.6 and 5.7. The ERS-1 results appear far noisier than the TOPEX/POSEIDON ones which may well be a indication of the superior precision of the TOPEX/POSEIDON altimeter. It should be noted that the average sea surface heights in the top graphs for ERS-1 are also noisier than for TOPEX/POSEIDON. This may be due to jitter in the on-board tracker for ERS-1. Table 5.3 gives the average standard deviations for the raw, IGDR and POL results for all 6 passes.

Table 5.3: Comparison of the s.d. between the raw, IGDR and POL ocean tide modelling: all the values are in cm and are a simple average of the rms along each profile from Figures 5.3 - 5.9.

Pass	Data points	Raw	IGDR	POL[1]	POL[2]
E1	141	18.8	9.4	6.2	7.2
E2	101	17.2	9.4	6.0	5.9
E3	96	19.5	17.1	7.4	5.9
T1	101	28.2	16.8	6.0	6.4
T2	71	48.4	19.7	6.1	5.9
T3	116	17.9	6.9	4.2	5.4

1 - both POL ocean tide and storm surge applied.

2 - only POL ocean tide applied (no storm surge).

As a further comparison, the POL ocean tide was corrected for whilst omitting the storm surge. The mean of the resulting variability is listed in the second POL column in Table 5.3. Figure 5.9 and 5.10 show the difference in the overall variability between including and omitting the surge effect.

Table 5.4 shows the constant component of the radial orbit error determined by a best-fit straight line. These values are derived when using the POL models to correct for the ocean tide and storm surge effect. Although this is not the pure radial orbit error as such, it does however give a good indication of how much better the TOPEX/POSEIDON orbits are over those of ERS-1.

Table 5.4: Comparison of the 'apparent' radial orbit error constant; all values are in metres.

	--- Repeat pass number ---								
Pass	1	2	3	4	5	6	7	8	9
E1	-2.08	1.51	0.12	-0.33	0.07	0.71			
E2	-0.90	-1.90	0.55	1.28	0.61	-1.33	-0.28	2.81	-0.86
E3	-2.24	0.12	-0.43	-0.76	-0.90	-0.99	1.72		
T1	0.14	0.05	-0.03	-0.11	-0.03	-0.13	0.12		
T2	-0.11	-0.16	0.11	0.05	0.10	-0.19	0.20		
T3	-0.24	-0.11	0.07	-0.17	0.07	0.29	0.09		

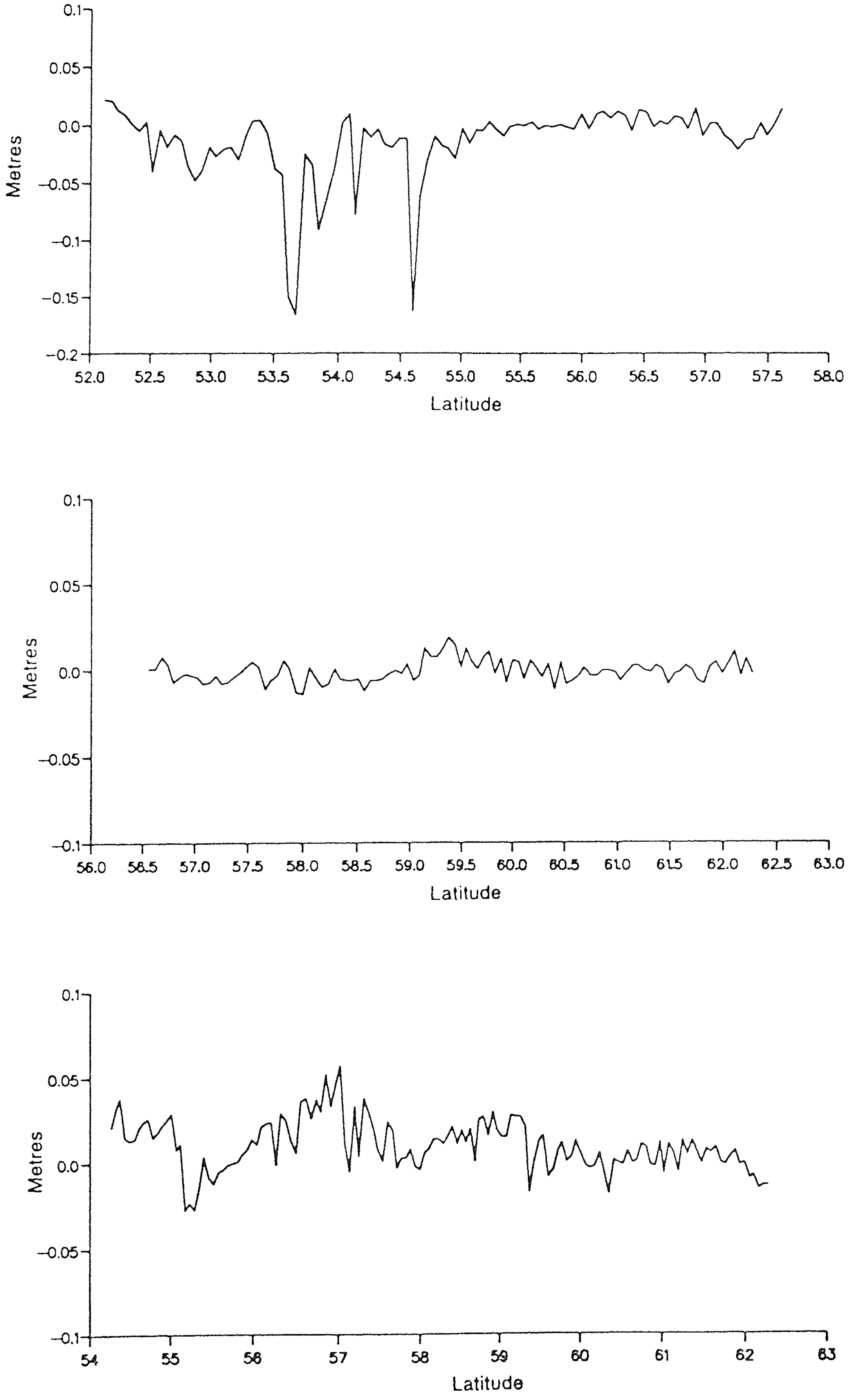

ERS-1 arcs E1, E2 & E3
Figure 5.9

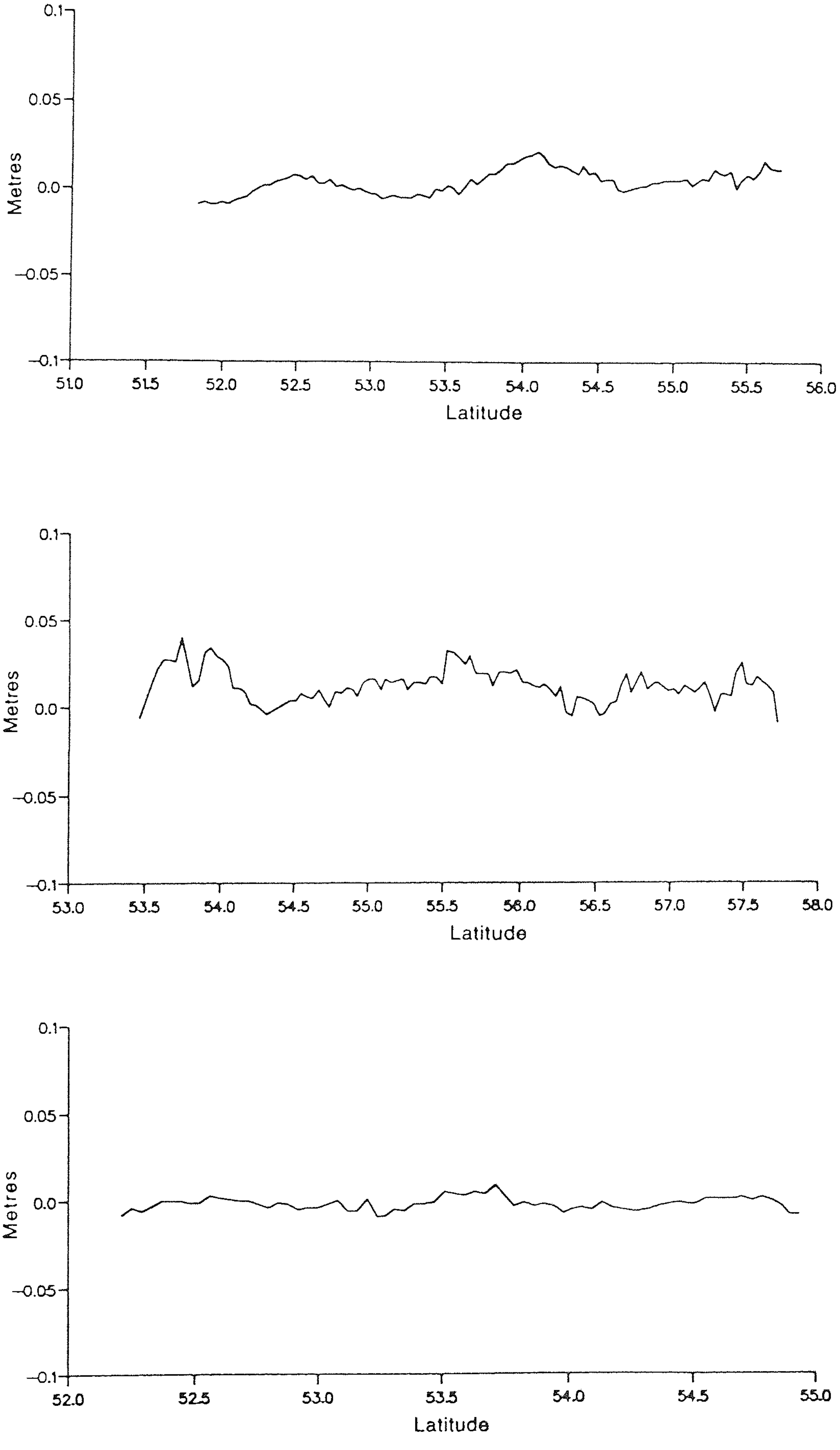

TOPEX/POSEIDON arcs T1, T2 & T3
Figure 5.10

§ 5.7 Conclusions

The method of deducing the sea surface variability from repeat altimeter tracks has been carried out for ERS-1 and TOPEX/POSEIDON over the North Sea. The low mesoscale variability of this sea allows a comparative test between the global Schwiderski and the POL ocean tide model for the U.K. seas. Findings show that the POL model is more accurate than the global model as expected; moreover the precision of the POL ocean tide and storm surge models are shown to be about 6 to 7 cm rms on average along the altimeter tracks.

CHAPTER 6

ON-SITE CALIBRATION OF THE ERS-1, TOPEX AND POSEIDON ALTIMETERS

§ 6.1 Introduction

An 'on-site' method for estimating the range biases associated with the ERS-1, TOPEX and POSEIDON altimeters is presented in this chapter. The technique is of the same principle as those carried out at the Venice Tower for ERS-1 [ESA, 1993] and Platform Harvest and Lampedusa for TOPEX/POSEIDON [JPL, 1992 a, b] and involves computing the satellite altitude and sea surface height for a number of suitable altimetric measurements. A stretch of water is usually chosen where the satellite overflies with good laser tracking and where tide gauges are easily set up or available. For this study the English Channel serves as the calibration site where the Newhaven tide gauge already operates and where the Herstmonceux laser ranger is nearby in Sussex, on the south coast of England. Appropriate arcs are chosen such that the satellite flies close to Herstmonceux and the Newhaven tide gauge.

§ 6.2 Methodology

The ERS-1 and TOPEX/POSEIDON ground tracks over the English Channel used for this exercise are depicted in Figure 6.1, along with the location of the Newhaven tide gauge (N) and the Herstmonceux laser ranger (Hx) . Newhaven is about 18 km southwest of Herstmonceux.

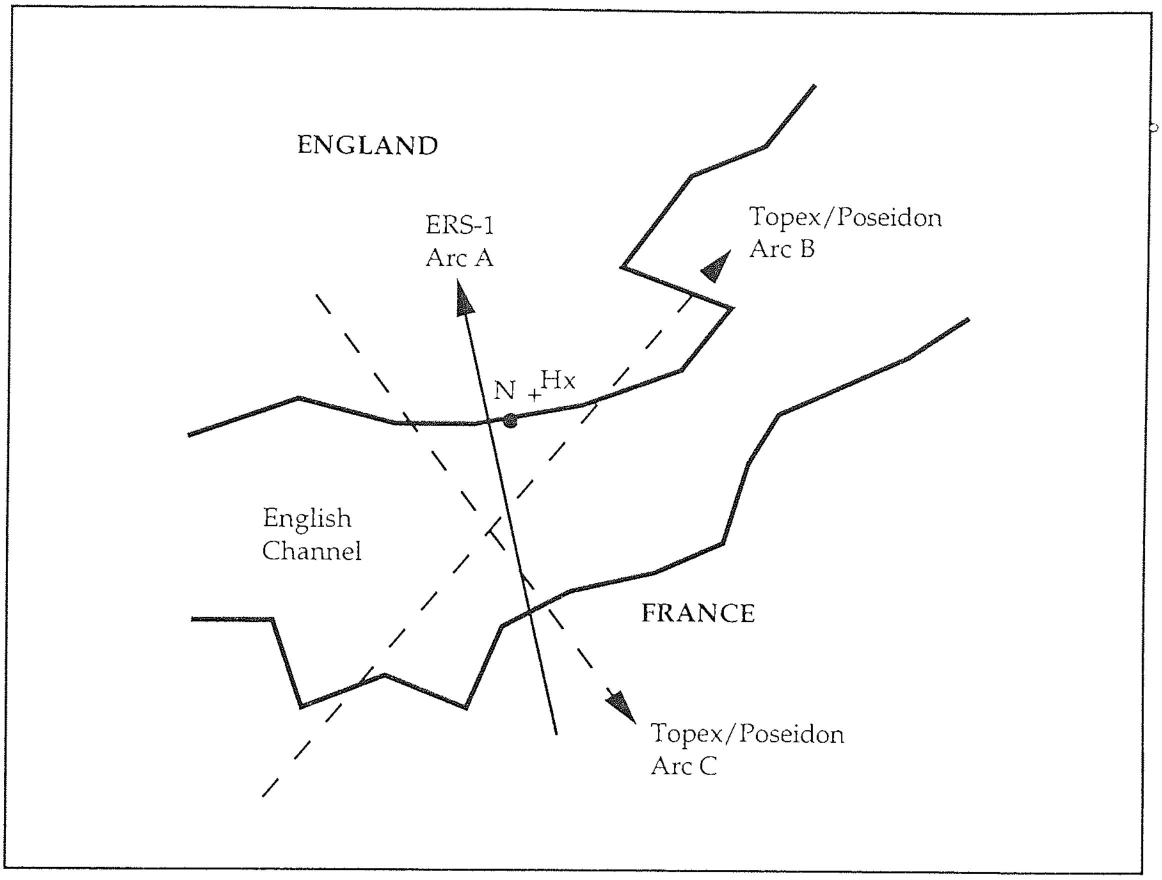

Figure 6.1

For ERS-1, Arc A is an ascending ground track during the 3 day repeat 'ice' phase (January 1992 to April 1992). The ground track of this phase was displaced some 2° to the west due to manoeuvres after the end of the previous 'commissioning' phase (see chapter 2). Fortunately this allowed ERS-1 to fly virtually overhead of Herstmonceux. For TOPEX/POSEIDON, Arc B is ascending pass 137 and Arc C is descending pass 222.

Each arc will yield a set of bias values, b_i, given by

$$b_i = h_i^{alt} + h_i^{sea} - h_i^{sat} \qquad (6.1)$$

where h_i^{alt} is the corrected observed altimeter range measurement, h_i^{sea} the computed instantaneous sea height, h_i^{sat} the computed satellite height and subscripts i refer to the ith measurement during the arc. A number of repeat passes are computed to check for consistency and it is then a simple procedure to compute the overall bias value as a mean of the derived b_i values since, given enough arcs, any time-dependent mismodelling can be assumed to average out to zero.

The same reference ellipsoid is used for the measurements h_i^{sea} and h_i^{sat} and hence the on-site biases are absolute estimates, unlike values determined from long arc studies in chapter 4.

§ 6.3 Altimeter data

For ERS-1, the ESA OPR 02 data [CNES, 1992] are used and for TOPEX/POSEIDON, the final GDR products as supplied on CD roms are employed [JPL, 1992 c].

Each of the above products provide the raw altimeter reading and corrections for the dry/wet tropospheric delay, ionospheric delay and sea-state bias (see section 4.2) and the the orbital height of the satellite. No preliminary range or time tag bias values have been applied.

§ 6.4 Precise satellite altitude

The near overflight of the satellites in the vicinity of the Herstmonceux laser ranger permits the precise spacecraft altitude to be computed from a reference orbit corrected using a simple short arc technique. The long arc orbits were computed at Aston University using all available laser observations for the required periods. The ERS-1 orbits were computed using 3 day orbits whereas 10 day arcs were used for

TOPEX/POSEIDON (this was most convenient from the work performed for chapter 4). The JGM-2 gravity field [Lerch et al., 1993] to degree and order 70 was used for both the ERS-1 and TOPEX/POSEIDON. Such arcs serve as reference trajectories and are used to determine the range residuals ΔR (the observed laser-tracked range minus the modelled range) for the overhead Herstmonceux laser data. From these ΔR residuals, a radial height correction can be calculated for the satellite.

§ 6.4.1 Short arc correction procedure

From simple geometric considerations (derived fully in chapter 7), ΔR may be expressed as

$$\Delta R = \frac{1}{R}(r - r_e \cos \phi \cos \Delta\lambda) \Delta r + \frac{r_e}{R}(\cos \phi \sin \Delta\lambda) \Delta c + \frac{r_e}{R} \sin \phi \, \Delta n \qquad (6.2)$$

where R is the range measurement, r and r_e the geocentric distance to the satellite and laser station respectively, ϕ the latitude of the station relative to the satellite ground track, $\Delta\lambda$ the longitude of the satellite along the ground track relative to the meridian of closest approach and Δr, Δc and Δn the components of ΔR in the radial, along-track and cross-track directions respectively. The geometry for ϕ, $\Delta\lambda$ is demonstrated in Figure 6.2.

At the point of closest approach, $\Delta\lambda = 0$ and equation 6.2 reduces to

$$\Delta R = \frac{1}{R}(r - r_e \cos \phi) \Delta r + \frac{r_e}{R} \sin \phi \, \Delta n . \qquad (6.3)$$

In general it is not possible to solve for both Δr and Δn from the range residuals from a single laser station as Δr and Δn are highly correlated. However, for near overhead passes, $\phi \approx 0$ and the cross-track component can be absorbed within Δr with little error. On substituting $\phi \approx 0$ into equation 6.3

$$\Delta R \approx \Delta r + \varepsilon_{\Delta R} \tag{6.4}$$

for near overhead passes where $\varepsilon_{\Delta R}$ is the error due to the neglect of Δn.

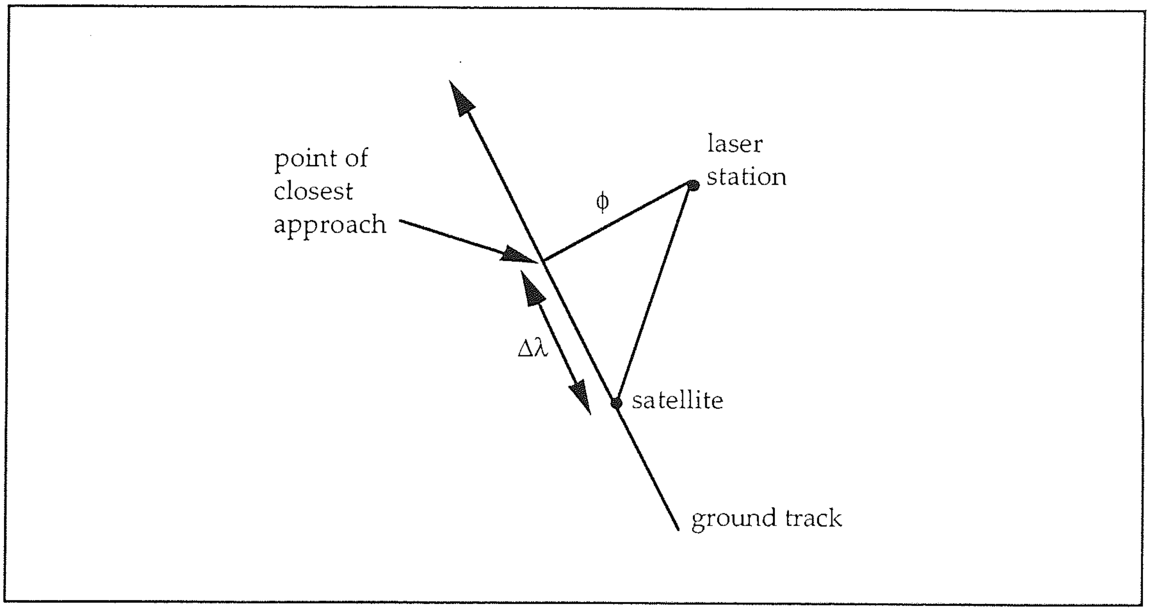

Figure 6.2

An estimate of $\varepsilon_{\Delta R}$ is possible for Herstmonceux data by using

$$\varepsilon_{\Delta R} \approx \frac{r_e}{R} \sin \phi \, \Delta n \tag{6.5}$$

with $r_e = 6378.137$ km. For ERS-1, $R = 785$ km, angle ϕ translates into ~25 km and across-track error $\Delta n = 50$ cm (for example) yields a radial error of 1.6 cm. Similarly for TOPEX/POSEIDON, putting $R = 1350$ km, angle ϕ equivalent to 50 km along the ground and across-track error $\Delta n = 30$ cm gives a radial error of 1.1 cm.

§ 6.4.2 Numerical computation for the satellite altitude

The long arc orbits are usually numerically integrated with a nominal step length of 30 seconds. However it is not sensible to interpolate for the satellite height using such discrete points over the English Channel. Hence, after the long arc orbits were converged with a step length of 30 seconds, the step length was reduced to 3 seconds (altimeter points are available approximately every 1 second) and the numerical integration process repeated once more to record the satellite position at each of these steps. These positions are then converted to geodetic heights (see Appendix B) and interpolated to yield the spacecraft height ,$h_i^{\text{long-arc}}$, at each altimeter observation over the English Channel.

At each of these 3-second points, the angle α subtended at the geocentre by the satellite and the laser station is computed and a quadratic curve fitted through α against time. The time at which α is at a minimum is the time of closest approach. Table 6.1 gives details of each pass. The altitude correction Δr can be determined for each arc by fitting either a quadratic or cubic curve through the normal point range residuals ΔR (depending on which fits better) and reading off the value at the time of closest approach. The corrected satellite altitude, h_i^{sat} is then simply the value $h_i^{\text{long-arc}} + \Delta r$.

This method is sensitive to errors in the Herstmonceux laser station coordinates, in particular, the geodetic height. For this study coordinates for both the long and short arc work were taken from LAGEOS based solutions obtained by the RGO in 1991. Table 6.2 shows the radial orbit error, Δr, determined for the ERS-1 arcs.

Table 6.1: Details of ERS-1 and TOPEX/POSEIDON short arcs; the MJD, GMT time and ground distance to Hestmonceux laser ranger at the satellite's point of closest approach are shown.

ERS-1

Date	Modified Julian date	Time of day (GMT)	Distance to Hx laser (km)
26/1/1992	48647.908 068	21:47:37	24.8
29/1/1992	48650.908 050	21:47:35	25.6
16/2/1992	48668.908 086	21:47:37	25.3
19/2/1992	48671.908 081	21:47:37	23.8
8/3/1992	48689.908 086	21:47:37	24.1

TOPEX/POSEIDON

Date	Modified Julian date	Time of day (GMT)	Distance to Hx laser (km)
28/9/1992	48893.492 750 (cycle 1, pass 137)	11:49:34	19.2
18/10/1992	48913.323 986 (cycle 3, pass 137)	7:47:00	20.2
21/10/1992	48916.617 236 (cycle 3, pass 222)	14:48:49	57.3
28/10/1992	48923.239 632 (cycle 4, pass 137)	5:45:04	19.7
31/10/1992	48926.532 888 (cycle 4, pass 222)	12:47:22	56.9
26/11/1992	48952.987 420 (cycle 7, pass 137)	23:41:53	20.1

Since the TOPEX/POSEIDON long arc orbits are known to be very accurate (to about 10 cm rms radially), the Aston orbit heights (with a short arc correction Δr applied) can be compared with the NASA and CNES values (also computed using JGM-2 gravity field) on the GDR CD roms at a single point over the English Channel (interpolated to geodetic latitude = 50.3^{o}) for each arc - see Table 6.3. The table also shows the short arc radial correction made to the Aston height.

Table 6.2: ERS-1 radial corrections and fit of long arc orbit; all measurements are in cm.

Date	Arc	Δr	Best fit curve σ	Long arc r.m.s	Laser points
26/1/1992	A	+0.7	1.5	19.6	129
29/1/1992	A	-14.5	1.6	27.5	184
16/2/1992	A	-39.3	1.3	23.3	278
19/2/1992	A	-35.3	1.3	24.3	291
8/3/1992	A	+0.8	0.3	6.1	136

The Aston heights for TOPEX/POSEIDON agree to within 5 cm with the NASA and CNES values and therefore confirms the precision of the altitudes derived for this exercise. Any such differences are probably due to the fact that no short arc adjustments were made to the NASA and CNES altitudes. It is also interesting to observe that the largest Δr value for TOPEX/POSEIDON is only 11 cm compared to the largest value of 39 cm for ERS-1. The geodetic satellite altitude, h_i^{sat}, are computed relative to an Earth semi-major axis of 6378137 metres and $1/f = 298.257$, which is the same used for determining the sea surface height, h_i^{sea}.

Table 6.3: Comparison of Aston, NASA and CNES orbital heights for TOPEX/POSEIDON over the English Channel; the values for each arc were interpolated for at geodetic latitude = 50.3°. The rms of fit for the Aston long arc orbits are shown in brackets.

Date	Arc	Δr (cm) (RMS)**	Aston (m)* (RMS)	NASA (m)*	CNES (m)*
28/9/92	B	-11.0 (1.7)	+21.304 (13.2)	+21.324	+21.343
18/10/92	B	+10.0 (2.6)	+12.347 (9.7)	+12.327	+12.349
21/10/92	C	+4.0 (1.6)	+71.846 (9.7)	+71.874	+71.885
28/10/92	B	-4.0 (1.5)	+30.251 (9.5)	+30.291	+30.306
31/10/92	C	+4.2 (1.6)	+103.611 (9.5)	+103.571	+103.592
26/11/92	B	+2.5 (1.5)	+103.377 (10.4)	+103.321	+103.348

* relative to an absolute height of 1349600 metres above a reference ellipsoid of semi-major axis of 6378136.3 metres and 1/f = 298.257.

** rms is of best fitting curve through range residuals.

§ 6.5 Instantaneous sea height

The sea surface height at the tide gauge, at some time t, is height of the tide gauge datum plus the tide gauge reading at time t, relative to some reference ellipsoid. The vicinity around the tide gauge moves vertically with solid earth tide and this needs to be included as well. In notation, this sea height, h_i^{TG}, is written

$$h_i^{TG} = h_{datum}^{TG} + h_{reading}^{TG} + h_{set}^{TG} \tag{6.6}$$

in which the solid earth tide h_{set}^{TG} (including the constant tidal component) is computed using software provided by POL. The position of the tide gauge datum, h_{datum}^{TG}, and the tide gauge reading , $h_{reading}^{TG}$, are discussed in section 6.5.1 and 6.5.2 respectively.

The sea heights between two nearby points (as for the tide gauge and some altimeter point) will only differ significantly with the geoid, ocean tide and storm surge effects. If these differences are known, the sea height, h_i^{sea}, at the altimeter point may be deduced relative to the sea height at the tide gauge, h_i^{TG}, namely

$$h_i^{sea} = h_i^{TG} + (h_g^{sea} - h_g^{TG}) + (h_{ot}^{sea} - h_{ot}^{TG}) + (h_{ss}^{sea} - h_{ss}^{TG}) \tag{6.7}$$

wherein

$h_g^{TG}, h_{ot}^{TG}, h_{ss}^{TG}$	:	geoid, ocean tide and storm surge heights at the tide gauge
$h_g^{sea}, h_{ot}^{sea}, h_{ss}^{sea}$	:	geoid, ocean tide and storm surge heights at the altimeter point.

Other effects such as the ocean loading tide and polar tide are omitted since they are at the 1 or 2 cm level. The differences in height between two nearby points at short wavelengths can be considered reliable for the ocean tide, storm surge and geoid models whereas absolute heights are not. The geoid model is detailed in section 6.5.3 whilst the ocean tide and storm surge models are discussed in section 6.5.4.

Naturally the values h^{TG}_{datum} and h^{TG}_{g} do not vary between arcs and h^{TG}_{g} is used here only in a differential sense. Any error in h^{TG}_{datum} will appear as a constant offset in all the bias results.

§ 6.5.1 Geodetic coordinates of the Newhaven tide gauge

The precise x, y, z coordinates of benchmarks located by GPS (Global Positioning System) receiver benchmarks (or stations) near the Newhaven tide gauge site are provided by a survey carried out by the Institute of Engineering Surveying and Space Geodesy, Nottingham University [Ashkenazi et al., 1990]. The coordinates are given in the ITRF 91 reference frame (epoch 1991.70) and are derived from 10 independent fiducial GPS network solutions. Each fiducial GPS network solution was performed with the inclusion of Tromso, Onsala, Wettzell, Madrid and Herstmonceux and their accuracy is around 5 cm (2σ). These coordinates (in the ITRF 91 reference frame) for the Newhaven benchmark and the solar pillar (a benchmark near the laser ranger at Herstmonceux) are listed in Table 6.4. Also listed are the coordinates [A] of the satellite laser ranger (SLR) itself which are derived from the GPS coordinates of the solar pillar plus the offset from the pillar to the optical centre of the SLR, determined from a local survey carried out by the Ordnance Survey in 1991. The SLR x, y, z position [A] may now be compared with those coordinates [B], supplied by the Royal Greenwich Observatory, used by the SATAN software for orbit determination.

Table 6.4: X, Y, Z coordinates for the correction of Newhaven GPS benchmark; also listed are the GPS plus local levelling position of the laser ranger compared to the position assumed by the orbit determination software. The difference is also is given.

Solar Pillar					
X =	4 033 459.140 m	Y =	23 626.319 m	Z =	4 924 303.140 m
Local levelling (Solar pillar to SLR)					
X =	+4.697 m	Y =	+36.059 m	Z =	+1.891 m
SLR (Solar Pillar + Local levelling) [A]					
X =	4 033 463.837 m	Y =	23 662.378 m	Z =	4 924 305.031 m
SLR (SATAN software) [B]					
X =	4 033 463.081 m	Y =	23 668.854 m	Z =	4 924 305.610 m
Difference [B - A]					
dX =	-0.756 m	dY =	+6.476 m	dZ =	+0.579 m
Newhaven (GPS benchmark) [C]					
X =	4 040 912.769 m	Y =	3 868.805 m	Z =	4 918 258.165 m
Newhaven (SATAN software) [C+(B-A)]					
X =	4 040 912.013 m	Y =	3 875.281 m	Z =	4 918 258.744 m

The difference [B-A] in Table 6.4 is interpreted as a translation between the origin of the reference frame used by the orbit determination relative to the origin of the reference frame used for the GPS measurements. If this difference is now added to the GPS coordinates [C], these new coordinates, [C+(B-A)], will then be in the same reference system as employed by the SATAN software. These x, y, z coordinates are converted into geodetic coordinates as shown in Table 6.5.

Table 6.5: Geodetic coordinates of the Newhaven GPS benchmark in the same reference system as the orbit determination process

$\phi =$ 50.781 614 319 $^{\circ}$ $\lambda' =$ 0.054 947 293 $^{\circ}$ h (GPS) = 50.542 m*

* relative to an Earth semi-major axis of 6378137 metres and 1/f = 298.257.

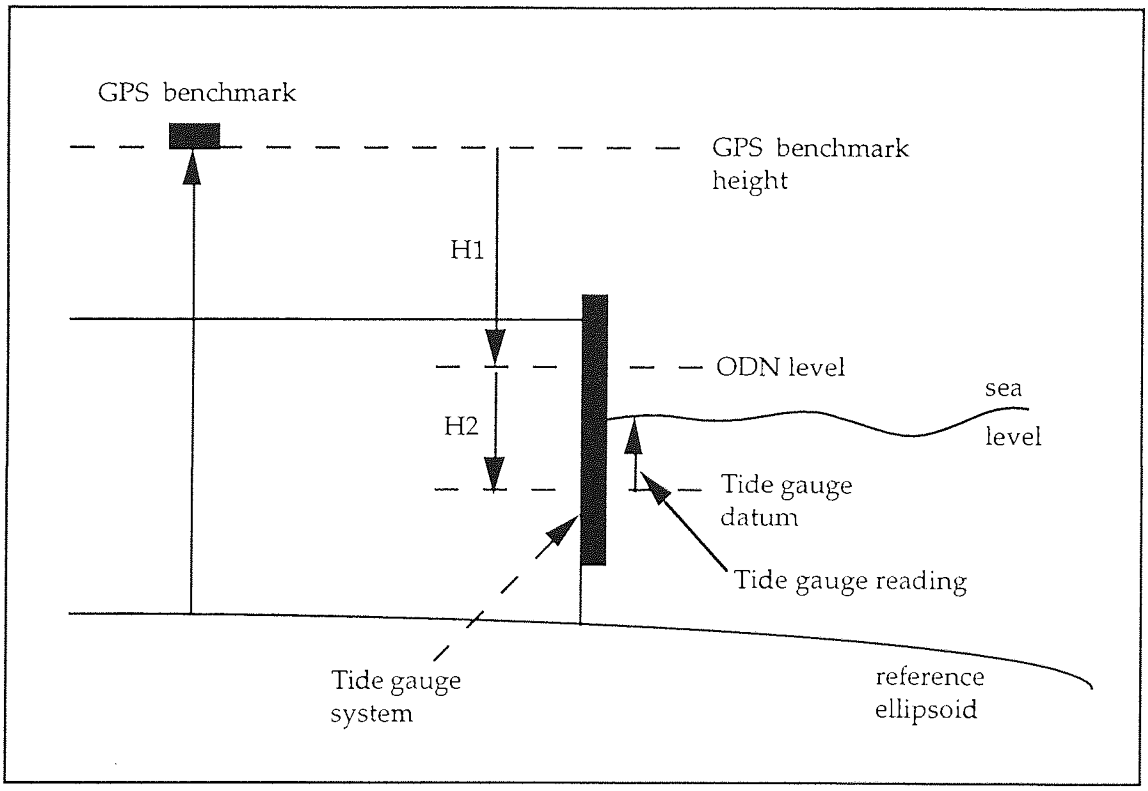

Figure 6.3

Local surveys of the Newhaven site, performed by the Ordnance Survey and POL, provide the height, H1, of the GPS benchmark above ODN (Ordnance Datum Newlyn) which is a fixed point of vertical reference. Furthermore, the height, H2, of tide gauge datum to ODN is known and so it is a simple procedure to derive the geodetic height of the tide gauge datum (see Table 6.6 and Figure 6.3). Hence a value of 41.193 cm is deduced for h^{TG}_{datum}, which is relative to the reference ellipsoid stated in Table 6.6.

Since the GPS benchmark is ~150 metres west of the Newhaven tide gauge, a correction $d\lambda$ of $+0.002145171^{\circ}$ in the longitude λ is allowed for.

Table 6.6: Final coordinates for the Newhaven tide gauge datum

GPS benchmark height	50.542 m
GPS benchmark height above ODN (H1)	5.829 m
Tide Gauge Datum below ODN (H2)	3.520 m
Tide Gauge Datum	50.542 - 5.829 - 3.520 = **41.193 m**

Final Coordinates for Newhaven Tide Gauge Datum

$\phi = \mathbf{50.781\,614\,319^{\circ}}$ $\lambda' = 0.054\,947\,293^{\circ}$ $h^{TG}_{datum} = \mathbf{41.193\ m}^{*}$

$+d\lambda = 0.002\,145\,171^{\circ}$

$\lambda = \mathbf{0.057\,092\,464^{\circ}}$

* relative to an Earth semi-major axis of 6378137 metres and 1/f = 298.257.

A final check on the GPS benchmark and solar pillar heights can be carried out by comparing these to the geoid height (from the Oxford model - see section 6.5.3) plus the height of the GPS benchmark above ODN. The difference should be a constant which describes the mismatch between the ODN level and the geoid elevation at Newlyn. Table 6.7 shows the constants to be well matched to within 6 cm.

Table 6.7: Check of GPS benchmark heights against the geoid plus ODN offset.

Site	GPS height (a)	Geoid height (b)	GPS benchmark above ODN (c)	Difference (a - b - c)
Solar Pillar	70.821 m	44.414 m	26.101 m	+ 0.306 m
Newhaven	50.542 m	44.458 m	5.829 m	+ 0.255 m

§ 6.5.2 Tide gauge at Newhaven

The tide gauge at Newhaven is a pneumatic system known as a bubbler gauge [Pugh, 1987] and operates by measuring the pressure at some fixed point below the sea surface. Compressed air is allowed to escape slowly and steadily at a pressure point below the sea surface, where the gas pressure is equal to the water pressure, see Figure 6.4. Suitable recording equipment collects the pressure data. These pressure readings are then converted to a sea level, D, above the pressure point by the following relationship

$$D = \frac{P - P_A}{g\rho} \tag{6.8}$$

in which P is the pressure at underwater pressure point, P_A is the atmospheric pressure acting on the water surface, ρ is the mean density of the overlying column of water and g is the gravitational constant.

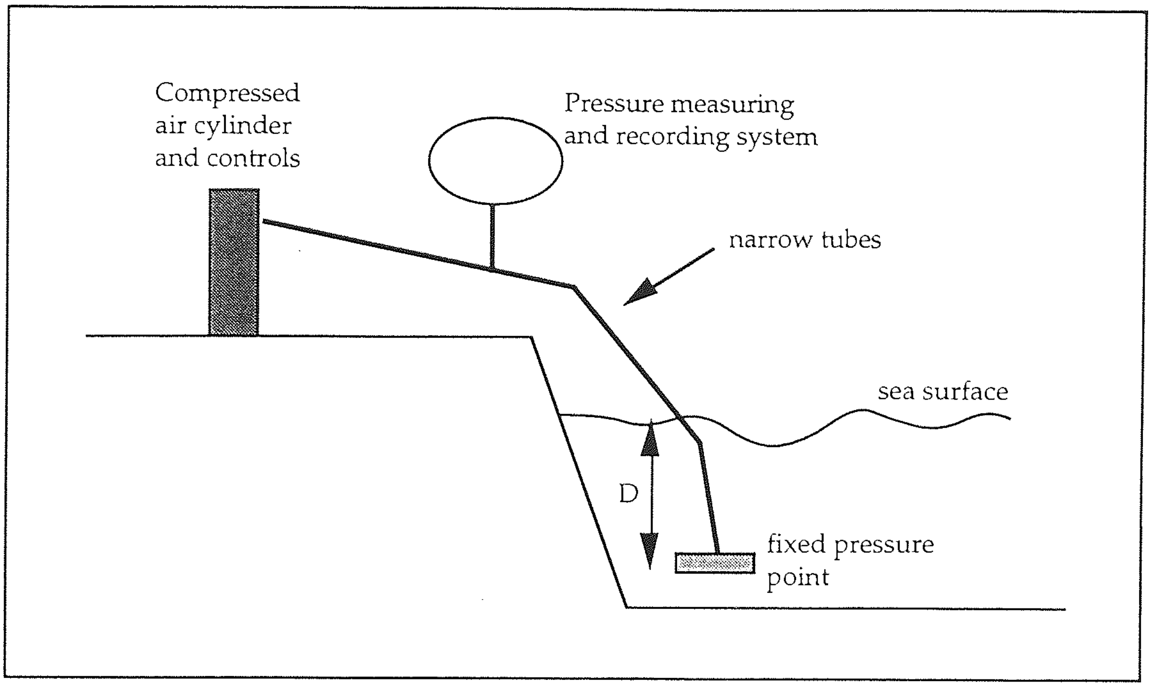

Figure 6.4

At POL, hourly tide gauge readings are produced and recorded. These reading are measured relative to the tide gauge datum. A tide gauge reading, $h^{TG}_{reading}$, at any time t can be found by fitting a cubic polynomial to four hourly data points (two readings before time t and two after) and interpolating at time t.

§ 6.5.3 Geoid model

The geoid is regarded as the equipotential surface of the Earth's gravitational field and centrifugal rotation which closely approximates the mean sea surface to about the one metre level. This definition is usually termed the 'zero' geoid ; if however the direct and indirect gravitational effect of the Sun and Moon on the Earth are included, then the 'mean' geoid results (see section 4.3 in chapter 4).

The geoid model used for determining the geoid differences between the tide gauge and the altimeter points is a precise gravimetric geoid computed at Oxford University [Featherstone, 1992]. The model covers the entire U.K. as well as the North Sea and English Channel. It utilises high resolution gravity data and GPS data to derive a solution relative to the OSU91A gravity field [Rapp and Cruz, 1986] to a computed resolution of 2' latitude by 4' longitude (4 km x 5 km). The Oxford geoid is presented as a list of heights (relative to GRS 80 reference ellipsoid) at regular grid points; the software to interpolate the data was written at Aston University. The accuracy of the geoid is quoted at the 8 cm level for wavelengths less then 215 km.

§ 6.5.4 Ocean tide and storm surge models

The ocean tide model used here is a U.K. model supplied by POL and has 50 tidal constituents. This is an updated version of the model described and used in chapter 5. Marine tides can reach in excess of 3 metres in the English Channel and so it was decided to take advantage of the better model. Preliminary tests showed that this model did make a significant difference over the 15-constituent model, both in an absolute and differential sense. The storm surge model used in this exercise is the same as that employed in chapter 5. A full description of these phenomena and models may be found under sections 5.2, 5.3 and 5.5.

§ 6.6 Results

Altimeter bias results for ERS-1 over 5 arcs were computed for the first 3 months of 1992. A point by point breakdown of each pass is presented in Tables 6.8 to 6.12. Each of these tables show the necessary information at both the tide gauge and altimeter points during that pass. The bias for each altimeter point is computed using

$$\begin{aligned} \text{bias} \;=\; & h^{alt} - h^{sat} \\ & + h^{TG}_{datum} + h^{TG}_{reading} + h^{TG}_{set} \\ & + (h^{sea}_{g} - h^{TG}_{g}) + (h^{sea}_{ot} - h^{TG}_{ot}) + (h^{sea}_{ss} - h^{TG}_{ss}) \end{aligned} \qquad (6.9)$$

which is an explicit form of equations 6.1, 6.6 and 6.7. The bias profiles for each pass in turn are depicted in Figures 6.5 to 6.9. It was decided to exclude altimeter points south of the 50° line of latitude since these points may yield erroneous values on account of being too far from the tide gauge.

Similarly the required information for the 6 TOPEX/POSEIDON passes are tabulated in Tables 6.13 to 6.18, with the bias profiles in Figures 6.10 to 6.15.

Table 6.8: ERS-1 bias results for pass 26/1/92; all figures in metres.

Details at NEWHAVEN TIDE GAUGE (at 21:47:37 GMT)

Tide gauge DATUM height : 41.193
Tide gauge GEOID height : 44.458
Tide gauge reading : 1.183

Solid earth tide : 0.034
Ocean tide : -1.962
Storm surge : -0.300

Details at ALTIMETER POINTS

Lat.	Long.	h^{alt}	h^{sat}	h_g^{sea}	h_{ot}^{sea}	h_{ss}^{sea}	bias
50.03550	0.34688	784931.461	784973.375	44.035	-2.452	-0.330	-0.447
50.09251	0.32183	784943.971	784986.011	44.090	-2.403	-0.328	-0.467
50.14953	0.29673	784956.535	784998.650	44.152	-2.354	-0.326	-0.430
50.20655	0.27158	784969.078	785011.288	44.202	-2.307	-0.324	-0.426
50.26354	0.24638	784981.621	785023.922	44.230	-2.262	-0.321	-0.440
50.32055	0.22112	784994.208	785036.558	44.242	-2.217	-0.319	-0.430
50.37756	0.19582	785006.778	785049.194	44.243	-2.174	-0.316	-0.449
50.43455	0.17047	785019.374	785061.827	44.242	-2.135	-0.313	-0.445
50.49153	0.14507	785031.965	785074.457	44.248	-2.097	-0.310	-0.437
50.54852	0.11961	785044.584	785087.089	44.262	-2.062	-0.307	-0.398
50.60551	0.09410	785057.123	785099.719	44.293	-2.028	-0.304	-0.421
50.66249	0.06854	785069.739	785112.348	44.340	-2.000	-0.302	-0.358
50.71945	0.04293	785082.222	785124.972	44.402	-1.974	-0.302	-0.410

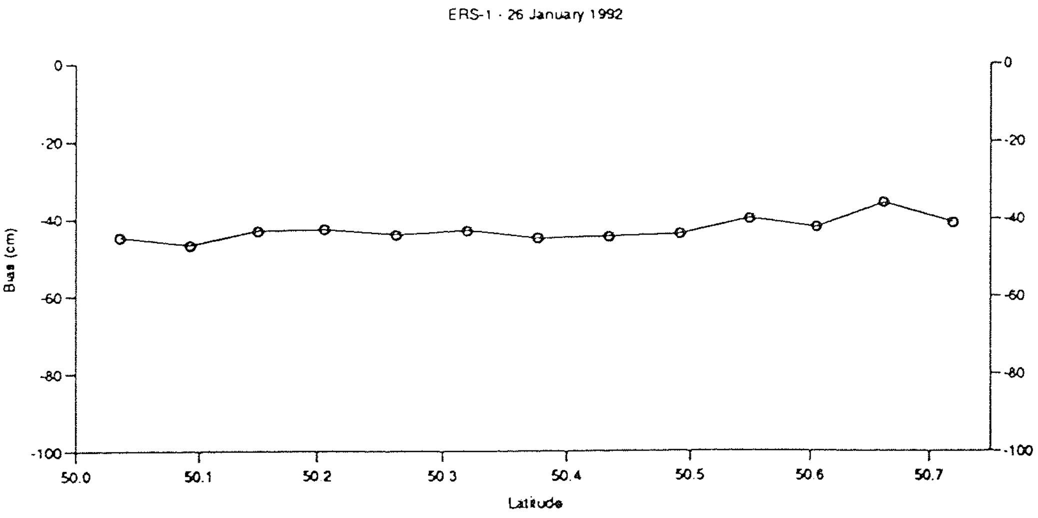

Figure 6.5

Table 6.9: ERS-1 bias results for pass 29/1/92; all figures in metres.

Details at NEWHAVEN TIDE GAUGE (at 21:47:35 GMT)

Tide gauge DATUM height : 41.193
Tide gauge GEOID height : 44.458
Tide gauge reading : 3.819

Solid earth tide : 0.151
Ocean tide : 0.621
Storm surge : -0.221

Details at ALTIMETER POINTS

Lat.	Long.	h^{alt}	h^{sat}	h_{g}^{sea}	h_{ot}^{sea}	h_{ss}^{sea}	bias
50.00671	0.36667	784927.106	784971.907	44.012	0.265	-0.246	-0.466
50.06374	0.34164	784939.697	784984.594	44.059	0.295	-0.246	-0.484
50.12076	0.31656	784952.323	784997.280	44.119	0.322	-0.245	-0.456
50.17778	0.29143	784964.937	785009.966	44.176	0.349	-0.244	-0.443
50.23478	0.26626	784977.537	785022.647	44.214	0.375	-0.242	-0.458
50.29179	0.24103	784990.221	785035.331	44.233	0.401	-0.241	-0.412
50.34879	0.21575	785002.870	785048.013	44.239	0.426	-0.239	-0.412
50.40578	0.19043	785015.550	785060.691	44.238	0.451	-0.237	-0.384
50.46278	0.16505	785028.187	785073.372	44.239	0.476	-0.235	-0.400
50.51977	0.13961	785040.783	785086.051	44.249	0.501	-0.232	-0.445
50.57675	0.11413	785053.441	785098.728	44.271	0.525	-0.229	-0.415
50.63372	0.08860	785066.033	785111.401	44.309	0.548	-0.226	-0.431
50.69070	0.06302	785078.658	785124.076	44.364	0.572	-0.222	-0.399

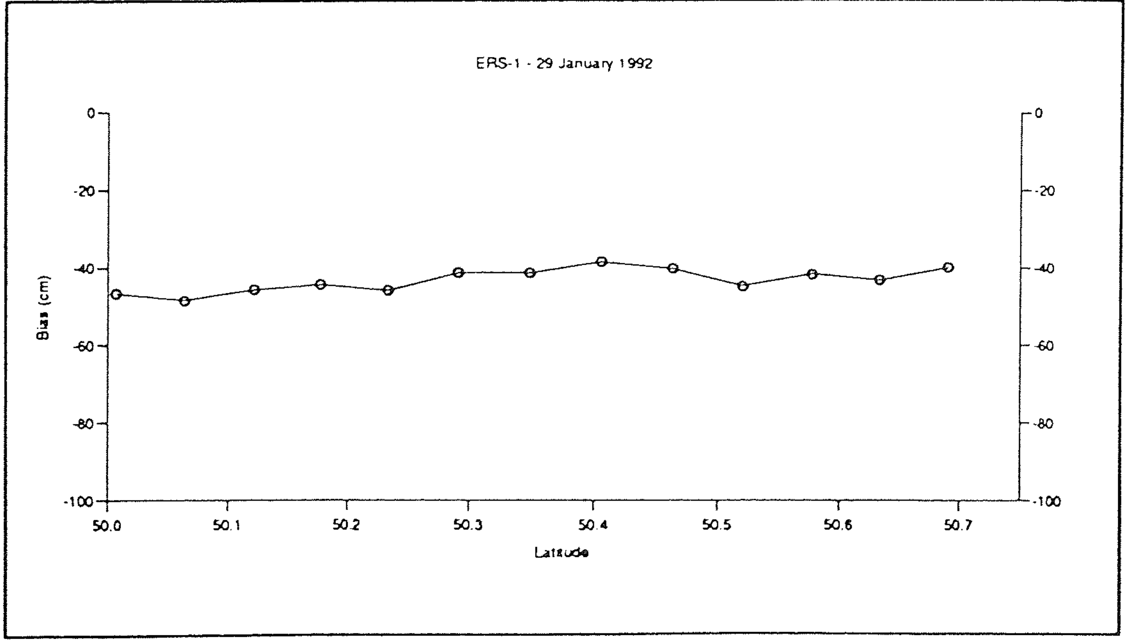

Figure 6.6

Table 6.10: ERS-1 bias results for pass 16/2/92; all figures in metres.

Details at NEWHAVEN TIDE GAUGE (at 21:47:37 GMT)

Tide gauge DATUM height : 41.193
Tide gauge GEOID height : 44.458
Tide gauge reading : 6.451

Solid earth tide : 0.143
Ocean tide : 2.641
Storm surge : 0.099

Details at ALTIMETER POINTS

Lat.	Long.	h^{alt}	h^{sat}	h^{sea}_{g}	h^{sea}_{ot}	h^{sea}_{ss}	bias
50.02828	0.35007	785037.565	785085.478	44.029	2.935	0.046	-0.314
50.08531	0.32503	785049.923	785097.892	44.082	2.907	0.048	-0.343
50.14232	0.29995	785062.235	785110.304	44.143	2.877	0.050	-0.410
50.19933	0.27481	785074.700	785122.717	44.196	2.848	0.052	-0.332
50.25635	0.24962	785087.111	785135.129	44.227	2.819	0.055	-0.328
50.31335	0.22438	785099.517	785147.540	44.241	2.789	0.059	-0.345
50.37034	0.19909	785111.945	785159.947	44.243	2.761	0.062	-0.347
50.42734	0.17375	785124.435	785172.356	44.242	2.735	0.068	-0.287
50.48434	0.14836	785136.815	785184.763	44.246	2.711	0.074	-0.328
50.54131	0.12292	785149.200	785197.166	44.260	2.687	0.080	-0.350
50.59830	0.09743	785161.603	785209.571	44.288	2.664	0.087	-0.340
50.65528	0.07188	785174.010	785221.974	44.332	2.645	0.091	-0.306
50.71225	0.04628	785186.264	785234.376	44.393	2.628	0.095	-0.406

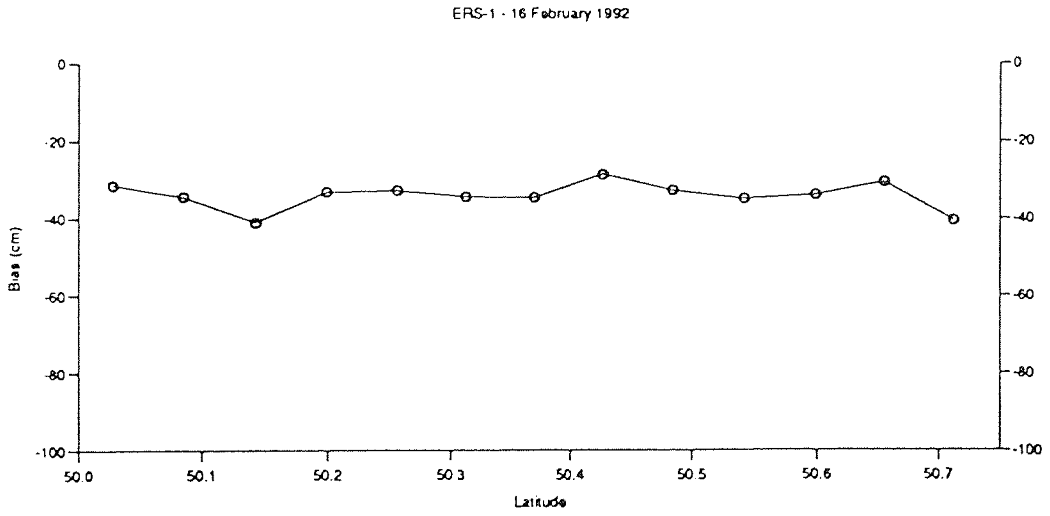

Figure 6.7

Table 6.11: ERS-1 bias results for pass 19/2/92; all figures in metres.

Details at NEWHAVEN TIDE GAUGE (at 21:47:37 GMT)

Tide gauge DATUM height :	41.193	Solid earth tide :	-0.072
Tide gauge GEOID height :	44.458	Ocean tide :	0.449
Tide gauge reading :	3.883	Storm surge :	-0.296

Details at ALTIMETER POINTS

Lat.	Long.	h^{alt}	h^{sat}	h^{sea}_{g}	h^{sea}_{ot}	h^{sea}_{ss}	bias
50.01811	0.35764	785012.167	785058.596	44.020	1.737	-0.295	-0.574
50.07514	0.33262	785024.713	785071.038	44.071	1.620	-0.296	-0.537
50.13215	0.30755	785037.200	785083.477	44.132	1.511	-0.297	-0.539
50.18916	0.28242	785049.731	785095.919	44.187	1.403	-0.298	-0.503
50.24618	0.25724	785062.270	785108.359	44.222	1.299	-0.299	-0.474
50.30317	0.23202	785074.815	785120.794	44.237	1.198	-0.299	-0.450
50.36018	0.20674	785087.368	785133.232	44.241	1.098	-0.300	-0.431
50.41718	0.18141	785099.899	785145.669	44.240	1.003	-0.300	-0.435
50.47417	0.15603	785112.470	785158.104	44.243	0.909	-0.300	-0.389
50.53115	0.13061	785124.945	785170.536	44.255	0.819	-0.299	-0.423
50.58814	0.10513	785137.542	785182.968	44.279	0.733	-0.300	-0.320
50.64512	0.07959	785150.012	785195.399	44.321	0.653	-0.300	-0.320
50.70210	0.05401	785162.406	785207.829	44.380	0.576	-0.300	-0.374

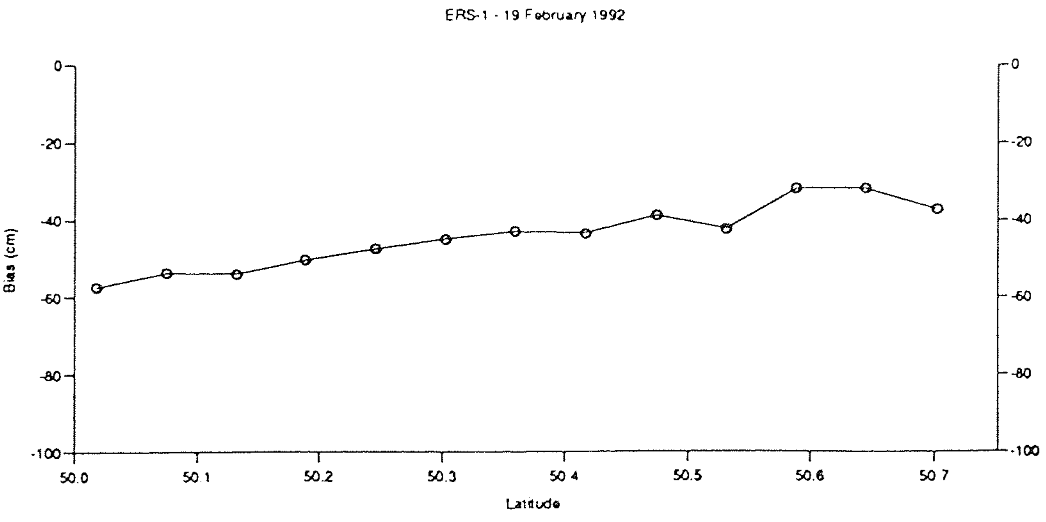

Figure 6.8

Table 6.12: ERS-1 bias results for pass 8/3/92; all figures in metres.

Details at NEWHAVEN TIDE GAUGE (at 21:47:37 GMT)

Tide gauge DATUM height :	41.193	Solid earth tide :	-0.102
Tide gauge GEOID height :	44.458	Ocean tide :	-1.329
Tide gauge reading :	2.122	Storm surge :	-0.148

Details at ALTIMETER POINTS

Lat.	Long.	h^{alt}	h^{sat}	h_g^{sea}	h_{ot}^{sea}	h_{ss}^{sea}	bias
50.01129	0.35872	785029.033	785073.139	44.015	-0.530	-0.200	-0.589
50.06831	0.33371	785041.462	785085.487	44.065	-0.612	-0.190	-0.530
50.12533	0.30865	785053.900	785097.838	44.125	-0.682	-0.187	-0.450
50.18235	0.28353	785066.216	785110.188	44.183	-0.750	-0.183	-0.490
50.23937	0.25837	785078.569	785122.537	44.219	-0.812	-0.180	-0.509
50.29637	0.23316	785090.976	785134.882	44.237	-0.874	-0.177	-0.488
50.35337	0.20790	785103.383	785147.228	44.242	-0.932	-0.173	-0.476
50.41037	0.18259	785115.871	785159.574	44.241	-0.989	-0.169	-0.388
50.46736	0.15723	785128.224	785171.915	44.243	-1.044	-0.164	-0.424
50.52435	0.13181	785140.656	785184.258	44.254	-1.094	-0.160	-0.371
50.58134	0.10634	785153.043	785196.600	44.277	-1.140	-0.155	-0.343

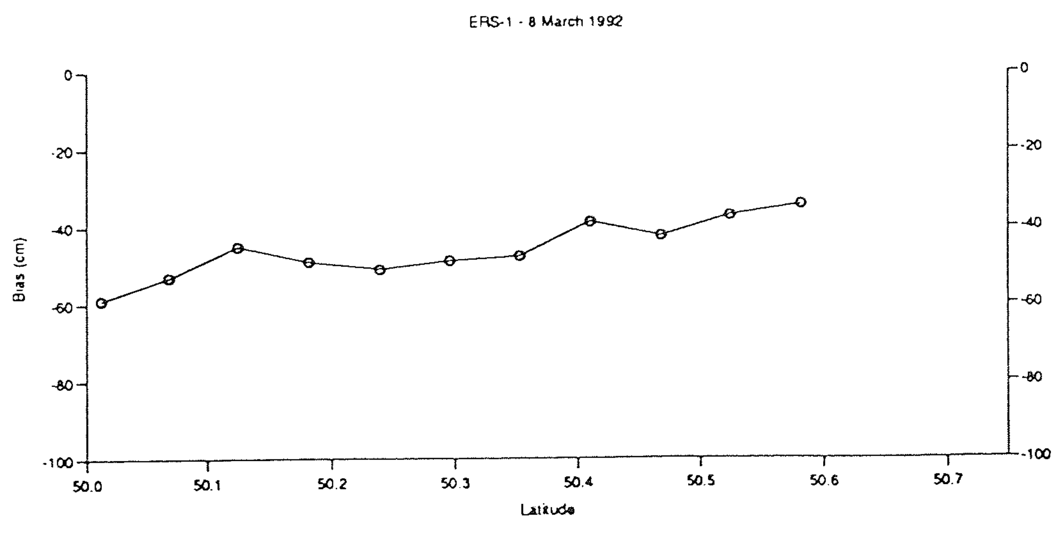

Figure 6.9

Table 6.13: TOPEX bias results for pass 28/9/92 (Arc B); all figures in metres.

Details at NEWHAVEN TIDE GAUGE (at 11:49:34 GMT)

Tide gauge DATUM height : 41.193
Tide gauge GEOID height : 44.458
Tide gauge reading : 7.118

Solid earth tide : -0.080
Ocean tide : 3.247
Storm surge : -0.022

Details at ALTIMETER POINTS

Lat.	Long.	h^{alt}	h^{sat}	h_{g}^{sea}	h_{ot}^{sea}	h_{ss}^{sea}	bias
50.01735	-0.28958	1349484.962	1349533.084	44.618	2.826	-0.015	-0.145
50.06206	-0.23769	1349498.741	1349546.934	44.572	2.893	-0.017	-0.197
50.10675	-0.18569	1349512.592	1349560.774	44.529	2.963	-0.017	-0.159
50.15142	-0.13359	1349526.371	1349574.601	44.487	3.032	-0.017	-0.180
50.19605	-0.08139	1349540.230	1349588.417	44.447	3.102	-0.018	-0.108
50.24066	-0.02908	1349553.977	1349602.221	44.410	3.168	-0.018	-0.135
50.28524	0.02334	1349567.701	1349616.013	44.374	3.233	-0.019	-0.175
50.32979	0.07587	1349581.487	1349629.793	44.333	3.297	-0.019	-0.147
50.37431	0.12850	1349595.234	1349643.562	44.287	3.356	-0.018	-0.156
50.41880	0.18124	1349608.952	1349657.318	44.239	3.414	-0.020	-0.185
50.46327	0.23408	1349622.627	1349671.062	44.197	3.470	-0.020	-0.239
50.50771	0.28704	1349636.433	1349684.794	44.166	3.520	-0.022	-0.149
50.55212	0.34010	1349650.088	1349698.513	44.148	3.568	-0.022	-0.183
50.64086	0.44656	1349677.408	1349725.915	44.156	3.670	-0.025	-0.158
50.68518	0.49995	1349691.020	1349739.598	44.178	3.719	-0.025	-0.157

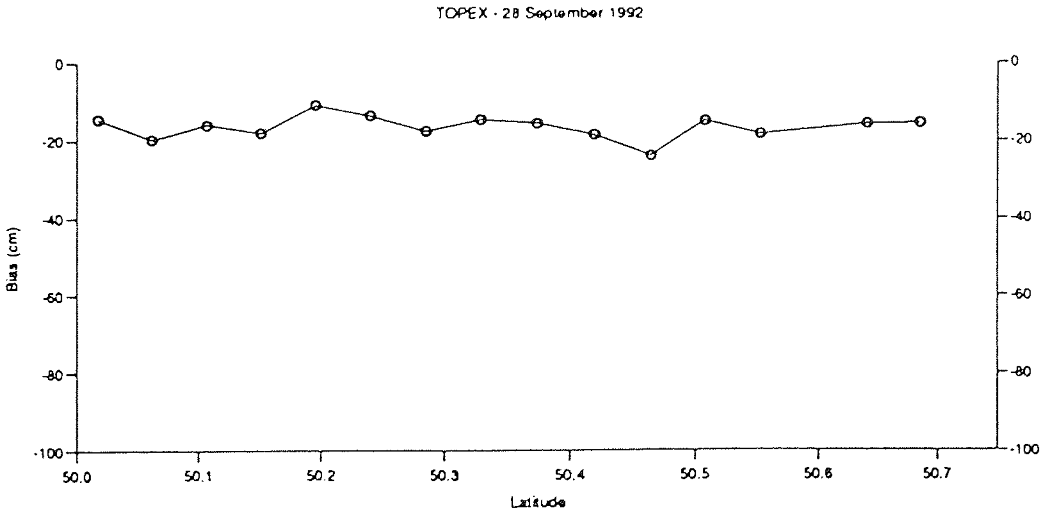

Figure 6.10

Table 6.14: TOPEX bias results for pass 18/10/92 (Arc B); all figures in metres.

Details at NEWHAVEN TIDE GAUGE (at 7:47:00 GMT)

Tide gauge DATUM height : 41.193
Tide gauge GEOID height : 44.458
Tide gauge reading : 2.120

Solid earth tide : 0.030
Ocean tide : -1.563
Storm surge : 0.088

Details at ALTIMETER POINTS

Lat.	Long.	h^{alt}	h^{sat}	h_g^{sea}	h_{ot}^{sea}	h_{ss}^{sea}	bias
50.03329	-0.25444	1349485.817	1349529.197	44.582	-1.789	0.088	-0.139
50.07800	-0.20251	1349499.655	1349543.027	44.540	-1.785	0.090	-0.167
50.12267	-0.15048	1349513.529	1349556.844	44.498	-1.782	0.090	-0.149
50.16732	-0.09834	1349527.304	1349570.651	44.457	-1.779	0.090	-0.219
50.21195	-0.04609	1349541.197	1349584.445	44.420	-1.775	0.090	-0.154
50.25654	0.00626	1349554.980	1349598.227	44.385	-1.771	0.090	-0.183
50.30111	0.05872	1349568.811	1349611.998	44.348	-1.768	0.090	-0.157
50.34565	0.11129	1349582.589	1349625.757	44.305	-1.763	0.090	-0.176
50.39016	0.16396	1349596.370	1349639.503	44.259	-1.757	0.089	-0.182
50.43465	0.21674	1349610.135	1349653.238	44.214	-1.753	0.090	-0.193
50.47910	0.26963	1349623.891	1349666.961	44.176	-1.748	0.090	-0.191
50.52353	0.32262	1349637.597	1349680.671	44.151	-1.741	0.088	-0.216
50.56793	0.37573	1349651.287	1349694.369	44.140	-1.736	0.089	-0.229
50.61230	0.42894	1349664.978	1349708.055	44.143	-1.730	0.085	-0.220
50.65664	0.48227	1349678.644	1349721.729	44.160	-1.727	0.086	-0.206

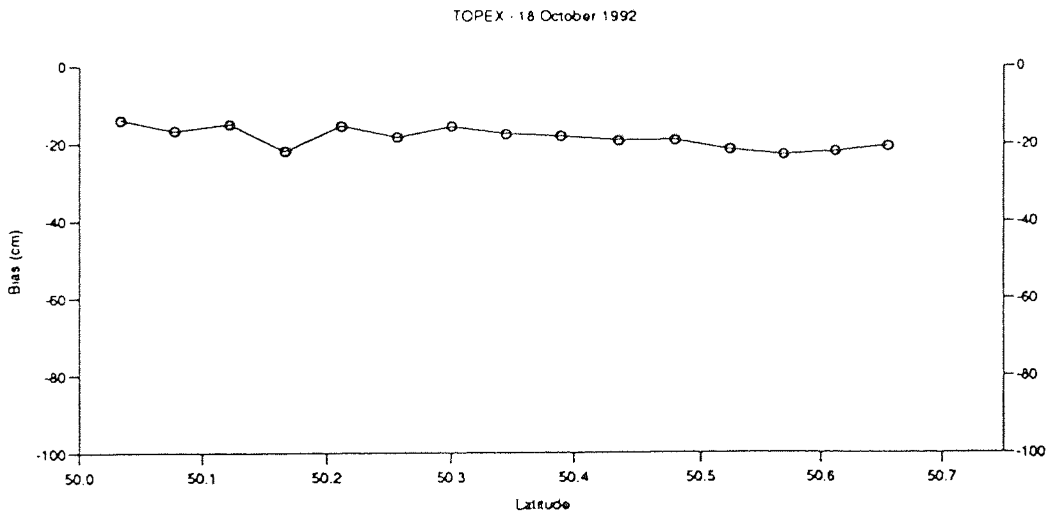

Figure 6.11

Table 6.15: POSEIDON bias results for pass 21/10/92 (Arc C); all figures in metres.

Details at NEWHAVEN TIDE GAUGE (at 14:48:49 GMT)

Tide gauge DATUM height : 41.193
Tide gauge GEOID height : 44.458
Tide gauge reading : 2.577

Solid earth tide : -0.167
Ocean tide : -1.192
Storm surge : 0.059

Details at ALTIMETER POINTS

Lat.	Long.	h^{alt}	h^{sat}	h_{g}^{sea}	h_{ot}^{sea}	h_{ss}^{sea}	bias
50.66008	-0.46496	1349737.446	1349781.644	44.803	-0.854	0.051	0.081
50.61900	-0.41554	1349724.921	1349769.049	44.738	-0.834	0.052	0.106
50.57790	-0.36622	1349712.270	1349756.444	44.678	-0.813	0.051	0.019
50.53678	-0.31699	1349699.655	1349743.828	44.625	-0.794	0.053	-0.011
50.49563	-0.26785	1349687.086	1349731.201	44.581	-0.777	0.049	0.016
50.41325	-0.16986	1349661.888	1349705.916	44.512	-0.747	0.052	0.068
50.37203	-0.12100	1349649.223	1349693.257	44.481	-0.733	0.050	0.042
50.33078	-0.07223	1349636.562	1349680.589	44.447	-0.718	0.052	0.031
50.28951	-0.02355	1349623.959	1349667.909	44.410	-0.706	0.053	0.085
50.20689	0.07353	1349598.530	1349642.519	44.323	-0.682	0.051	-0.019
50.16555	0.12193	1349585.915	1349629.809	44.267	-0.672	0.053	0.032
50.12418	0.17024	1349573.208	1349617.088	44.201	-0.661	0.053	-0.010
50.08278	0.21847	1349560.532	1349604.357	44.127	-0.650	0.054	-0.017
50.04137	0.26660	1349547.866	1349591.616	44.059	-0.638	0.055	0.003

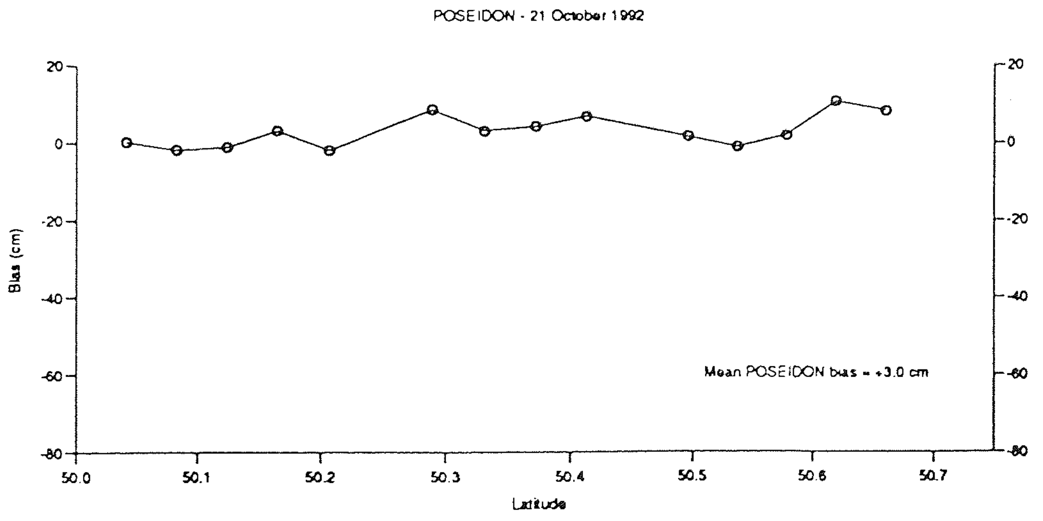

Figure 6.12

Table 6.16: TOPEX bias results for pass 28/10/92 (Arc B); all figures in metres.

Details at NEWHAVEN TIDE GAUGE (at 5:45:04 GMT)

Tide gauge DATUM height :	41.193	Solid earth tide :	-0.040
Tide gauge GEOID height :	44.458	Ocean tide :	-2.524
Tide gauge reading :	1.074	Storm surge :	0.179

Details at ALTIMETER POINTS

Lat.	Long.	h^{alt}	h^{sat}	h_{g}^{sea}	h_{ot}^{sea}	h_{ss}^{sea}	bias
50.02315	-0.27159	1349501.472	1349543.816	44.599	-2.756	0.241	-0.146
50.06786	-0.21969	1349515.380	1349557.669	44.555	-2.767	0.227	-0.160
50.11255	-0.16768	1349529.279	1349571.510	44.513	-2.778	0.230	-0.152
50.15720	-0.11556	1349543.181	1349585.340	44.471	-2.788	0.233	-0.129
50.20183	-0.06334	1349557.051	1349599.157	44.432	-2.797	0.218	-0.138
50.24644	-0.01102	1349570.887	1349612.963	44.398	-2.801	0.221	-0.144
50.29101	0.04142	1349584.770	1349626.757	44.361	-2.804	0.205	-0.111
50.33556	0.09396	1349598.569	1349640.539	44.319	-2.806	0.208	-0.135
50.38008	0.14661	1349612.409	1349654.309	44.273	-2.801	0.211	-0.103
50.42457	0.19936	1349626.240	1349668.067	44.227	-2.797	0.194	-0.090
50.46903	0.25222	1349639.899	1349681.813	44.187	-2.792	0.196	-0.209
50.51347	0.30519	1349653.594	1349695.546	44.157	-2.781	0.178	-0.283

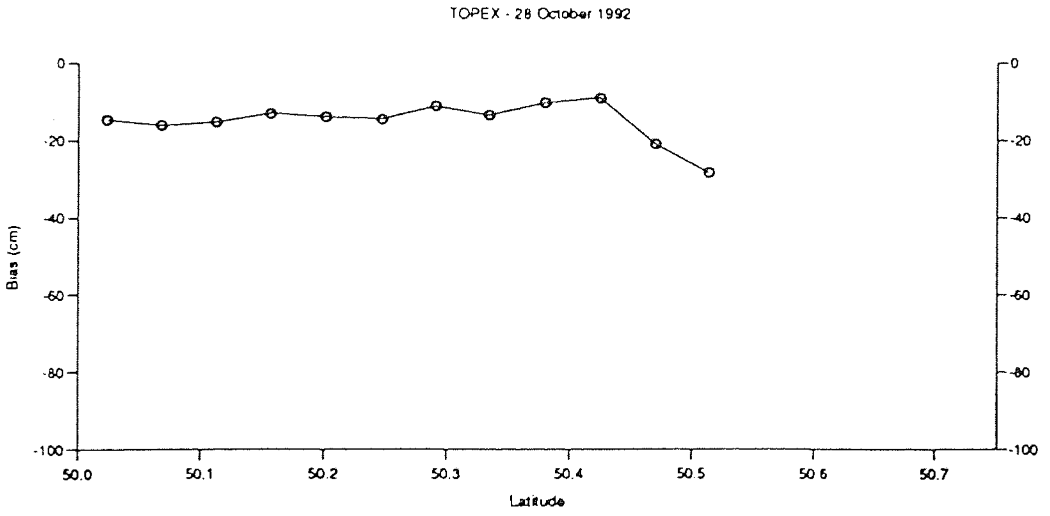

Figure 6.13

Table 6.17: TOPEX bias results for pass 31/10/92 (Arc C); all figures in metres.

Details at NEWHAVEN TIDE GAUGE (at 12:47:22 GMT)

Tide gauge DATUM height :	41.193	Solid earth tide :	-0.127
Tide gauge GEOID height :	44.458	Ocean tide :	1.277
Tide gauge reading :	5.096	Storm surge :	-0.070

Details at ALTIMETER POINTS

Lat.	Long.	h^{alt}	h^{sat}	h_g^{sea}	h_{ot}^{sea}	h_{ss}^{sea}	bias
50.62150	-0.41867	1349755.238	1349801.621	44.742	1.180	-0.069	-0.034
50.57714	-0.36543	1349741.646	1349788.004	44.677	1.236	-0.071	-0.019
50.53274	-0.31230	1349728.012	1349774.374	44.621	1.296	-0.070	-0.019
50.48832	-0.25928	1349714.309	1349760.733	44.574	1.358	-0.073	-0.069
50.44387	-0.20637	1349700.656	1349747.079	44.536	1.421	-0.073	-0.042
50.39939	-0.15356	1349686.981	1349733.413	44.502	1.484	-0.072	-0.021
50.35488	-0.10087	1349673.249	1349719.735	44.467	1.550	-0.075	-0.048
50.31034	-0.04828	1349659.537	1349706.045	44.429	1.615	-0.075	-0.042
50.26578	0.00421	1349645.769	1349692.342	44.388	1.680	-0.077	-0.085
50.22118	0.05658	1349632.048	1349678.628	44.340	1.746	-0.077	-0.073
50.17656	0.10885	1349618.332	1349664.902	44.283	1.812	-0.076	-0.054
50.13192	0.16101	1349604.542	1349651.164	44.214	1.878	-0.078	-0.111
50.08724	0.21307	1349590.775	1349637.415	44.135	1.944	-0.078	-0.141
50.04254	0.26502	1349577.048	1349623.653	44.060	2.011	-0.079	-0.116

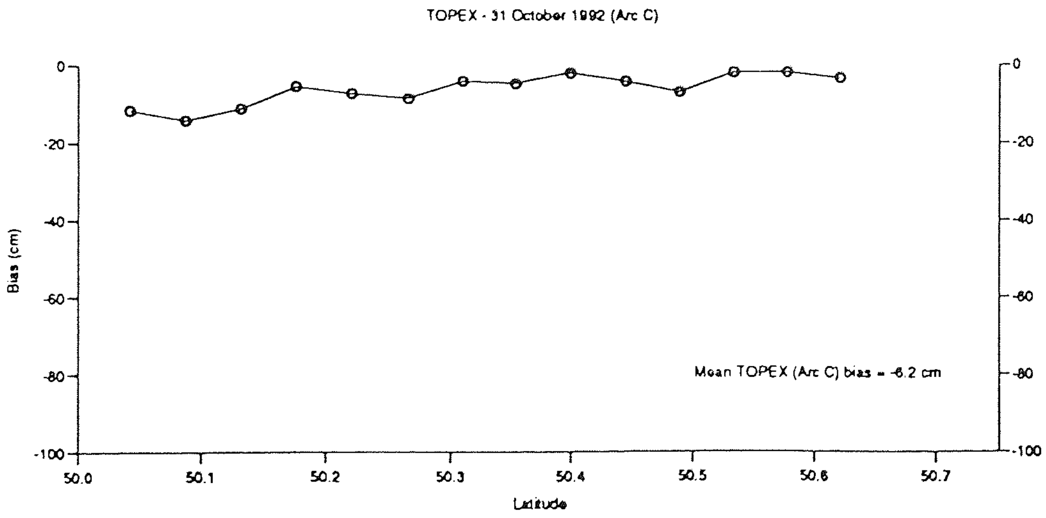

Figure 6.14

Table 6.18: TOPEX bias results for pass 26/11/92 (Arc B); all figures in metres.

Details at NEWHAVEN TIDE GAUGE (at 23:41:53 GMT)

Tide gauge DATUM height :	41.193	Solid earth tide :	0.149
Tide gauge GEOID height :	44.458	Ocean tide :	2.368
Tide gauge reading :	6.339	Storm surge :	0.046

Details at ALTIMETER POINTS

Lat.	Long.	h^{alt}	h^{sat}	h^{sea}_{g}	h^{sea}_{ot}	h^{sea}_{ss}	bias
50.00467	-0.30148	1349562.440	1349610.277	44.628	2.315	-0.003	-0.088
50.04940	-0.24962	1349576.501	1349624.277	44.582	2.346	-0.005	-0.044
50.09410	-0.19766	1349590.451	1349638.266	44.539	2.377	0.006	-0.084
50.13878	-0.14560	1349604.407	1349652.243	44.496	2.409	0.004	-0.118
50.18342	-0.09342	1349618.391	1349666.209	44.455	2.442	0.015	-0.097
50.22804	-0.04115	1349632.321	1349680.162	44.418	2.473	0.013	-0.128
50.27263	0.01124	1349646.248	1349694.103	44.383	2.504	0.011	-0.148
50.31720	0.06373	1349660.129	1349708.033	44.344	2.534	0.022	-0.195
50.36173	0.11633	1349674.020	1349721.951	44.298	2.562	0.020	-0.241
50.40624	0.16903	1349687.962	1349735.856	44.251	2.590	0.032	-0.212
50.45072	0.22184	1349701.880	1349749.749	44.207	2.617	0.030	-0.206
50.49517	0.27476	1349715.735	1349763.630	44.173	2.643	0.028	-0.243
50.53960	0.32779	1349729.587	1349777.499	44.151	2.666	0.041	-0.245
50.62836	0.43418	1349757.236	1349805.199	44.151	2.719	0.052	-0.232

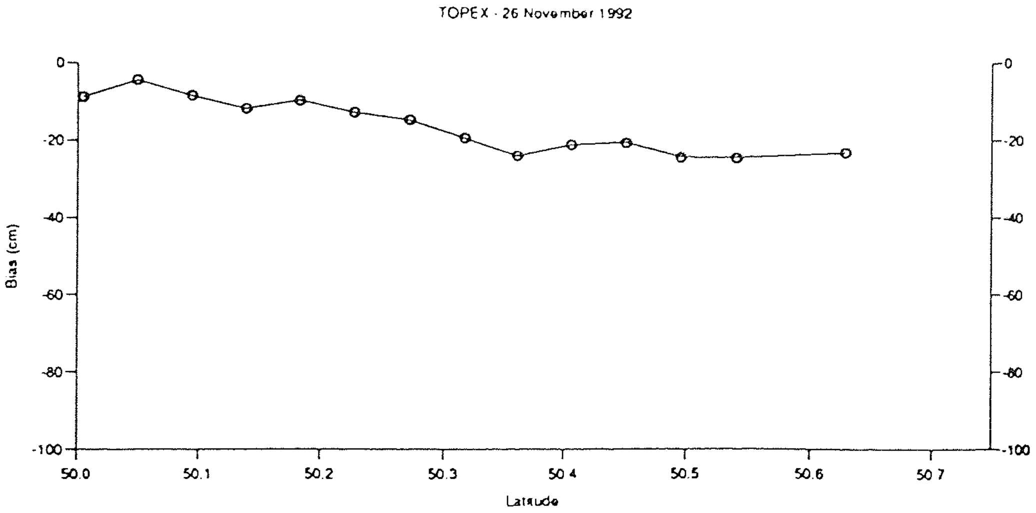

Figure 6.15

All the bias values derived for the 5 ERS-1 passes are plotted in Figure 6.16. The bias values resulting from the 4 TOPEX 'Arc B's are displayed in Figure 6.17.

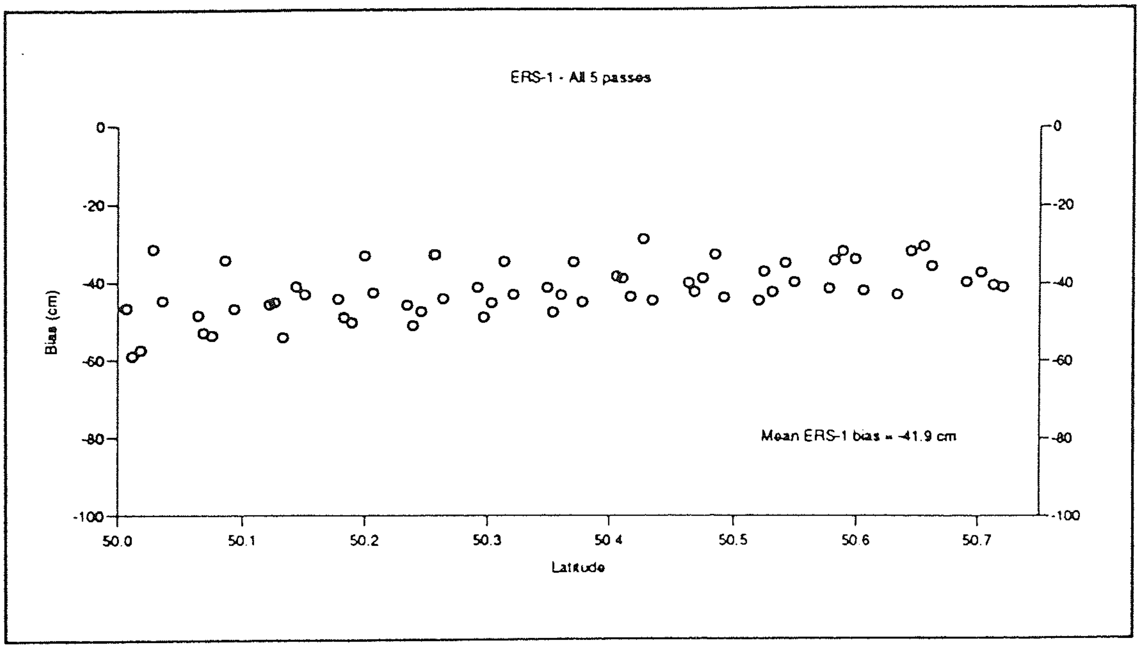

Figure 6.16

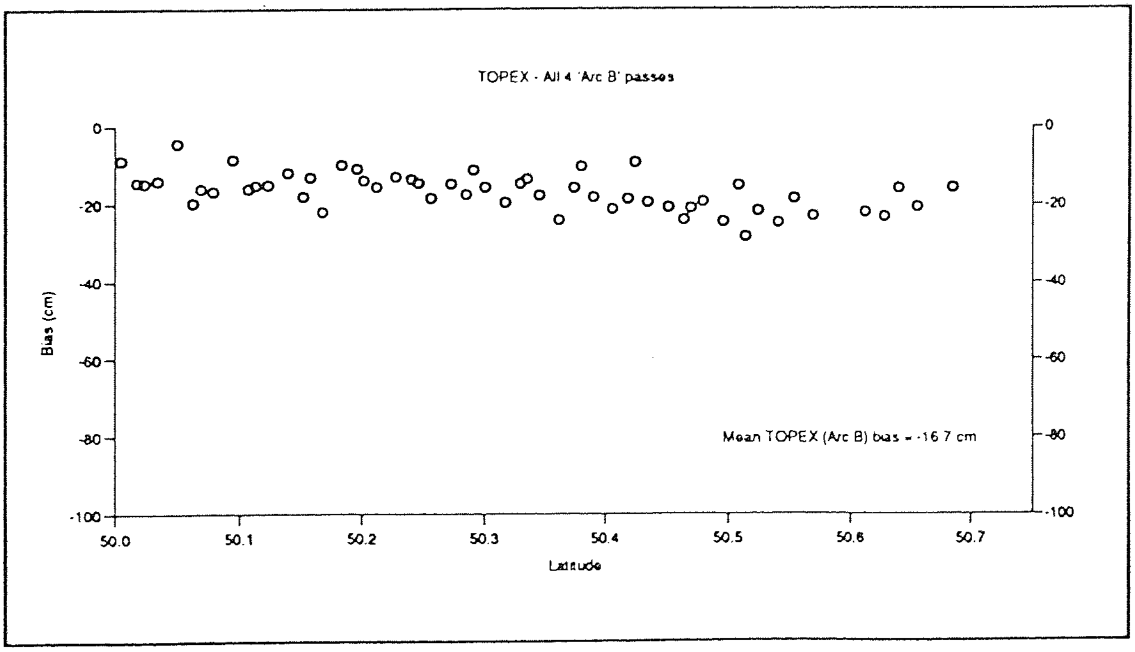

Figure 6.17

The bias values in Figure 6.16 are more spread out near latitude 50° and begin to tighten as the satellite travels closer to the Newhaven tide gauge where the differential corrections in equation 6.9 become smaller. A simple mean of all 63 data points yields an overall ERS-1 bias of -41.9 cm with a s.d. of 6.6 cm.

Similarly Figure 6.17 shows all the bias values for the 4 'Arc B' passes and a simple mean of all 56 data points gives an overall TOPEX bias of -16.7 cm with a s.d. of 4.7 cm.

The two 'Arc C' passes are shown in Figures 6.12 and 6.14. The former estimates the POSEIDON altimeter bias at +3.0 cm with a s.d. of 4.0 cm whilst the latter returns a value of -6.2 cm with s.d. 3.7 for TOPEX. This is some 10 cm short of the value observed for the 4 'Arc B' passes and the reason for this is presently unknown. Hence this value is not considered in the final bias for TOPEX. The result for the single POSEIDON pass agrees well with values obtained by other groups and may be due to some good fortune.

Table 6.19: Aston 'on-site' altimeter bias results

Altimeter	Number of passes	Number of points	Arc	Bias (cm)	σ (cm)
ERS-1	5	63	A	-41.9	6.6
TOPEX	4	56	B	-16.7	4.7
TOPEX	1	14	C	-6.2	3.7
POSEIDON	1	14	C	+3.0	4.0

Table 6.19 summarises the findings of this chapter. The ERS-1 bias value of -41.9 cm is similar to the ESA value of -42 cm determined from the Venice Tower campaign [ESA, 1993]. The TOPEX bias of -16.7 cm and POSEIDON bias of +3 cm also agree very well with results observed at Platform Harvest and Lampedusa [JPL, 1992 b, c]. The fact that these figures agree so well in an absolute sense vindicates, in particular, the accuracy of the height deduced for the Newhaven tide gauge datum in section 6.5.1.

The Aston on-site difference of ~20 cm between TOPEX and POSEIDON compares very well against ~22 and ~21 cm determined by the long arc study and repeat track analysis respectively in chapter 4. Moreover, the Aston on-site difference between ERS-1 and TOPEX of ~25 cm agrees well with the long arc difference of ~30 cm (see chapter 4). Seasonal variations of the ocean heights affect the long arc solutions (determined in chapter 4) and recent reports [ESOC, 1994] appear to show the ERS-1 altimeter developing a serious drift problem with its range measurements.

The method of analysing dual crossover points for ERS-1 and TOPEX [Carnochan et al., 1994] can also help establish the difference between the two altimeters. Such studies reveal a value of ~20 cm, with ERS-1 measuring shorter than TOPEX [Le Traon et al., 1994; Shum et al., 1994].

§ 6.7 Recommendations for future work

The English Channel poses some problems as a calibration site in that marine tides can reach almost 4 metres (see Table 6.13) and therefore makes accurate forecasting difficult, particularly near the coast as required for the differential correction in equation 6.7. Differences in the surge elevation from the POL model are, on average, small (~2 to 3 cm) over short distances.

The orbits computed for arcs overflying Herstmonceux were observed to be fairly robust which was only to be expected since it was possible to treat the laser range data as absolute radial information.

Therefore, assuming the corrected altimeter heights to contain minimal error, the key source of error is the differential ocean tide correction in equation 6.9. One suggestion is to use the waters off the Lowestoft tide gauge (see Figure 6.18) as a second possible calibration site.

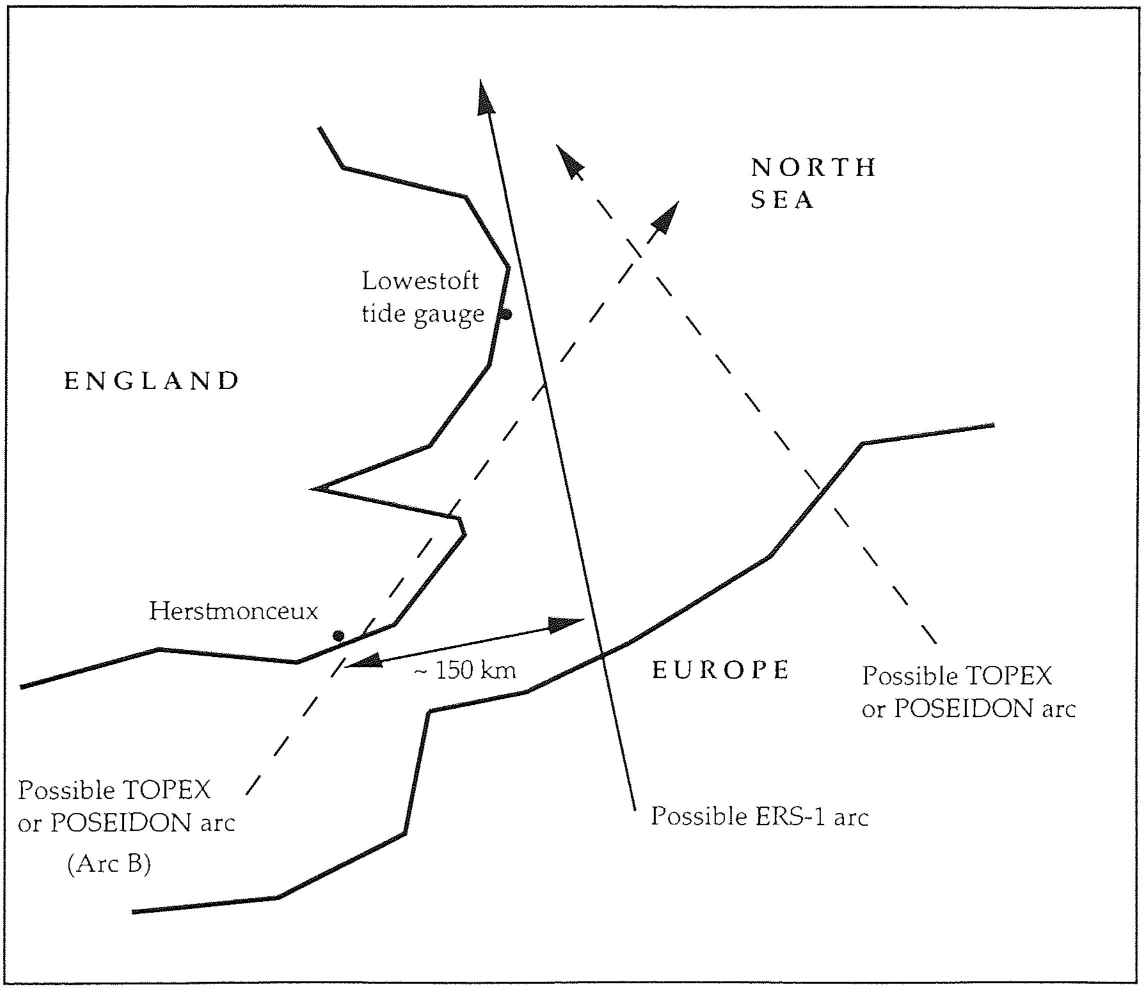

Figure 6.18

This area is known for its low tides and the tide gauge has been surveyed by GPS in the same way as the one at Newhaven. A number of possible ERS-1 arcs near Lowestoft should be available during the 35 day repeat phase. These will be laser ranged by other European laser sites as well as Herstmonceux and hence short arc correction using a suitable combination of these stations should provide reliable orbits. Moreover, the TOPEX/POSEIDON 'Arc B' can be used to 'tie' together the results from Newhaven and Lowestoft. It is also a good idea to collect a reasonable number of bias profiles for the POSEIDON altimeter since only one pass was processed for this chapter.

Continual monitoring of the these 3 altimeters is straightforward using the method discussed. POL maintains the tide gauge itself and processes the readings; therefore new bias values can be determined as and when laser and altimeter data becomes available. Suitable arcs during 1993 now need to be scrutinized to observe any bias drift, in particular, for ERS-1 during late 1993 / early 1994 [ESOC, 1994].

§ 6.8 Conclusions

Altimeter data points over the English Channel for ERS-1 and TOPEX/POSEIDON were used in conjunction with precise satellite orbits and computed sea heights (using tide gauge, GPS, geoid, ocean tide and storm surge data) to determine the altimeter range biases. The altimetric datasets used were OPR 02 for ERS-1 and the GDR CD roms for TOPEX and POSEIDON.

This exercise estimates the ERS-1 bias at -41.9 cm (during early 1992), TOPEX bias at -16.7 cm and POSEIDON bias at +3.0 cm (during late 1992). These values are independent of the Earth semi-major axis (unlike the results from long arc analyses) and may be regarded as absolute measurements.

Further on-site calibration studies will continue at Aston University to monitor the bias values for ERS-1, TOPEX and POSEIDON during 1993 and 1994.

CHAPTER 7

SHORT ARC ANALYSIS

§7.1 Introduction

The technique of improving the radial component of a long arc orbit for short distances or arcs (which may be from a few 100 to a few 1000 km) by non-dynamic adjustment has been well researched [Sinclair, 1985, 1986 & 1989; Wagner and Melchioni, 1989]. It involves an analysis of the range residuals determined from a number of ground stations (laser or PRARE) simultaneously tracking the satellite along the short arc. The radial, along-track and across-track errors are then solved for empirically either as simple constants or as functions in time using a least squares minimisation procedure. From the solution, the covariance matrix may be interrogated to compute the correlations between the solve-for parameters which will affect the reliability of the result. For short arc work, it is important to obtain a reliable separation of the three orbital components. This chapter will detail a simple theory to predict the correlations and rms errors of the solution.

The simplest scenario is when a satellite flies immediately over a laser tracking station; here the observed laser range at the point of closest approach may be taken as the true spacecraft altitude and the along-track and across-track components may be ignored. The long arc trajectory over the station is then modified so that its height coincides with this observed range. Such a technique was employed in chapter 6 to determine the precise height of ERS-1 and TOPEX/POSEIDON over Herstmonceux laser ranger. However this is a special case; usually two or more rangers observe a satellite simultaneously in which the trajectory does not overfly any one particular station and in this case the along-track and across-track components do need to be considered.

§ 7.2 Orbit errors

It is convenient to discuss the orbit error resolved into three orthogonal directions, namely the radial, along-track and across-track components as illustrated in Figure 7.1. The orbit error in these three directions are denoted by Δr, Δc (c for circumferential) and Δn (n for normal) respectively.

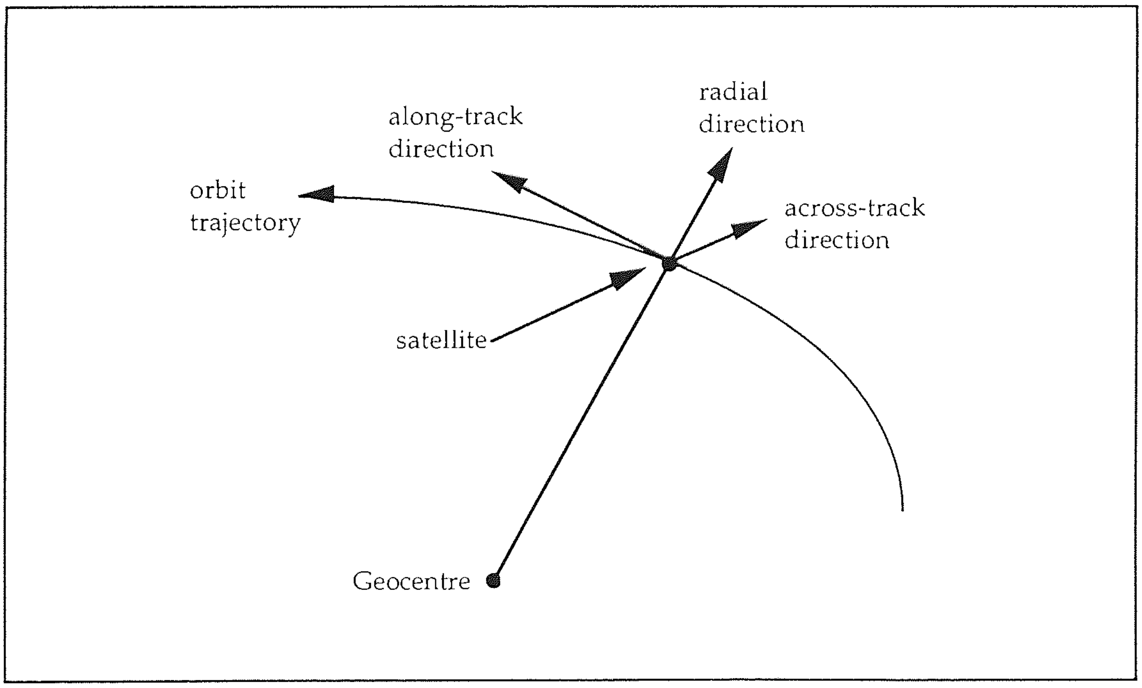

Figure 7.1

Mathematical analysis shows that the orbit errors Δr, Δc and Δn due to gravity field mismodelling are predominately once per revolution, i.e.

of low frequency [Wagner, 1985]. This involves the expansion of the Earth's gravity potential in terms of Keplerian elements followed by the integration of the linearised Lagrange planetary equations such as to observe the major effect of gravity field mismodelling upon the orbital elements [Kaula, 1966]. Figure 7.2 shows a typical graph of the radial orbit error Δr, simulated from differencing the orbit computed from a 'true' gravity field and an orbit calculated from a randomly perturbed gravity field (see PRARE simulations in chapter 8 for more detail).

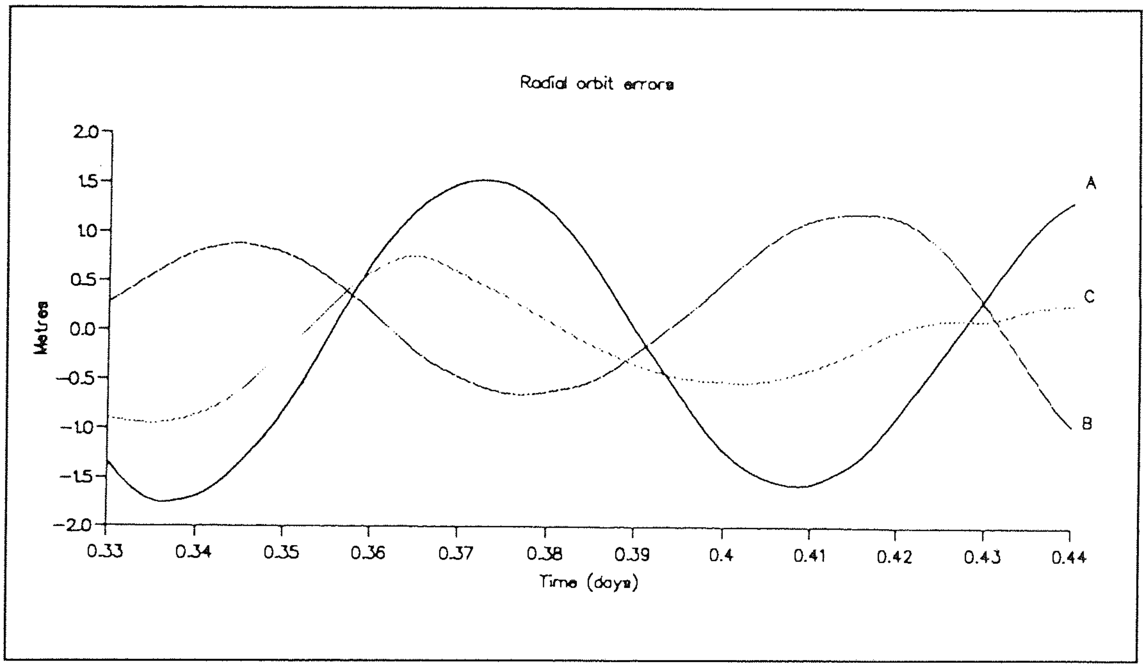

Figure 7.2

Over a short distance, say, of a few 100 km, the orbit errors Δr, Δc and Δn may be approximated by a constant. For longer distances up to about 1000 km, they may be assumed to change linearly with time which is the method adopted in chapter 5. For short arcs of a few 1000 km in length, it is possible to model the orbit errors by periodic functions [Sinclair, 1988] such as AcosM + BsinM where M is the mean anomaly or perhaps by quadratic functions in time. These corrections are said to be non-dynamic (or empirical) in the sense that the corrected orbit trajectory is not an exact solution resulting from the numerical integration of the force equations.

As will be demonstrated in chapter 8, the inclusion of more parameters for the orbit errors will significantly increase the correlation between these parameters in their solution. The following work in this chapter will take the orbit errors as constant; chapter 8 will investigate the consequences of allowing these errors to vary with time.

§ 7.3 Derivation of the range residual ΔR

An expression for the range residual ΔR may be deduced in terms of radial, along-track and across-track components by geometric considerations, as in Figure 7.3, in which r_e is the radius of the Earth which is assumed spherical, r the radial satellite distance and R the range distance between the satellite and the ground laser station.

By the cosine rule,

$$R^2 = r_e^2 + r^2 - 2rr_e \cos \alpha \tag{7.1}$$

and taking small differences

$$\Delta R = \frac{1}{R}(r - r_e \cos \alpha) \Delta r + \frac{rr_e}{R} \sin \alpha \, \Delta\alpha \tag{7.2}$$

Figure 7.4 shows the geometry on the surface of the Earth, where the satellite's orbit is projected radially onto the Earth's surface to give the ground track. A unit sphere is used here because it is the angles which are of primary concern.

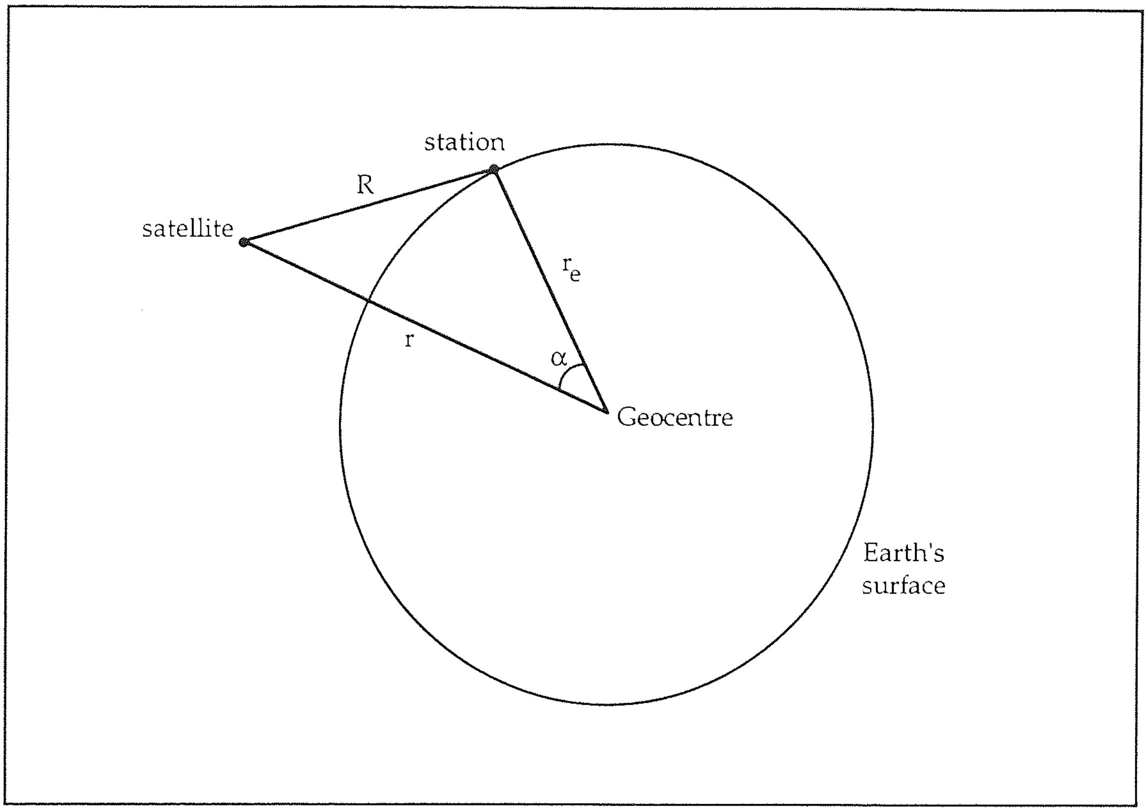

Figure 7.3

The angle subtended at the Earth's centre by the ground station and the satellite is α; likewise ϕ is the angle between the station and the satellite's point of closest approach and $\Delta\lambda$ is the angle between the satellite and the point of closest approach. The value ϕ (in radians) is the parameter used throughout this work to denote a station's proximity to the ground track. A small change $\Delta\alpha$ in α results in the satellite moving $r\Delta\alpha$ in space which may be written as

$$r\Delta\alpha = \cos\xi\,\Delta c + \sin\xi\,\Delta n \tag{7.3}$$

and multiplying through by $\sin\alpha$ yields

$$r\sin\alpha\,\Delta\alpha = \sin\alpha\cos\xi\,\Delta c + \sin\alpha\sin\xi\,\Delta n. \tag{7.4}$$

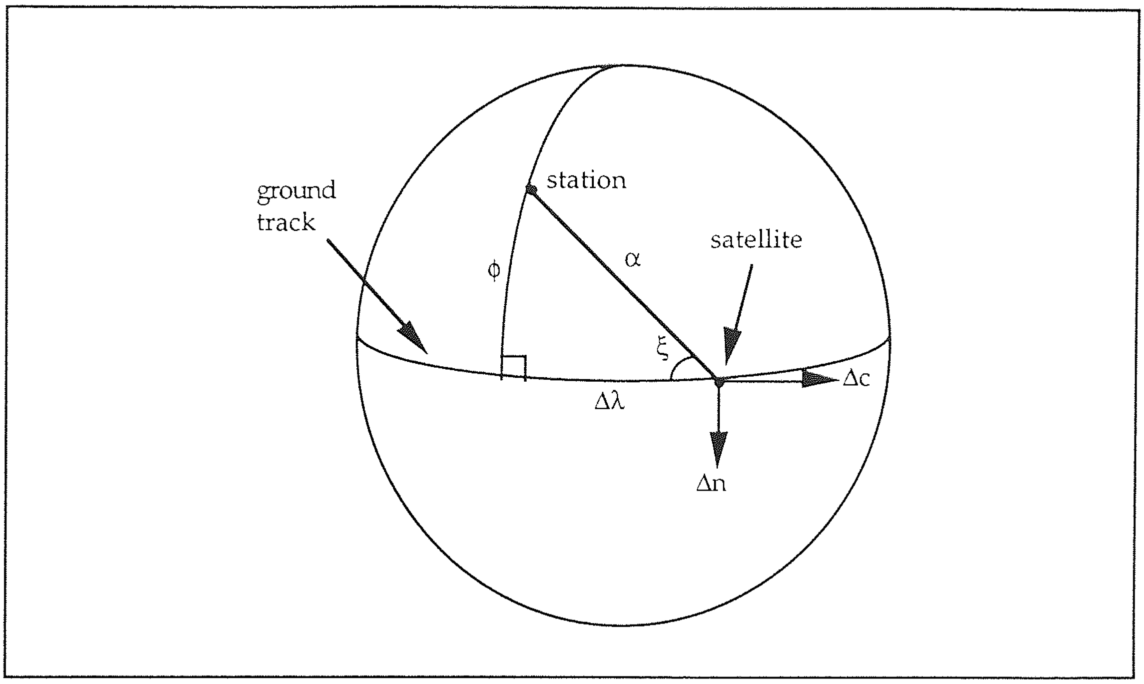

Figure 7.4

From the spherical triangle formed by great arcs α, ϕ and $\overset{\circ}{\Delta\lambda}$, the spherical cosine and sine rules provide the following relationships,

$$\cos\alpha = \cos\phi \cos\Delta\lambda$$

$$\sin\alpha \cos\xi = \cos\phi \sin\Delta\lambda$$

and

$$\sin\alpha \sin\xi = \sin\phi . \tag{7.5}$$

Finally, substituting equations 7.4 and 7.5 into 7.2 yields

$$\Delta R = \frac{1}{R}(r - r_e \cos\phi \cos\Delta\lambda)\, \Delta r + \frac{r_e}{R}(\cos\phi \sin\Delta\lambda)\, \Delta c + \frac{r_e}{R} \sin\phi\, \Delta n \tag{7.6}$$

which is an expression for the range residual in terms of radial, along-track and across-track directions. The coefficients of equation 7.6 are essentially direction cosines and hence the sum of their squares is 1. If the station is sited very close to the ground track then $\phi \approx 0$ and equation 7.6 simplifies to

$$\Delta R \approx \frac{1}{R}(\, r - r_e \cos \Delta\lambda \,)\, \Delta r + \frac{r_e}{R}(\, \sin \Delta\lambda \,)\, \Delta c \tag{7.7}$$

wherein the across-track component is negligible. Moreover at the point of closest approach, $\Delta\lambda=0$ which yields

$$\Delta R \approx \frac{1}{R}(\, r - r_e \,)\, \Delta r \tag{7.8}$$

and since $r - r_e$ is simply the range at this point then

$$\Delta R \approx \Delta r\,. \tag{7.9}$$

This 'overhead' technique for the radial orbit error was employed in section 6.4 to deduce Δr for ERS-1 and TOPEX/POSEIDON overflying the Herstmonceux laser ranger.

§ 7.4 Least squares solution for ΔR

The result of equation 7.6 can now be used in a least squares solution in which the difference between the observed range residual ΔR^{ob} and the calculated range residual ΔR needs to be minimised over all the laser tracking observations; hence it is required to minimise the function I defined as

$$I = \sum_{obs} \left(\Delta R^{ob} - \Delta R \right)^2 \tag{7.10}$$

where $\Delta R^{ob} = R^{ob} - R^{cal}$, i.e. the observed range minus the computed range from a long arc orbit. Unit weights are assumed throughout this chapter. For simplification, put

$$A_1 = \frac{1}{R}(r - r_e \cos\phi \cos\Delta\lambda)$$

$$A_2 = \frac{r_e}{R}\cos\phi \sin\Delta\lambda$$

$$A_3 = \frac{r_e}{R}\sin\phi \tag{7.11}$$

which are the coefficients from ΔR. The partial derivatives of I from equation 7.10 with respect to Δr, Δc and Δn (taken as constants) are

$$\frac{\partial I}{\partial \Delta r} = \sum_{obs}\left(\Delta R^{ob} - \Delta R\right)A_1 = 0$$

$$\frac{\partial I}{\partial \Delta c} = \sum_{obs}\left(\Delta R^{ob} - \Delta R\right)A_2 = 0$$

$$\frac{\partial I}{\partial \Delta n} = \sum_{obs}\left(\Delta R^{ob} - \Delta R\right)A_3 = 0. \tag{7.12}$$

Substitution of equation 7.6 into equations 7.12 gives three equations in three unknowns which in matrix notation is

$$\begin{pmatrix} N_{11} & N_{12} & N_{13} \\ N_{12} & N_{22} & N_{23} \\ N_{13} & N_{23} & N_{33} \end{pmatrix}\begin{pmatrix}\Delta r \\ \Delta c \\ \Delta n\end{pmatrix} = \begin{pmatrix} b_1 \\ b_2 \\ b_3 \end{pmatrix} \tag{7.13}$$

or more succintly

$$N\underline{x} = \underline{b} \tag{7.14}$$

wherein

$$N_{rs} = \sum_{obs}\left(A_r\, A_s\right) , \qquad b_r = \sum_{obs}\left(A_r\, \Delta R^{ob}\right) . \tag{7.15}$$

On assuming all observations are available and symmetric, then from Figure 7.5 for each observation with angle $-\Delta\lambda$, there is one with angle $+\Delta\lambda$. Since $\sin(-\Delta\lambda) = -\sin\Delta\lambda$ then on summing over all the observations, $N_{12} = N_{23} = 0$. Equation 7.13 then becomes

$$\begin{pmatrix} N_{11} & 0 & N_{13} \\ 0 & N_{22} & 0 \\ N_{13} & 0 & N_{33} \end{pmatrix} \begin{pmatrix} \Delta r \\ \Delta c \\ \Delta n \end{pmatrix} = \begin{pmatrix} b_1 \\ b_2 \\ b_3 \end{pmatrix} \tag{7.16}$$

which can now be separated into two equations, namely

$$\begin{pmatrix} N_{11} & N_{13} \\ N_{13} & N_{33} \end{pmatrix} \begin{pmatrix} \Delta r \\ \Delta n \end{pmatrix} = \begin{pmatrix} b_1 \\ b_3 \end{pmatrix} \tag{7.17}$$

and

$$N_{22}\, \Delta c = b_2 . \tag{7.18}$$

Hence, theoretically, the along-track correction Δc can always be solved for; in practice Δc will always be correlated with Δr and Δn to some degree.

On inverting equation 7.17, the equation becomes

$$\begin{pmatrix} \Delta r \\ \Delta n \end{pmatrix} = \frac{1}{N_{11}N_{33} - N_{13}^2} \begin{pmatrix} N_{33} & -N_{13} \\ -N_{13} & N_{11} \end{pmatrix} \begin{pmatrix} b_1 \\ b_3 \end{pmatrix} \tag{7.19}$$

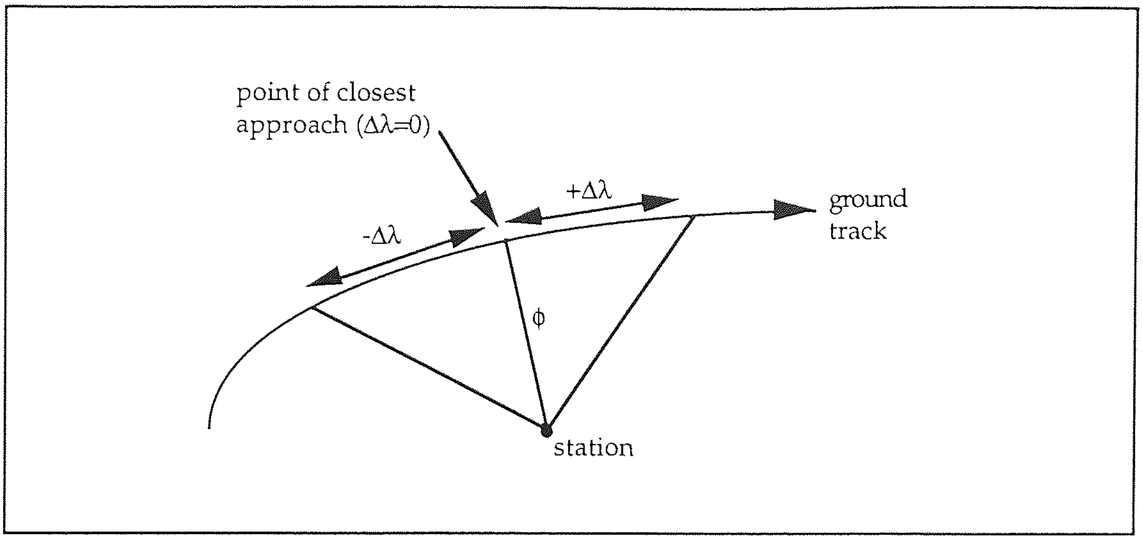

Figure 7.5

wherein the inverted matrix is known as the 'covariance' matrix whose elements in this case are dimensionless. From this matrix the correlation between Δr and Δn is

$$\text{corr}\,(\Delta r, \Delta n) \; = \; \frac{-\,N_{13}}{\sqrt{N_{11}\,N_{33}}} \tag{7.20}$$

and the computed root mean squares (rms) errors are

$$\sigma_{\Delta r} \; = \; \sigma_0 \sqrt{\left(\frac{N_{33}}{N_{11}\,N_{33} - N_{13}^2}\right)}$$

$$\sigma_{\Delta c} \; = \; \sigma_0 \sqrt{\frac{1}{N_{22}}}$$

$$\sigma_{\Delta n} \; = \; \sigma_0 \sqrt{\left(\frac{N_{11}}{N_{11}\,N_{33} - N_{13}^2}\right)} \tag{7.21}$$

where σ_0 is the standard error defined by

$$\sigma_0 = \sqrt{\left(\sum_{obs}\left(\Delta R^{ob} - \Delta R\right)^2\right) \Big/ \left(M - U + 1 \right)} \qquad (7.22)$$

and M is the total number of acceptable observations and U the number of unknowns. The value σ_0 is approximately equal to the rms after fit for small U. The standard error cannot be evaluated here as no real observations are considered but simulations with actual SEASAT arcs in section 7.6 means this parameter is available. For the same reason, $\underline{b}$ cannot be determined and analysis is confined to that of calculating the correlations and rms errors of the unknowns from the covariance matrix.

§ 7.5 Expected correlations and errors for certain station configurations

It is possible to derive numerical results from the above theory by writing some straightforward computer software to construct the normal equation 7.17. For each station of angle ϕ from the ground track, 15 pseudo observations (to 15° elevation) are computed such that they are symmetrical around a single observation at the point of closest approach. Each pseudo observation, R, is used to compute the partial derivatives given by equations 7.12 and these are incorporated in the normal eqaution using equation 7.15. As many stations of different ϕ can be included. The parameter ϕ is strictly an angle (in radians) but on the unit sphere it may be interpreted as a distance. To translate ϕ into a distance over the Earth, it is only necessary to multiply ϕ by 6378 km.

A value of, say, 1 metre is taken for the standard error σ_0.

§ 7.5.1 One station observing

For a single laser station observing the satellite, it can be seen from Figure 7.5 that if the spacecraft is vertically over the station then $\phi \approx 0$ which means $A_3 \approx 0$ and hence $N_{13} \approx 0$. However from the results in Table 7.1 the value corr(Δr,Δn) is very high which means $\sqrt{N_{11}\, N_{33}}$ must work out to be just fractionally larger than N_{13} and consequently no reliable separation is possible. Fortunately, for small ϕ it is the case that Δn will not contribute significantly to ΔR as illustrated by equation 7.7 and the across-track component may be omitted with little error.

Table 7.1: Expected correlation and rms errors (m) for Δr, Δc and Δn for a single observing station; the distance of the station to the ground track is given by ϕ in radians. The standard error σ_0 is taken to be 1 metre.

ϕ (rad)	km	corr(Δr,Δn)	$\sigma_{\Delta r}$	$\sigma_{\Delta c}$	$\sigma_{\Delta n}$
0.001	6.4	0.9985	6.068	0.404	798.784
0.01	63.8	0.9985	6.122	0.399	80.849
0.1	637.8	0.9989	8.455	0.435	11.737
0.2	1275.6	0.9999	33.704	0.848	25.209
0.001	6.4	0.0000	0.335	0.404	*
0.01	63.8	0.0000	0.340	0.399	*

* = Δn suppressed

As the station moves away from the ground track, slightly more across-track information is available for the solution which explains why $\sigma_{\Delta n}$ in Table 7.1 decreases dramatically from 768.8 m to 11.7 m, though only up to a point. If the station is near the ground track (~100 km or less), the parameter Δn may be suppressed in the solution with little error to Δr, as illustrated by equation 7.7. Table 7.1 shows this for $\phi = 0.001$ and 0.01; the rms error for Δr comes down to below 40 cm.

§ 7.5.2 Two stations observing

For two stations observing, ideally they should be on opposite sides of the ground track and the same distance from it, i.e. $\phi_1 = -\phi_2$ (the minus sign denotes a station on the other side of the ground track). Then summing over both sets of observations, $N_{13} = 0$ which results in a zero correlation between Δr and Δn. This is reflected from the numerical results in part (a) of Table 7.2. Moreover the rms errors are far more favourable than for just the single station. Again as the station pair moves away from the ground track, $\sigma_{\Delta n}$ decreases from 31.2 m to 0.24 m as more across-track information becomes available to the solution.

Table 7.2: Expected correlation and rms errors (m) for Δr, Δc and Δn for two stations observing simultaneously; the distance of the stations to the ground track is given in radians. The standard error σ_0 is taken to be 1 metre.

	ϕ_1	ϕ_2	corr(Δr,Δn)	$\sigma_{\Delta r}$	$\sigma_{\Delta c}$	$\sigma_{\Delta n}$
(a)	0.001	-0.001	0	0.237	0.286	31.226
	0.01	-0.01	0	0.240	0.282	3.171
	0.1	-0.1	0	0.280	0.308	0.387
	0.2	-0.2	0	0.320	0.600	0.240
(b)	0.001	-0.1	-0.6369	0.332	0.296	0.712
	0.01	-0.1	-0.5541	0.309	0.294	0.654
	0.2	-0.1	0.1648	0.301	0.387	0.292

Part (b) of Table 7.2 gives some examples of the stations being different distances from the ground track. The correlation now is still low enough for Δr and Δn to be well solved for and this is generally true for two stations straddling the ground track at a reasonable distance, say, ~300 kilometres or more.

§ 7.5.3 Three stations observing

The number of 3 station layouts possible is large but a few simple examples are listed in Table 7.3. Part (a) shows two stations ϕ_1 and ϕ_2 fixed at a distance of 0.1 radians (~636 km) on the same side from the ground track with the third station ϕ_3 allowed to move away from the ground track on the other side. As this station moves out, the correlation is reduced as are the rms errors for Δr and Δn.

Table 7.3: Expected correlation and rms errors (m) for Δr, Δc and Δn for three stations observing simultaneously; the distance of the stations to the ground track is given in radians. The standard error σ_0 is taken to be 1 metre.

	ϕ_1	ϕ_2	ϕ_3	corr(Δr,Δn)	$\sigma_{\Delta r}$	$\sigma_{\Delta c}$	$\sigma_{\Delta n}$
(a)	0.1	0.1	-0.001	0.7618	0.331	0.245	0.599
	0.1	0.1	-0.01	0.7137	0.308	0.244	0.552
	0.1	0.1	-0.1	0.3330	0.242	0.251	0.336
	0.1	0.1	-0.2	0.1628	0.241	0.289	0.256
(b)	0.1	-0.1	0.001	0.0056	0.215	0.245	0.388
	0.1	-0.1	0.01	0.0546	0.216	0.244	0.387
	0.1	-0.1	0.1	0.3330	0.242	0.251	0.336
	0.1	-0.1	0.2	0.3960	0.259	0.289	0.278

Part (b) shows two stations ϕ_1 and ϕ_2 straddling the ground track at a distance of 0.1 radians with the third one ϕ_3 allowed to move away from the ground track as before. When ϕ_3 is very near to the ground track, the correlation and $\sigma_{\Delta r}$ are at a minimum and this seems to be the most favourable layout. Note that the third example in part (b) is identical to the third one in part (a).

§ 7.6 Comparison of expected and observed SEASAT short arcs

Three short arcs for SEASAT during its 3 day repeat cycle were analysed during the period 19th to 26th of September 1978 using the SATAN software package and solving for constant orbit errors Δr, Δc and Δn. Launched by NASA on June 16th 1978, SEASAT was one of the first

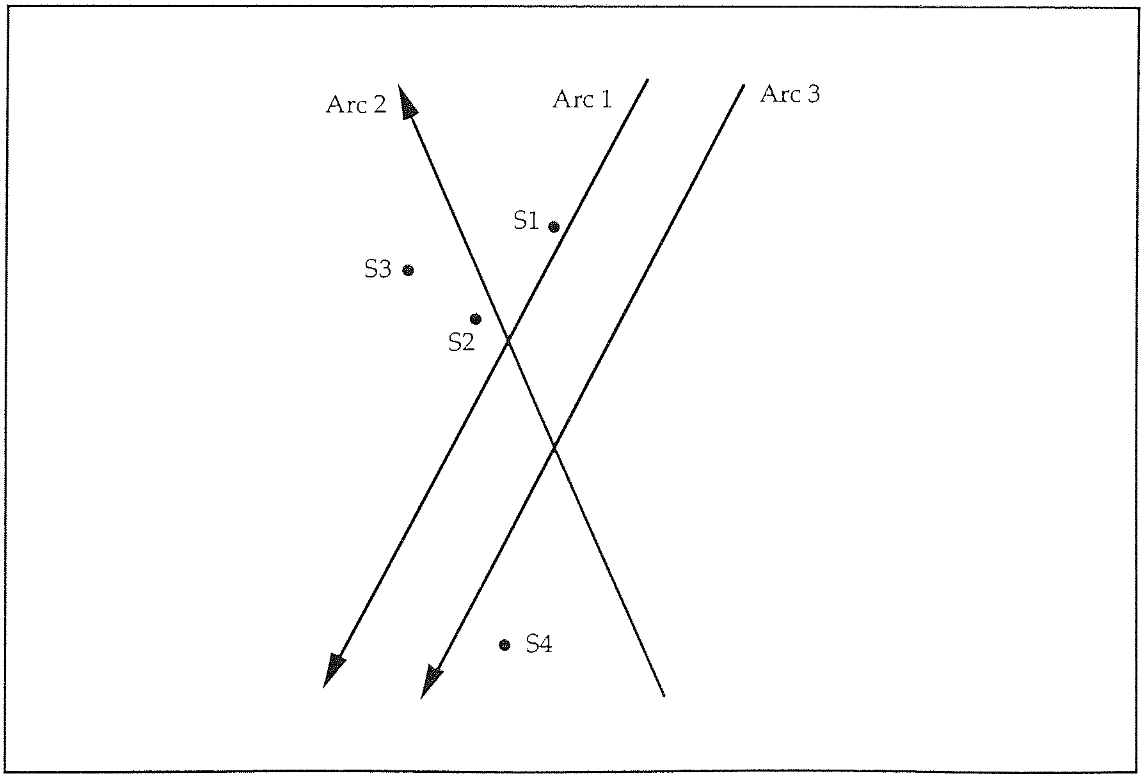

Figure 7.6

satellites dedicated entirely to ocean study and demonstrated the potential of the radar altimeter as a reliable height sensor. A disastrous power failure cut short the mission after a mere 4 months of operation. Figure 7.6 illustrates the 3 ground tracks in relation to the laser sites. Each short arc is ranged by, at most, 3 stations simultaneously.

By omitting one of the stations, a solution involving the other two may be attempted. The laser sites labelled S1 to S4 are detailed in Table 7.5. The times of the first and last observation by each station in each arc are presented in Table 7.4 along with the observation window or duration and the time of closest approach of SEASAT to that station. The base MJD epochs are subtracted from the given times.

Table 7.4: Times of the first and last observation by each laser station and the time of closest approach; all times in days, except duration.

Stations	Time of first observation	Time of last observation	Duration (seconds)	Time of closest approach
Arc 1 (MJD 43770)				
S1	+0.14460	+0.14670	8.6	+0.14410
S3	+0.14450	+0.14666	186.6	+0.14583
S4	+0.15190	+0.15570	328.3	+0.15312
Arc 2 (MJD 43770)				
S1	+0.61006	+0.61343	291.2	+0.61146
S2	+0.60888	+0.61207	275.6	+0.61007
S3	+0.61257	+0.61411	133.1	+0.61181
Arc 3 (MJD 43777)				
S1	+0.14002	+0.14427	367.2	+0.14201
S2	+0.14331	+0.14640	267.0	+0.14444
S4	+0.14860	+0.15442	502.8	+0.15104

Table 7.5: Details of ground laser sites S1 to S4

Label	Station I.D.	Name	Latitude	Longitude
S1	7067	Bermuda Is., USA	32.35	295.34
S2	7068	Grand Turk Is., USA	21.46	288.87
S3	7069	Patrick AFB, USA	28.23	279.39
S4	7907	Arequipa, Peru	-16.46	288.51

§ 7.6.1 Results

The first two sets of results for Arc 1 (in Table 7.6) show a large discrepency between the observed and expected rms errors and this is most likely because station S1 only has a mere 5 observations. The values for the standard error σ_0 are taken from the SATAN results. In practice, if a set of laser observations is well spread along the short arc, then one expects to find the time of closest approach somewhere in the middle of a long observation window. Table 7.4 reveals how the observation window for S1 is very small; moreover the time of closest approach is outside this window. This lack of symmetry plus the small number of actual observations for S1 explains why these results are poor. The result for S2+S3 is good as is the case for all 3 stations, though the latter may be due to some good fortune.

Table 7.6: Arc 1 - observed SEASAT and expected correlations and rms errors (m); observed values are in bold.

Station	**ϕ (rad)**	**Observations**
S1	0.0083	5
S3	0.1986	37
S4	-0.2203	39

Station layout	**corr (Δr,Δn)**	$\sigma_{\Delta r}$	$\sigma_{\Delta c}$	$\sigma_{\Delta n}$
S1 + S3	0.913	0.102	0.067	0.085
	0.973	**0.288**	**0.174**	**0.182**
S1 + S4	0.896	0.170	0.158	0.130
	0.970	**0.384**	**0.170**	**0.269**
S3 + S4	0.047	0.054	0.124	0.039
	0.122	**0.066**	**0.136**	**0.044**
S1 + S3 + S4	0.039	0.057	0.116	0.044
	0.107	**0.075**	**0.127**	**0.050**

Arc 2 has some mixed results (in Table 7.7). The predicted correlation is somewhat low except for the S2+S3 result where the prediction is higher than the observed and the rms errors are poorly estimated. Again from Table 7.4, although S3 has a healthy number of observations, the time of closest approach is outside the period of observation and all the range measurements are skewed to one side. Hence the reason for S1+S2 being the only good result for this arc.

Table 7.7: Arc 2 - observed SEASAT and expected correlations and rms errors (m); observed values are in bold.

Station	**ϕ (rad)**	**Observations**
S1	-0.1603	43
S2	0.0022	45
S3	0.0896	39

Station layout	**corr (Δr,Δn)**	$\sigma_{\Delta r}$	$\sigma_{\Delta c}$	$\sigma_{\Delta n}$
S1 + S2	0.585	0.015	0.015	0.022
	0.726	**0.022**	**0.035**	**0.025**
S1 + S3	0.195	0.027	0.034	0.033
	0.683	**0.050**	**0.070**	**0.046**
S2 + S3	0.649	0.028	0.025	0.069
	0.534	**0.070**	**0.142**	**0.116**
S1 + S2 + S3	0.133	0.029	0.035	0.044
	0.648	**0.054**	**0.089**	**0.058**

In Table 7.8, the results for Arc 3 are by far the best, with the correlations and rms errors all agreeing very well. Referring to Table 7.4 once more, all three stations observe for long periods around the time of closest approach, thus maintaining a high degree of symmetry.

Table 7.8: Arc 3 - observed SEASAT and expected correlations and rms errors (m); observed values are in bold.

Station	ϕ (rad)	Observations
S1	0.1138	45
S2	0.1438	45
S4	-0.0888	45

Station layout	corr $(\Delta r, \Delta n)$	$\sigma_{\Delta r}$	$\sigma_{\Delta c}$	$\sigma_{\Delta n}$
S1 + S2	0.994	0.310	0.041	0.341
	0.993	**0.302**	**0.051**	**0.326**
S1 + S4	0.072	0.107	0.121	0.147
	0.196	**0.112**	**0.123**	**0.150**
S2 + S4	0.129	0.116	0.134	0.140
	0.189	**0.125**	**0.142**	**0.145**
S1 + S2 + S4	0.415	0.090	0.095	0.109
	0.497	**0.096**	**0.101**	**0.113**

§ 7.7 Conclusions

From geometric considerations, an expression for the range residual in terms of the radial, along-track and across-track components has been derived and employed in a least squares solution. The resulting theory permitted an analysis of the expected correlations and rms errors which arise from certain configurations of ground laser stations simultaneously tracking a passing satellite. It was found that for one station, it must be sited as near the ground track as possible. For 2 or 3 stations, there should be one on each side of the ground track at a fair distance from it, say, a few 100 km at least.

A comparison between the theory and actual SEASAT arcs showed good agreement where symmetry was present in the actual observation data and the findings give credence to the theory, which will be extended in the next chapter as preparation for PRARE simulations.

CHAPTER 8

PRARE SIMULATIONS FOR ERS-1

§ 8.1 Introduction

ERS-1 is the first satellite to carry the experimental microwave ranging facility PRARE (Precise Range and Range-rate Equipment). However, soon after the launch, the onboard segment of PRARE suffered fatal radiation damage and consequently no range measurements were ever made with this system. Nevertheless PRARE is due to fly again on a weather satellite, Meteor 3, in early 1994 which will hopefully iron out any problems before its planned launch on ERS-2 in 1994/5.

The key aims of PRARE are to provide accurate range and range-rate measurements at a low cost. The ground segment is designed to be portable enough so that it may be set up in any part of the world and thus provide valuable satellite tracking over the Southern Hemisphere where laser coverage is particularly lacking. Moreover the microwave principle of PRARE means that tracking is possible during most weather conditions, unlike laser ranging.

This chapter investigates the possibility of correcting long arc orbits by non-dynamic short arc methods along distances up to 16,000 km which are well-tracked either by lasers or PRARE. The study begins by extending the analysis in chapter 7 to predict which station configurations will allow a short arc empirical refinement using periodic and quadratic functions in time. Simulations are then carried out for arcs of various lengths and station layout.

§ 8.2 PRARE tracking system

The microwave tracking system PRARE allows precise two-way, dual frequency range and range-rate measurements in almost all weather conditions [Wilmes and Reigber, 1987; ESA, 1992]. The equipment consists of three components; the 'space segment' onboard ERS-1, the 'ground segment' which is the network of ground stations or transponders and the 'control segment' which oversees the control operations and data transfer to and from the spacecraft. The system can range up to 4 ground stations simultaneously.

As ERS-1 flies within range of a ground station, two signals are sent simultaneously to Earth, one in the S-band (2.2 GHz) and the other in X-band (8.5 GHz). The delay in the reception of the two signals at the ground station is noted and this information is retransmitted to the spacecraft for later correction of the ionospheric delay. The X-band signal is then sent back at 7.2 GHz to ERS-1 and the onboard equipment records the time between sending and receiving this signal and from which the range measurement is deduced. Moreover the relative velocity of the spacecraft to the ground station is calculated to yield the range-rate. Signal delay due to the troposphere is corrected for using meteorological data recorded at the ground station at the time of observation.

These measurements are stored onboard the spacecraft; every 2 or 3 days the information is transmitted to the master station where it is decoded, checked and corrected to produce the final product. The resulting range measurements are predicted to have an accuracy of 10 cm but there will be some uncertainty in the precise location of the ground stations whose heights may only be known to, say, 20 or 30 cm during the initial stages of the mission. Moreover the system needs calibrating and the proposed site was to have been at Wettzell.

For all intents and purposes, PRARE ranging may be treated as laser tracking data, the key difference being that laser tracking is 'ground to satellite to ground' whereas PRARE is 'satellite to ground to satellite'. The simulations carried out later in this chapter are therefore equally valid for laser stations as well as PRARE.

§ 8.3 Corrections as functions of time

In section 7.4 the radial, along-track and across-track components, denoted by Δr, Δc and Δn respectively, are assumed constant and therefore invariant with time along the short arc. This is a fair assumption if the short arc is brief, say, a few 100 km. For longer distances in the order of a few 1000 km, it is necessary to allow these components to vary with time and use periodic or quadratic functions as outlined in section 7.2. Mathematically the periodic corrections are expressed as

$$\begin{aligned} \Delta r &= r_0 \cos \omega t + r_1 \sin \omega t \\ \Delta c &= c_0 \cos \omega t + c_1 \sin \omega t \\ \Delta n &= n_0 \cos \omega t + n_1 \sin \omega t \end{aligned} \tag{8.1}$$

where the coefficients are constant, ω is the orbital frequency and t is the time taken from the midpoint of the arc. For small t, these corrections are approximately linear. The quadratic corrections are written as

$$\begin{aligned} \Delta r &= r_0 + r_1 t + r_2 t^2 \\ \Delta c &= c_0 + c_1 t + c_2 t^2 \\ \Delta n &= n_0 + n_1 t + n_2 t^2 \end{aligned} \tag{8.2}$$

where again the coefficients are constant and t is the time taken from the midpoint of the arc.

Upon substituting equations 8.1 into 7.6 and differentiating equation 7.10 partially with respect to the six parameters in a least squares manner (unit weights assumed), the 6x6 normal matrix in partitioned form

$$N^P = \begin{pmatrix} [N \cos^2\omega t] & [N \sin\omega t \cos\omega t] \\ [N \sin\omega t \cos\omega t] & [N \sin^2\omega t] \end{pmatrix} \tag{8.3}$$

is obtained where the block [N $\cos^2\omega t$] (and similarly for the others) is a 3x3 submatrix whose elements are

$$[\,(N \cos^2\omega t)_{rs}\,] = \sum_{obs}\left(A_r\, A_s \cos^2\omega t\right), \qquad 1 \leq r, s \leq 3 \tag{8.4}$$

and the functions A are defined by equation 7.11. The solution vector $\underline{x}$ is taken to be $(r_0, c_0, n_0, r_1, c_1, n_1)^T$.

Repeating for equations 8.2, the 9x9 normal matrix in partitioned form

$$N^Q = \begin{pmatrix} [N] & [Nt] & [Nt^2] \\ [Nt] & [Nt^2] & [Nt^3] \\ [Nt^2] & [Nt^3] & [Nt^4] \end{pmatrix} \tag{8.5}$$

is obtained where again each of the blocks are 3x3 submatrices as described by equation 8.4 and $\underline{x}$ is taken to be $(r_0, c_0, n_0, r_1, c_1, n_1, r_2, c_2, n_2)^T$. The correlation between any two solve-for parameters x_i and x_j is

$$\mathrm{corr}(x_i, x_j) = \frac{N_{ij}^{-1}}{\sqrt{N_{ii}^{-1}\, N_{jj}^{-1}}} \tag{8.6}$$

where N^{-1} is the covariance matrix, i.e. the inverse of any particular normal matrix N. The computed rms errors for the periodic solution are

$$\sigma_{\Delta r}^2 = \sigma_0^2 \left(N_{11}^{-1} \cos^2\omega t + N_{44}^{-1} \sin^2\omega t + 2\, N_{14}^{-1} \sin\omega t \cos\omega t \right)$$

$$\sigma_{\Delta c}^2 = \sigma_0^2 \left(N_{22}^{-1} \cos^2\omega t + N_{55}^{-1} \sin^2\omega t + 2\, N_{25}^{-1} \sin\omega t \cos\omega t \right)$$

$$\sigma_{\Delta n}^2 = \sigma_0^2 \left(N_{33}^{-1} \cos^2\omega t + N_{66}^{-1} \sin^2\omega t + 2\, N_{36}^{-1} \sin\omega t \cos\omega t \right) \tag{8.7}$$

and for the quadratic solution

$$\sigma_{\Delta r}^2 = \sigma_0^2 \left\{ N_{11}^{-1} + N_{44}^{-1} t^2 + N_{77}^{-1} t^4 + 2 \left(N_{14}^{-1} t + N_{17}^{-1} t^2 + N_{47}^{-1} t^3 \right) \right\}$$

$$\sigma_{\Delta c}^2 = \sigma_0^2 \left\{ N_{22}^{-1} + N_{55}^{-1} t^2 + N_{88}^{-1} t^4 + 2 \left(N_{25}^{-1} t + N_{28}^{-1} t^2 + N_{58}^{-1} t^3 \right) \right\}$$

$$\sigma_{\Delta n}^2 = \sigma_0^2 \left\{ N_{33}^{-1} + N_{66}^{-1} t^2 + N_{99}^{-1} t^4 + 2 \left(N_{36}^{-1} t + N_{39}^{-1} t^2 + N_{69}^{-1} t^3 \right) \right\} . \tag{8.8}$$

The standard error σ_0 is assumed to be defined by equation 7.22.

§ 8.4 Expected correlations and errors for certain station configurations

As for section 7.5 in which constant orbit errors are assumed, computer software was written to construct the normal matrices for periodic and quadratic orbit errors given a particular station layout. These matrices are then inverted and the correlations and rms errors calculated from the above definitions. A standard error of 1 metre is used and a nominal number of 15 pseudo range observations (to 15° elevation) allotted to each station.

It is pertinent to note that for the results in section 7.5, the definition of where a station is along the ground track relative to another was not an issue because the orbit errors were assumed constant. For the study here, 'time' is measured as an angle from the midpoint of the short arc. Figure 8.1 shows how the angle between the satellite and the midpoint of the arc varies along the ground track as it passes stations S1 and S2. The angles ϕ and $\Delta\lambda$ are taken here as defined in section 7.3.

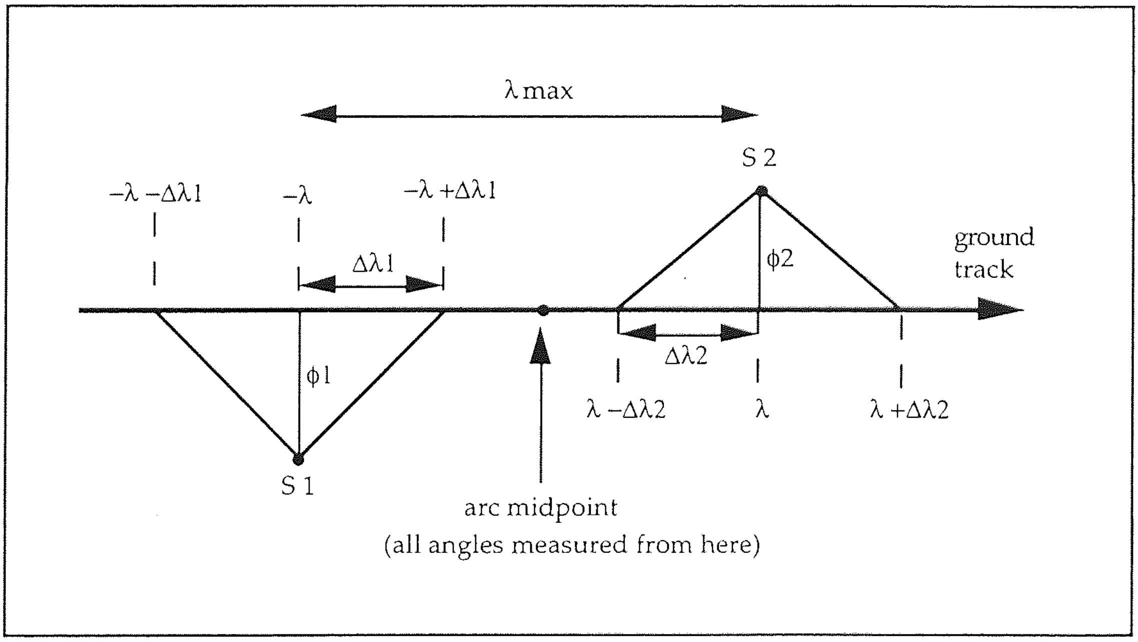

Figure 8.1

Each station is now defined by two parameters, ϕ and λ. For station S1, the satellite moves from $-\Delta\lambda 1$ from its point of closest approach through to $+\Delta\lambda 1$ and if station S1 is $-\lambda$ from the arc midpoint (the minus sign denotes the station is before the midpoint) then the angle between the satellite and the arc midpoint is $-\lambda \pm \Delta\lambda 1$. This angle is equal to ωt and proportional to time t. For the quadratic case, time t is taken to be exactly the angle ωt in radians which is reasonable as the elements of the normal matrix before and after inversion are of the same magnitude.

Table 8.1 lists the correlations and rms errors for a simple 2 station layout. The angle ϕ of 0.1 radians is equivalent to about 640 km. The arc length λmax is also in radians and is the distance between stations S1 and S2 along the ground track. S1 is therefore taken to be -λmax/2 from the arc midpoint and S2 λmax/2 from the same point.

Table 8.1: Expected correlation and rms errors (m) for Δr, Δc and Δn for two stations observing; the length of the arc and the distance of the station to the ground track is given in radians. The standard error is taken to be 1 metre. The rms errors are quoted at the arc midpoint.

Periodic						
λ max	ϕ_1	ϕ_2	Max corr	$\sigma_{\Delta r}$	$\sigma_{\Delta c}$	$\sigma_{\Delta n}$
0.5	0.1	-0.1	0.9979	1.013	2.692	6.217
1.0	0.1	-0.1	0.9979	3.830	1.719	6.966
Quadratic						
λ max	ϕ_1	ϕ_2	Max corr	$\sigma_{\Delta r}$	$\sigma_{\Delta c}$	$\sigma_{\Delta n}$
0.5	0.1	-0.1	1.0000	1.329	1158.6	2854.1
1.0	0.1	-0.1	1.0000	6.256	1107.9	5200.0

The very high correlations and large rms errors indicate that two stations do not provide sufficient tracking information to determine the orbit errors as periodic or quadratic functions.

Table 8.2 shows the findings for 3 stations observing. Station S1 is taken to be -λmax/2 from the arc midpoint, S2 is at the midpoint and S3 is at λmax/2.

Table 8.2: Expected correlation and rms errors (m) for Δr, Δc and Δn for three stations observing; the length of the arc and the distance of the station to the ground track is given in radians. The standard error is taken to be 1 metre. The rms errors are quoted at the arc midpoint.

Periodic							
λ max	ϕ_1	ϕ_2	ϕ_3	Max corr	$\sigma_{\Delta r}$	$\sigma_{\Delta c}$	$\sigma_{\Delta n}$
0.5	0.1	-0.1	0.1	0.8611	0.279	0.360	0.342
0.5	0.1	0.001	-0.1	0.9972	0.297	2.244	5.356
1.0	0.1	-0.1	0.1	0.9582	0.263	0.361	0.355
1.0	0.1	0.001	-0.1	0.9967	0.326	1.225	5.504
Quadratic							
λ max	ϕ_1	ϕ_2	ϕ_3	Max corr	$\sigma_{\Delta r}$	$\sigma_{\Delta c}$	$\sigma_{\Delta n}$
0.5	0.1	-0.1	0.1	0.9299	0.757	0.466	1.040
0.5	0.1	0.001	-0.1	0.9995	0.342	11.453	30.209
1.0	0.1	-0.1	0.1	0.9934	0.321	0.684	4.859
1.0	0.1	0.001	-0.1	0.9994	0.609	11.376	73.730

From the results it seems that smaller arc lengths of around 0.5 radians (or ~3000 km) are preferable and, in particular, station layouts similar to (a) rather than (b) in Figure 8.2.

The results for 4 stations are presented in Table 8.3 and demonstrate how the extra station can significantly reduce correlations and rms errors. The 4 stations are evenly spaced along the ground track at λmax/3 intervals. The arc length of 1.5 radians represents about ~9500 km so it would seem that arcs of this length are permissible providing there are two well sited (~700 km from the ground track) on both sides of the satellite path. An example with 3 stations on one side and 1 on the other is also included and shows that such a configuration can prove useful.

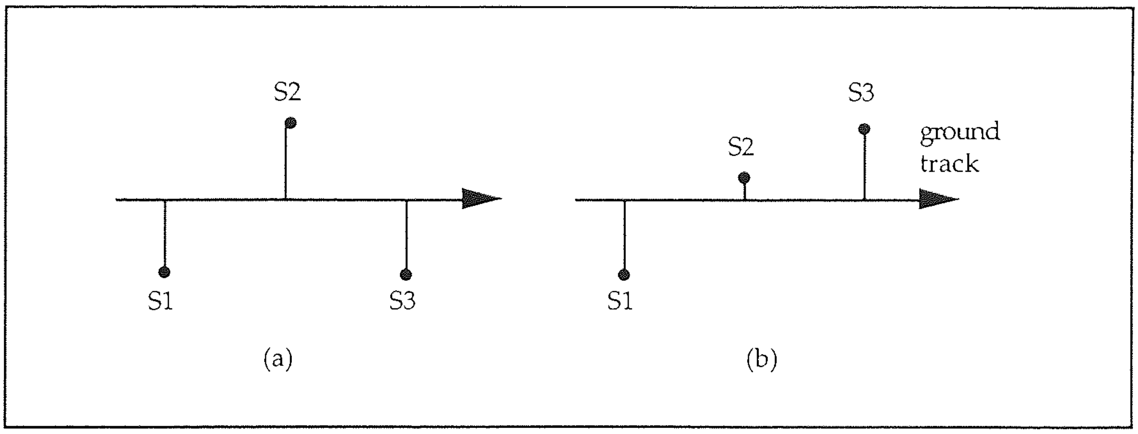

Figure 8.2

Table 8.3: Expected correlation and rms errors (m) for Δr, Δc and Δn for four stations observing; the length of the arc and the distance of the station to the ground track is given in radians. The standard error is taken to be 1 metre. The rms errors are quoted at the arc midpoint.

Periodic								
λ max	ϕ_1	ϕ_2	ϕ_3	ϕ_4	Max corr	$\sigma_{\Delta r}$	$\sigma_{\Delta c}$	$\sigma_{\Delta n}$
1.5	0.1	0.1	-0.1	-0.1	0.8341	0.400	0.281	0.588
1.5	0.1	-0.1	0.1	-0.1	0.2905	0.242	0.259	0.336
1.5	0.1	0.1	-0.1	0.1	0.9762	0.515	0.314	0.731
Quadratic								
λ max	ϕ_1	ϕ_2	ϕ_3	ϕ_4	Max corr	$\sigma_{\Delta r}$	$\sigma_{\Delta c}$	$\sigma_{\Delta n}$
1.5	0.1	0.1	-0.1	-0.1	0.9852	0.616	0.483	1.291
1.5	0.1	-0.1	0.1	-0.1	0.9738	0.672	0.582	1.007
1.5	0.1	0.1	-0.1	0.1	0.9931	0.602	0.436	0.835

To conclude, it is found by theoretical means that orbit errors may be modelled as periodic and quadratic functions in time providing there are at least 3 stations observing the satellite simultaneously. Correlations in excess of 0.999 may prove too high for a reliable solution. The correlations for the periodic method are lower than for the quadratic one because there are only 6 parameters to solve for as opposed to 9 for the latter method. For 3 stations a layout such as Figure 8.2a is preferred in order to minimise correlations and rms errors. Moreover any reasonable 4 station configuration should permit a full set of parameters to be solved for reliably.

§ 8.5 PRARE Simulations

Short arcs in the Southern Hemisphere are of particular interest to oceanographers and PRARE provides the opportunity to refine orbits over these parts of the world. The objective is to obtain an orbit trajectory where the radial component is of comparable accuracy with the corrected altimeter measurement, i.e. better than 10 cm.

§ 8.5.1 Selected simulation arc

The arc selected for the simulation is depicted in Figure 8.3. It is a descending arc travelling over the North Atlantic ocean and down to seas around the Drake Passage. Along this path, the satellite is tracked by a number of proposed PRARE ground stations. Figure 8.4 gives a more schematic view of the arc and the stations; the distance of the stations to the ground track is exaggerated for clarity.

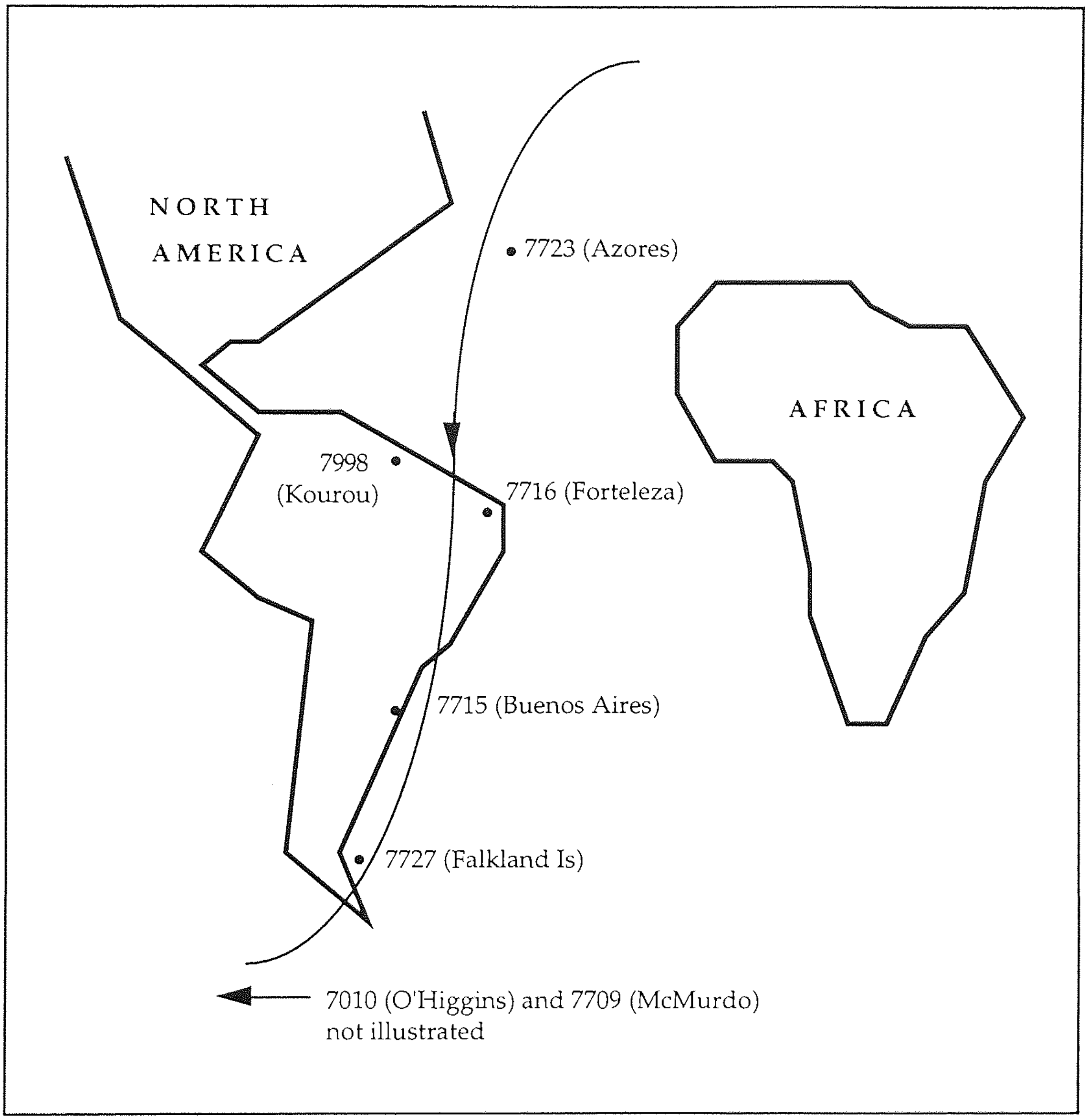

Figure 8.3

A simulated ERS-1 start vector with the rather arbitrary date MJD 43742 was used and is about 16,000 km in length between the two extreme stations 7723 and 7709 (McMurdo is on the coast of Antarctica). Table 8.4 presents details about the stations. The definition of 'short arc' as used here refers to the section of ground track between the closest approach points of the two end stations. The base epoch of MJD 43742 are subtracted from the times in Table 8.4.

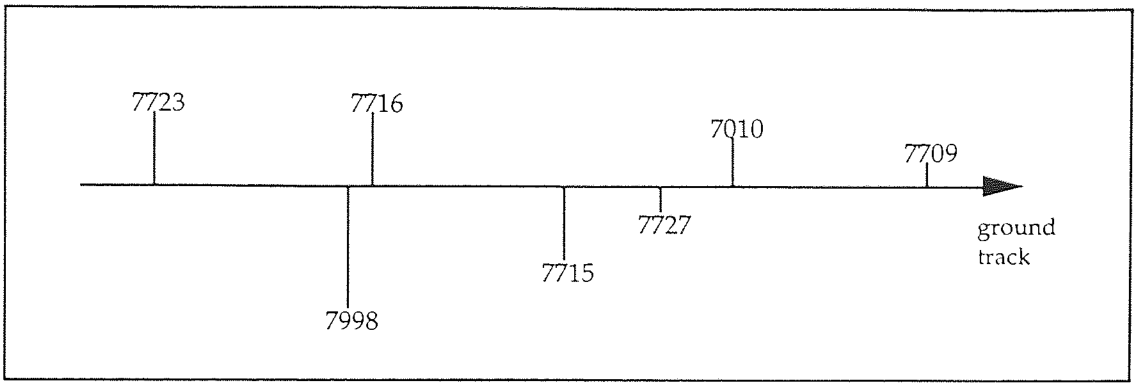

Figure 8.4

Table 8.4: Simulated PRARE ground station details; includes distance and time of stations to closest approach (C/A) point on arc and the distance between one station the the next.

Station	Name	Obs	C/A dist (km)	Dist to next station (km)	C/A Time (days)
7723	Azores	28	495	4220	0.38472
7998	Kourou	18	1200	600	0.39201
7716	Forteleza	28	545	3800	0.39305
7715	Buenos Aires	26	700	1800	0.39965
7727	Falkland Is	30	65	1200	0.40278
7010	O Higgins	28	305	4210	0.40503
7709	McMurdo	30	125	---	0.41215

Station	Name	Latitude (deg)	Longitude (deg)	Height (m)
7723	Azores	38.65872	332.77657	129.031
7998	Kourou	5.2	307.5	0.0
7716	Forteleza	-3.87751	321.57452	25.507
7715	Buenos Aires	-34.55528	301.26953	33.412
7727	Falkland Is	-51.68761	302.221	32.357
7010	O Higgins	-63.32105	302.09817	68.655
7709	McMurdo	-77.84775	166.67462	-20.222

§ 8.5.2 Simulation method

For the purpose of simulation, a reference long arc orbit with orbit characteristics of ERS-1 was produced using the SATAN software and GEM-T1 gravity field [Marsh et al., 1988] and fitted exactly to sets of pseudo range observations (15 second points down to 20° elevation) for each ground station along the arc. This is treated as the 'true' orbit. In order to obtain realistic rms errors, random noise of ±5 cm was added to these range values to simulate the expected uncertainty of genuine PRARE observations. This noise should not affect the final solution of the orbit correction so long as the noise is truly random.

The GEM-T1 gravity field is now randomly perturbed three times to produce gravity fields A, B and C which will be referred to as 'clones'. These random errors are based on the variances of the GEM-T1 field and are interpreted here to be the present uncertainty of current gravity field models. Employing these clones, three new orbits are generated which need correcting to the true orbit. Table 8.5 lists the rms and maximum errors between the trajectories computed from clones A, B and C with respect to the true orbit along the chosen arc, i.e. between times 0.385 and 0.412.

Table 8.5: Rms and maximum errors in the radial, along-track and across-track directions during the period 0.385 to 0.412; all values in metres

	--- radial ---		--- along-track ---		--- across-track ---	
Field	rms	max	rms	max	rms	max
A	1.12	-1.58	3.86	5.60	0.19	-0.36
B	0.79	1.18	3.04	-4.00	1.39	-1.80
C	0.37	-0.52	1.40	-2.20	0.97	-1.46

Figure 8.5 shows the radial, along-track and across-track orbit error along 1.5 revolutions for the trajectories computed with clones A, B and C.

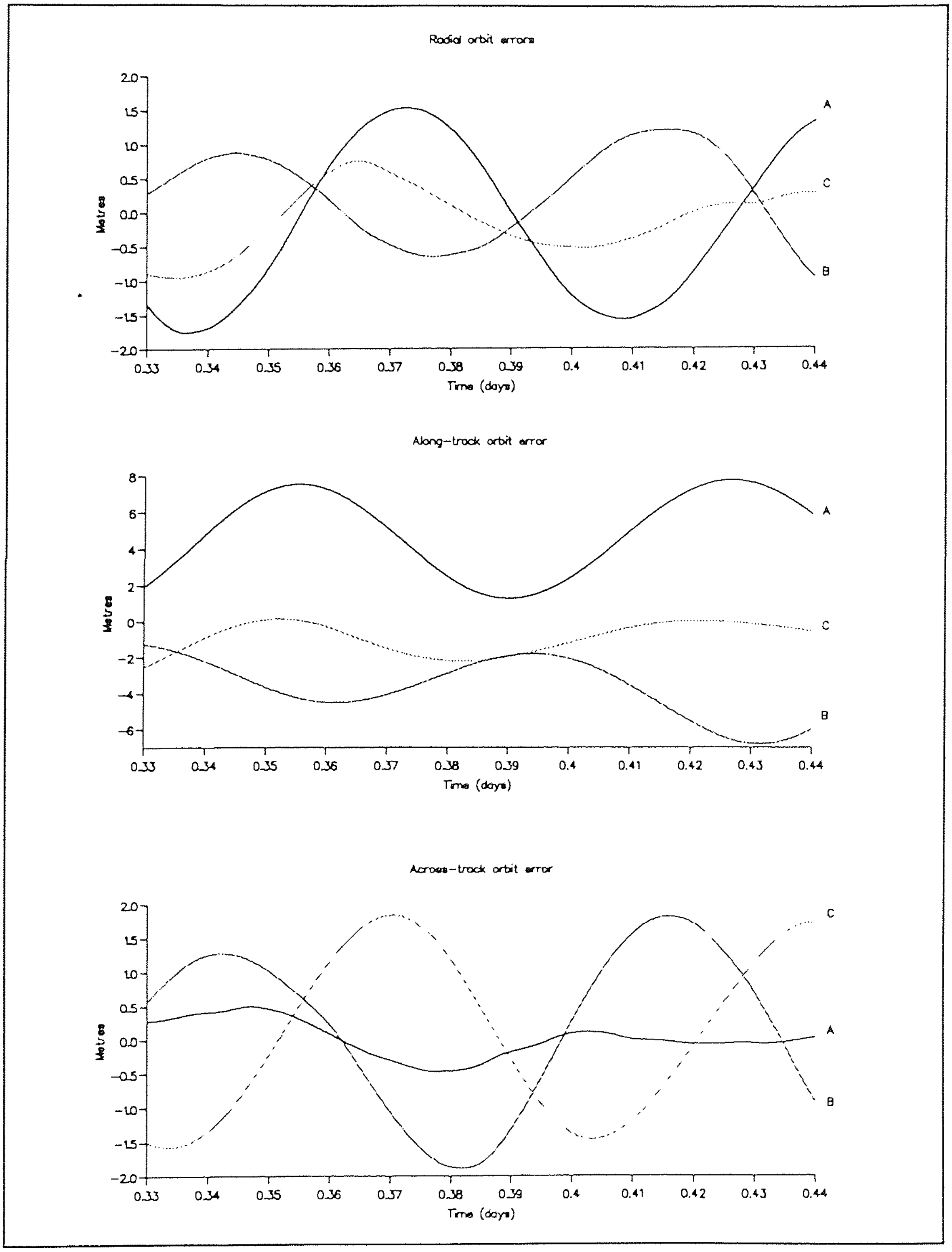

Figure 8.5

A mathematical formulation for the solution of these orbit errors now needs to be derived.

§ 8.5.3 Least squares solution for the orbit errors

Let the radial vector to the satellite be denoted by $\underline{r}$ and its along-track vector by $\underline{v}$. These are easily determined from the computed ephemeris generated by the SATAN software which contain the spacecraft position (x, y, z) as well as the velocities $(\dot{x}, \dot{y}, \dot{z})$. Thus

$$\underline{r} = x\,\underline{i} + y\,\underline{j} + z\,\underline{k} \tag{8.9}$$

and

$$\underline{v} = \dot{x}\,\underline{i} + \dot{y}\,\underline{j} + \dot{z}\,\underline{k}\,. \tag{8.10}$$

The across-track vector may be defined as

$$\underline{n} = \underline{r} \times \underline{v} = n_x\,\underline{i} + n_y\,\underline{j} + n_z\,\underline{k} \tag{8.11}$$

wherein the coefficients are

$$\begin{aligned} n_x &= (y\dot{z} - z\dot{y}) \\ n_y &= (z\dot{x} - x\dot{z}) \\ n_z &= (x\dot{y} - y\dot{x})\,. \end{aligned} \tag{8.12}$$

In addition the range vector is

$$\underline{R} = (x - x_s)\,\underline{i} + (y - y_s)\,\underline{j} + (z - z_s)\,\underline{k} \tag{8.13}$$

where the station coordinates are given by (x_s, y_s, z_s). The length of vector $\underline{r}$ is denoted r and is expressed by

$$r = \sqrt{x^2 + y^2 + z^2} \tag{8.14}$$

with similar definitions for lengths v, n and R.

It is now possible to resolve the range residual ΔR into the radial, along-track and across-track components (Δr, Δc and Δn respectively) by considering the relevant direction cosines, namely

$$\Delta R = \alpha \, \Delta r + \beta \, \Delta c + \gamma \, \Delta n \tag{8.15}$$

where α is the cosine of the angle between $\underline{R}$ and $\underline{r}$, β the cosine of the angle between $\underline{R}$ and $\underline{v}$ and γ the cosine of the angle between $\underline{R}$ and $\underline{n}$. These cosines are derived simply from the dot product definition and thus

$$\Delta R = (\hat{\underline{R}} . \hat{\underline{r}}) \, \Delta r + (\hat{\underline{R}} . \hat{\underline{v}}) \, \Delta c + (\hat{\underline{R}} . \hat{\underline{n}}) \, \Delta n \tag{8.16}$$

wherein the ^ symbol denotes the unit vector.

The technique to solve for periodic and quadratic orbit errors is similar to that detailed in section 7.4 and involves the minimisation of the function (unit weights assumed)

$$I = \sum_{i=1}^{M} \left(\Delta R_i^{ob} - \Delta R_i \right)^2 \tag{8.17}$$

where $\Delta R_i^{ob} = R_i^{ob} - R_i^{cal}$, i.e. the 'observed' pseudo range minus the computed range from a long arc orbit (using perturbed gravity fields A, B or C) and M is the number of acceptable observations. Minimising I with respect to some parameter p_j yields

$$\frac{\partial I}{\partial p_j} = -2 \sum_{i=1}^{M} \left(\Delta R_i^{ob} - \Delta R_i \right) \left(\frac{\partial \Delta R_i}{\partial p_j} \right) = 0 \tag{8.18}$$

If the the orbit errors are assumed constant then the required partial derivatives from equation 8.16 are

$$\frac{\partial \Delta R}{\partial \Delta r} = \hat{\underline{R}} \cdot \hat{\underline{r}} = \left\{ (x - x_s) x + (y - y_s) y + (z - z_s) z \right\} / \ Rr$$

$$\frac{\partial \Delta R}{\partial \Delta c} = \hat{\underline{R}} \cdot \hat{\underline{v}} = \left\{ (x - x_s) \dot{x} + (y - y_s) \dot{y} + (z - z_s) \dot{z} \right\} / \ Rv$$

$$\frac{\partial \Delta R}{\partial \Delta n} = \hat{\underline{R}} \cdot \hat{\underline{n}} = \left\{ (x - x_s) n_x + (y - y_s) n_y + (z - z_s) n_z \right\} / \ Rn. \quad (8.19)$$

On substituting the periodic functions proposed by equation 8.1 into equation 8.16 and using the definitions in equations 8.19, the required partials for the periodic solution are

$$\frac{\partial \Delta R_i}{\partial r_0} = \frac{\partial \Delta R}{\partial \Delta r} \cos \omega t_i, \quad \frac{\partial \Delta R_i}{\partial c_0} = \frac{\partial \Delta R}{\partial \Delta c} \cos \omega t_i, \quad \frac{\partial \Delta R_i}{\partial n_0} = \frac{\partial \Delta R}{\partial \Delta n} \cos \omega t_i$$

$$\frac{\partial \Delta R_i}{\partial r_1} = \frac{\partial \Delta R}{\partial \Delta r} \sin \omega t_i, \quad \frac{\partial \Delta R_i}{\partial c_1} = \frac{\partial \Delta R}{\partial \Delta c} \sin \omega t_i, \quad \frac{\partial \Delta R_i}{\partial n_1} = \frac{\partial \Delta R}{\partial \Delta n} \sin \omega t_i \quad (8.20)$$

and similarly the partials for the quadratic solution from equation 8.2 are

$$\frac{\partial \Delta R_i}{\partial r_0} = \frac{\partial \Delta R}{\partial \Delta r}, \quad \frac{\partial \Delta R_i}{\partial c_0} = \frac{\partial \Delta R}{\partial \Delta c}, \quad \frac{\partial \Delta R_i}{\partial n_0} = \frac{\partial \Delta R}{\partial \Delta n}$$

$$\frac{\partial \Delta R_i}{\partial r_1} = \frac{\partial \Delta R}{\partial \Delta r} t_i, \quad \frac{\partial \Delta R_i}{\partial c_1} = \frac{\partial \Delta R}{\partial \Delta c} t_i, \quad \frac{\partial \Delta R_i}{\partial n_1} = \frac{\partial \Delta R}{\partial \Delta n} t_i$$

$$\frac{\partial \Delta R_i}{\partial r_2} = \frac{\partial \Delta R}{\partial \Delta r} t_i^2, \quad \frac{\partial \Delta R_i}{\partial c_2} = \frac{\partial \Delta R}{\partial \Delta c} t_i^2, \quad \frac{\partial \Delta R_i}{\partial n_2} = \frac{\partial \Delta R}{\partial \Delta n} t_i^2 . \quad (8.21)$$

where the time t_i is the time of the ith observation from the arc midpoint.

From Figure 8.5, it can be seen that the along-track errors have a constant offset and this needs to be included in the periodic solution using the partial

$$\frac{\partial \Delta R_i}{\partial c_c} = \frac{\partial \Delta R}{\partial \Delta c} \tag{8.22}$$

wherein c_c is the constant in the along-track direction for the periodic correction. The system of equations resulting from the least squares procedure is written in matrix form as $N\underline{x} = \underline{b}$ where the element of N and $\underline{b}$ are

$$N_{jk} = \sum_{i=1}^{M} \left(\frac{\partial \Delta R_i}{\partial p_j}\right)\left(\frac{\partial \Delta R_i}{\partial p_k}\right)$$

$$b_j = \sum_{i=1}^{M} \Delta R_i^{ob} \left(\frac{\partial \Delta R_i}{\partial p_j}\right) \tag{8.23}$$

for $1 \le j,k \le L$ and $\underline{x}$ is the column vector of the L parameters.

Instead of using the geographic midpoint of the arc of a particular station layout, the mean time of all the observations of all the stations included in that configuration is taken as the reference time T_0. This is subtracted from the observation times to derive time t as required in equations 8.1 and 8.2. ERS-1 is assumed to complete 14.333 revolutions in one day and hence has an orbital frequency ω of 90.057 radians per day.

It is a simple procedure to modify the SATAN software to solve for these time dependent corrections since the programs already have code to solve for constant corrections.

§ 8.6 Simulation results

A total of 8 short arcs of varying numbers of ground laser stations and geometry were selected for tests. All 9 parameters as specified in equation 8.2 for the quadratic solution are solved for in all 8 tracks. Concerning the periodic method only a constant bias in the along-track direction was solved for along with the parameters specified in equation 8.1 for tracks 1 to 7 inclusive; however since 5 stations are present for track 8, constants in the radial and across-track directions were also included in the solution. It is emphasised that all the orbital corrections were solved for without any constraints being applied to the normal equation.

§ 8.6.1 Comparison of corrected orbits to the 'true' orbit

For each track, a number of stations were chosen to range the satellite simultaneously. It is therefore the geometry of these stations which is under scrutiny when presented to the perturbed orbits for short arc correction. Details of these tracks are available from Table 8.6 along with the arc length between the closest approach points of the two extreme stations. It is best to refer to Figure 8.4 to see how the stations are laid out with respect to the ground track.

It can be seen from Tables 8.5 and 8.6 as well as Figure 8.5 that the gravity field clones have produced trajectories with rather large orbit errors and hence present a severe test for the short arc correction methods. Long arc orbits computed in chapter 4 reveal how for ERS-1 a laser range fit of around 15 cm rms is possible; similarly a value of around 10 cm rms was observed for TOPEX/POSEIDON. Nevertheless a radial orbit error of around 50 cm may occur over the oceans where there is no laser data to constrain the trajectory. In view of this, it is perhaps the results from clone B or C which have the most relevence for correcting either ERS-1 or TOPEX/POSEIDON orbits using these short arc techniques.

Table 8.6: Details of the 8 short arcs used for simulation tests; the stations involved, the length of the arc and the rms fit (in metres) of the laser ranges before correction are stated.

			--- Gravity Field ---		
Track	Stations	Length(km)	A	B	C
1	7715, 7727, 7010	3000	1.960	1.374	0.820
2	7998, 7716, 7727	6200	1.391	1.241	0.844
3	7716, 7715, 7010	6800	1.592	1.227	0.891
4	7715, 7727, 7010, 7709	7210	2.489	1.725	0.708
5	7723, 7998, 7716, 7715	8620	0.945	1.104	1.105
6	7998, 7716, 7715, 7709	11610	2.086	1.576	0.884
7	7723, 7998, 7715, 7709	15830	2.119	1.630	0.992
8	7723, 7998, 7715, 7010, 7709	15830	2.164	1.618	0.897

The residual radial orbit errors after short arc correction (periodic and quadratic) are depicted graphically for tracks 1 to 8 in Figures 8.6 to 8.13 respectively. The stations involved for each arc are clearly marked at their closest approach times with a ±10 cm error bar.

Considering the results for clone C for the moment, it is clear that both the periodic and quadratic methods perform well by reducing the radial orbit error to within 10 cm, especially for tracks 1 to 5 (up to 8620 km). For the longer arc of track 6, the quadratic has problems towards station 7709. Track 7 (15830 km) proves to be too demanding for either method but when the fifth station 7010 is added, both methods work admirably.

The results for clone B are remarkably similar to clone C with track 6 demonstating more vividly that 4 stations is not enough for a arc length of over 11000 km.

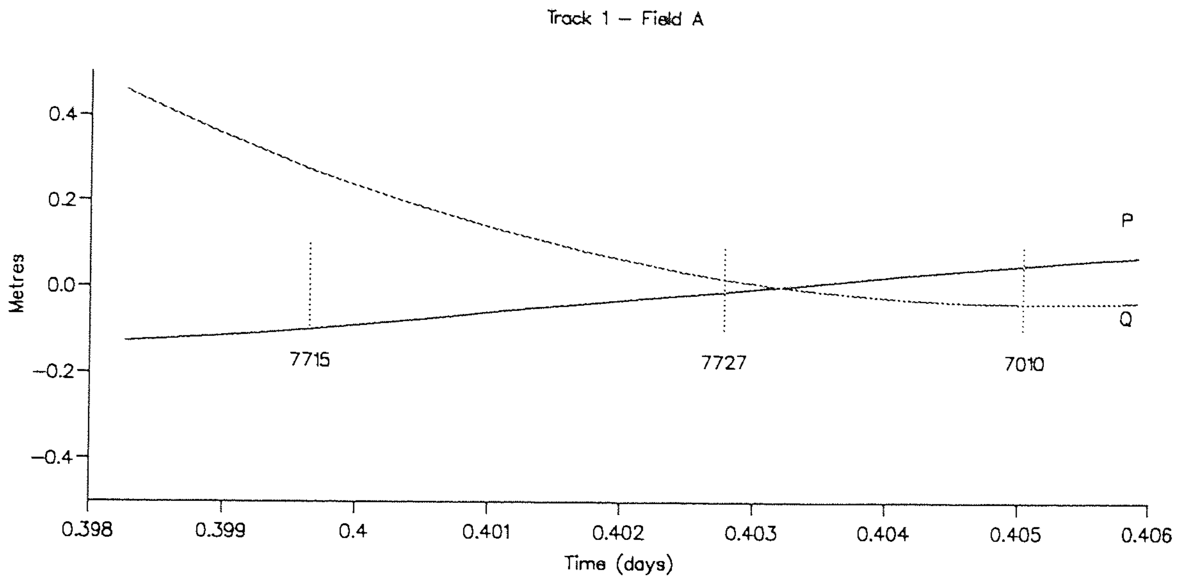
Track 1 – Field A
Metres
0.4
0.2
0.0
–0.2
–0.4
P
Q
7715
7727
7010
0.398
0.399
0.4
0.401
0.402
0.403
0.404
0.405
0.406
Time (days)

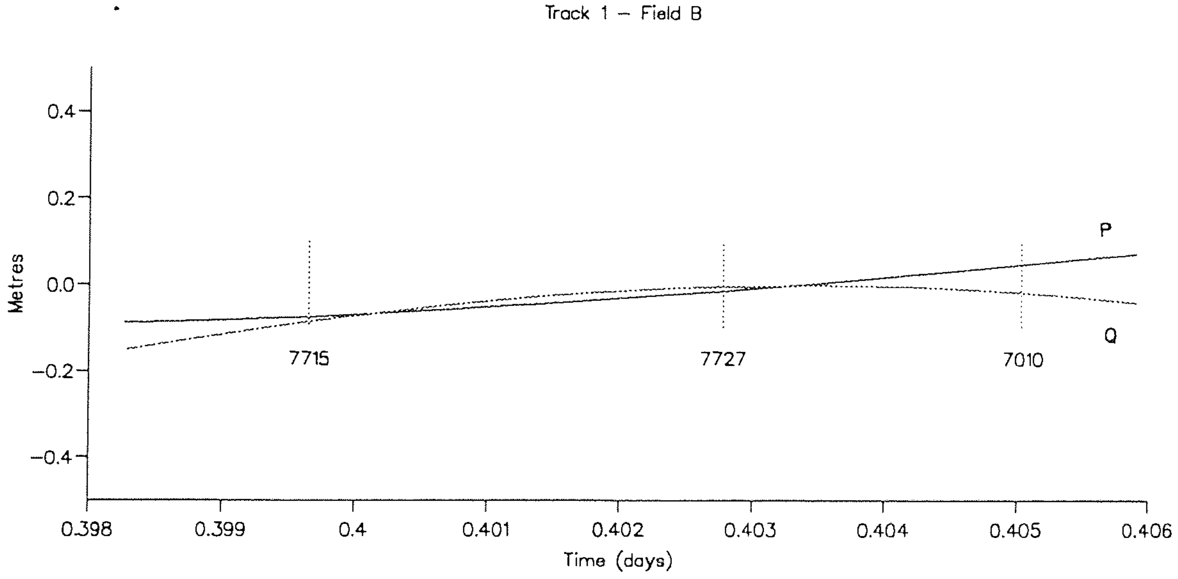
Track 1 – Field B
Metres
0.4
0.2
0.0
–0.2
–0.4
P
Q
7715
7727
7010
0.398
0.399
0.4
0.401
0.402
0.403
0.404
0.405
0.406
Time (days)

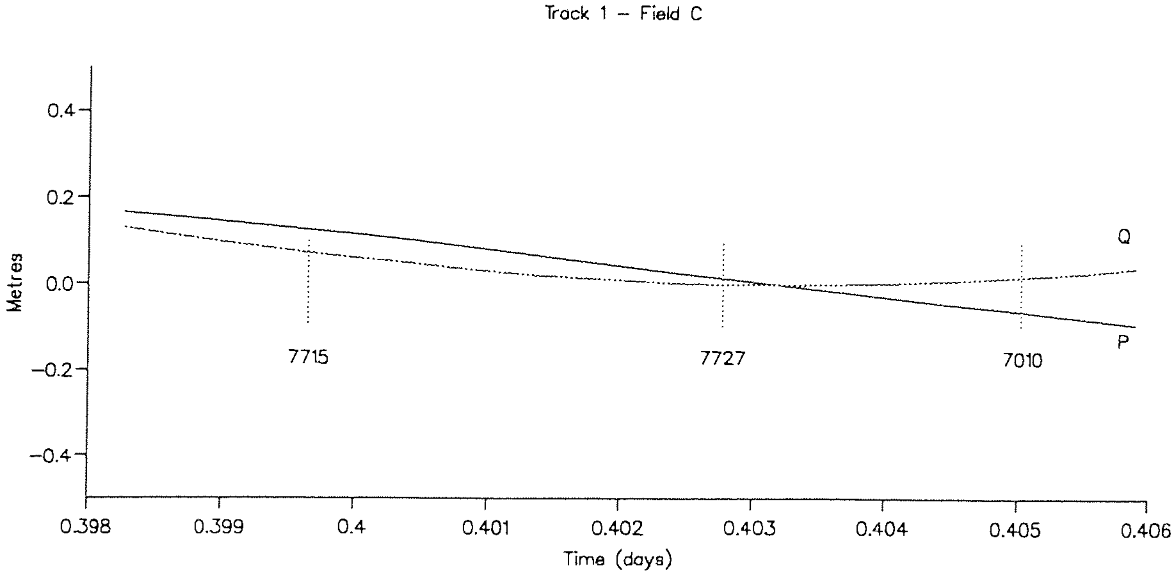
Track 1 – Field C
Metres
0.4
0.2
0.0
–0.2
–0.4
Q
P
7715
7727
7010
0.398
0.399
0.4
0.401
0.402
0.403
0.404
0.405
0.406
Time (days)

Figure 8.6

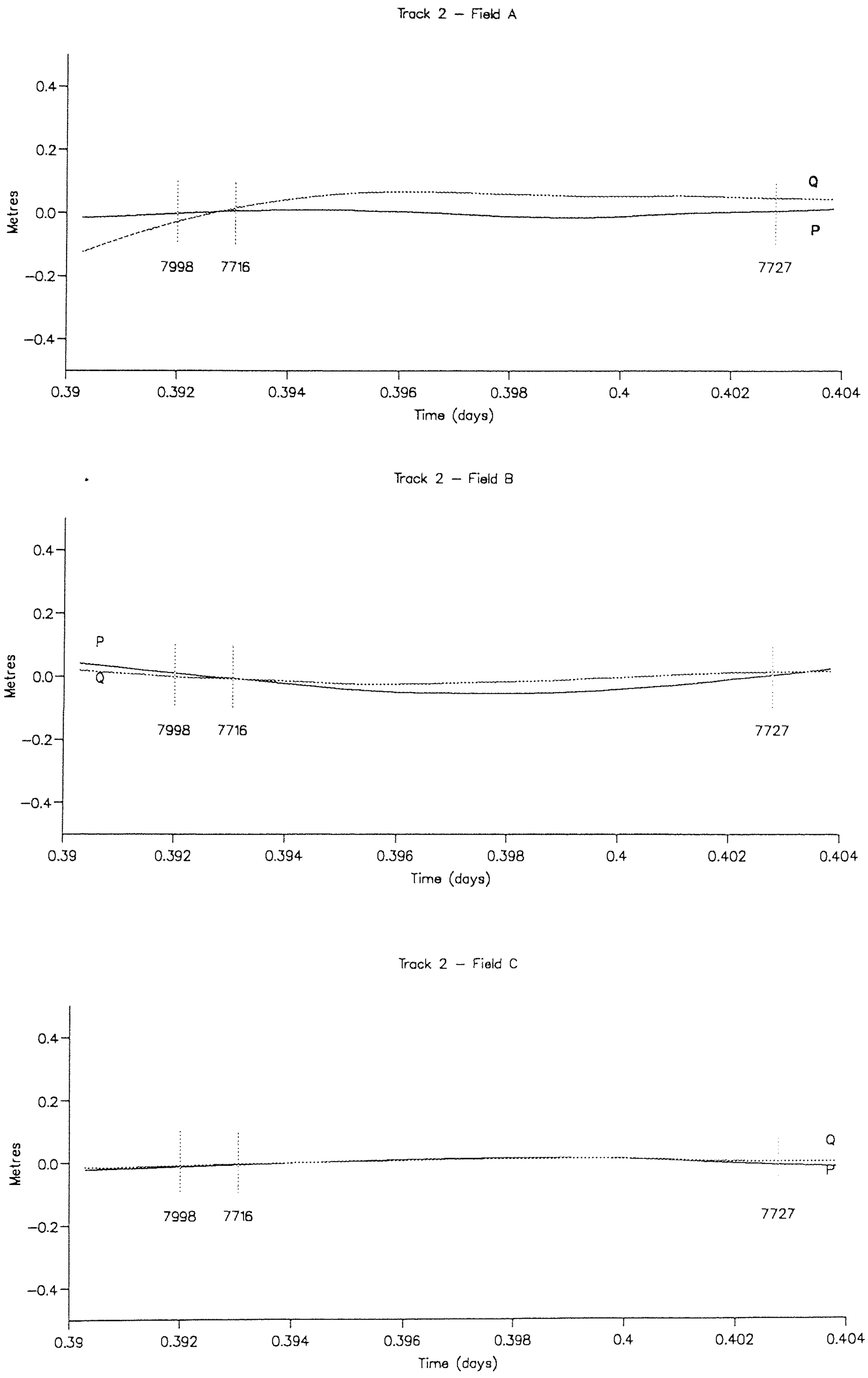
Track 2 — Field A
Metres
0.4
0.2
0.0
−0.2
−0.4
Q
P
7998
7716
7727
0.39
0.392
0.394
0.396
0.398
0.4
0.402
0.404
Time (days)
Track 2 — Field B
Metres
0.4
0.2
0.0
−0.2
−0.4
P
Q
7998
7716
7727
0.39
0.392
0.394
0.396
0.398
0.4
0.402
0.404
Time (days)
Track 2 — Field C
Metres
0.4
0.2
0.0
−0.2
−0.4
Q
P
7998
7716
7727
0.39
0.392
0.394
0.396
0.398
0.4
0.402
0.404
Time (days)

Figure 8.7

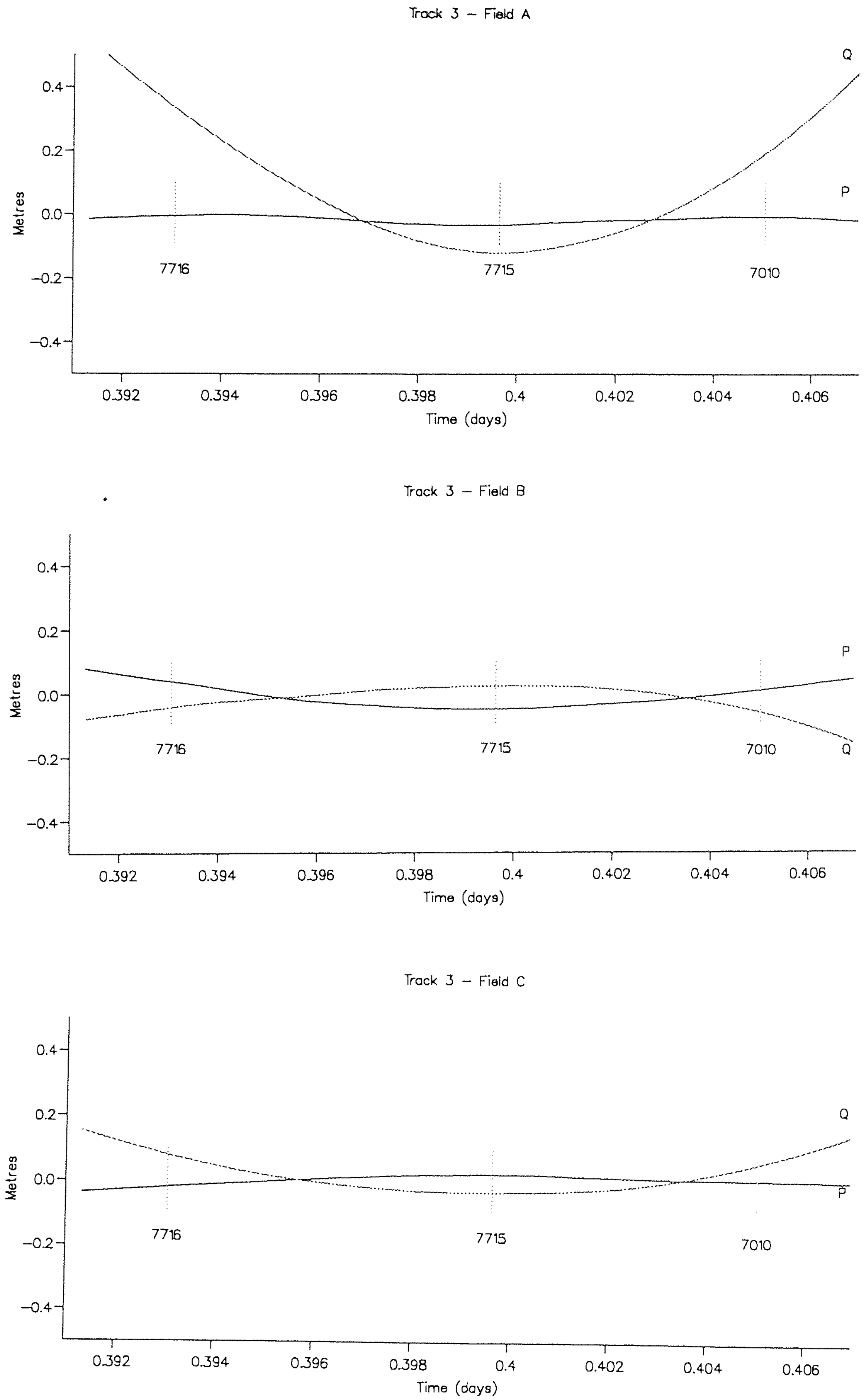
Track 3 – Field A
Track 3 – Field B
Track 3 – Field C
Metres
Time (days)
0.4
0.2
0.0
–0.2
–0.4
0.392
0.394
0.396
0.398
0.4
0.402
0.404
0.406
P
Q
7716
7715
7010

Figure 8.8

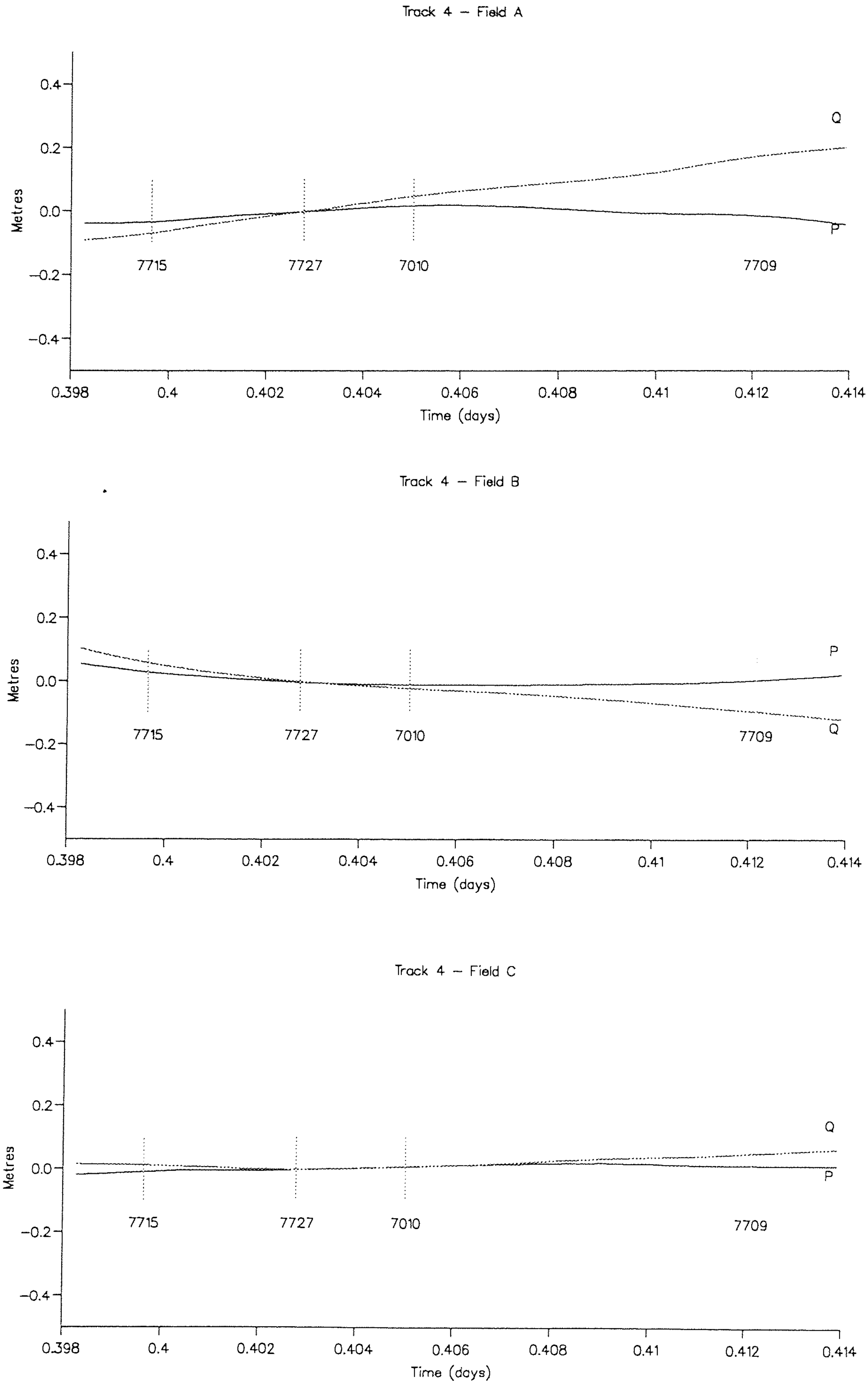
Track 4 — Field A
Metres
0.4
0.2
0.0
−0.2
−0.4
Q
P
7715
7727
7010
7709
0.398
0.4
0.402
0.404
0.406
0.408
0.41
0.412
0.414
Time (days)
Track 4 — Field B
Metres
0.4
0.2
0.0
−0.2
−0.4
P
Q
7715
7727
7010
7709
0.398
0.4
0.402
0.404
0.406
0.408
0.41
0.412
0.414
Time (days)
Track 4 — Field C
Metres
0.4
0.2
0.0
−0.2
−0.4
Q
P
7715
7727
7010
7709
0.398
0.4
0.402
0.404
0.406
0.408
0.41
0.412
0.414
Time (days)

Figure 8.9

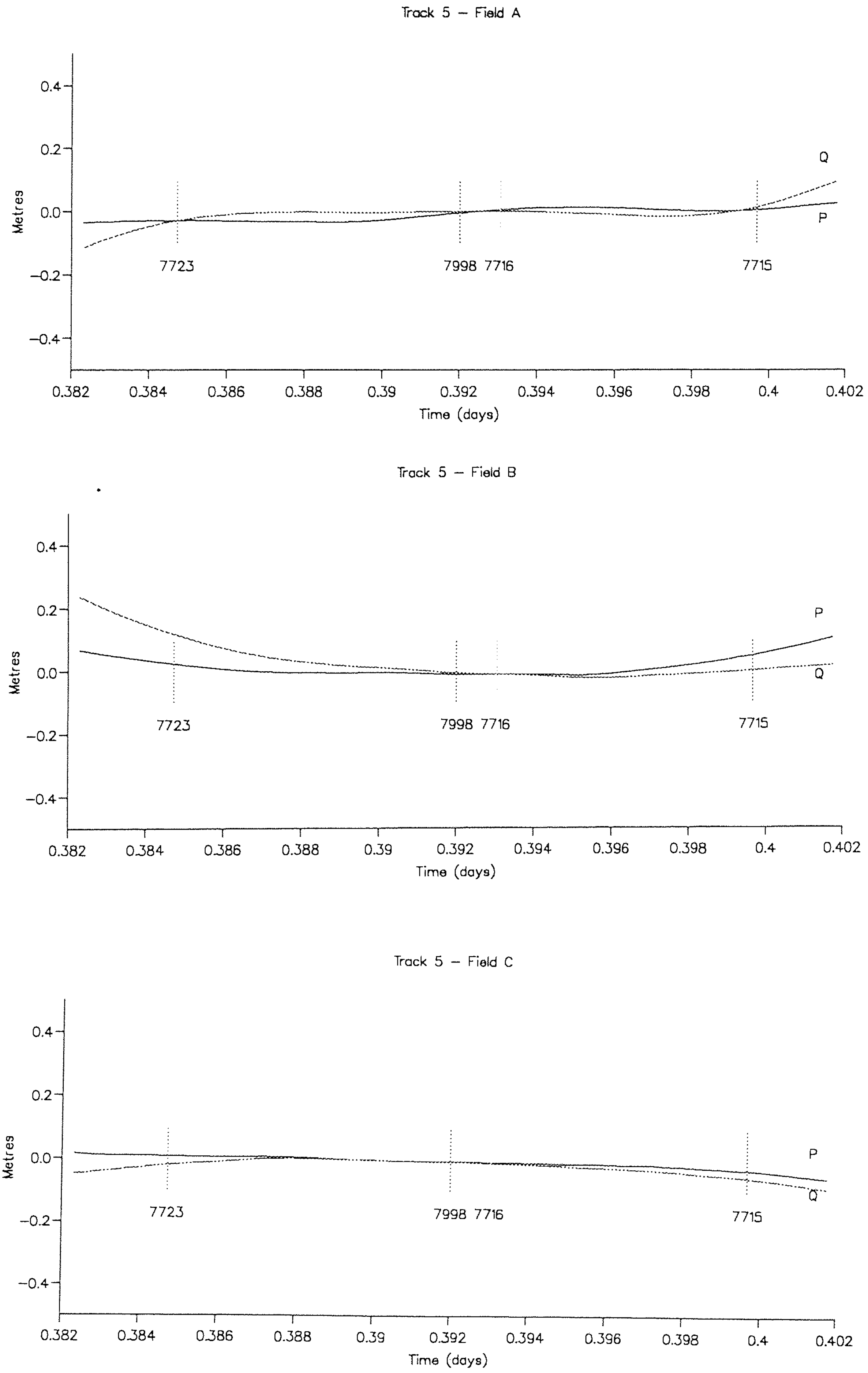
Track 5 – Field A
Metres
0.4
0.2
0.0
−0.2
−0.4
Q
P
7723
7998 7716
7715
0.382
0.384
0.386
0.388
0.39
0.392
0.394
0.396
0.398
0.4
0.402
Time (days)
Track 5 – Field B
Metres
0.4
0.2
0.0
−0.2
−0.4
P
Q
7723
7998 7716
7715
0.382
0.384
0.386
0.388
0.39
0.392
0.394
0.396
0.398
0.4
0.402
Time (days)
Track 5 – Field C
Metres
0.4
0.2
0.0
−0.2
−0.4
P
Q
7723
7998 7716
7715
0.382
0.384
0.386
0.388
0.39
0.392
0.394
0.396
0.398
0.4
0.402
Time (days)

Figure 8.10

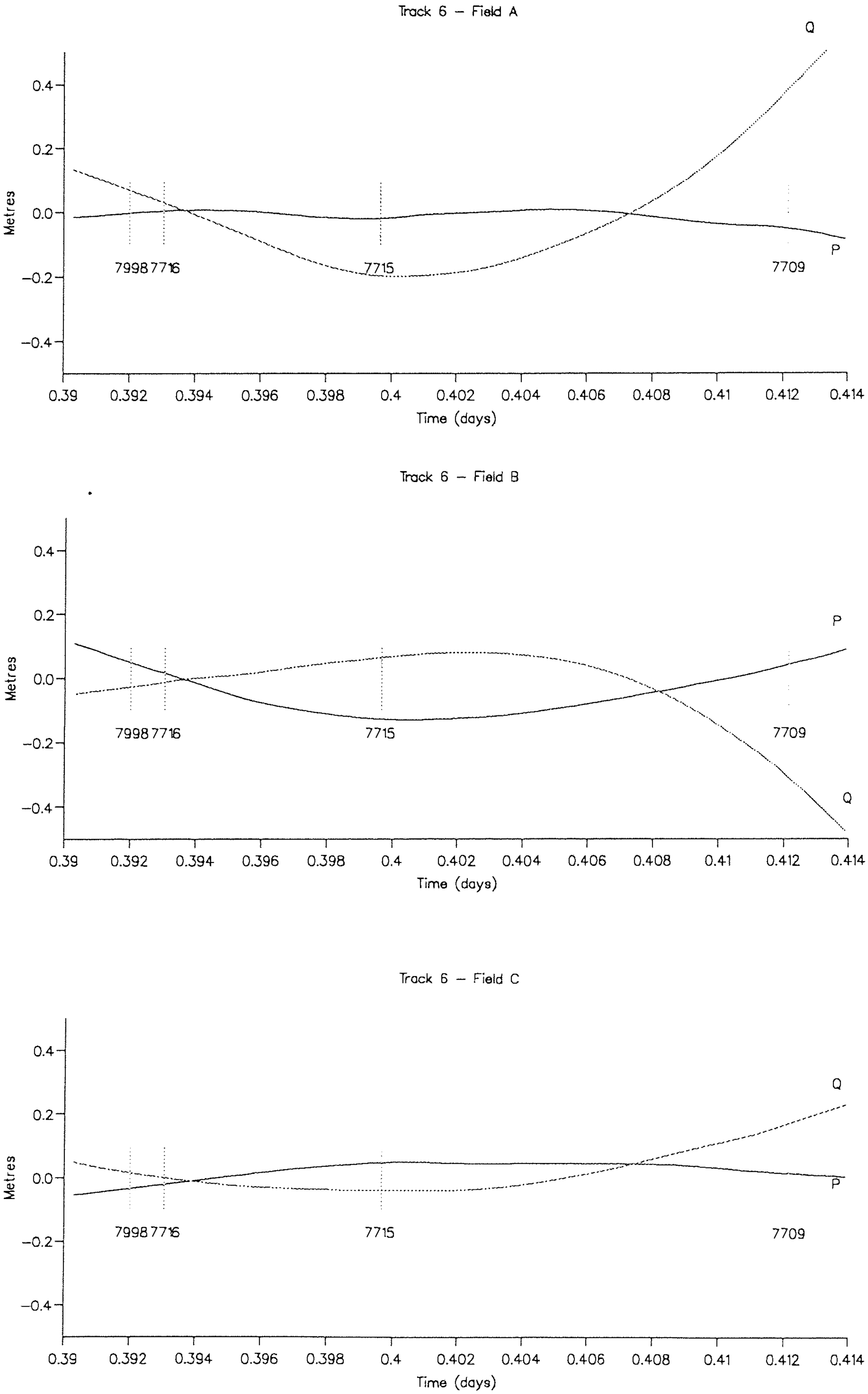
Track 6 – Field A
Q
P
0.4
0.2
0.0
−0.2
−0.4
Metres
7998
7716
7715
7709
0.39
0.392
0.394
0.396
0.398
0.4
0.402
0.404
0.406
0.408
0.41
0.412
0.414
Time (days)
Track 6 – Field B
P
Q
0.4
0.2
0.0
−0.2
−0.4
Metres
7998
7716
7715
7709
0.39
0.392
0.394
0.396
0.398
0.4
0.402
0.404
0.406
0.408
0.41
0.412
0.414
Time (days)
Track 6 – Field C
Q
P
0.4
0.2
0.0
−0.2
−0.4
Metres
7998
7716
7715
7709
0.39
0.392
0.394
0.396
0.398
0.4
0.402
0.404
0.406
0.408
0.41
0.412
0.414
Time (days)

Figure 8.11

Track 7 — Field A

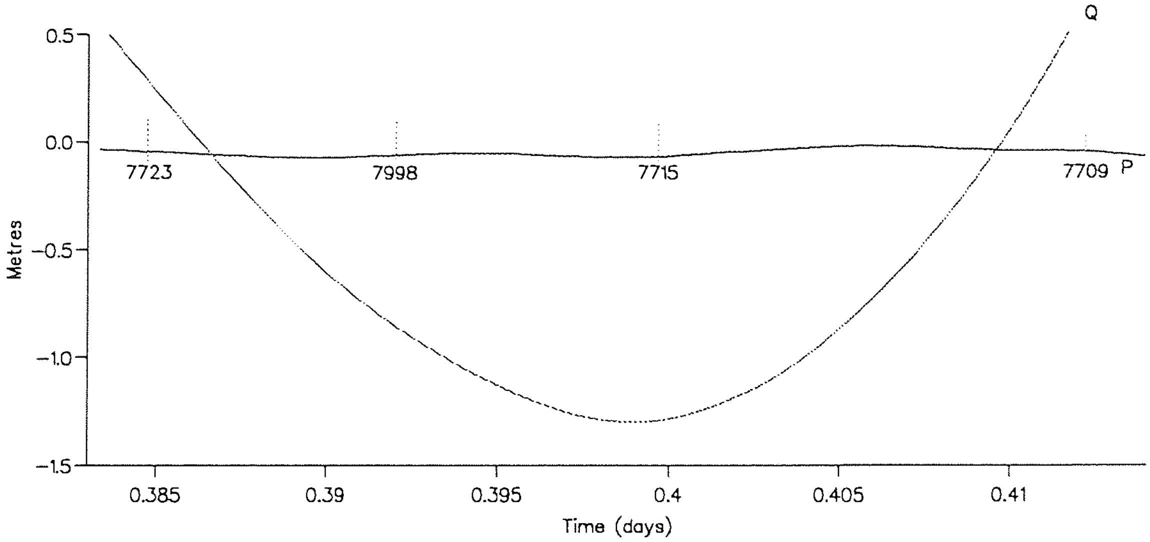

Track 7 — Field B

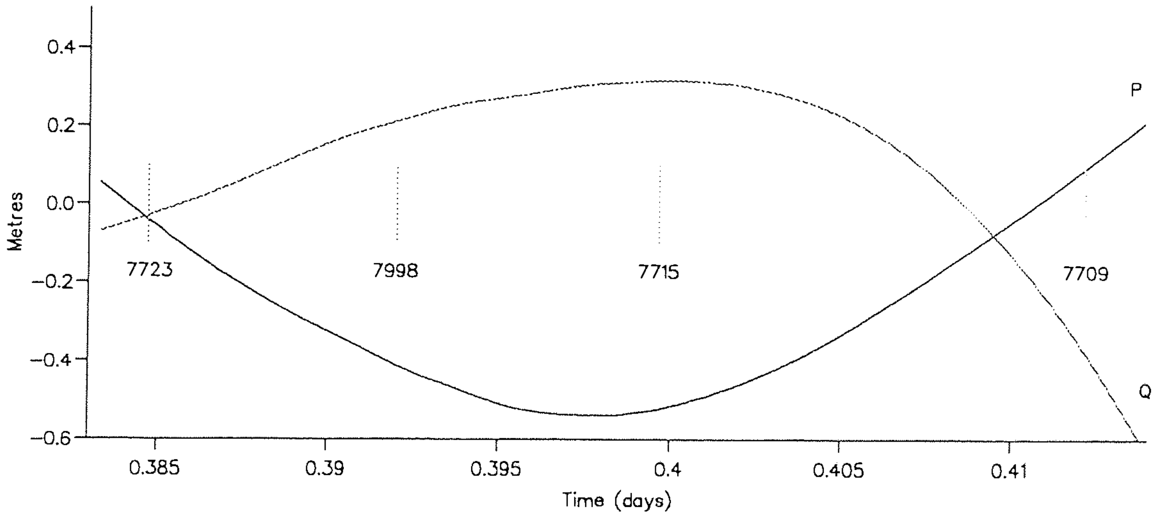

Track 7 — Field C

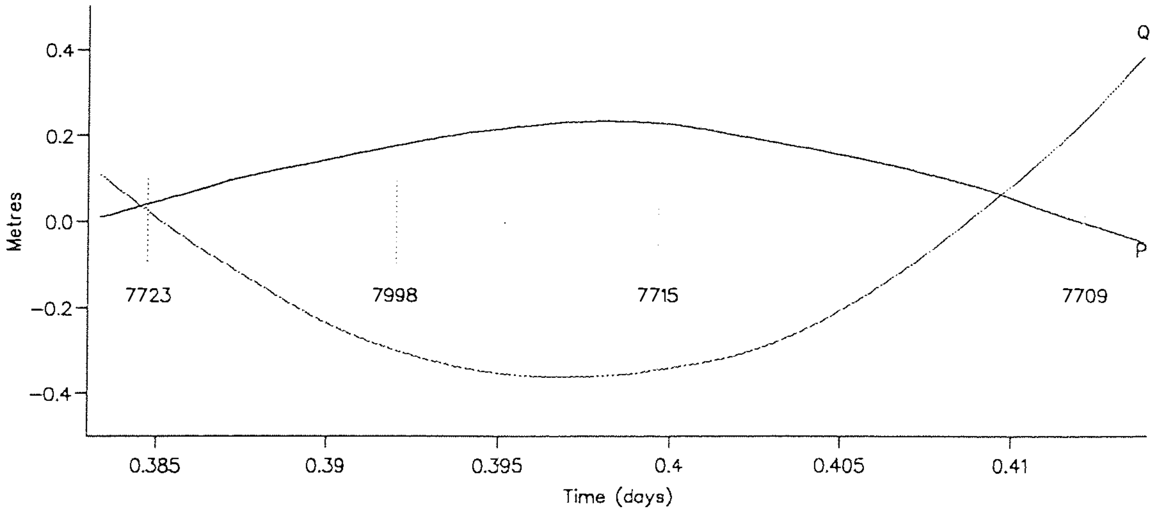

Figure 8.12

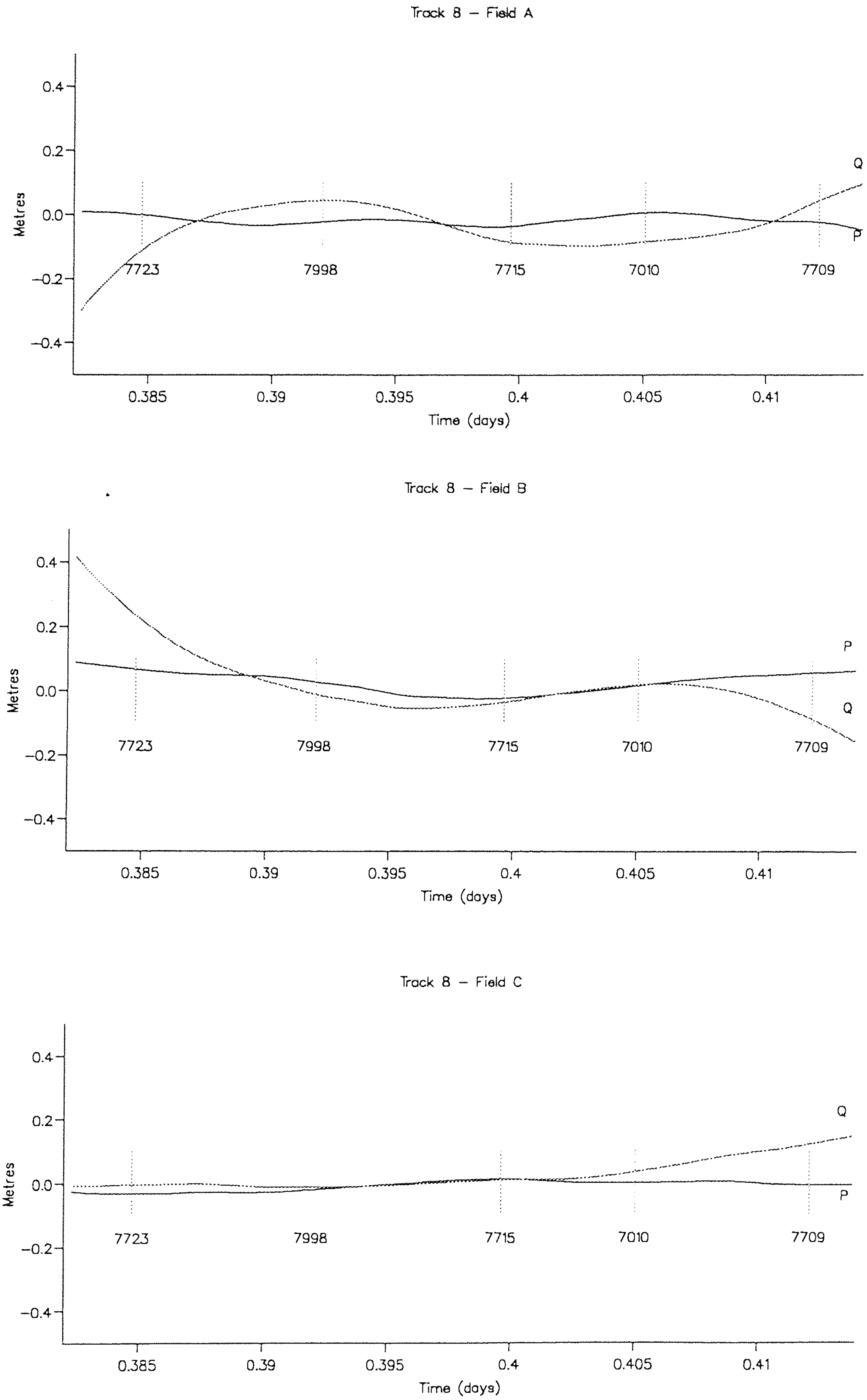
Track 8 — Field A
Metres
0.4
0.2
0.0
−0.2
−0.4
0.385
0.39
0.395
0.4
0.405
0.41
Time (days)
Q
P
7723
7998
7715
7010
7709
Track 8 — Field B
Metres
0.4
0.2
0.0
−0.2
−0.4
0.385
0.39
0.395
0.4
0.405
0.41
Time (days)
P
Q
7723
7998
7715
7010
7709
Track 8 — Field C
Metres
0.4
0.2
0.0
−0.2
−0.4
0.385
0.39
0.395
0.4
0.405
0.41
Time (days)
Q
P
7723
7998
7715
7010
7709

Figure 8.13

Clone A produced the largest radial orbit error (1.12 m rms) and consequently provides the severest test. Despite this, the graphs reveal that the periodic method performs exceptionally for all 8 tracks. However, Figure 8.5 shows that the across-track error is no more than about 10 cm for the most part of this trajectory and certainly substantially smaller than for either clones B or C. Hence the optimistic results from clone A for the periodic technique are perhaps not to be taken too literally.

Overall the 7 parameter periodic method worked much better than the 9 parameter quadratic.

§ 8.6.2 Correlation analysis

The maximum correlations in the solution using both methods are presented in Table 8.7 and although the periodic method produced the best results, it can be seen that the correlations are slightly higher than for the quadratic. The values in Table 8.7 are high since none of the solutions were constrained. Only one set of correlations for each method is given in Table 8.7 since the correlations are computed from the inverted normal matrix which is independent of the 'observed' residuals.

It is also interesting to note that for tracks 1, 2 and 3 which each have 3 stations, the highest correlation of over 0.999 is for track 1 whose station geometry resembles Figure 8.2 (b). Such a configuration was predicted in section 8.4 to yield the higher correlations (see Table 8.2). In reality, there is little to choose between the accuracy of solutions depicted for tracks 1 to 3. Four stations are used for tracks 4 to 7 and maximum correlation decreases, in particular, for the quadratic method. The periodic method yields a highest correlation of 0.9045 for track 7 whose solution is poorly determined whilst for track 8 (with 5 stations) the maximum correlation is 0.9979 but in this case the solution is excellent. It is therefore concluded that the correlations can give misleading information about how good a solution is.

Table 8.7: Maximum correlation for each track using the Periodic and Quadratic methods.

Track	Number of stations	--- Periodic --- Max. corr.	--- Periodic --- Parameters	--- Quadratic --- Max. corr.
1	3	0.9997	7	0.9992
2	3	0.9977	7	0.9935
3	3	0.9962	7	0.9935
4	4	0.9968	7	0.9849
5	4	0.9909	7	0.9747
6	4	0.9778	7	0.9768
7	4	0.9045	7	0.9951
8	5	0.9979	9	0.8160

The highest correlation for the periodic method for tracks 1 to 7 is attributed to the interdependence of the constant and the cosine term in the along-track direction.

§ 8.6.3 Analysis of computed RMS errors

An analysis of the rms errors from the covariance matrix was carried out for only two instances; track 7 with clone B and track 8 with clone A. The question is whether or not it is possible to forecast the accuracy of a solution from the associated rms errors specified by equations 8.7 and 8.8 (equations 8.7 need slight modification if a constant is included). The previous section showed how the correlations do not provide much help to this end. The rms errors for the radial, along-track and across-track corrections (R, AL and ACR respectively) are plotted in Figure 8.14 for both examples.

The periodic rms errors for track 7 clone B and track 8 clone A are extremely low when in fact the solution for track 7 with clone B is very poor. On referring to equations 8.7 for the computed rms errors, if the coefficients N^{-1}_{11}, N^{-1}_{44} and N^{-1}_{14} are small and of the same magnitude, then the resulting error will be a small constant with a small periodic variation in time. Examination of these coefficients confirm this explanation, even for the poorly determined solution. Consequently the periodic rms errors do not provide any useful indication as to the true error.

The plots for the quadratic method give a different story. The radial rms error curve (R) for track 7 clone B suggests a poorly determined solution and follows the trend of the actual absolute error well, the maximum and minimum parts coinciding well the true error. For track 8 clone A, the radial rms error is well within 10 cm and the actual error is also small and within 10 cm. Therefore it seems that the rms errors for the quadratic method do provide some insight as to the precision of the radial correction.

Finally the across-track rms curves (ACR) for the quadratic solutions suggest a large across-track error. The graph in Figure 8.15 confirms this and shows the residual across-track error after correction by a quadratic. This explains somewhat why the quadratic solution for track 8 with clone A is superior to that of track 7 with clone B.

Track 7 – Field B (Periodic RMS error)

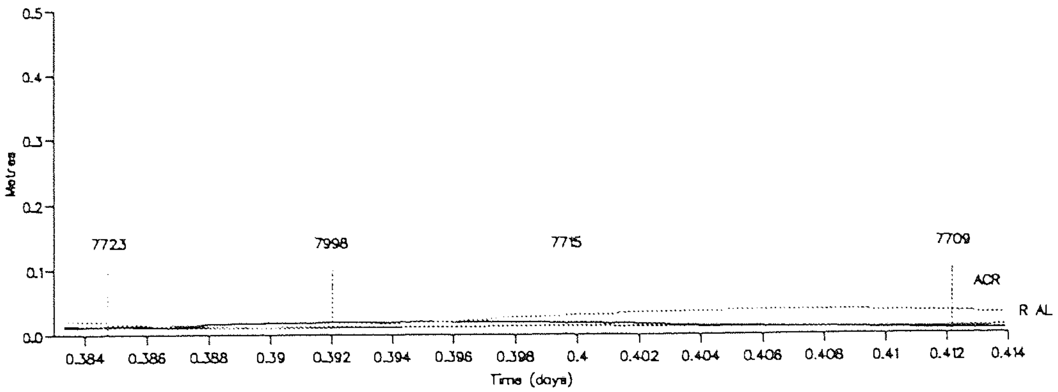

Track 7 – Field B (Quadratic RMS error)

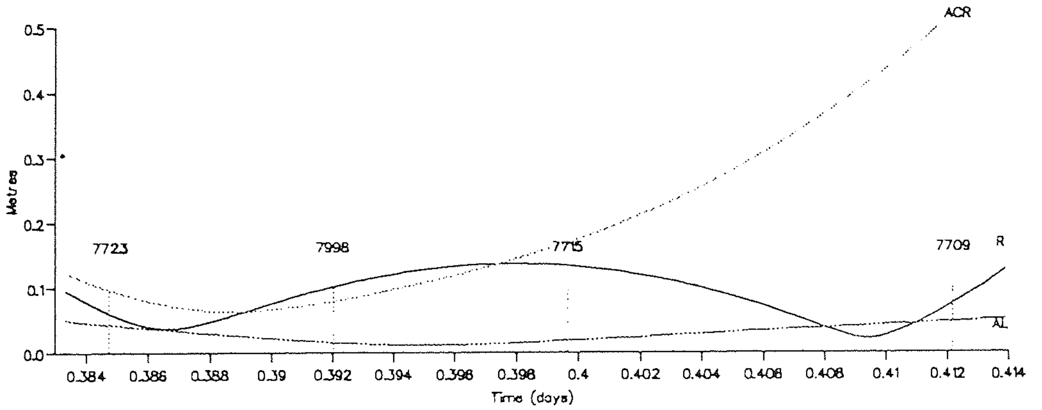

Track 8 – Field A (Periodic RMS error)

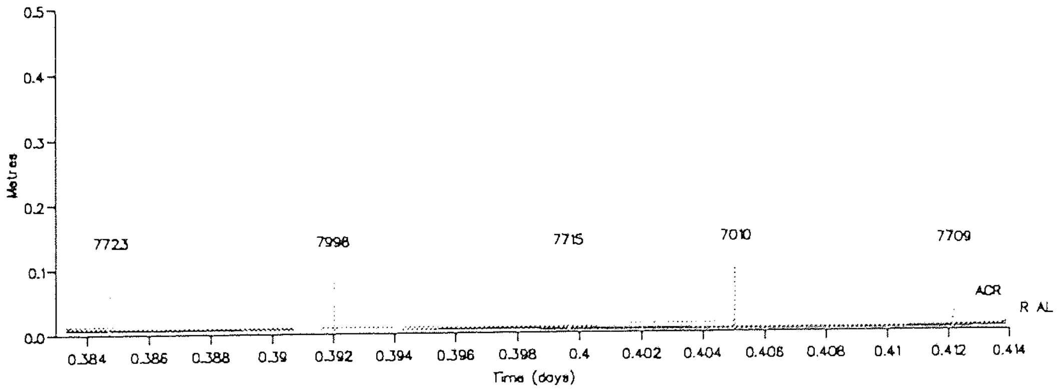

Track 8 – Field A (Quadratic RMS error)

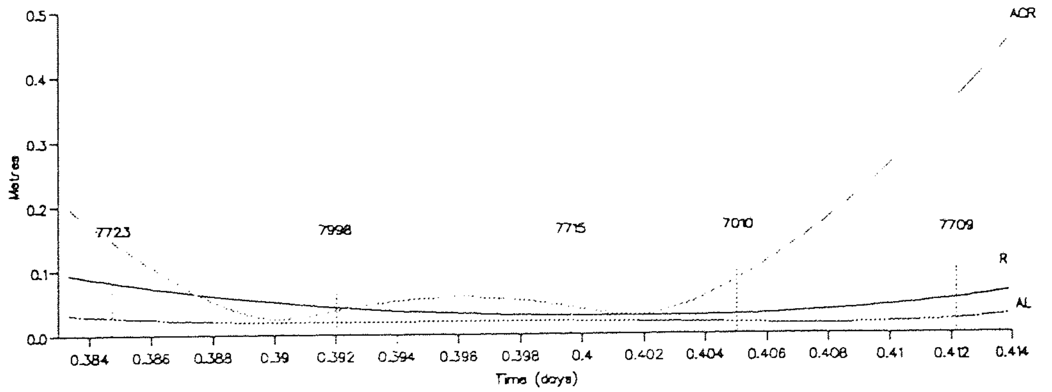

Figure 8.14

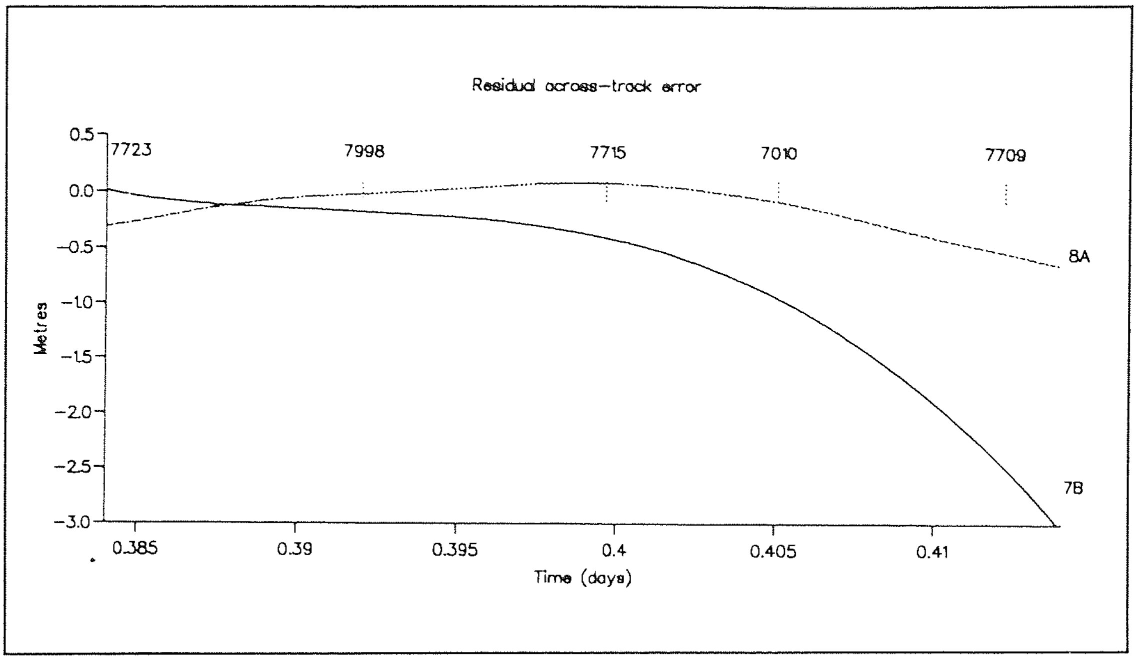

Figure 8.15

§ 8.7 Conclusions

The analytical approach to determine the correlations and rms errors for a constant short arc solution initiated in chapter 7 was extended in this chapter to examine the effects of solving for periodic and quadratic corrections in time over longer arcs. It was found for most 3 station and practically all 4 station configurations that the high correlations would probably not inhibit a reliable solution provided the stations were well distributed along the arc.

PRARE simulations for ERS-1 were then performed for 8 short arcs over the North and South Atlantic oceans using the periodic (1/rev) and quadratic empirical orbit correction methods. Unconstrained solutions showed that the periodic method is the better technique and short arcs of lengths up to 16000 km are possible given 5 stations ranging at the same time. However for 4 stations, arc lengths up to about 8500 km whilst for 3 stations track lengths up to 7000 km are possible. In each of these cases, the periodic method reduces the absolute radial orbit error to less than 10 cm.

For such favourable short arcs with 3, 4 or even 5 stations viewing the satellite simultaneously, an all weather system such as PRARE is vital. This data may in turn be augmented by laser and vertical transponder range data. PRARE is scheduled to fly again on ERS-2 in late 1994 and present rms range fits for ERS-1 of about 15 cm suggest that PRARE will contribute towards orbit improvement in both short and long arc computations.

CHAPTER 9

SHORT ARC ADJUSTMENTS FOR STATION COORDINATES

§ 9.1 Introduction

In order to obtain precise long arc satellite orbits from laser ranging data alone, the coordinates of the optical centres of the laser rangers need to known as accurately as possible. Of particular importance is the vertical height of the rangers above the reference ellipsoid; an error in this direction will adversely affect the spacecraft altitude. This applies equally to the ground receivers of the proposed microwave ranging facility PRARE and, to a lesser extent, the DORIS Doppler range-rate system.

As demonstrated in chapters 7 and 8, it is possible to adjust the satellite position by solving empirically for small corrections in the radial, along-track and across-track directions for a short arc during which there are a number of laser rangers tracking the spacecraft. In addition to determining the orbital corrections, it is also possible to solve for corrections to the station coordinates, in particular, the vertical component. Not surprisingly, the vertical correction to the station is very highly correlated to the radial orbital correction but this problem may be circumvented by combining a number of short arcs together and then solving for the station errors [Sinclair, 1989 b].

In this chapter, a solution for the coordinates of the mobile laser 7542 at Monte Venda is attempted by combining 6 individual short arcs. The orbital corrections are solved for as constants, periodic and quadratic forms. Finally the new coordinates are used in a long arc test to see by much the overall fit improves.

§ 9.2 Multiple short arc method

The work detailed in section 8.5.3 may be easily extended to solve for corrections to station coordinates and the partial derivatives required are deduced as follows. The range distance between the satellite and some chosen station is expressed as

$$R^2 = (x - x_s)^2 + (y - y_s)^2 + (z - z_s)^2 \tag{9.1}$$

wherein the satellite position is (x, y, z) and the station position is given by (x_s, y_s, z_s), both in cartesian coordinates. These are assumed to be in the Earth-fixed system and are obtained by rotating the J2000 coordinates (as used in the SATAN software) to allow for precession, nutation, polar motion and Earth rotation [Sinclair, 1987]. Moreover the coordinates (x_s, y_s, z_s) are related to the geocentric spherical coordinates (r_s, ϕ, λ) by

$$x_s = r_s \cos\phi \cos\lambda$$

$$y_s = r_s \cos\phi \sin\lambda$$

$$z_s = r_s \sin\phi \tag{9.2}$$

where r_s is the radial distance to the laser station, ϕ is the latitude and λ is the longitude. Conversely

$$r_s = \sqrt{x_s^2 + y_s^2 + z_s^2}$$

and

$$\phi = \sin^{-1}\left(\frac{z_s}{r_s}\right) \; ; \qquad \lambda = \tan^{-1}\left(\frac{y_s}{x_s}\right) \tag{9.3}$$

with λ adjusted to the appropriate quadrant. On taking small changes in equation 9.1 and assuming the satellite position to be accurate

$$\Delta R = \frac{-1}{R} \Big((x - x_s) \Delta x_s + (y - y_s) \Delta y_s + (z - z) \Delta z_s \Big) \tag{9.4}$$

and the small changes Δx_s, Δy_s and Δz_s may be derived from equations 9.3, namely

$$\Delta x_s = \Delta r_s \cos\phi \cos\lambda - r_s \sin\phi \cos\lambda \, \Delta\phi - r_s \cos\phi \sin\lambda \, \Delta\lambda$$

$$\Delta y_s = \Delta r_s \cos\phi \sin\lambda - r_s \sin\phi \sin\lambda \, \Delta\phi + r_s \cos\phi \cos\lambda \, \Delta\lambda$$

$$\Delta z_s = \Delta r_s \sin\phi + r_s \cos\phi \, \Delta\phi \, . \tag{9.5}$$

Substituting equations 9.5 into 9.4 and differentiating ΔR partially with respect to, say, Δr_s yields

$$\frac{\partial \Delta R}{\partial \Delta r_s} = \frac{-1}{R} \Big((x - x_s) \cos\phi \cos\lambda + (y - y_s) \cos\phi \sin\lambda + (z - z_s) \sin\phi \Big) \tag{9.6}$$

which is more simply expressed using equations 9.2 as

$$\frac{\partial \Delta R}{\partial \Delta r_s} = \frac{-1}{R r_s} \Big((x - x_s) x_s + (y - y_s) y_s + (z - z_s) z_s \Big) \, . \tag{9.7}$$

Similiarly

$$\frac{\partial \Delta R}{\partial \Delta \phi} = \frac{r_s}{R} \Big((x - x_s) \sin\phi \cos\lambda + (y - y_s) \sin\phi \sin\lambda - (z - z_s) \cos\phi \Big) \tag{9.8}$$

and

$$\frac{\partial \Delta R}{\partial \Delta \lambda} = \frac{r_s}{R} \Big((x - x_s) \cos\phi \sin\lambda - (y - y_s) \cos\phi \cos\lambda \Big) \, . \tag{9.9}$$

These partials are computed for all range observations for that particular station over the short arc and are used in the least squares method to solve for the station corrections (Δr_s, $\Delta\phi$, $\Delta\lambda$) as detailed in section 8.5.3. Naturally, more than one set of station coordinates can be corrected for in this way.

For each short arc a normal set of equations $N\underline{x}=\underline{b}$ is formed wherein $\underline{x}$ is the solution containing both the orbital and station corrections. Repeating this for other short arcs, the resulting systems of equations may be combined for the solution of the station corrections. Usually the Helmert-Wolf blocking process (Appendix A) is used to eliminate the orbital parameters to leave a system of equations $M\underline{x}'=\underline{b}'$ in which $\underline{x}'$ is the solution for the station corrections alone. However because it may be useful to see how the correlations arise for the periodic and quadratic orbit correction methods, it was decided to combine the normal equations such that all the orbital parameters for all the arcs and the station errors were explicitly solved for. This method is also detailed in Appendix A.

Using multiple short arcs in this manner allows the station corrections (which are arc independent) to be reliably separated from the orbital parameters (which are arc dependent).

§ 9.3 Correction of the Monte Verdi laser site 7542 coordinates

The mobile laser at Monte Verdi tracked ERS-1 during the first few months after its launch in July 1991 as part of the Venice Tower experiment [ESA, 1993] to determine the altimeter bias. Being mobile, the location of this laser was not well known and hence provides a good opportunity to determine corrections for it by the multiple short arc method. Figure 9.1 illustrates the ERS-1 ground tracks during the commissioning phase and the laser stations over Europe.

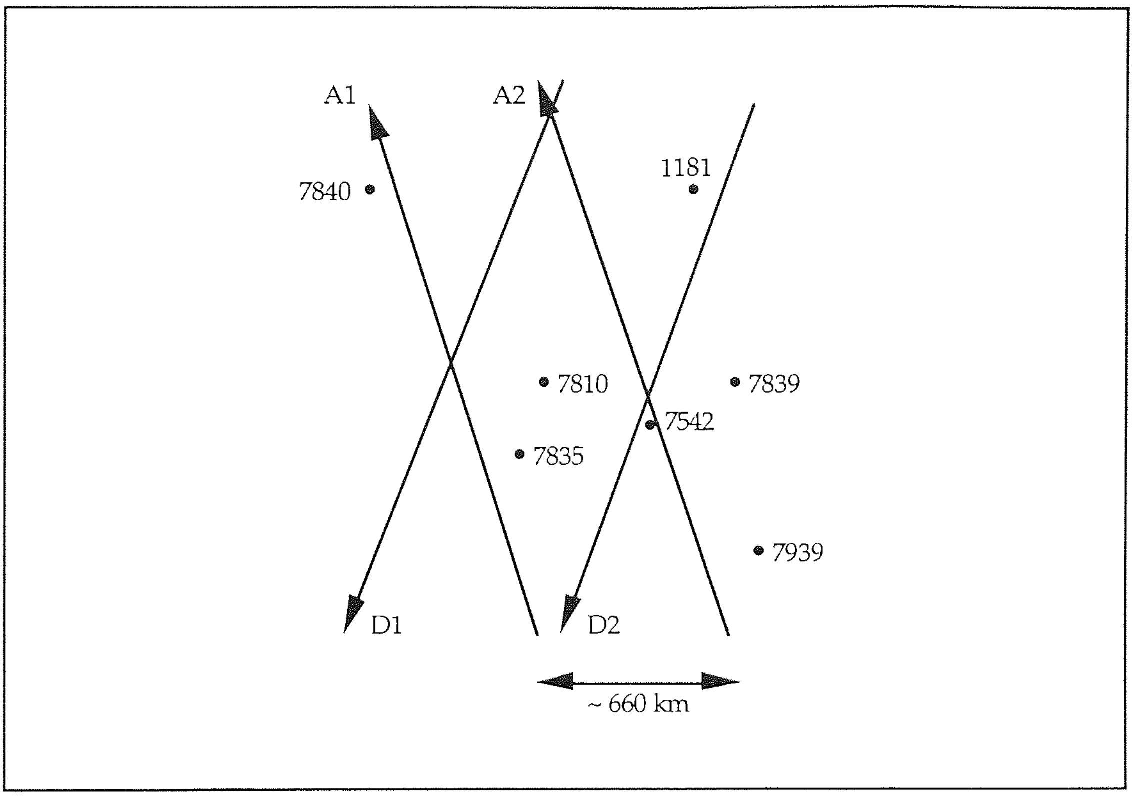

Figure 9.1

The stations in Figure 9.1 are 1181 Potsdam, 7542 Monte Verdi, 7810 Zimmerwald, 7835 Grasse, 7839 Graz, 7840 Herstmonceux and 7939 Matera.

Only short arcs with 3 or more stations (one of which has to be 7542) were chosen so that periodic and quadratic orbital corrections could be determined. The ideal situation would be to have 3 or 4 of arcs A2 and D2 since these would provide the most radial information for station 7542. Unfortunately over the period concerned, no suitable D1 or D2 arcs were found to be tracked by 7542. However a fair number were found for both A1 and A2. This is probably due to the fact that the ascending arcs A1 and A2 were night time passes and therefore are easier to 'hit' whereas descending passes D1 and D2 were flown during the day. The 6 short arcs chosen are listed below in Table 9.1.

Table 9.1: Details of the 6 short arcs used to determine station corrections to Monte Verdi (7542); the number of normal laser points is given for each station included in the analysis.

MJD	Arc	1181	7542	7810	7835	7839	7840
48483.88	A2	15	11	17	10	-	15
48489.88	A2	3	24	14	25	-	13
48503.90	A1	17	23	15	-	20	17
48504.88	A2	18	25	9	-	12	16
48512.90	A1	11	19	-	-	-	11
48483.88	A2	-	20	2	33	15	13

§ 9.4 Results

The modification needed to the SATAN programs to solve for station coordinates was minimal. Long arc orbits of typically 3 or 4 days were generated using the GEM-T3A gravity field [Lerch et al., 1992] for required epochs of the short arcs. The normal equations of these were computed and stored. The multiple short arc method was performed three times to deduce the station corrections to 7542 with all other stations held fixed; firstly solving for the orbital corrections as constants, secondly as periodic functions in time (as defined by equation 8.1) and finally as quadratics in time (as defined in equation 8.2). It was hoped that these realistic orbit corrections will help determine more precisely the station errors. Moreover it was found that the solution for the single 7542 station did not need to be constrained; however if a number of stations are corrected for simultaneously, a mild constraint may be required [Sinclair, 1989].

Table 9.2 documents the findings. These are corrections in a geocentric sense and are of the magnitude expected.

Table 9.2: Corrections to station coordinates of Monte Verdi (7542); rms errors are given in brackets.

		--- Arc-seconds ---		--- cm ---	
Orbital correction	Δr_s (cm)	$\Delta\phi$	$\Delta\lambda$	$\Delta\phi$	$\Delta\lambda$
Constant	-81.8	-0.013587	-0.022128	-42.0	-48.1
	(2.7)	(0.005)	(0.014)		
Periodic	-62.6	-0.010316	-0.021849	-31.9	-47.5
	(1.4)	(0.002)	(0.007)		
Quadratic	-66.5	-0.007757	-0.019975	-24.0	-43.4
	(1.7)	(0.003)	(0.008)		

In all 6 arcs, the periodic cosine terms agreed very well with the quadratic constants and the rms errors for all the parameters were only a few centimetres at the most. In addition there were no correlations >0.8 for either the constant or periodic method; for the quadratic method the highest correlation was 0.95.

The solution tended to become stable after 4 or 5 arcs, provided both A1 and A2 arcs were used. Table 9.3 shows the original coordinates of 7542 used and the updated sets.

Table 9.3: Updated coordinates for Monte Verdi (7542) laser station.

Orbital correction	Height (m)	Geodetic Latitude ϕ^{o}	Longitude λ^{o}
None (original)	525.341	45.32181112	11.69311539
Constant	524.523	45.32180735	11.69310924
Periodic	524.715	45.32180825	11.69310932
Quadratic	524.676	45.32180897	11.69310984

Relative to an Earth semi-major axis of 6378137 metres and 1/f = 298.257.

§ 9.5 Long arc orbit test of the new 7542 station coordinates

To test these newly derived coordinates, they were used to converge an ERS-1 6 day orbit over the period MJD 48498.80 to 48504.90 (30th August to 5th September 1991). This test period therefore includes 2 of the short arcs listed in Table 9.1. During the 6 days, 1005 laser normal points were accepted, 201 of which were from the 7542 station. The results of this exercise are found in Table 9.3.

The results first show that the ERS-1 orbits for this period are rather poor; these were computed about a year before those detailed in chapter 4. The later orbits included a 1/rev term in the along-track direction, used the new JGM-2 gravity field and a tighter rejection level for the laser residuals. This aside, it can be seen that the 3 new sets of 7542 coordinates have improved the overall rms fit. In particular, the periodic and quadratic sets have brought the 7542 laser residuals fit down from 63.6 cm to about 53.3 cm and the mean has also improved. The periodic and quadratic functions have absorbed the arc dependent orbit errors more successfully than by just using constants (which is not surprising) and thus allowed the 7542 station corrections to be better determined.

Table 9.4: Comparison of the derived sets of coordinates for 7542 using a 6 day long arc test; all values in cm.

7542 Coordinates corrected by	Long arc RMS error	--- Laser residuals for 7542 --- RMS error	Mean
None (original)	55.8	63.6	23.0
Constant	53.3	55.5	-16.1
Periodic	52.8	53.4	-6.6
Quadratic	52.8	53.3	-7.9

This provides a reasonable demonstration that the new coordinates are more reliable than the original set. However these were derived from an extremely limited dataset, a mere total of 6 arcs over 33 days. Also the ERS-1 orbits were rather poor (a laser residual fit of 40 to 60 cm rms) and the lack of any D1 and D2 arcs did not assist the exercise. A far more reliable solution would be obtained if 6 to 12 month's worth of data over many different arcs were employed [Sinclair, 1989] in which case the orbit errors average out. The solution also depends to a certain extent how well the positions of the other stations in the short arcs are known.

§ 9.6 Conclusions

The method of combining a number of short arcs together in order to solve for station coordinate corrections has been discussed. An exercise to determine corrections to the mobile laser 7542 at Monte Verdi was carried out using 6 ERS-1 short arcs over Europe during August and September 1991. Three solutions were obtained, firstly solving empirically for the arc dependent orbit errors using constants, secondly using periodic functions in time and thirdly quadratics in time. Each newly derived set of coordinates for 7542 was then used to converge an ERS-1 6 day orbit which demonstrated that the new sets did improve the overall rms fit. The corrections obtained by the periodic and the quadratic methods were comparable in accuracy and superior to those from the constant method. A larger dataset of many more distinct arcs and covering a longer time span will help determine the station coordinates even better.

CHAPTER 10

CONCLUSIONS

The work demonstrated in this thesis has been varied and wide ranging. It has been shown in chapter 4 that the SATAN software for orbit determination as implemented at Aston University is capable of producing 6 day long arc orbits for ERS-1 with a laser fit of ~15 cm rms and a crossover fit of ~23 cm rms. For TOPEX/POSEIDON, the orbits are clearly superior with values of 10 and 14 cm respectively for long arcs of a 10 day duration. The higher altitude of TOPEX/POSEIDON provides more laser tracking data to be available and also diminishes the consequences of poor drag force modelling, thus providing more accurate ephemerides to be computed. Solving for a sea surface topography, to degree and order 30, brings the rms error for the altimeter residuals down to ~33 cm for ERS-1 and ~22 cm for TOPEX/POSEIDON.

The long arc solution for the time tag bias showed that its effect is negligible for all three altimeters. The long arc solution for the altimeter range bias yielded a value of -69 cm for ERS-1 (during the 35 day repeat cycle in September 1992), -41 cm for TOPEX (from cycles 2 to 10, 21 and 22) and -18 cm for POSEIDON (cycle 20) relative to an Earth semi-major axis of 6378136.3 metres. These results are consistent with findings from other research groups [JPL, 1992 a, b]. A repeat track analysis revealed a difference of ~22 cm between the altimeter biases of TOPEX and POSEIDON (TOPEX measuring 22 cm shorter than POSEIDON) and is consistent with the long arc values. Moreover, sea surface topography maps were computed and plotted for all three altimeters to degree and order 30.

In chapter 5, the sea surface variability exercise for the North Sea validated the POL ocean tide and storm surge models and a rms error of less than 7 cm was observed. This was encouraging since the storm surge model and an enhanced version of the ocean tide model are used in chapter 6 for the English Channel altimeter bias calibration. The ERS-1 altimetry was also observed to be noisier than TOPEX/POSEIDON which would seem to vindicate TOPEX and POSEIDON being the superior devices as expected.

In chapter 6, the range bias for all three altimeters was computed using an 'on-site' or 'short-arc' method and is in principle the same as the dedicated exercises carried out at the Venice Tower for ERS-1 and Lampedusa and Platform Harvest for both TOPEX and POSEIDON. The English Channel served as the calibration site and precise orbit determination was facilitated by the nearby laser ranger at Herstmonceux. Final results give an overall bias of -41.9 cm for ERS-1 (5 passes in early 1992), -16.7 cm for TOPEX (4 passes in late 1992) and +3.0 cm for POSEIDON (a single pass in late 1992). A difference of ~20 cm between TOPEX and POSEIDON is therefore observed, along with a difference of ~25 cm for TOPEX and ERS-1. These relative values agree very well with those determined by long arc methods in chapter 4, with the constant offset due, perhaps, to the uncertainty of the Earth semi-major axis.

The orbits produced at Aston and by other groups are now very good and a radial rms error of ~10 cm (deduced from crossover residuals) is commonplace. Therefore the role of short arc correction for precise orbit detemination is somewhat less important than envisaged when PRARE was proposed for ERS-1. Nevertheless, these techniques are still required when the precise satellite altitude is needed, for instance, when calibrating the altimeter. Analytical consideration of the range residual in chapter 7 led a useful model to predict the troublesome correlations which arise from a short arc solution for constant orbit parameters from laser tracking data. This model was well validated by comparing its predictions for rms errors and correlations to observed SEASAT short arcs.

The above model was then extended in chapter 8 to analyse the correlations when solving for time-dependent periodic and quadratic corrections. The results showed that most 3 ground station and practically all 4 ground station configurations for laser tracking will allow a reliable separation of the orbital parameters without the need to constrain the solution. Subsequently, simulations for the microwave tracking system, PRARE, were performed and illustrated how the periodic method reduced the absolute radial orbit error down to below 10 cm, rather more convincingly than for the quadratic method which suffered from high correlations. The 10 cm accuracy was observed for short arcs of ~12,000 km in length (with 4 stations viewing) and no constraints were applied to the orbital corrections to achieve this.

Finally in chapter 9, the multiple short arc method was used to determine corrections to coordinates for the mobile laser at Monte Verdi from ERS-1 short arcs. The orbital parameters were solved for as constants, periodic and quadratic functions in time. A long arc test suggested that the sets of corrections determined when solving for periodic/quadratic orbit corrections to be more reliable (in a least squares sense) than when solving for just constant orbit parameters.

RECOMMENDATIONS FOR FURTHER WORK

Although this thesis contains a variety of different work, the key results are those pertaining to the assessment of the ERS-1, TOPEX and POSEIDON altimeter biases, in particular the on-site calibration demonstrated in chapter 6. This exercise is presently continuing at Aston University and will, in time, yield a complete record of the altimeter bias values throughout the duration of their lifetime. Variations on the exercise were suggested in section 6.7.

The proposed launch of ERS-2 carrying the PRARE tracking system may renew interest in the short arc work carried out in chapters 7, 8 and 9. Certainly short arcs can refine orbits to a level of accuracy permissible for their employment for on-site altimeter bias determination.

REFERENCES

[1] Ashkenazi V., Basker G.A., Davison M. and Dodson A.H., **Dynamic Sea Level and the Geoid by Gravimetric and GPS Measurements**, Final Report, Institute of Engineering Surveying and Space Geodesy, University of Nottingham, U.K., 1990.

[2] AVISO, **AVISO CD ROM User Manual : Merged TOPEX/POSEIDON Products**, AVI-NT-101-CN, Edition 1, 1992.

[3] Baker T.F., **Tidal deformations of the Earth**, Science Progress, 69, pp.197-233, 1984.

[4] Bomford G., **Geodesy**, 4th ed., Oxford Science Publications, U.K., 1980.

[5] Carnochan S., Moore P., Ehlers S., Lam C. and Woodworth P., **Improvement of the Radial Positioning of ERS-1 Through Dual Crossover Analysis with TOPEX/POSEIDON**, Proceedings Second ERS-1 Symposium, ESA SP-361, pp.753-758, 1994.

[6] Cheney R.E., Marsh J.G. and Beckley B.D., **Global Mesoscale Variability From Collinear Tracks of SEASAT Altimeter Data**, Journal of Geophysical Research Vol. 88, No. C7, pp.4343-4354, 1983.

[7] CNES, **Altimeter Products User Manual**, Ref : C1-EX-MUT-A21-01-CN Issue 2 Revision 1, 1992.

[8] Ehlers S., **Various Techniques and Procedures for Refining ERS-1 Orbits**, submitted for PhD thesis, Aston University, U.K., 1993.

[9] Engelis T. and Knudsen P., **Orbit Improvement and Determination of the Ocean Geoid and Topography from 17 days of Seasat data**, Manuscripta Geodaetica 14, pp.193-201, 1989.

[10] ESA, **ERS-1 System**, SP-1146, 1992.

[11] ESA, **The Calibration of the ERS-1 Radar Altimeter**, Report : ER-RP-ESA-RA-0257, Issue 2.0, 1993.

[12] ESOC, **ERS-1 Orbit Monthly Report No. 24 : March 1994.**

[13] Featherstone W.E., **A GPS Controlled Gravimetric Determination of the Geoid of the British Isles**, D.Phil thesis, Oxford University, U.K., 1992.

[14] Flather R.A., Procter R and Wolf J., **Oceanographic Forecast Models**, in 'Computer Modelling in the Environment Sciences', edited by Farmer D.G. and Rycroft M.J., Clarendon Press, Oxford, U.K., pp.15-30, 1991.

[15] JPL, **Satellite Altimetric Measurements of the Ocean - Report of the TOPEX Science Working Group**, March 1981.

[16] JPL, **TOPEX/POSEIDON CALVAL Bulletin No. 3**, February 1992 a.

[17] JPL, **TOPEX/POSEIDON CALVAL Bulletin No. 4**, July 1992 b.

[18] JPL, **TOPEX/POSEIDON Project - GDR User's Handbook**, JPL D-8944, 1992 c.

[19] JPL, **TOPEX/POSEIDON Research News**, Issue 1, JPL, September 1993 a.

[20] JPL, **Verification Workshop**, 22-25 February 1993 b.

[21] Kaula W.M., **Theory of Satellite Geodesy**, Blaisdell Publishing Company, Waltham, Massachusetts, 1966.

[22] King-Hele D., **Theory of Satellite Orbits in an Atmosphere**, Butterworth and Co., London U.K., 1964.

[23] Kolenkiewicz R. and Martin C.F., **SEASAT Altimeter Height Calibration**, Journal of Geophysical Research Vol. 87, No. C5, pp.3189-3197, 1982.

[24] Lam C.W. and Moore P., **TOPEX/POSEIDON Altimeter Calibration Over the English Channel**, TOPEX/POSEIDON Research News Issue 1, pp.9-11, JPL, 1993 a.

[25] Lam C.W., Moore P. and Woodworth P.L., **Calibration of ERS-1 Altimetry over the North Sea**, Proceedings of the First ERS-1 Symposium at Cannes, France, pp. 85-90, ESA SP-359, 1993 b.

[26] Lambeck K., Cazenave A. and Balmino G., **Solid Eath and Ocean Tides Estimated from Satellite Orbit Analyses**, Rev. Geophys. Space Phys., 12, pp.421-34, 1974.

[27] Lambeck K., **The Earth's Variable Rotation**, Cambridge University Press, U.K., 1980.

[28] Lerch F.J. and 18 other authors, **Geopotential Models of the Earth from Satellite Tracking, Altimeter and Surface Gravity Observations : GEM-T3 and GEM-T3S**, NASA Technical Memorandum 104555, GSFC, Greenbelt, USA, 1992.

[29] Lerch F.J. and 18 other authors, **Gravity Model Improvement for TOPEX /POSEIDON**, EOS Trans., American Geophysical Union, 74(16), p.16, 1993.

[30] Le Traon P.Y., Gaspar P., Bouyssel F. and Makhmara H., **Reducing ERS-1 Orbit Error using TOPEX/POSEIDON Data**, Proceedings Second ERS-1 Symposium, ESA SP-361, pp.759-763, 1994.

[31] Marsh J.G. and Williamson R.G., **SEASAT Altimeter Timing Bias Estimation**, Journal of Geophysical Research Vol. 87, No. C5, pp.3232-3238, 1982.

[32] Marsh J.G. and 17 other authors, **A New Gravitational Model for the Earth from Satellite Tracking Data : GEM-T1**, Journal of Geophysical Research Vol. 93, pp.6169-6215, 1988.

[33] Martin C.F. and Kolenkiewicz R., **Calibration Validation for the GEOS 3 Altimeter**, Journal of Geophysical Research Vol. 86, pp.6369-6381, 1981.

[34] Melchior P., **The Tides of the Planet Earth**, Pergamon Press, Oxford, U.K., 1978.

[35] Merit Standards, April 1983.

[36] Merson R.H., **Numerical Integration of the Equations of Celestial Mechanics**, RAE Tech. Report 74184, 1975.

[37] Moritz H., **Advanced Physical Geodesy**, Abacus Press, Tunbridge Wells, Kent, U.K., 1980.

[38] Oskam D., **Sea Surface Variability in the North Sea as derived from SEASAT altimetry**, Geophys. J. Int. 100, 1-7, 1990.

[39] Pugh D.T., **Tides, surges and mean sea-level : A handbook for engineers and scientists**, Wiley, Chicester, U.K., 1987.

[40] Rapp R.H. and Cruz J.Y., **Spherical Harmonic Expansion of the Earth's Gravitational Potential to Degree 360 using 30^0 Mean Anomalies**, Report 376, Dept. of Geodetic Science and Surveying, Ohio State University, USA, 1986.

[41] Rapp R.H., Wang Y.M. and Pavlis N.K., **The Ohio State 1991 Geopotential and Sea Surface Topography Harmonic Coefficient Models**, Report 410, Dept. of Geodetic Science and Surveying, Ohio State University, USA, 1991.

[42] Ries J.C., Shum C.K. and Tapley B.D., **Surface Force Modeling for Precision Orbit Determination**, IUGG XX General Assembly, Symposium U15, In press, 1992.

[43] Robinson I.S., **Satellite Oceanography - An Introduction for Oceanographers and Remote-Sensing Scientists**, Ellis Horwood Limited, Chichester, U.K., 1985.

[44] Rothwell D.A., **Precise Orbit Determination and Analysis from Satellite Altimetry and Laser Ranging**, PhD thesis, Aston University, U.K., 1989.

[45] Schrama E.J.O., **The Role of Orbit Errors in Processing of Satellite Altimeter Data**, Netherlands Geodetic Commission, 1989.

[46] Schwiderski E.W., **Ocean Tides. Part I: Global ocean equations. Part II: A hydrodynamical interpolation model**, Marine Geodesy, Vol. 3, pp. 161-255, 1980.

[47] Schutz B.E., Tapley B.D. and Shum C., **Evaluation of the SEASAT Altimeter Time Tag Bias**, Journal of Geophysical Research Vol. 87, No. C5, pp.3239-3245, 1982.

[48] Shum C.K., Yuan D.N., Ries J.C., Smith, J.C., Schutz B.E. and Tapley B.D., **Precision Orbit Determination for the Geosat Exact Repeat Mission**, Journal of Geophysical Research, Vol. 95, No. C3, pp.2887-2898, 1990.

[49] Shum C.K., Tapley B.D., Kozel B.J., Visser P., Ries J.C. and Seago J., **Precise Orbit Analysis and Global Verification Results from ERS-1 Altimetry**, Proceedings Second ERS-1 Symposium, ESA SP-361, pp.747-752, 1994.

[50] Sinclair A.T., **The Radial Accuracy of Orbits determined from SLR Data**, SLR Technical Note 7, Royal Greenwich Observatory, U.K., 1985.

[51] Sinclair A.T., **The Use of Short-Arc Techniques for Determining the Radial Distance of ERS-1**, Royal Greenwich Observatory, U.K., 1986.

[52] Sinclair A.T. and Appleby G.M., **SATAN - Programs for the Determination and Analysis of Satellite Orbits from SLR Data**, SLR Technical Note 9, Royal Greenwich Observatory, U.K., 1986.

[53] Sinclair A.T., **Earth Rotation and Reference Systems**, Lecture Notes at the Summer School in Space Geodesy at Nottingham University, Royal Greenwich Observatory, U.K., 1987.

[54] Sinclair A.T., **The Determination of Orbit Corrections by Short-Arc techniques with Application to ERS-1**, Manuscripta Geodaetica 14, pp.238-246, 1989 a.

[55] Sinclair A.T., **The determination of station coordinates and baselines from the 1986 and 1987 WEGENER/MEDLAS data by global and short-arc solutions**, Proc. 4th Int. Conf. on WEGENER/MEDLAS Project, Scheveningen, 1989 b.

[56] Smith D.E. et al., **LAGEOS Geodetic Analysis - SL7.1**, NASA Technical Memorandum 104549, GSFC, Greenbelt, USA, 1991.

[57] Thurman H.V., **Introductory Oceanography**, 3rd Edition, Charles E. Merrill Publishing Company, Colombus, Ohio, USA, 1981.

[58] Vincent M.A., **Orbit Characteristics - TOPEX/POSEIDON Project**, JPL D-7511, June 1990.

[60] Wagner C.A., **Radial Variations of a Satellite Orbit Due to Gravitational Errors : Implications for Satellite Altimetry**, Journal of Geophysical Research Vol. 90, No. B4, pp.3027-3036, 1985.

[61] Wagner C. and Melchioni E., **On using Precise Laser Ranges to Provide Vertical Control for Satellite Altimetric Surfaces**, Manuscripta Geodaetica 14, pp.305-338, 1989.

[62] Wakker K.F., Ambrosius B.A.C. and Aardoom L., **Precise Orbit Determination for ERS-1**, ESA Contract Report, TU Delft, 1983.

[63] Wilmes H. and Reigber C.H., **Precise Range and Range Rate Equipment On Board ERS-1**, DGFI, Presented at the XIX I.U.G.G. General Assembly, 1987.

APPENDIX A

SEPARATION OF ARC DEPENDENT AND ARC INDEPENDENT PARAMETERS IN A LEAST SQUARES SOLUTION

It is often the case that a system of normal equations, $N\underline{x}=\underline{b}$, arises from a least squares minimisation procedure wherein the vector $\underline{x}$ includes parameters such as the satellite initial position and velocity which are arc dependent and parameters such as corrections to station coordinates or sea surface topography which are deemed arc independent. Many such systems of normal equations may be combined together so that the solution for the arc independent parameters are better determined. Two methods are now detailed, each computationally different but both of which lead to precisely the same solution for the arc independent parameters.

§ A.1 Helmert Wolf blocking method

The normal equation $N^{(k)}\underline{x}^{(k)} = \underline{b}^{(k)}$ resulting, for example, from arc k may be written in partitioned form as

$$\begin{pmatrix} N_D & N_C \\ N_C^T & N_I \end{pmatrix}^{(k)} \begin{pmatrix} \underline{x}_D^{(k)} \\ \underline{x}_I \end{pmatrix} = \begin{pmatrix} \underline{b}_D \\ \underline{b}_I \end{pmatrix}^{(k)} \tag{A.1}$$

within which the subscripts D denote the arc dependent parameters, I the independent parameters and C those parameters common to both. The superscript T denotes the transpose of a matrix. Expanding equation A.1 gives

$$N_D^{(k)}\,\underline{x}_D^{(k)} + N_C^{(k)}\,\underline{x}_I = \underline{b}_D^{(k)} \tag{A.2}$$

$$N_C^{T(k)}\,\underline{x}_D^{(k)} + N_I^{(k)}\,\underline{x}_I = \underline{b}_I^{(k)}\,. \tag{A.3}$$

From equation A.2,

$$\underline{x}_D^{(k)} = \left(N_D^{(k)}\right)^{-1}\left(\underline{b}_D^{(k)} - N_C^{(k)}\,\underline{x}_I\right) \tag{A.4}$$

and upon substituting equation A.4 into A.3

$$\left(N_I - N_C^T N_D^{-1} N_C\right)^{(k)}\underline{x}_I = \left(\underline{b}_I - N_C^T N_D^{-1}\,\underline{b}_D\right)^{(k)} \tag{A.5}$$

which is more succintly expressed as

$$N^{*(k)}\,\underline{x}_I = \underline{b}^{*(k)}\,. \tag{A.6}$$

Hence for each arc, it is possible to eliminate the arc dependent parameters and deduce a system of normal equations as given by equation A.6. Combining these normal equations from the different arcs is then a simple process of adding together the normal matrices $N^{*(k)}$ and the column vectors $\underline{b}^{*(k)}$ to yield

$$\left(\sum_k N^{*(k)}\right)\underline{x}_I = \sum_k \underline{b}^{*(k)} \tag{A.7}$$

which leads to the solution

$$\underline{x}_I = \left(\sum_k N^{*(k)}\right)^{-1}\left(\sum_k \underline{b}^{*(k)}\right), \tag{A.8}$$

the result of which is the same as if all the arc dependent parameters had been explicitly solved for.

§ A.2 Explicit solution for arc dependent and independent parameters

It is sometimes desirable to solve for the arc dependent parameters along with the arc independent parameters especially to see how the addition of more arcs affects the correlations between the unknowns. The normal equations $N^{(k)}\underline{x}^{(k)} = \underline{b}^{(k)}$ from the different arcs can be patched together to produce one overall normal equation $M\underline{y}=\underline{c}$. For example if the normal equations $N^{(k)}\underline{x}^{(k)} = \underline{b}^{(k)}$ are available for k=1..2, then on referring to equation A.1, the equation $M\underline{y}=\underline{c}$ would take the form

$$\begin{pmatrix} N_D^{(1)} & 0 & N_C^{(1)} \\ 0 & N_D^{(2)} & N_C^{(2)} \\ N_C^{T(1)} & N_C^{T(2)} & \sum_{k=1}^{2} N_I^{(k)} \end{pmatrix} \begin{pmatrix} \underline{x}_D^{(1)} \\ \underline{x}_D^{(2)} \\ \underline{x}_I \end{pmatrix} = \begin{pmatrix} b_D^{(1)} \\ b_D^{(2)} \\ \sum_{k=1}^{2} b_I^{(k)} \end{pmatrix} \tag{A.9}$$

and similarly for k=1..3, namely

$$\begin{pmatrix} N_D^{(1)} & 0 & 0 & N_C^{(1)} \\ 0 & N_D^{(2)} & 0 & N_C^{(2)} \\ 0 & 0 & N_D^{(3)} & N_C^{(3)} \\ N_C^{T(1)} & N_C^{T(2)} & N_C^{T(3)} & \sum_{k=1}^{3} N_I^{(k)} \end{pmatrix} \begin{pmatrix} \underline{x}_D^{(1)} \\ \underline{x}_D^{(2)} \\ \underline{x}_D^{(3)} \\ \underline{x}_I \end{pmatrix} = \begin{pmatrix} b_D^{(1)} \\ b_D^{(2)} \\ b_D^{(3)} \\ \sum_{k=1}^{3} b_I^{(k)} \end{pmatrix} \tag{A.10}$$

which is manageable if the individual normal equations $N^{(k)}\underline{x}^{(k)} = \underline{b}^{(k)}$ are not too large in dimension and too many in number, otherwise the Helmert Wolf blocking method is preferred. The solution is then obtained by inverting M to yield the result $\underline{y}=M^{-1}\underline{c}$.

APPENDIX B

CONVERSION BETWEEN GEOCENTRIC AND GEODETIC COORDINATES

The cartesian coodinates (x, y, z) of a point P in space are related to the geocentric spherical polar coordinates (r, ϕ, λ) by

$$x = r\cos\phi\cos\lambda\,; \qquad y = r\cos\phi\sin\lambda\,; \qquad z = r\sin\phi \tag{B.1}$$

wherein r is the radial distance to point P, ϕ is the latitude measured from the equatorial plane and λ is the longitude. Conversely

$$r = \sqrt{x^2 + y^2 + z^2}$$

and

$$\phi = \sin^{-1}\left(\frac{z}{r}\right) \quad ; \qquad \lambda = \tan^{-1}\left(\frac{y}{x}\right) \tag{B.2}$$

with λ adjusted to the appropriate quadrant. Since the Earth is better approximated by an oblate spheroid, it is desirable to define P geodetically by (h, ϕ', λ) such that

$$\begin{aligned} x &= (N + h)\cos\phi'\cos\lambda \\ y &= (N + h)\cos\phi'\sin\lambda \\ z &= \{(1 - e^2)N + h\}\sin\phi' \end{aligned} \tag{B.3}$$

in which N is the radius of curvature; h is the distance to point P in a normal direction from the surface of the ellipsoid at (ϕ', λ) defined by equatorial radius R_E and eccentricity e; see Figure B.1. The angle ϕ' is known as the geodetic latitude with longitude λ taking the same definition as before. The eccentricity e is related to f (flattening or ellipticity) by

$$(1-f)^2 = (1-e^2) \tag{B.4}$$

wherein f is defined by

$$f = \frac{a-b}{a} \tag{B.5}$$

and a is the semi major axis and b the semi minor axis. The reciprocal flattening (1/f) is approximately 298.257 for the Earth.

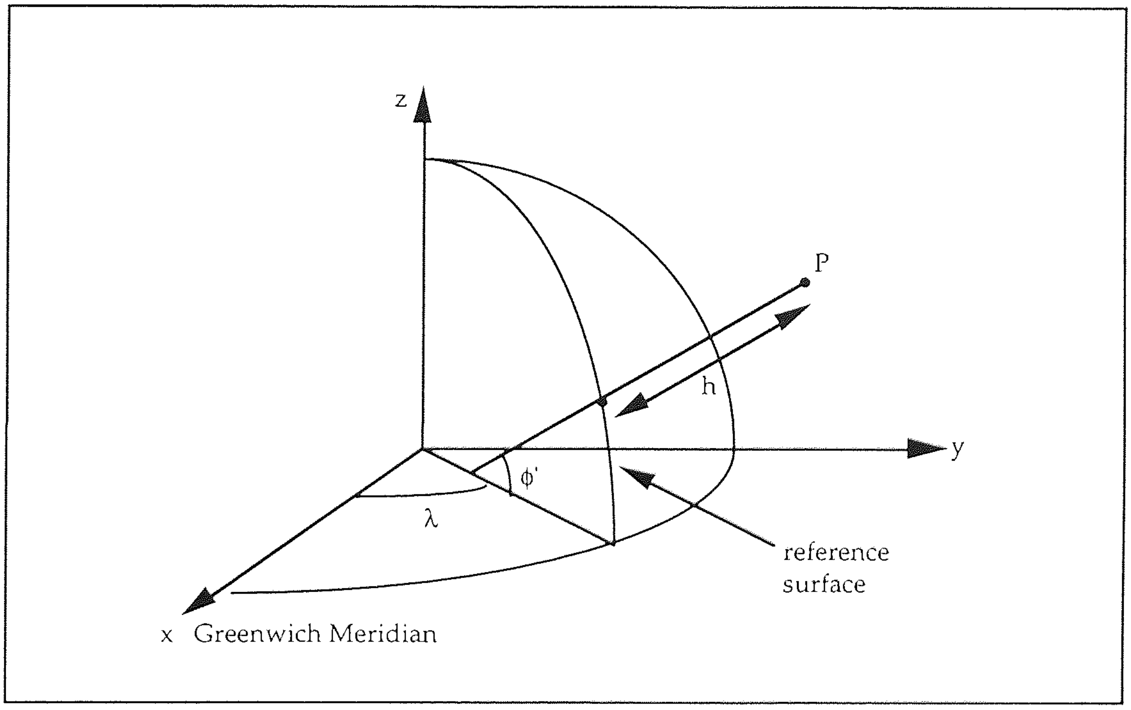

Figure B.1

The parameter N is the radius of curvature at (ϕ', λ) given by

$$N = \frac{R_E}{\sqrt{(\cos^2\phi' + (1-e^2)\sin^2\phi')}} \tag{B.6}$$

The inverse of equations B.3 are

$$h = \frac{\sqrt{(x^2+y^2)}}{\cos\phi'} - N$$

$$\phi' = \tan^{-1}\left\{\frac{z}{\sqrt{(x^2+y^2)}}\left(1-\frac{e^2 N}{N+h}\right)^{-1}\right\}$$

$$\lambda = \tan^{-1}\left(\frac{y}{x}\right) \qquad \text{(B.7)}$$

and these are solved iteratively using the geocentric latitude ϕ as a first approximation to ϕ'.